Progress in Particle and Nuclear Physics 139 (2024) 104119

Contents lists available at ScienceDirect

Progress in Particle and Nuclear Physics

journal homepage: www.elsevier.com/locate/ppnp

Review

Multifaceted character of shape coexistence phenomena in atomic nuclei

S. Leoni [a,b,*], B. Fornal [c], A. Bracco [a,b], Y. Tsunoda [d], T. Otsuka [e,f]

[a] Dipartimento di Fisica dell'Università degli Studi di Milano, Milan 20133, Italy
[b] INFN, Sezione di Milano, Milan 20133, Italy
[c] Institute of Nuclear Physics Polish Academy of Sciences, Krakow 31-342, Poland
[d] Center for Nuclear Study, The University of Tokyo, 7-3-1 Hongo, Bunkyo, Tokyo 113-0033, Japan
[e] Department of Physics, The University of Tokyo, 7-3-1 Hongo, Bunkyo, Tokyo 113-0033, Japan
[f] RIKEN Nishina Center, 2-1 Hirosawa, Wako, Saitama 351-0198, Japan

ARTICLE INFO

Keywords:
Nuclear structure
Shape coexistence
Shape isomers
Superdeformed bands

ABSTRACT

This article is devoted to a review of decay properties of excited 0^+ states in regions of the nuclear chart well known for shape coexistence phenomena. Even–even isotopes around the Z=20 (Ca), 28 (Ni), 50 (Sn), 82 (Pb) proton shell closures and along the Z=36 (Kr), Z=38 (Sr) and Z=40 (Zr) isotopic chains are mainly discussed. The aim is to identify examples of *extreme shape coexistence*, namely highly deformed structures, well localized in the Potential Energy Surface in the deformation space, which could lead to γ decays substantially hindered. This is in analogy to the 0^+ fission shape isomers in the actinides region and to the superdeformed (SD) states at the decay-out spin in medium/heavy mass systems. In this survey, the Hindrance Factor (HF) of the E2 transitions de-exciting 0^+ states or SD decay-out states is a primary quantity which is used to differentiate between types of shape coexistence. The 0^+ states, examined with the help of the hindrance factor, reveal a multifaceted scenario of shape coexistence. A limited number of 0^+ excitations (in the Ni, Sr, Zr and Cd regions) exhibit large HF values (>10), some of which are associated with the clear separation of coexisting wave functions, while in most cases the decay is not hindered, due to the mixing between different configurations. Comparisons with theory predictions based on various models are also presented, some of which shed light on the microscopic structure of the considered states and the origin of the observed hindrances. The impact of shape ensembles at finite temperature on the decay properties of highly-excited states (Giant Dipole Resonances) is also discussed. This research area offers a complementary approach for identifying regions where extreme shape coexistence phenomena may appear.

1. Introduction

In many body quantum systems, the phenomenon of coexistence of different arrangements of constituents, within the same object, is present on different scales. In chemistry, for example, molecules or polyatomic ions with identical molecular formulae – that is, same number of atoms of each element – but distinctly different arrangements of atoms in space, were originally termed isomers. In the so-called "stereoisomerism" (or "spatial isomerism"), for example, the bonds are the same but the relative positions of the atoms differ and isomers can be created just by rotations about single bonds.

* Corresponding author at: Dipartimento di Fisica dell'Università degli Studi di Milano, Milan 20133, Italy.
E-mail address: silvia.leoni@mi.infn.it (S. Leoni).

https://doi.org/10.1016/j.ppnp.2024.104119

Available online 29 May 2024

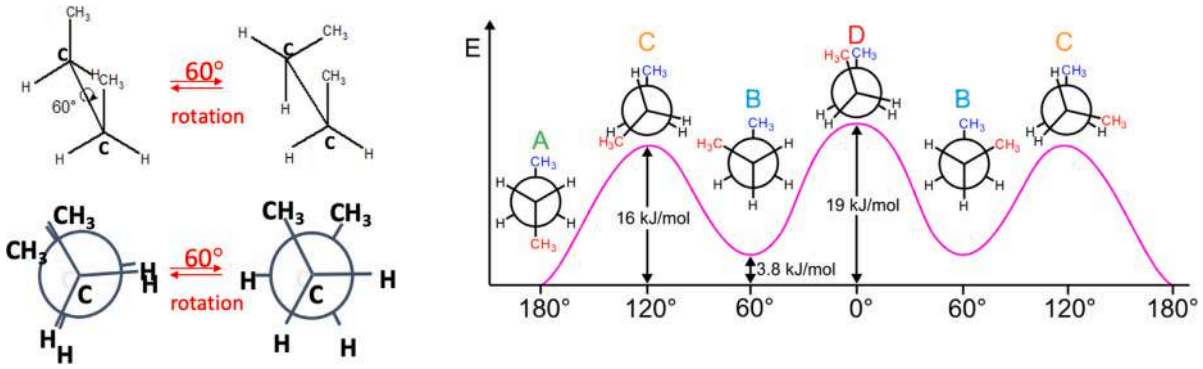

Fig. 1. Example of isomers from chemistry: the conformational isomers of the butane molecule C_4H_{10}. (a) Rotation about single bond of butane to interconvert one conformation to another (top: three dimensional spatial orientations; bottom: two-dimensional projections). (b) Relative conformation energy diagram of butane as a function of dihedral angle [1,2].

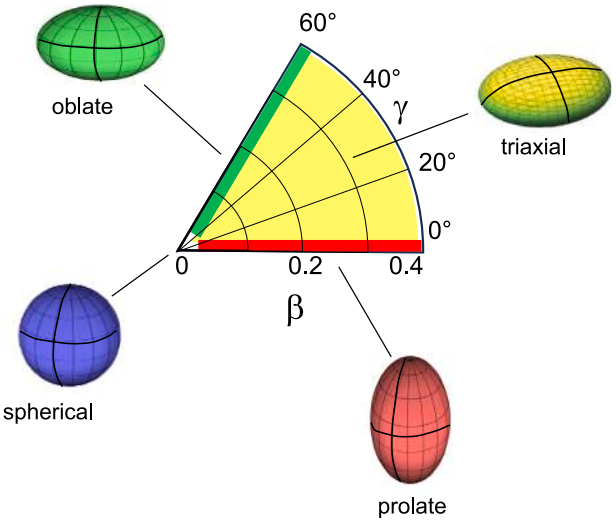

Fig. 2. Nuclear shapes of ellipsoidal symmetry, represented in the so-called $\beta - \gamma$ plane. The β parameter gives the total deformation of the nucleus ($\beta = 0$ is a sphere and $\beta \neq 0$ is an ellipsoid), while the parameter γ describes the deviations from axial symmetry (resulting in triaxiality). The typical scale for β is 0.2 for normal deformed shapes, and 0.6 for strongly elongated shapes. (See Eq. (1) and related discussion).

An example of spatial isomerism is shown in Fig. 1(a), in the case of the butane molecule. Different conformations can be obtained by any two arrangements of atoms in a molecule that differ by rotation about single bonds, and conformations that correspond to local minima on the potential energy surface are specifically called conformational isomers or conformers (see Fig. 1(b)). Rotations about single bonds involve overcoming an "angular-displacement" energy barrier to convert one conformer into another. If the energy barrier is low, a sample of the compound exists as a mixture of multiple conformers, corresponding to different "angular-displacement" rotations. On the contrary, if the barrier is high enough then the rotation is restricted to a specific configuration, and a molecule may exist for a relatively long time as a stable rotational isomer (named "rotamer"). In such a case, the time scale for the conversion of the molecule into a different configuration can be long enough (half-life of 1000 s or longer) sufficient for the isolation of individual rotamers [1,2].

In nuclear physics, different spacial arrangements of nucleons can also be found within the same nucleus, made of Z protons and N neutrons, leading to eigenstates which can be associated with different 'shapes' of the overall system (see Fig. 2). The very concept of 'shape' for an object like the nucleus, made of closely packed, strongly interacting fermions, is far from obvious, but has a solid experimental evidence. Within the model introduced by Bohr and Mottelson [3], the nuclear density, defined by a mean field which confines the nucleons, can perform collective motions in terms of rotations and vibrations. This leads to an (approximate) separation of collective and single-particle degrees of freedom which allows to define an intrinsic system characterized by a nuclear shape. Such a concept represents one of the essential tools to interpret and classify nuclear structures through the nuclear chart, and allows to make comparisons with other physical phenomena characterized by spontaneous symmetry breaking [4–7]. This 'macroscopic' picture of the nucleus can be extended to consider the possibility that a given nucleus displays different configurations corresponding to different intrinsic shapes, with similar excitation energies, a phenomenon which is named "shape coexistence". The

main theoretical tool to determine such shapes resides in mean-field (Hartree–Fock-type) calculations constrained to produce given values of the relevant deformation parameters [8,9]. The resulting Potential Energy Surfaces, and the local minima they display, represent a very valuable mean to understand the nuclear behavior, and will be one of the central tools adopted in the present review.

The appearance of two well separated minima in the potential energy surface of the nuclear system, described as a liquid drop, was first discussed in the '50s, by Hill and Wheeler, in connection with possible consequences on fission phenomena [10]. However, the specific idea of shape coexistence emerged in the '60s by studying fission shape isomers observed in the actinides, which were considered as an "exotic rarity" [11–13]. Subsequent studies demonstrated the appearance of "regions of coexistence" in different places of the nuclear chart. In the '70s, indication of shape coexistence came unexpectedly from optical hyperfine structure studies of the Hg isotopes, performed at CERN-ISOLDE, with the observation of an extremely large isotope shift between A = 185 and 187 [14]. The identification of 0^+ states with rotational bands built on them immediately followed from in-beam and decay-spectroscopy investigations, and an island of shape-coexistence phenomena was gradually identified in the neutron-deficient Hg and Pb region [15]. More or less at the same time, first indication of shape coexistence in the Z = 50 region came from the observation of collective bands in even Sn isotopes, around the stability valley [16], while subsequent studies spread this concept down to the region of Kr, Sr, and Zr isotopes, in particular around mass A = 100 [17], where shape-coexistence phenomena were predicted by Skalski et al. employing the Nilsson–Strutinsky method with the cranked Woods–Saxon potential [18]. On the proton-rich side, Kr isotopes were also found to display peculiar properties of fully degenerate configurations exhibiting oblate and prolate shapes [19,20]. In more recent years, extended spectroscopic investigations along the Z = 28 Ni chain gave evidence for a complex scenario of multiple shape coexistence, extending across the N = 40 neutron-subshell closure and already appearing in nuclei such as ^{62,64}Ni, considered to be spherical within a mean field approach [21]. For still lighter nuclei, the existence of ground state deformation in the ^{32}Mg semi-magic nucleus was evidenced already in the '80s, paving the way to the discovery of an "island of inversion" around ^{32}Mg, i.e., the appearance of deformed structures at low excitation energy in Na, Mg and Al isotopes at N = 20, which were located in a series of studies [22–24]. The phenomenon was interpreted on the basis of shell model calculations, performed already in the '90s, as resulting from an exchange of the relative position of the lowest spherical and lowest neutron 2p-2h intruder deformed 0^+ states [25]. Additional peculiar examples in rather light systems, at the stability valley, are ^{24}Mg, where a recent E0 measurement indicated a significant shape change between the ground state and first-excited 0^+ state [26], and ^{28}Si, exhibiting an oblate ground state, a first excited 0^+ state with suggested prolate shape, and an expected superdeformed band tentatively located at high excitation energy [27]. It follows that the shape-coexistence phenomenon is now considered to be present over virtually the entire region of the nuclear chart, up to the driplines [28].

Even though the shape-coexistence phenomenon in nuclei has been known for more than six decades, it is still one of the important topics which requires theory developments unveiling hidden properties of known nuclei and explorations further into exotic regions of the Segrè chart.

There exists a vast literature which discusses various aspects of the shape coexistence in nuclei, focusing on low spins. In a series of review papers, Heyde and Wood provided an extensive overview, from both theoretical and experimental perspectives, of this phenomenon in odd-mass nuclei (Heyde et al. 1983 [29]), in even–even nuclei (Wood et al. 1992 [30]), of the occurrence of electric monopole E0 transitions with shape coexistence (Wood et al. 1999 [31]), and an update toward a unified view (Heyde et al. 2011 [15]). Recent advances in the field were summarized in 2016 in the Focus Issue of Journal of Physics G, edited by Wood and Heyde [32], and in 2022 by the experimental overview of Garrett et al. [24] and Kibedi et al. for electric monopole E0 transitions [33].

In the '80s, the development of large arrays of γ-ray detectors [34], starting with the TESSA array in Daresbury and later leading to complex instruments like EUROBALL [35–37], GAMMASPHERE [38,39] and successors, extended the concept of shape coexistence to superdeformed (SD) bands at high spins, although no clear connection to shape coexistence at low spins was made [40,41]. This was caused by the sparseness of experimental information on highly-deformed structures at low spins (see Sections 3.2.1 and 3.2.2), and by the difficulties in providing a unified theoretical description of both phenomena in medium- and heavy-mass systems. At present, while a fully microscopic, quantum-mechanical approach starts to be computationally capable of describing nuclear structure properties at low-spins, at least in light- and medium-mass nuclei, its application at high-spins is still rather limited. In this high-spin regime, semiclassical models, such as for example Total Routhan surfaces (TRS) calculations [42–45], offer the best results – a comprehensive description of shape coexistence from 0 to high spins is still a challenge.

In our review, we would like to discuss the shape coexistence phenomenon from a specific perspective, i.e., by distinguishing two main classes of this phenomenon, namely (i) the case of "extreme" shape coexistence, with shape isomers and superdeformation as outstanding examples, and (ii) the most common case of "mixed-shape" coexistence. In the following sections, we will first define these two classes by focusing on 0^+ states in even–even systems. In the discussion we will use the theoretical concepts of Potential Energy Surfaces (PES) and distributions of wave function components in the deformation space (Section 2). Experimental observables which may reveal shape coexistence in atomic nuclei and characterize its type will be introduced. Of primary interest will be the hindrance of transition probabilities of E2 decays connecting states with different shapes, which is sensitive to the separation of the wave functions in the deformation space. Hindrance factors (HF), spanning a very large range of experimental values (from $\sim 10^{-2}$ to $\sim 10^{8}$), will be used to classify the type of shape-coexistence scenario. Next, we will concentrate on the case of "extreme" shape coexistence (Section 3) which encompasses fission shape isomers and superdeformation at high spins, as archetypal example of extreme shape coexistence.

In Section 4, a survey of experimental 0^+ excitations will be presented focusing on even–even isotopes around Z = 20 (Ca), Z = 28 (Ni), Z = 50 (Sn), Z = 82 (Pb) proton shell closures and along Z = 36 (Kr), Z = 38 (Sr) and Z = 40 (Zr) isotopic chains. The main

aim is to identify 0^+s with highly deformed shapes which could provide additional examples of shape isomers in medium/heavy mass regions. Anticipating, as a result of this extended investigation, only one clear case of shape-isomers-like structure and few other candidates have been identified in the Ni, Sr, Zr and Cd nuclei, while the vast majority of the known 0^+ states is found to exhibit characteristics typical of "mixed" shapes.

The issue of shape coexistence and triaxiality will be discussed in Section 5, while Section 6 will deal with nuclear shapes at finite temperature, in particular when the excitation energy of the nucleus is much higher than the nucleon binding energy. In this excitation-energy regime, a thermodynamical approach is needed to describe the ensemble of states with different deformation, which is then probed by studying Giant Resonances [46]. Perspectives in experimental searches and conclusions will be given in Section 7.

2. Nuclear shapes and shape coexistence

In the context of the Bohr and Mottelson model [3], it has been common to describe the nucleus as a liquid drop with a uniform density, as originally proposed by N. Bohr and J. A. Wheeler [47]. In this approach, the nuclear shape can be parametrized in the body-fixed frame by writing the radius R in polar coordinates, as an expansion in spherical harmonics

$$R(\theta,\gamma) = R_0(1 + \sum_{\lambda\mu} \alpha_{\lambda\mu} Y_{\lambda\mu}(\theta,\phi)) \tag{1}$$

where $R_0 = 1.2$ fm $A^{1/3}$ is the radius of the sphere of the same uniform density, with A being the mass number. The most considered nuclear shapes have quadrupole deformation ($\lambda = 2$), which corresponds to an ellipsoid. In this case, only two $\alpha_{\lambda\mu}$ coefficients in the $R(\theta,\gamma)$ expression are real and independent variables, α_{20} and $\alpha_{22} = \alpha_{2-2}$, and they can be expressed in terms of β and γ parameters, as follows:

$$\begin{aligned} \alpha_{20} &= \beta cos\gamma \\ \alpha_{22} &= \frac{1}{\sqrt{2}}\beta sin\gamma \end{aligned} \tag{2}$$

Fig. 2 shows the convention for shapes of ellipsoidal symmetry, using the so-called (β,γ) plane, which is widely used in mean-field based models. Other theoretical approaches may not start from an explicit use of the concept of 'deformation'. For example, advanced shell-model calculations, carried out in a large model space with appropriate effective interactions, can lead to microscopic predictions of nuclear configurations and of the electromagnetic transitions connecting them [48–50]. We will discuss the use of such shell model techniques mostly within the Monte Carlo Shell Model (MCSM) formalism [51–54].

The shell-model configurations can be associated with different matter and charge densities in the proper body-fixed frame, and can be put in relation with the 'shapes' assumed by more intuitive approaches. Such a connection can be made by inspecting the distribution of the corresponding wave function components in the Potential Energy Surface (PES) in the (β,γ) plane. If the wave function is localized in a specific region of the plane, the nuclear shape is well represented by the corresponding (β,γ) deformation parameters, while for a state with a spread distribution of wave function components, the shape may become less defined. Fig. 3 illustrates this concept in the cases of $0^+_{1,2,4}$ (panels (a), (c) and (d)) and 2^+_1 (b) excitations in ^{66}Ni, using the PES obtained from the Hamiltonian employed in the Monte Carlo Shell Model (MCSM) calculations of Tsunoda et al. [55], discussed in details in Section 4.2.1. Circles on the PES represent the main components of the corresponding wave functions, with sizes proportional to their overlap probabilities and locations associated with the intrinsic shape. The PES is characterized by a rather shallow valley (blue region), extending from the main spherical minimum to an oblate secondary minimum, with no energy barrier in between. A well defined prolate (β~0.4) secondary minimum is also found, well shielded by a sizeable barrier from the spherical-oblate well. The wave functions of the 0^+_1 ground state and 2^+_1 excited state are mainly localized in the spherical region of the (β,γ) plane, what indicates a dominant spherical shape for these states, although several (minor) components spread into the oblate side. On the contrary, the 0^+_2 and 0^+_4 excitations are well contained in the oblate and prolate minima, thus implying oblate and prolate shapes for these states, respectively.

Within the microscopic framework discussed above, the shape coexistence phenomenon occurs when in a nucleus there exist states of the same spin and parity (and similar excitation energy) with wave functions well localized in different regions of the PES, i.e., corresponding to clearly distinguishable shapes. From the perspective of MCSM calculations mentioned in the previous paragraph, ^{66}Ni provides a clear example of shape coexistence. Similar conclusions on ^{66}Ni and other systems in different mass regions were also achieved, in the '80s, by mean-field based approaches from a pure inspection of the PES landscape [15,42,56–59].

In the following sections, we will first briefly discuss the origin of the shape coexistence phenomenon in the general context of shell evolution (Section 2.1), highlighting the important role of the monopole component of tensor forces of the NN interaction. We will then introduce experimental signatures for shape coexistence (Section 2.2), encompassing energy spectra, electromagnetic transition probabilities and moments, and specific features of population mechanisms. In Section 2.3, we will schematically discuss the variety of shape coexistence scenario focusing on even–even nuclei, where 0^+ states can be considered as the ground states of different shapes. The hindrance factor (HF) of the E2 decay will be introduced in Section 2.2, as a simple, yet useful, guidance to categorize a large variety of shape coexistence cases.

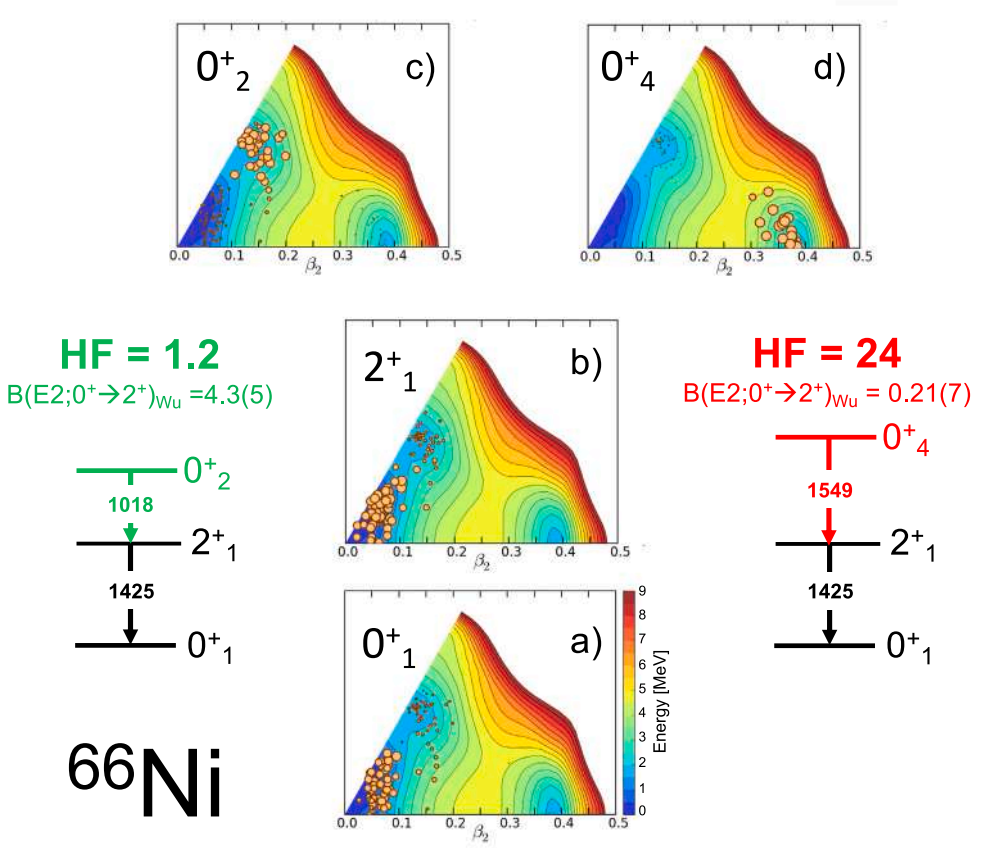

Fig. 3. Potential Energy Surface (PES) of ^{66}Ni in the (β, γ) plane, as obtained by the Hamiltonian used in the Monte Carlo Shell Model (MCSM) calculations of Tsunoda et al. [55]. Circles show the main components of the wave function for the ground state 0^+_1 (a), the first excited state 2^+_1 (b), and the 0^+_2 (c) and 0^+_4 (d) states. Decay schemes for the $0^+_{2,4} \rightarrow 2^+_1 \rightarrow 0^+_1$ cascades are shown on the left and right side, with measured B(E2; $0^+_{2,4} \rightarrow 2^+_1$) and corresponding hindrance factors (HF), defined by Eq. (3) and referring to the decay from high to low spins (note B(E2;$2^+ \rightarrow 0^+$) = 1/5 B(E2;$0^+ \rightarrow 2^+$)). Energies (in MeV) are given by the common color scale in (a). See Sections 2.2.2 and 4.2.1 for further details.

2.1. Origin of shape coexistence in the context of shell evolution

It is nowadays well established that the shape of a nucleus varies as Z or N changes along a shell, being nearly spherical close to magic numbers, while more deformed shapes appear toward the middle of the shell. At the same time, magic numbers can change when moving away from stability, as a consequence of modifications of the shell structure due to nuclear forces in systems with larger N/Z imbalance – this is referred to as *shell evolution*. Review articles on shell evolution can be found in Refs. [60,61].

Fig. 4 displays how the shell evolution occurs due to the monopole component of tensor forces of the NN interaction. Panel (a) shows the relevant shell structure when this monopole interaction is switched off. In exotic nuclei, the spin–orbit splitting between $j_>(= l + 1/2)$ and $j_<(= l - 1/2)$ proton orbits is reduced as neutrons occupy $j'_>(= l' + 1/2)$ orbits as shown in panels (b) and (c). This phenomenon has been observed in many nuclei since it was pointed out in Refs. [60,62]. Fig. 5 shows one of the early examples, exhibiting proton single-particle energies of $1h_{11/2}$ and $1g_{7/2}$ in Sb isotopes: experimental values are taken from Ref. [63]. The theoretical values were obtained by considering the mechanism illustrated in Fig. 4 (b) and (c), where, as the neutron $1h_{11/2}$ orbit is filled by more neutrons, the proton $1h_{11/2}$ is raised but the proton $1g_{7/2}$ is lowered. The same effect on the proton $h_{11/2}$ and $g_{7/2}$ orbitals can be obtained if neutrons are placed into the $j'_>(= l' + 1/2)$ orbit by moving them from some orbits below. If neutron holes are created in $j''_<$ orbit (see panel (d)), the tensor monopole interaction reinforces the reduction of the spin–orbit splitting. In this way, certain neutron particle-hole excitations can significantly change proton shell structure, and such changes can be magnified as more neutrons are excited (panel (e)). This latter phenomenon is called *Type II shell evolution* [55], while the shell evolution by the change of N or Z is referred to as *Type I*, if necessary [62,64].

The discussed phenomena can be effectively illustrated by examining the structure of Ni nuclei around A = 68, as predicted by shell model calculations [62,64]. This analysis is particularly relevant in connection with the emergence of coexisting shapes. In ^{66}Ni, for example, according to MCSM calculations, the 0^+_1, 0^+_3 and 2^+_1 states are spherical – major components of their wave functions are concentrated in the main, spherical minimum of the PES (see Fig. 3 for the 0^+_1 and 2^+_1 states). With respect to these spherical states, 0^+_2 and 0^+_4 are found to be composed of sizeable excitations of protons across the Z = 28 shell gap (from $f_{7/2}$ to

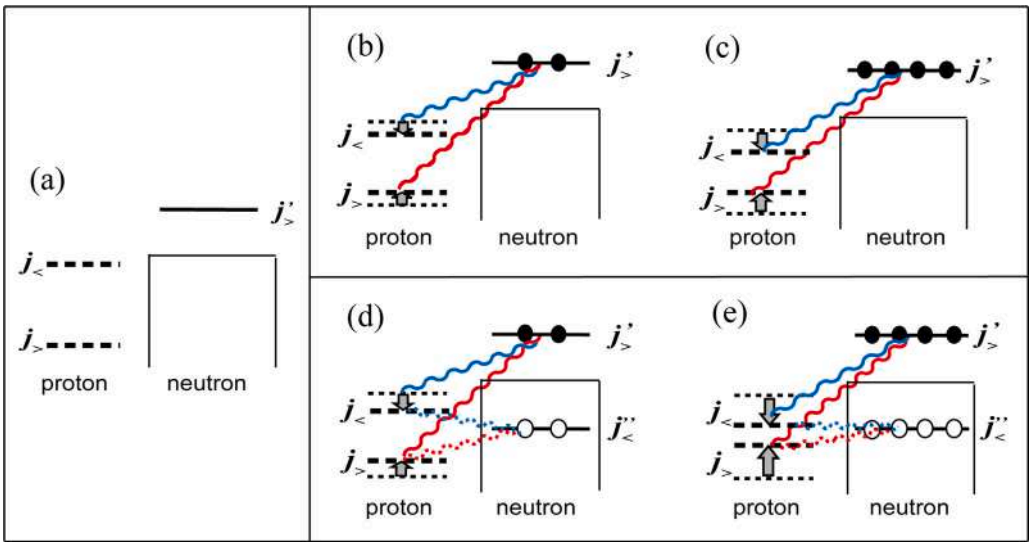

Fig. 4. Schematic illustration of the microscopic mechanisms named *Type I shell evolution* (panels (b) and (c)), and *Type II shell evolution* (panel (d) and (e)), induced by the monopole component of tensor forces of the NN interaction. (wavy lines). Closed (open) circles denote neutron particles (holes). See text for details.
Source: Taken from [64].

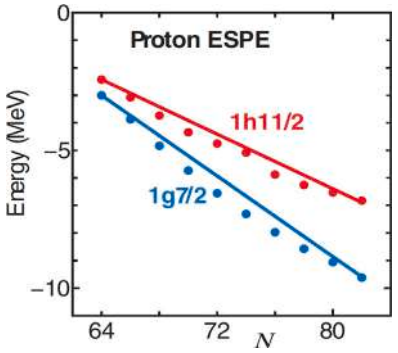

Fig. 5. Proton single-particle energies of $1h_{11/2}$ and $1g_{7/2}$ orbitals of Sb isotopes as functions of the neutron number. The symbols are experimental values from (α,t) transfer-reaction studies [63] and β-decay spectroscopy (for ^{133}Sb) [65], while the lines are theoretical predictions including the tensor force effect.
Source: Taken from [62].

$f_{5/2}$ and $p_{3/2;1/2}$), as well as neutrons across the N = 40 subshell gap (from $f_{5/2}$ and $p_{3/2;1/2}$ to $g_{9/2}$ and $d_{5/2}$) (see Fig. 6, left). These excitations create valence particles in the upper shell and holes in the lower shell, which facilitates the development of deformation in the 0^+_2 and 0^+_4 excited states. To be more concrete, in the 0^+_2 state, of ^{66}Ni, ∼1 proton and ∼1.5 neutrons are excited, whereas these numbers are twice as large in the 0^+_4 state. The proton shell structure then differs between the 0^+_2 and 0^+_4 states, and the decreased $f_{7/2}$–$f_{5/2}$ spin–orbit splitting produces much weaker resistance against the deformation, as the deformation is largely due to mixing of single-particle orbits (a realization of the so-called *Jahn–Teller effect* in atomic nuclei [4,5,7]). As a consequence, stronger deformation occurs in the 0^+_4 state compared to the 0^+_2: the first one (i.e., 0^+_4) lies in a deep prolate well of the PES, while 0^+_2 is located in a shallow oblate minimum. Similar phenomena can be seen in other Ni isotopes, such as ^{68,70}Ni, producing eminent shape coexistence phenomena. As shown in Fig. 6 (right), the single-particle active orbitals in Sn isotopes, around A = 114, are expected to be, for neutrons $h_{11/2}$, and for protons $g_{9/2}$ and $g_{7/2}$. Therefore, one may speculate that a similar mechanism of *Type II shell evolution* may give rise to 0^+ excitations with different deformation also in the Sn chain (See Section 4.4.1).

2.2. Experimental signatures of shape coexistence

There are several spectroscopic fingerprints that may reveal shape coexistence in atomic nuclei. These are: (i) energies of low-lying states, (ii) probabilities of γ decay connecting nuclear states, (iii) strength of E0 transitions, (iv) electromagnetic multipole moments, and (v) population mechanisms. A final complete picture of shape coexistence, for a given nuclear system, can only be achieved by gathering all mentioned information, what requires the employment of different reaction mechanisms and experimental

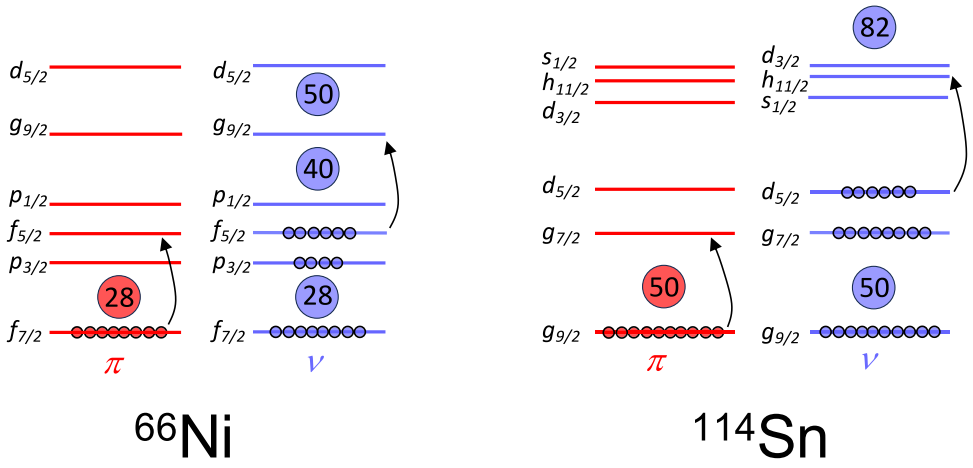

Fig. 6. Active shell-model orbitals for ^{66}Ni (Z = 28 and N = 38), left, and ^{114}Sn (Z = 50 and N = 64), right. Arrows indicate the excitation process promoting neutrons into the unique parity orbitals $g_{9/2}$ ($h_{11/2}$), which favors proton excitations from $f_{7/2}$ to $f_{5/2}$ ($g_{9/2}$ to $g_{7/2}$), due to a reduction of the spin–orbit splitting. Energy spacing between orbitals is indicative. See text for details.

techniques. In reality, this is a very difficult task and often one has to rely on partial knowledge and comparison with theory predictions.

In the following, we characterize in more detail the aforementioned nuclear properties, which may signal coexistence of different shapes at low excitation energy and spin.

2.2.1. Energy spectra

One of the most straightforward hints of shape coexistence phenomena is provided by the level structure at low spin. For example, in even–even spherical nuclei, the presence of low-lying 0^+ states may indicate the existence of excited structures with different deformation. Such situation occurs mostly in the vicinity of major closed shells (or sub-shells), where low-lying 0^+ states may arise from promotion of pairs of particles to orbitals lying above the shell closure. These excitations gain their binding energy from correlations, including quadrupole deformation. As a consequence, moving along isotopic chains, the excitation energies of shape-coexisting states are often found to follow a parabolic-like trend, with the centroid of the parabola around mid-shell [15]. Examples of parabola-like behavior of 0^+ states will be shown in Section 4 for isotopic chains around Z = 28, 40, 50 and 82.

Next, the observation of specific energy-level patterns could give a first indication of the properties of the coexisting shapes. In particular, a sequence of states with energies characteristic of rotational bands built on top of excited 0^+ states, while the ground state is spherical or weakly deformed, can be seen as strong fingerprint of shape coexisting structures. These types of state sequences have been reported in a number of cases, as for example in the Zr and Sn regions, as well as in heavier nuclei, e.g., Hg and Pb isotopes [15,24]. The situation is illustrated in Fig. 7, where the level energy systematics is given for even–even neutron deficient Pb isotopes [66]. In Section 4, various examples of rotational bands built on excited 0^+ states, of oblate and prolate nature, will be given.

The appearance of superdeformed bands, with very regular rotational energy patterns, is a special case of shape coexistence. Here, looking at the PES as a function of spin, it is found that the deformed minimum, above a certain spin, becomes lower in excitation energy than the spherical or normal deformed (ND) minimum at the same spin. The nucleus is then trapped in the superdeformed (SD) well. Vice versa, with decreasing spin, the superdeformed states come to lie above the ND yrast line and, becoming embedded in a sea of normal deformed states, coexist with those states. Such a scenario will be discussed in Section 3.2.

2.2.2. Electromagnetic transition probabilities

The pattern of the excitation spectrum is not a sufficient condition to firmly establish the type of shape coexistence, and detailed spectroscopy investigation is needed to assess, for example, the collectivity of a rotational band built on top of an excited 0^+ state, or to pin down the degree of mixing between states residing in different locations of the Potential Energy Surface.

The electromagnetic quadrupole (E2) transitions are among the most sensitive probes of the collectivity of a band – the B(E2) decay probability between in-band states can be directly related to the quadrupole moment of the excited structure and, consequently, to the deformation parameter β (see discussion in Section 2.2.3). E2 transitions are also very sensitive to the degree of shape mixing between an excited 0^+ state and lower-lying states in the main minimum.

One expects that quantum states corresponding to very different shapes will be associated to quite different nucleonic configurations, and that the matrix elements of operators like E2, connecting them, will be generally small, compared to those between states associated with more similar shapes (the E2 operator can move just one nucleon from a single-particle state to another, while the rest of the nucleons remain unchanged). This hindrance is often interpreted as a consequence of the existence of sizeable barriers in a more macroscopic description based on Potential Energy Surfaces. On the other hand, the transition matrix

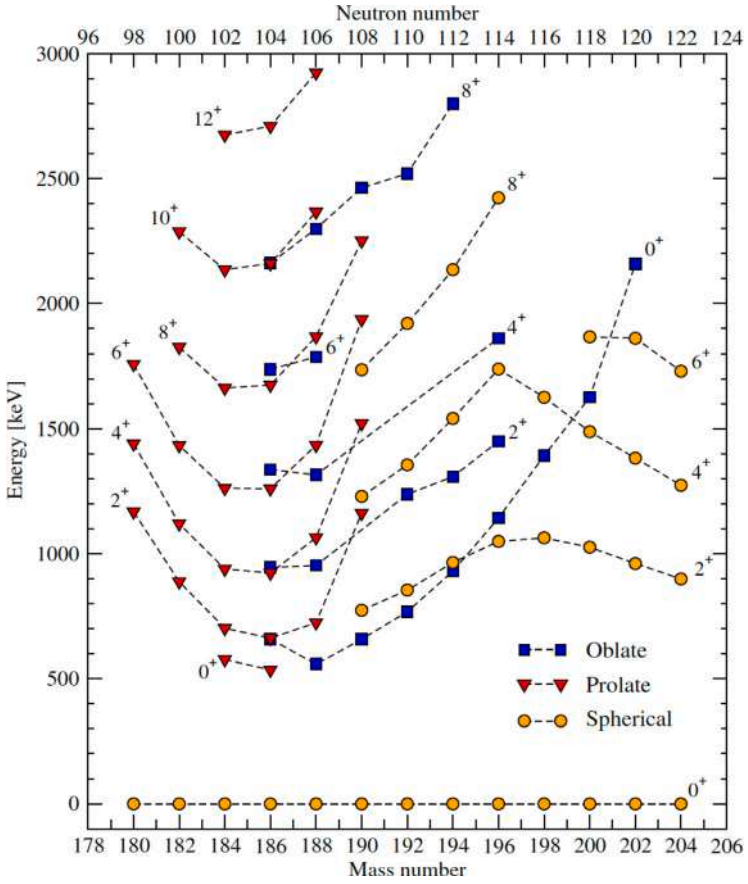

Fig. 7. Adopted level energy systematics of the neutron-deficient even-mass Pb nuclei [67]. The different predominant intrinsic configurations are marked by different labels and are connected with dashed lines.
Source: Taken from [66].

elements may cancel each other due to quantum interference, and it may happen that matrix elements between states associated with similar shapes are small or vanishing.

In the example of ^{66}Ni shown in Fig. 3, the significant overlap of wave functions, in the (β, γ) plane, between the 0_2^+ and 2_1^+ states, calculated by the MCSM, should imply a rather fast E2 decay. Indeed, the experimentally observed E2 transition probability, B(E2; $0_2^+ \rightarrow 2_1^+$) = 4.3(5) W.u., is not low [68]. On the contrary, an hindered E2 decay is expected between the prolate 0_4^+ and the spherical 2_1^+ states, since the wave functions, localized in different PES minima shielded by a sizeable barrier, have no significant overlap. Experimentally, a very small B(E2) value, below the single-particle reference of 1 Weisskopf unit (W.u.), has been measured (B(E2; $0_4^+ \rightarrow 2_1^+$) = 0.21(7) W.u. [68]).

From the above discussion, it follows that the hindrance of E2 transitions is a primary quantity which can be used to differentiate between the types of shape coexistence, where significant mixing in the wave functions or their more distinct separation occurs. According to Löbner [69], the hindrance factors (HF) can be defined from the experimental B(E/Mλ) reduced transition probabilities, relative to the Weisskopf estimates:

$$HF(E/M\lambda) = \frac{T_{1/2\gamma}(exp)}{T_{1/2\gamma}(1\ W.u.\ estimate)} = \frac{1}{B(E/M\lambda)(exp)_{W.u.}} \tag{3}$$

where $T_{1/2\gamma}$(exp) is the experimental partial half-life of the γ transition, $T_{1/2\gamma}$(1 W.u. estimate) is the Weisskopf estimate for the corresponding transition multipolarity, and B(E/Mλ)(exp)$_{W.u.}$ is the experimental reduced transition probability in Weisskopf units (W.u.). In the current paper, HF(E/Mλ) values are always referred to decay from high to low spins, therefore, for E2 decays from 0^+ states, HF(E2) are calculated for B(E2;$2^+ \rightarrow 0^+$) = 1/5 B(E2;$0^+ \rightarrow 2^+$). From the systematics available in literature, typical (reference) HF values for E2 transitions (with $\Delta K = 0$) are of the order of 1 [69], therefore HF > 1 values correspond to retarded transitions, while HF < 1 point to fast decays, as in the case of collective E2 transitions or decays between states with significant overlaps of wave functions.

Main sources of experimental information on B(E2) transition probabilities are nuclear state lifetimes, decay branchings and transition multipolarity mixing ratios [70]. These observables are accessible by standard γ-spectroscopy investigations, provided the

nuclear states of interest are reachable in this kind of studies. In this context, the employed reaction mechanisms play an important role: fusion evaporation is best suited to study medium-high spins, while low-spin states, which are of primary interest here, can be reached using near-barrier transfer reactions, neutron capture, β decay or nuclear resonance fluorescence. Of special interest are studies employing Coulomb excitation reactions. These studies offer, in an independent manner, information on B(E2) transition probabilities which are derived from transitional matrix elements $\langle I_f \| \mathrm{E2} \| I_i \rangle$ [71–74].

2.2.3. Electromagnetic moments

In addition to transition probabilities, multi-step Coulomb excitation measurements can be used to obtain the spectroscopic quadrupole moment, Q_s, which is related to the apparent overall elongation of the charge distribution in a given state, in the laboratory frame [71–74]. However, to extract the intrinsic deformation of the nucleus in that state is not straightforward. In fact, Q_s vanishes not only for a spherical charge distribution, but also for states with J = 0, 1/2 (regardless of the intrinsic deformation), for states which are mixed, with an equal probability of prolate and oblate wave function components, and for γ-soft cases.

There exists a method which allows to determine intrinsic nuclear quadrupole moments, in the intrinsic body-fixed frame, based on a complete set of electromagnetic matrix elements measured in multi-step Coulomb excitation [72,73,75–77]. Information on the intrinsic deformation is obtained by evaluating rotationally invariant scalar products of the electric quadrupole operator. In particular, the quantities Q and δ, representing the quadrupole charge distribution in the intrinsic frame of the nucleus, are obtained from the following expressions:

$$\begin{aligned} \langle I \| [E2 \times E2]_0 \| I \rangle &= \frac{Q^2}{\sqrt{5}} \\ \langle I \| [E2 \times E2]_2 \times E2 \| I \rangle &= -\sqrt{\tfrac{2}{35}} Q^3 cos(3\delta) \end{aligned} \tag{4}$$

Q and δ can be related to the deformation parameters β and γ (defined in Eq. (2)) of the mass distribution of the Bohr model ([77] and references therein), as follows:

$$\begin{aligned} Q^2 &= (\tfrac{3}{4\pi} ZeR_0^2)^2 (\beta^2 + \tfrac{1}{2}\sqrt{\tfrac{5}{4\pi}}\beta^3 cos(3\gamma) + \tfrac{5}{64\pi}\beta^4 + \cdots) \approx (\tfrac{3}{4\pi} ZeR_0^2)^2 \beta^2 \\ Q^3 cos(3\delta) &= (\tfrac{3}{4\pi} ZeR_0^2)^3 (\beta^3 cos(3\gamma) + \tfrac{3}{4}\sqrt{\tfrac{5}{4\pi}}\beta^4 + \tfrac{15}{64\pi}\beta^5 cos(3\gamma) + \cdots) \approx (\tfrac{3}{4\pi} ZeR_0^2)^3 \beta^3 cos(3\gamma) \end{aligned} \tag{5}$$

After expanding the $E2$ invariants, appearing in the left-hand side of Eq. (4), over all possible intermediate states, the deformation parameters are determined by a sum-rule technique, namely by summing over all closed loops of $E2$ matrix elements connected to a specific state (including the diagonal ones), although only a few key states usually contribute to the invariants in a meaningful way. This approach allows to obtain information on deformation parameters also in the case of 0^+ states, provided all $E2$ matrix elements connected to the specific 0^+ excitation are available, to avoid biases on the extraction of Q and δ. We note that in the case of the ground state of an even–even nucleus, the contributions to Q^2 are dominated by the coupling to the first excited 2_1^+ state, which takes more than 90% of the total. As a consequence, one can write

$$Q^2(0_1^+) \approx |\langle 2_1^+ \| E2 \| 0_1^+ \rangle|^2 \tag{6}$$

which leads to the frequently-used expression linking β and B(E2; $0_1^+ \rightarrow 2_1^+$):

$$\beta^2 \approx \frac{4\pi}{3ZeR_0^2} \sqrt{B(E2; 0_1^+ \rightarrow 2_1^+)} \tag{7}$$

Similarly, the largest contributions to $Q^3 cos(3\delta)$ for the ground state of an even–even nucleus come from the following matrix elements products: $\langle 0_1^+ \| E2 \| 2_1^+ \rangle \langle 2_1^+ \| E2 \| 2_1^+ \rangle \langle 2_1^+ \| E2 \| 0_1^+ \rangle$ and $\langle 0_1^+ \| E2 \| 2_1^+ \rangle \langle 2_1^+ \| E2 \| 2_2^+ \rangle \langle 2_2^+ \| E2 \| 0_1^+ \rangle$.

For completeness, we here report the basic relations in the particular case of an axially symmetric rigid rotor, with rotational energy $E_{rot} = \frac{\hbar^2}{2\Im}(I(I+1) - K^2)$, where $\Im$ denotes the moment of inertia of the system, and K is the projection of the angular momentum I onto the symmetry axis of the nucleus. It is found that the reduced matrix elements of the $E2$ operator are related to Q, as follows

$$\langle K I_f \| E2 \| K I_i \rangle = \sqrt{(2I_i + 1)} \langle I_i, K, 2, 0 | I_f, K \rangle \sqrt{\frac{5}{16\pi}} Q \tag{8}$$

where $\langle I_i, K, 2, 0 | I_f, K \rangle$ is the Clebsch–Gordon coefficient, from which one gets the reduced transition probability

$$B(E2, K I_i \rightarrow K I_f) = \frac{5}{16\pi} Q^2 \langle I_i, K, 2, 0 | I_f, K \rangle^2 \tag{9}$$

We remind that an intrinsic quadrupole moment Q derived from a B(E2) value via the expressions above is often referred to as transitional quadrupole moment Q_t.

Under the assumption of quadrupole deformation, it is also possible to obtain a direct relation between the spectroscopic and intrinsic quadrupole moments, Q_s and Q:

$$Q_s = \langle I, K, 2, 0 | I, K \rangle \langle I, I, 2, 0 | I, I \rangle Q = \frac{3K^2 - I(I+1)}{(I+1)(2I+3)} Q \tag{10}$$

The sign of the intrinsic quadrupole moment is positive for prolate and negative for oblate shapes, respectively. It follows that for states with K = 0 the spectroscopic and intrinsic quadrupole moments have opposite signs, therefore the observed shape in the laboratory frame appears to be different from the intrinsic shape. Hence, the measured spectroscopic quadrupole moment does not necessarily provide an unambiguous and model-independent information on the intrinsic shape.

2.2.4. E0 transitions

Complementary information on the type of shape coexistence (i.e., extreme versus mixed-shape coexistence) is offered by electric monopole transitions ($E0$), which are the only allowed decay mode between states with spin $I_i = I_f = 0$. In this case, the photon emission is forbidden and the decay proceeds only via electron conversion emission and electron–positron pair emission (if the decay energy exceeds the mass of the pair, i.e., $\Delta E > 1.022$ MeV) [78].

The $E0$ transitions strength is governed by the $E0$ operator which, for a point-like charge distribution, can be expressed in terms of single-nucleon degrees of freedom, as

$$m(E0) = \sum_k e_k r_k^2 \tag{11}$$

Here, e_k is the effective charge of the *k-th* nucleon and r_k is its position relative to the center of mass of the nucleus. It follows that the diagonal matrix elements of $m(E0)$ are directly related to mean-square charge radii, which are well known to reveal shape changes in nuclei (see, e.g., Ref. [30]).

The E0 transition strength, ρ(E0), between an initial state $|i\rangle$ and a final state $|f\rangle$ is obtained from the matrix element of the electric monopole operator, expressed in dimensionless units [78]:

$$\rho(E0) = \frac{\langle f|m(E0)|i\rangle}{eR_0^2} \tag{12}$$

where $R_0 = 1.2$ fm $A^{1/3}$ indicates the radius of an ideal nucleus with a sharp spherical surface (see also Eq. (1)). In literature, usually one reports the square of ρ(E0) in milliunits, since the typical values of ρ^2(E0) are of the order of 10^{-1}–10^{-3}. It is clear that ρ(E0) is the key quantity which carries all the information about the nuclear structure. In particular, the square of ρ(E0) gives the reduced E0 transition probability:

$$B(E0) = \rho(E0)^2 e^2 R_0^4 \tag{13}$$

Experimentally, ρ(E0) can be determined directly from the partial mean life of the E0 transition, τ(E0), via the expression

$$\frac{1}{\tau(E0)} = W(E0) = W_{IC}(E0) + W_\pi(E0) = \Omega(E0) \times \rho^2(E0) \tag{14}$$

where W(E0), W_{IC}(E0), and W_π(E0) are the total (E0) transition probability and the transition probabilities for internal–conversion electron and electron–positron pair emission, respectively. The factor Ω(E0) is an electronic factor defined by the sum Ω(E0) = Ω_{IC}(E0)+Ω_π(E0), as introduced by Church and Weneser [78]. These Ω factors are functions of the atomic number Z and of the transition energy, and can be calculated independently of nuclear properties.

Alternatively to Eq. (14), ρ(E0) can be determined by the rate, W_γ(E2), of the E2 transition deexciting the state of interest, if available:

$$\rho(E0) = q_K^2(E0/E2) \times \frac{\alpha_K(E2)}{\Omega_K(E0)} \times W_\gamma(E2) \tag{15}$$

where $q_K^2(E0/E2)$ can be deduced from the experimental ratio of the intensities of E0 and E2 K-electron components between the initial and final states:

$$q_K^2(E0/E2) = \frac{I_K(E0)}{I_K(E2)} \tag{16}$$

or from the observed internal pair intensities for the E0 and E2 transitions, via a relation which holds for all atomic shells:

$$q_K^2(E0/E2) = \frac{I_\pi(E0)}{I_\pi(E2)} \times \frac{\Omega_K(E0)}{\Omega_\pi(E0)} \times \frac{\alpha_\pi(E2)}{\alpha_K(E2)} \tag{17}$$

where $\Omega_{K,\pi}$ and $\alpha_{K,\pi}$ are the relevant electronic factors and conversion coefficients, as defined in Ref. [79].

For an extensive summary of the status of $E0$ transitions in nuclei we refer to the 2022 review paper of Kibedi et al. [33], and to previous compilations of Refs. [31,80], while a microscopic model for electric monopole transition matrix elements can be found in Ref. [81]. An overview of adopted values of $10^3 \times \rho^2$(E0) (for both $0_2^+ \rightarrow 0_1^+$ transitions (filled symbols) and for $0_i^+ \rightarrow 0_f^+$, $i > 2$ transitions (open symbols)) is given in Fig. 8. The dashed line corresponds to $10^3 \times \rho^2_{s.p.}(E0) = 0.5\ A^{-2/3}$, which is the expected scaling with the mass number for "single-particle" values [31].

To get a general insight into the relation between ρ^2(E0) and shape coexistence, one usually considers a simple two-level model, which assumes two configurations, $|0_1^+\rangle$ and $|0_2^+\rangle$ corresponding to two shapes with different quadrupole equilibrium deformation [31]. The mixing between these two configurations will result in two eigenstates $|0_i^+\rangle$ and $|0_f^+\rangle$, as follows

$$\begin{aligned} |0_i^+\rangle &= \alpha|0_1^+\rangle + \beta|0_2^+\rangle \\ |0_f^+\rangle &= -\beta|0_1^+\rangle + \alpha|0_2^+\rangle \end{aligned} \tag{18}$$

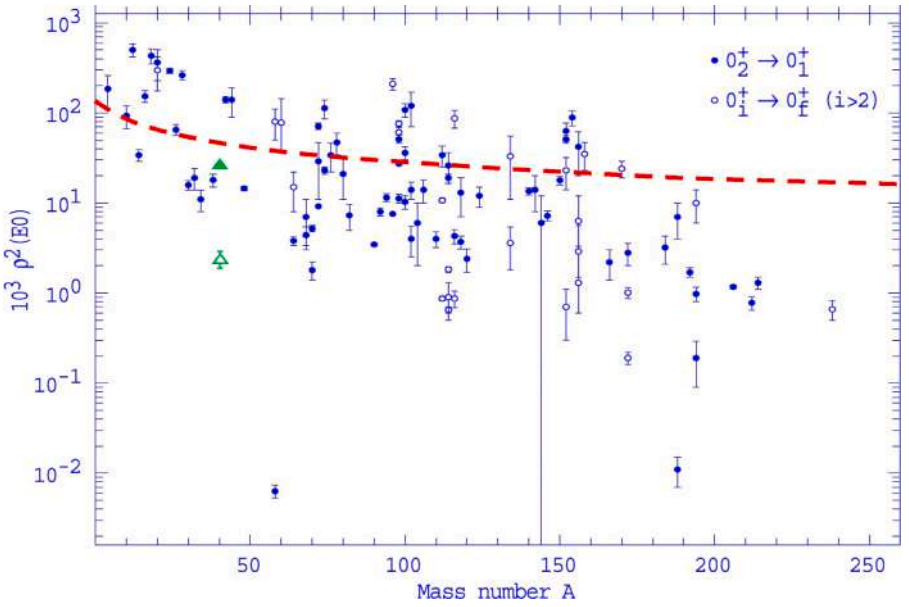

Fig. 8. Adopted values as a function of mass number A for $10^3 \times \rho^2(E0)$ for $0_2^+ \rightarrow 0_1^+$ transitions (filled symbols) and for $0_i^+ \rightarrow 0_f^+$, $i > 2$ transitions (open symbols), from the survey of Ref. [80]. Transitions for which only limits are known have been omitted. The data point for the remarkably small $10^3 \times \rho^2(E0)$ value of $0.66(16) \times 10^{-6}$ in ^{238}U is omitted, while green triangles refer to the recent values for $0_{2,3}^+ \rightarrow 0_1^+$ E0 transitions in ^{40}Ca from Ref. [82]. The dashed line gives the expected scaling with the mass number A for "single-particle" values, i.e., $10^3 \times \rho^2_{s.p.}(E0) = 0.5\ A^{-2/3}$ [31].
Source: Adapted from [80].

where the mixing coefficients α and β satisfy $\alpha^2 + \beta^2 = 1$. In this case, the transition strength $\rho(E0)$ between $|0_i^+\rangle$ and $|0_f^+\rangle$ states takes the form

$$\begin{aligned}\rho(E0) &= \frac{\langle 0_f^+|m(E0)|0_i^+\rangle}{eR^2} \\ &= \frac{1}{eR^2}\left[\alpha\beta\left(\langle 0_1^+|m(E0)|0_1^+\rangle - \langle 0_2^+|m(E0)|0_2^+\rangle\right)\right. \\ &\left. + (\alpha^2 - \beta^2)\langle 0_2^+|m(E0)|0_1^+\rangle\right]\end{aligned} \tag{19}$$

For the case of extreme shape coexistence, i.e., when the mixing between the two states is very low, $\alpha\beta \sim 0$. Moreover, since the wave functions are mainly localized at different points in deformation space, the matrix element $\langle 0_2^+|m(E0)|0_1^+\rangle$ is also close to 0. Therefore, $\rho^2(E0) \simeq 0$.

In the case of strong mixing, the matrix element $\langle 0_2^+|m(E0)|0_1^+\rangle$ is again close to 0, while the absolute value of α and β are of the order of $1/\sqrt{(2)}$. In this approximation the E0 strength becomes

$$\rho(E0) \simeq \frac{1}{2}\frac{1}{eR^2}\left(\langle 0_1^+|m(E0)|0_1^+\rangle - \langle 0_2^+|m(E0)|0_2^+\rangle\right) \tag{20}$$

which for different axial quadrupole deformations (namely associated with different mean-square charge radii $\langle r^2\rangle$) reduces to

$$\rho(E0) \simeq \alpha\beta\,\Delta\langle r^2\rangle \tag{21}$$

As a result, nuclei characterized by coexisting shapes having different deformations will exhibit strong $\rho^2(E0)$ values if the states associated with the coexisting shapes become mixed. Therefore, strong E0 transitions should be considered as an empirical proof for strong shape mixing and not extreme shape coexistence, as it is often erroneously discussed. In exceptional cases, similarly to the γ decay, microscopic quantum mechanical effects may contribute to significantly hinder an E0 decay between states characterized by strongly mixed shapes, as a consequence of destructive interference between matrix elements. This is the case, for example, of the unusually small $\rho^2(E0)$ value recently reported for the $0_3^+ \rightarrow 0_1^+$ E0 decay of ^{40}Ca, within a scenario of shape mixing [82] (see Fig. 8 and Section 4.1). Another scenario in which $\rho(E0)$ can be very small is the case of strong mixing and small difference in deformation of the connected states, as results from Eq. (21).

2.2.5. Population mechanisms

Two-nucleon transfer processes populating the 0^+ states can provide a crucial information on the nuclear structure of the 0^+ excitations. In these processes, typically, the transfer cross section for the $0_{gs}^+ \rightarrow 0_{gs}^+$ transition dominates but the situation might be different if the excited states are mixed with the ground state. In general, a large cross section of the two-nucleon transfer to an

excited 0^+ state (in comparison to the ground state population) indicates that the final 0^+ state has a special character. Particularly interesting in this context is the scenario of shape coexistence, where we may have the situation of a strong or weak mixing of states with different shapes, leading to the presence of different configurations in the wave function also of the ground state, as discussed above. In such situations, two-particle transfer reactions can be approximately described within a simplified IBM-like framework [83–85]. However, to have a deeper insight into the details of state wave functions compositions, the experimental transfer data should be compared to the calculated two-neutron transfer cross sections, obtained using transfer amplitudes provided by the state-of-the-art shell-model calculations. Indeed, as will be mentioned in Sections 4.2–4.4, the MCSM approach has recently been able to deliver detailed wave function compositions of the low-lying 0^+ states in the semi magic Ni, Zr and Sn nuclei. So far, fully microscopic calculations, considering both reaction mechanism and structure, were performed for two-neutron transfer processes (t,p) on even $^{90-96}$Zr targets [85], for which experimental data are available [86]. The overall results reproduced reasonably well the experimental trend what supports the view that the pair transfer probabilities are an important probe of the details of the microscopic wave functions. Several types of two-nucleon transfer reactions were used to populate 0^+ states which will be discussed in this review. Some examples in which large cross section for two-proton transfer to the higher lying 0^+ states was observed are the (^{3}He, n) reactions leading to the 0^+_3 states in ^{58}Ni and ^{60}Ni, and 0^+_4 in ^{62}Ni [87–89]. These states indeed are special in the sense that they have very strong E0 transitions to the ground state, what points to a sizeable configuration mixing. Other example of two-proton transfer processes which showed enhanced 0^+_2 states population in ^{114,116,118}Sn are the Cd(^{3}He, n) reactions [90]. Here, this enhancement was recognized as an indicator of shape coexistence. In lighter tin isotopes, ^{108,112}Sn, larger cross sections to 0^+ states in the excitation energy range of 3.5–5 MeV were observed [90]. In contrast, in the (p,t) or (t,p) two-neutron transfer reactions the excited 0^+ states are populated rather weakly in comparison with the ground state [91–94,94–97]. The features discussed above are visible in Fig. 63, borrowed from Ref. [24], which displays a comparison between the (^{3}He, n) and (p,t) reactions for ^{112,114,116,118}Sn.

Another support for the presented picture comes also from the work of Flavigny et al. [98], in which the two-neutron transfer reaction in inverse kinematics, ^{66}Ni(t,p)^{68}Ni, was studied to unravel the microscopic configurations involved in the low-lying 0^+ states in ^{68}Ni. It was shown that a quantitative description of the cross section for populating individual 0^+ states (strong population of 0^+_{gs}, weak population of 0^+_2 and non-observation of 0^+_3) could be reached by using two-nucleon transfer amplitudes (TNAs) provided by the MCSM calculations, which assume that the 0^+_1 ground state is dominated by neutrons in the *pf* shell, whereas the 0^+_2 contains a strong contribution from configurations where neutrons are excited from the *pf* shell to the $g_{9/2}$ orbital above the N = 40 gap. The non-observation of the population of the 0^+_3 state (only upper limit was established for its feeding) is also consistent with the MCSM calculations which predict that this state include important components of proton excitations above Z = 28. In such a case, the two-nucleon transfer amplitudes between the ^{66}Ni ground state and this 0^+_3 state in ^{68}Ni are very small resulting in a very low calculated cross section of 7 μb only. One might naturally assume that two-proton transfer is better suited to investigate the structure of this state. However, the potential involvement of at least four excited neutrons beyond $N = 40$ (as mentioned in Ref. [98]) could limit the corresponding TNAs and cross section. The two-nucleon transfer reactions selectively populating 0^+ states are not limited to the (t, p), (p, t), (^{3}He, n) processes. Reactions involving the transfer of a pair of nucleons, performed with heavier projectiles also have high potential in directly feeding selected 0^+ states. This was demonstrated for example in the study of ^{66}Ni [68], where the 2n-transfer reaction, (^{18}O, ^{16}O), was used to access the three lowest lying 0^+ excitations in ^{66}Ni.

One-nucleon transfer reactions present another possibility for accessing the 0^+ excitations. These reactions prove particularly efficient in populating 0^+ states, when the entrance channel's nucleus ground state is 1/2. The cross-sections for processes resulting in 0^+ states in the final nucleus exhibit a strong dependence on the structure of these states. From a broader perspective, it should be stressed that the pair or one-neutron transfer reactions display strong sensitivity to the underlying nuclear structure of the 0^+ excitations wave functions, but the proper interpretation of experimental data requires information on the transfer amplitudes provided by the shell-model calculations. Such calculations are very demanding as the wave functions of 0^+ states in heavier nuclei can be very complex.

An alternative method to populate 0^+ states in atomic nuclei involves β- or α- decay processes. In β decay, states within $1\hbar$ of the parent nucleus's spin are primarily populated, limiting the identification of 0^+ excitations through this process. However, when the angular momentum of the decaying nucleus does not restrict the population of 0^+ states, another distinct selectivity emerges in directly feeding these excitations: decays between states with similar deformation are significantly preferred, while transitions to states with differing deformation are notably suppressed (see, e.g., the β-decay study of ^{64,66}Ni [99,100], discussed in Section 4.2.1). Likewise, in the instances of α decays, crucial information on the structure of 0^+ states, which are populated through this process, can be acquired, as the decays connecting states with different microscopic configurations are hindered. A remarkable example of α-decay studies as a probe of the structure of 0^+ states in neutron-deficient Po, Pb, Hg and Pt isotopes can be found in Refs. [58,66,101–103]. Large variation in the hindrance factors of the α decay to the 0^+_2 intruder excitation, with respect to the corresponding 0^+ ground state transition, was observed in these nuclei and used to probe the proton particle–hole character of the 0^+ states characterized by different shapes. In this way, the α decay can be considered as a powerful tool to explore shape transition phenomena. It is important to highlight that radioactive decays are considered a preferred method for investigating 0^+ states in the far-from-stability nuclei. It is so because in-beam spectroscopy experiments, commonly employed in such studies, predominantly populate states lying at or near the yrast line.

Neutron capture also can serve as a valuable method for investigating 0^+ states due to its non-selective nature in populating levels below the capture state. This non-selectivity originates from the fact that wave functions of states above the neutron separation energy are very complex – they are composed of numerous configurations. The only restriction arises from the spin of the target nucleus. When this spin is low and, consequently, the capture state possesses spin 0 or 1, the 0^+ states can be easily populated via direct E1 or M1 transitions. An example of recent study of excited 0^+ states with this method is reported in Marginean et al. [21], in the case of ^{64}Ni.

2.3. Different scenarios of shape coexistence

From the arguments discussed in Section 2.2.2, it follows that the hindrance factor (HF), defined by Eq. (3) for E2 transitions connecting 0^+ states with lower-lying states of different shapes, is a primary quantity which can be used to differentiate between types of shape coexistence. By inspecting experimentally available HFs over the entire nuclear chart, a wide range of values (from $\sim 10^{-2}$ to $\sim 10^{8}$) is found, pointing to a multifaceted shape-coexistence scenario, as schematically illustrated in Fig. 9 using a one-dimensional PES. In this picture, the decay properties of shape-coexisting states are considered to be driven, in the first approximation, by the features of the PES landscape. The PES is a handy and widely-applicable tool to foresee the appearances of a variety of shapes of atomic nuclei without performing sophisticated quantum many-body calculations which require more computational resources. The PES can be drawn by performing mean-field calculations constrained by shape variables for a given Hamiltonian, exhibiting estimated energies of states of specified shapes [15,42,56–59]. It has been also utilized in many Density Functional Theory (DFT)-type studies and in the MCSM calculations (see, e.g., Refs. [55,104–108]). It is important to remember that the matrix elements governing the states decay may depend on detailed properties of the quantum wavefunctions which cannot be adequately reflected in the PES, as it does not contain all relevant effects from correlations by definition. Nevertheless, in the following we use the PES as a very useful tool for grasping overall features of the underlying microscopic structure which governs the mechanism of transitions between states (see Fig. 3 and related discussion). This helps to characterize the different situations in which shape mixing can occur.

In Fig. 9(a), a featureless, parabolic-like potential is shown. Correlations between nucleons produce groups of states within potential energy surfaces restricted to a given configuration (dashed lines), the total surface being the envelope of these partial potentials. Different groups of states can be mixed and the identification of the shape is not sharp. Generally, no hindrance appears in this case.

Panel (b) displays instead a totally different extreme situation in which states of different shapes (here normally deformed and very-strongly deformed) are well localized in minima of the PES which are separated by a high (~3 MeV) and thick barrier (see Fig. 14). As a result, the admixture of wave functions is very small (they overlap only weakly) resulting in a large hindrance of the decay (HF $\gg$ 100) – we call it "extreme" shape coexistence. This situation is very rare and is currently known only in the case of fission shape isomers, observed in the 60's in the actinides region [12,13]. So far, in two cases only (i.e., ^{236}U and ^{238}U), hundreds-ns isomeric 0^+ states, located in secondary minima at large deformation, have been observed to decay toward lower-lying, normally-deformed states, via extremely retarded transitions, with measured HF values of the order of 10^7-10^9 for E2 decays. These are by far the largest HF values reported in the nuclear chart (see Section 3.1). Superdeformation at high spins is an additional example of "extreme" coexistence. Here, significantly hindered decays (HF $\sim 10^2$–10^3) toward spherical/normally-deformed lower-lying states are observed to occur from superdeformed prolate states with ps half lives, located at several units of spins, as discussed in Section 3.2.2.

Panels (c) and (d): Only very recently, two additional cases of 0^+ states deexciting via hindered E2 decays due to a shape change have been reported, although with much reduced hindrances. They are the 0^+_4 excitations in ^{64}Ni and ^{66}Ni, with half lives > 1 ps and ~20 ps, and corresponding HF values >63 and 24, respectively (see Section 4.2.1). Due to their reduced hindrances as compared with the ^{236,238}U cases, the 0^+_4 states in ^{64,66}Ni are named "shape-isomer-like" structures. In these cases, the calculated potential barrier is less pronounced than in the actinides, but still present. Microscopic quantum mechanical effects may also contribute to vary the hindrance of the decay between states with different shapes, as a consequence of correlation/cancellation effects between matrix elements connecting the initial and final states (panel (d)). As a result, sizeable hindrance factors might be observed also for decays between states localized in different, but not so deep minima of the PES, as in the case of the 0^+_4 state in ^{64}Ni, or for 0^+ states decaying to lower-lying states with similar deformation, e.g., the spherical 0^+_3 states in ^{64,66}Ni (see Section 4.2.1).

Panel (e): By reducing even further the size of the barrier, the admixture of wave functions will become more and more sizeable and the decay will show moderate hindrance or even no hindrance, if the barrier is weak or absent, as in the case of 0^+_2 state in ^{66}Ni, discussed above (see Fig. 3). We term these case "mixed-shape" coexistence.

Panel (f): The possibility also exists that states associated with different shapes reside in two distinct minima at very similar absolute energy, as in the case of the 0^+_2 excitation in ^{74}Kr (see Section 4.3.2). In such a case, the minima are called "degenerate" and a maximum admixture of wave functions might occur, thus resulting in a fast (not hindered) decay between states associated with the different shapes.

As discussed later in Section 4, when examining the entire nuclear chart with A $\gtrsim$ 40, only few 0^+ states can be considered "shape-isomer-like" structures, exhibiting moderate/strong hindrance factors HF $\gtrsim$ 10 (examples are shown in Fig. 9(c) and (d)). The case of "mixed-shape" coexistence is instead the most common, with hindrance-factor values concentrated in the restricted range 0.1 $\lesssim$ HF < 10 (e.g., Fig. 9(e) and (f)). We note that absolute half lives of 0^+s are observed to vary over a very wide range, from sub ps to hundreds ns, independently of the type of shape coexistence. This shows the limited significance of long half lives, by themselves, in establishing shape isomerism. Instead, the primary indication of shape isomerism appears to be given by large hindrance-factor values (and/or significantly hindered ρ^2(E0), if available, see Section 2.2.4).

3. Extreme shape coexistence

In this section we discuss the known cases of "extreme" shape coexistence, i.e., *(i)* shape isomers observed in actinide nuclei at spin zero (Section 3.1), and (ii) superdeformed nuclei at high spins (Section 3.2). Both cases are characterized by the appearance of two prominent minima in the potential energy surface, separated by a high barrier (see Fig. 9(b)).

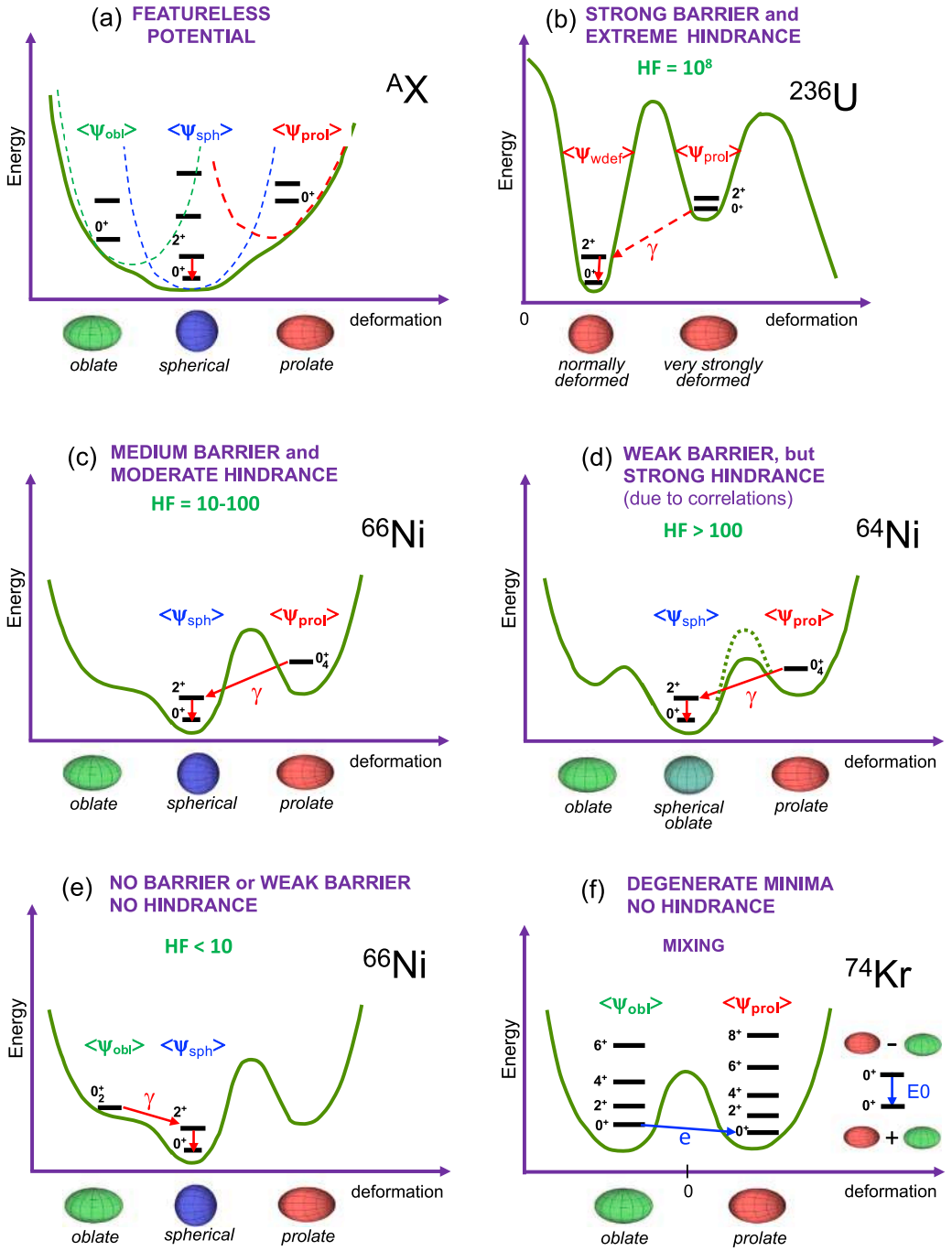

Fig. 9. Schematic representation of Potential Energy Surfaces (PES) associated to different types of shape coexistence scenarios, in even–even nuclei, involving states with wave functions $\langle\psi\rangle$ dominated by spherical (sph), oblate (obl), prolate (prol) and weakly-deformed (wdef) components. Red and blue arrows (and γ and e symbols) indicate decays of 0^+ states via γ and electron-conversion emission, respectively. Panel (a): featureless PES with groups of states (produced by correlations between nucleons) located in local PESs restricted to a given configuration (dashed lines). Different groups of states can mix, the identification of the shape is not sharp, no hindrance generally appears in the decay. (b): PES with high barrier between minima, with no mixing between different shapes and "extreme" hindrance factor for E2 decay (HF $\sim 10^8$) (e.g., shape isomers in ^{236,238}U); (c): medium-size barrier and moderate hindrance (HF $\sim$ 10–100) (e.g., shape-isomer-like prolate 0^+_4 excitation in ^{66}Ni); (d): weak barrier but strong hindrance (HF > 100) induced by correlations effects in the wave functions (e.g., prolate 0^+_4 excitation in ^{64}Ni); (e): no barrier or weak barrier, and no hindrance (HF < 10), (e.g., oblate 0^+_2 excitation in ^{66}Ni). (f): degenerate minima and no hindrance, strong mixing between 0^+ states associated to different deformation (e.g., oblate and prolate 0^+ states in ^{74}Kr). See Section 4 for discussion on specific cases.

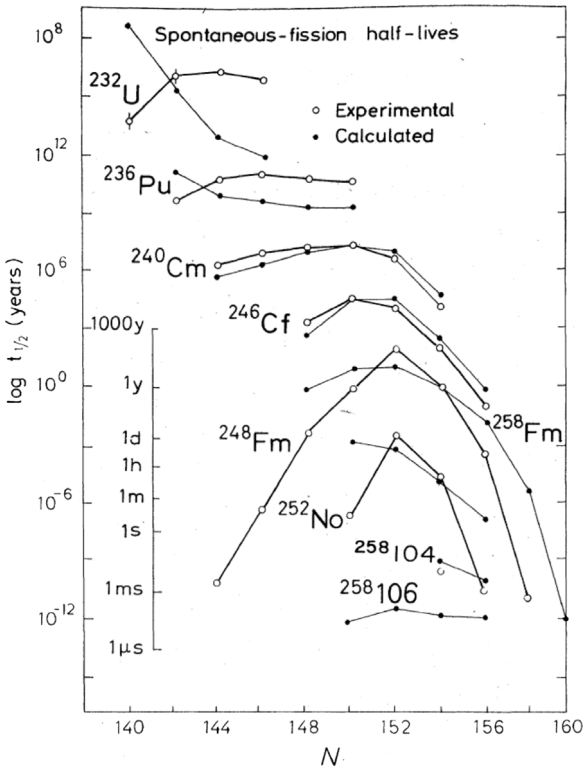

Fig. 10. Ground-state spontaneous-fission half-lives. Experimental and calculated values (with a semiempirical function) are given by empty and full circles, respectively.
Source: Taken from [111].

3.1. Fission shape isomers

The discovery of shape isomers dates back to 1961. In the search for new elements at Z > 102, in which a plutonium target (Z = 94) was bombarded with neon ions (Z = 10), Flerov and co-workers in Dubna observed a radioactive product decaying by spontaneous fission with a half-life of 14 ms, which could be attributed to a new element with Z = 104, as shown in Fig. 10. However, in subsequent experiments, this activity was found to be associated to a reaction product with Z ≤ 100 [11,109], and, eventually, attributed to an isomeric state in ^{242}Am (Z = 95), produced by a transfer reaction [110].

This finding was a great surprise, since it implied a dramatic reduction of the fission barrier in comparison to the non-fissioning ground state of ^{242}Am. The situation became even more puzzling when Bjørnholm et al. in 1967 [112], showed that the isomer excitation energy was of the order of 3 MeV, making it very difficult to also explain the resistance of the isomer to γ decay to the ground state. Apparently, the new isomer was not of the types known at that time, such as a high spin isomer, or an isomer very near the ground state. Among possible explanations, there was the idea of shape isomerism, proposed by Polikanov and Flerov, which assumed the existence of an intermediate potential energy minimum, associated with larger deformation, in which the isomer could be located [11,113].

The idea of shape isomerism gained acceptance as soon as Myers and Swiatecki schematically incorporated shell effects into the liquid drop description of nuclear potentials, using a semi-empirical formula. In 1966, first numerical results of shell model corrections were obtained by Strutinsky and a quantitative description of fission barriers became possible [114].

To obtain accurate estimates of absolute nuclear energies, Strutinsky calculated the shell-correction term, E_{shell}, by summing the energies e_i of occupied single-particle Nilsson orbitals in a potential well of given deformation (see Fig. 11) and, subsequently, by subtracting the energy $\langle \sum_i e_i \rangle$ calculated using an average single-particle level density

$$E_{shell} = \sum_i e_i - \langle \sum_i e_i \rangle \tag{22}$$

By adding such a E_{shell} correction to the normal liquid drop term, E_{LDM}, absolute nuclear energies could be obtained

$$E = E_{LDM} + E_{shell} \tag{23}$$

The calculations showed that for a certain region of actinides nuclei the smooth liquid drop fission barrier was split into two barriers, among which a second minimum appeared (see Fig. 12). ^{242}Am lied in that region. Within this framework, the observed

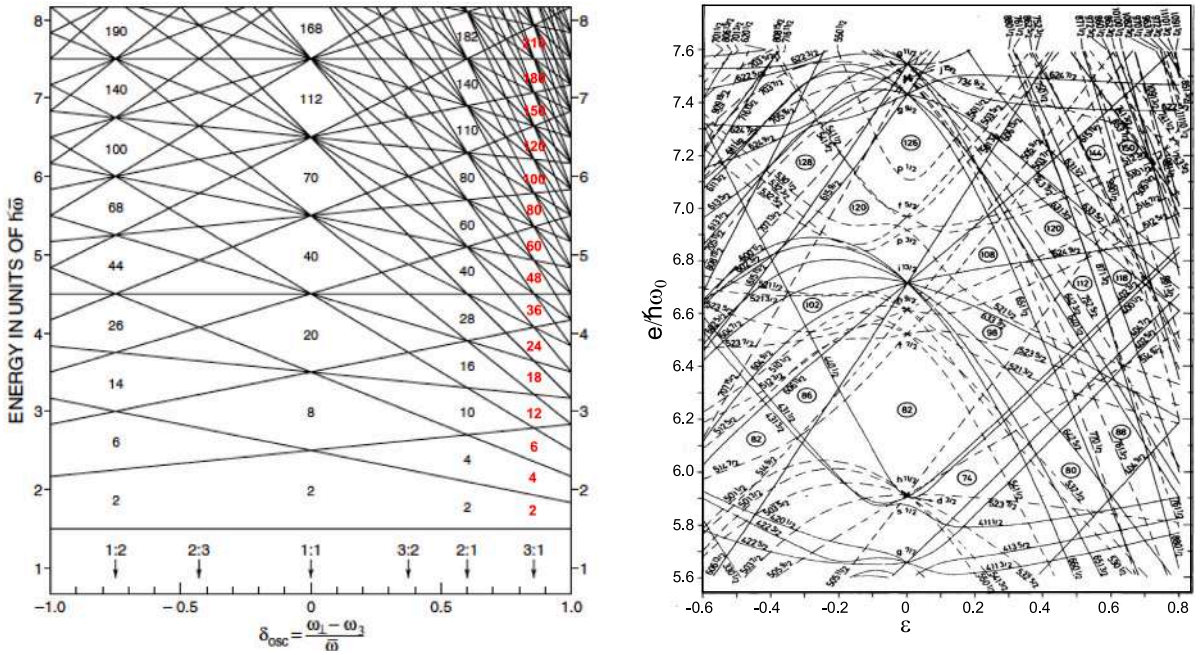

Fig. 11. Left: Single-particle levels calculated for an axially symmetric harmonic oscillator potential, as a function of the elongation coordinate δ_{osc}. Magic numbers of nucleons for spherical systems correspond to 1:1 axis ratio, while second and third shell closures are expected for very elongated nuclei with 2:1 and 3:1 axis ratios, i.e., superdeformed and hyperdeformed configurations, respectively. Right: neutron single-particle orbits obtained from the modified harmonic oscillator potential (which allows for shapes different from ellipsoid), as a function of the deformation parameter ϵ. Parameters for rare-earth nuclei are used. Regions of low level densities are found for neutron numbers N = 80–88, 112–118 and 144–150, at large deformation ($\epsilon \approx 0.6$).
Source: Adapted from [115].

isomer state of ^{242}Am could be considered as a state in the second potential well. Such a picture explains the strong increase in the probability of spontaneous fission, since the fission barrier felt by the isomer is much lower than for the ground state. Furthermore, the electromagnetic transitions from the state in the second potential well must be greatly hindered by the high barrier separating the two potential minima, in line with the experiment.

Based on these ideas, the whole region of actinides was explored, confirming the existence of several other shape isomers [116], using techniques for detecting isomers with half-lives shorter than milliseconds and microseconds. By now, similar metastable states have been identified in more than 30 nuclei from uranium to berkelium, forming an island centered around neutron number N = 146, as shown in the nuclear chart of Fig. 13.

The extension of the island of fission isomers toward the "south" and "west" (i.e., decreasing N and Z) is governed by a change in the relative importance of the inner and outer barrier: the fission barrier increases, leading to the γ decay toward the main minimum as the dominating decay mode. Here, one encounters the fundamental difficulty of reaching the sensitivity which is needed for the identification of weakly populated γ decaying isomers [121]. In this case, help comes from borderline nuclei in which both types of decays are possible. Indeed, the only cases where delayed γ transitions from the shape isomers were observed are ^{236}U and ^{238}U, where the isomers were first identified through their (weak) spontaneous fission decay branch. As reported in Fig. 14 and Table 1, the measured hindrances for electromagnetic transitions from these isomers are exceptionally large (of the order of 10^{-6}, 10^{-11}, and 10^{-7} for E0, E1 and E2 transitions, respectively), the largest reported in the nuclear chart. To date, ^{236}U and ^{238}U remain the best examples of extreme shape coexistence ever observed.

The experimental mapping of shape isomers further south and south-west becomes extremely challenging, owing to their very low population and the total dominance of the γ-decay mode. Indeed, no shape isomers have clearly been identified at Z = 92 and below, except for ^{236}U and ^{238}U [13], even though they were predicted to exist [12].

In addition to the island of shape isomers discussed above, there are other regions in the nuclear chart where various theoretical models predicted the existence of secondary minima at large deformation in the PES, at low spin. Already in the '70s, detailed calculations performed by Pashkevich [123] and Tsang and Nilsson [124] showed the appearance of a second minimum in Po isotopes, although with considerably smaller inner barrier relative to the outer barrier (see Fig. 15), implying a decay mode fully dominated by γ emission. So far, it has not been possible to identify this additional island of shape isomers in nuclei near Pb.

Similar calculations for the existence of secondary minima in the potential energy surface, at larger deformation, were extended to even lighter nuclei and showed that indeed such minima could exist, as a consequence of the appearance of new shell gaps at given nucleon numbers (see Fig. 11). These minima, at zero spin, were very high lying in energy and by far too shallow to expect any hindrance in their decay toward the main minimum. The situation was instead found to dramatically change when the rotation degree of freedom was considered.

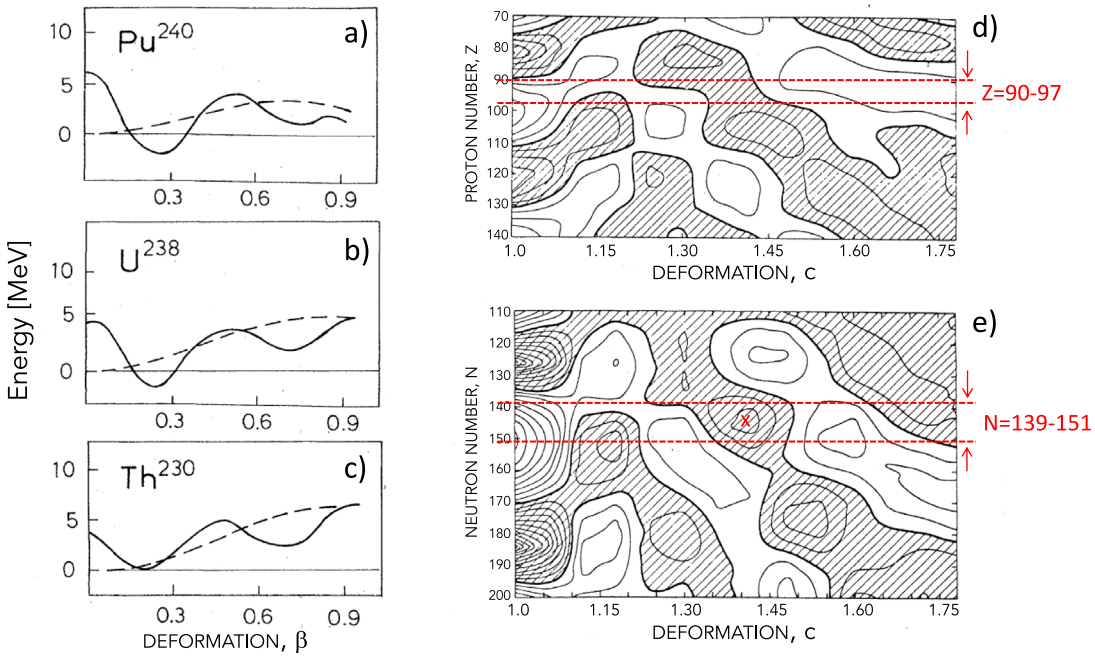

Fig. 12. Left: Potential energy curves for ^{240}Pu, ^{238}U and ^{230}Th ((a)–(c)), as a function of the β deformation parameter, as calculated by Strutinsky considering the shell correction energy [114] superposed on the liquid drop energy (given by dashed lines). Right: Contour maps of the shell correction energy for protons (d) and neutrons (e), respectively, calculated using a Woods–Saxon potential with parameters appropriate for Pu. The thick curves correspond to zero energy and the increment per line is 1 MeV. Shaded areas correspond to negative values. The deformation parameter c = 1 and 1.3 correspond to a sphere and to an axially symmetric ellipsoid with major-to-minor axis ratio 2:1, respectively. Dashed lines delimit the Z = 90–97 and N = 139–151 regions where fission shape isomers have been experimentally observed. The cross marks the minimum occurring for c = 1.42 and neutron number N = 144.
Source: Adapted from [12].

Table 1
Characteristics of the decays of the fission shape isomers observed in ^{236}U and ^{238}U: E_i, E_f and I_i^π, I_f^π are the initial and final excitation energies and spin-parities, respectively; U is the excitation energy above yrast (here, it coincides with E_i,); $T_{1/2}$ is the half life; E_γ and E_{e^-} are the γ and electron transition energies, with branching BR and multipolarity $E/M\lambda$; $B(E/M\lambda)$ are the corresponding reduced transition probabilities in Weisskopf units (in squared brackets if deduced from the spins and parities of the initial and final levels). For ^{236}U, the full electromagnetic decay strength is measured, and the ratio between the γ decay and isomeric fission (SF) amounts to 6.5(8), which corresponds to a fission branch of 13.3%. In the case of ^{238}U, 46% of the electromagnetic decay is unresolved, while the intensity of the fission branch is 5% [13,67,117].

Nucleus	E_i [MeV]	I_i^π	U [MeV]	$T_{1/2}$ [ns]	E_f [MeV]	I_f^π	E_γ or E_{e^-} [MeV]	BR [%]	$E/M\lambda$	$B(E/M\lambda)/\rho^2(E0)$ [W.u.]/[m.u.]	Refs.
^{236}U	2.81(2)	(0^+)	2.81(2)	116	0.000	0_1^+	2.81(2)	<0.9	E0		[13,117]
					0.045	2_1^+	2.769	<2.5	[E2]	$1.2\ 10^{-8}$	
					2.244	(1^-)	0.570	11.4	[E1]	$1.1\ 10^{-10}$	
					1.807	$(1^-/(2^+))$	1.007	8.7	[E1/(E2)]	$1.6\ 10^{-11}/(5.5\ 10^{-6})$	
					1.604	$(1^-/(2^+))$	1.210	13.2	[E1/(E2)]	$1.4\ 10^{-11}/(3.3\ 10^{-6})$	
					0.967	(1^-)	1.847	32.8	[E1]	$9.5\ 10^{-12}$	
					0.688	1^-	2.126	17.2	[E1]	$3.3\ 10^{-12}$	
							SF	13.3			
^{238}U	2.558	(0^+)	2.558	280(6)	0.000	0_1^+	2.558	0.3	E0	$1.7\ 10^{-6}$[a]	[31,67]
					0.045	2_1^+	2.513	35	[E2]	$1.0\ 10^{-7}$	
					0.680	1^-	1.879	13	[E1]	$1.5\ 10^{-11}$	
							γ(unres.)	46	E/M		
							SF	5			

[a] Most recent evaluated value [33]: $\rho^2(E0) \times 10^3 = 0.66(16)\ 10^{-6}$.

3.2. Superdeformation

Extreme shape coexistence, of which shape isomers observed in actinide nuclei at spin zero are a peculiar example (see Section 3.1), is also at the origin of the phenomenon of superdeformation in rotating nuclei [125–127]. Nevertheless, the studies of superdeformation have developed virtually in a completely independent manner from other investigations of shape coexistence,

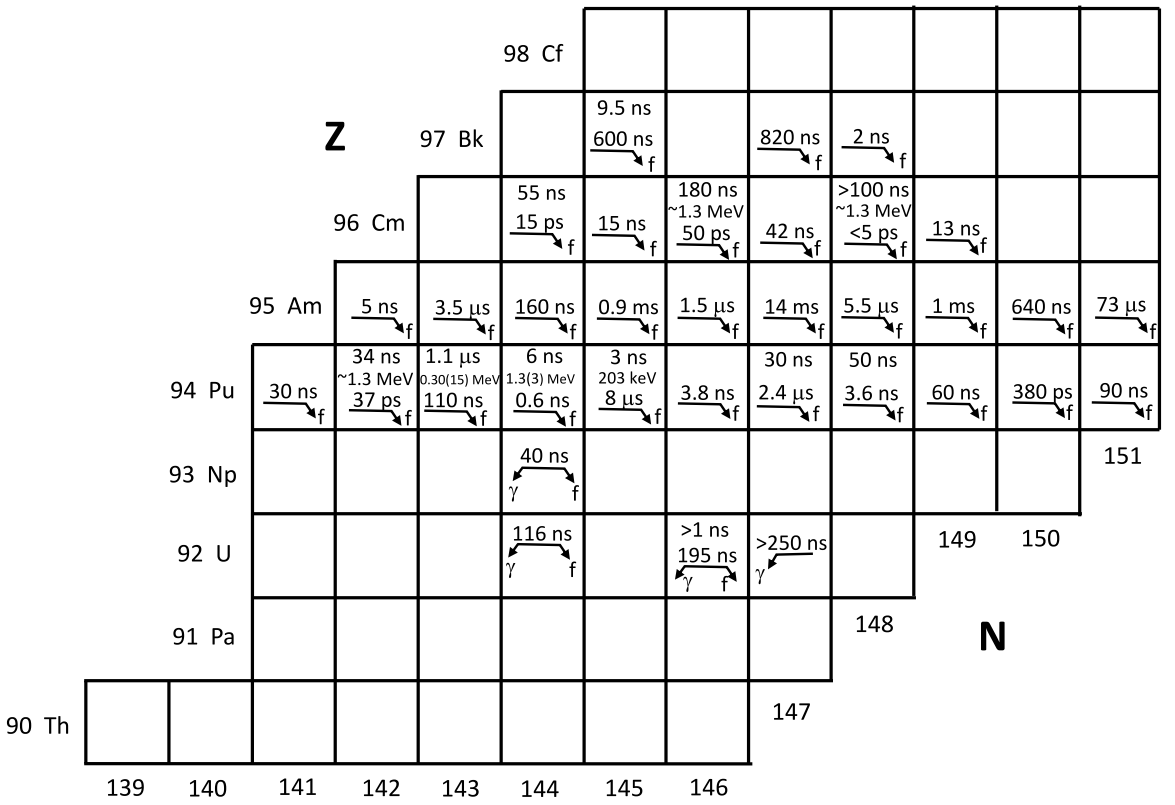

Fig. 13. Portion of the chart of nuclei showing the fission isomers currently known (34 cases in total) [13,67]. A second half live value for the same nucleus indicates the presence of a spin isomeric state in the second minimum. A direct γ decay from the second minimum back into the first minimum was observed only in ^{236,238}U [67,117,118], while indications for a γ branch were obtained for ^{237}Np [119] and ^{239}U [120].
Source: Adapted from [13].

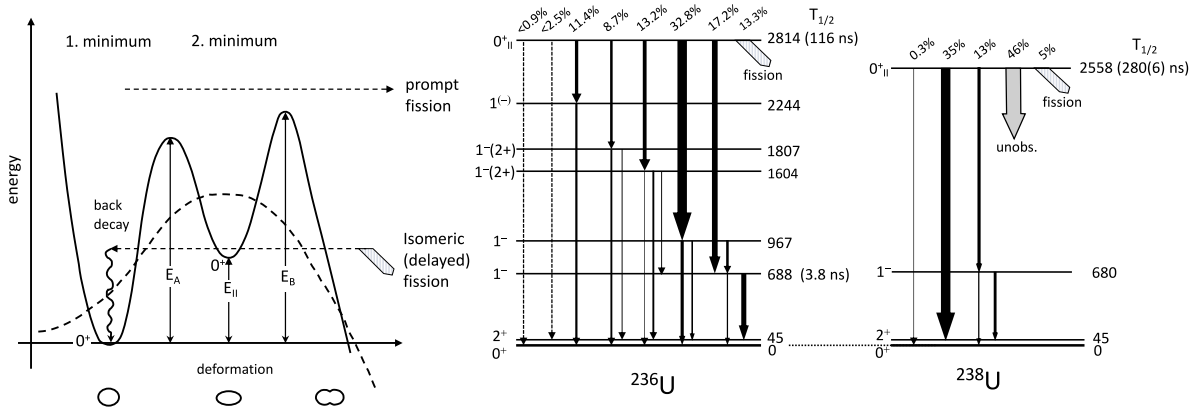

Fig. 14. Left: schematic representation of the double-humped potential energy (solid line) and macroscopic liquid-drop potential energy (dashed curve), as a function of the nuclear deformation. Values are given for the specific case of ^{236}U: the barrier heights are E_A = (5.6 ± 0.3) MeV and E_B = (5.7 ± 0.3) MeV [122]; E_{II} = 2.81 MeV is the energy of the 0^+ ground state in the second minimum, with respect to the ground state of the first well. Center and right: decay scheme of the 0^+ fission shape isomers of ^{236}U and ^{238}U, located at 2.81 and 2.56 MeV above the ground state, respectively. The corresponding half lives are $T_{1/2}$ = 116 and 280(6) ns.
Source: Adapted from [13,67,117].

mainly because they were carried out almost always in the high-spin regime, while the others were related to low-spin phenomena, as pointed out by Heyde and Wood [15]. A serious obstacle in unifying the two approaches has been the sparseness of experimental information on SD bands at low spins (see Section 3.2.2), and different experimental tools used by the low- and high-spin communities.

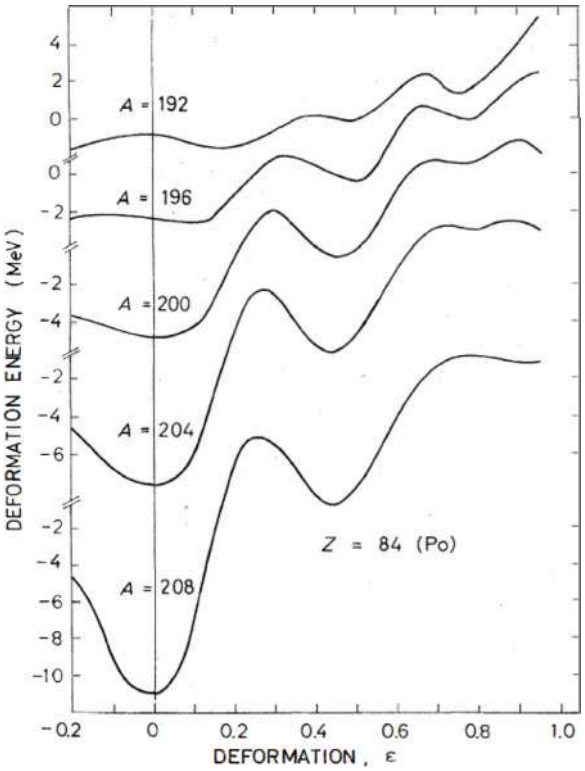

Fig. 15. Potential energy curves for polonium isotopes (Z = 84) near neutron number N = 118, predicting the existence of shape isomers with a deformation parameter $\epsilon = 0.4$.
Source: Taken from [124].

Similarly to shape isomers, in the case of superdeformation, the appearance of two well separated minima in the potential energy surface originates from shell corrections, at a certain rotational frequency. As it was illustrated in Fig. 11 and by Eq. (22), at spin zero, the shell correction energy E_{shell} is a direct measure of the density of single-particle levels around the Fermi surface. In a similar way, in the formalism of the cranking model, suitable to describe collective rotation at high angular momentum [128,129], it is convenient to consider the shell correction energy in the rotating frame [130–132]

$$E^{\omega(I)}_{shell} = \sum_i e^{\omega}_i - \langle \sum_i e^{\omega}_i \rangle \tag{24}$$

where the sum runs over all the occupied Routhians e^{ω}_i, that is, over the single-particle eigenvalues of the cranking Hamiltonian $H^{\omega} = H_0 - \hbar\omega j_x$, describing the collective rotation of a nucleus around an axis perpendicular to the $z-$symmetry axis. Going to the laboratory frame, the energy $E(I)$ at angular momentum I is then given by

$$E(I) = E^{\omega(I)}_{shell} + E_{RLDM}(I) \tag{25}$$

where E_{RLDM} denotes the rotating liquid drop energy

$$E_{RLDM}(I) = E_{LDM} + \frac{\hbar^2}{2\Im} I^2, \tag{26}$$

which contains the rigid moment of inertia $\Im$, appropriate for high angular momentum states, when static pairing correlations have been suppressed by the rotation. The rotation frequency $\omega(I)$ is determined so that the average value of j_x is equal to I, $\sum_i \langle j^i_x \rangle = \langle \chi^{\omega}_i | j_x | \chi^{\omega}_i \rangle = I$, where χ^{ω}_i denote the single-particle eigenfunctions of H^{ω}.[1]

It follows that, for a fixed particle number, also at high spins, gaps or low-density regions in the single-particle spectra identify regions of strongly negative shell energies. As shown in Fig. 16 for a pure harmonic oscillator, when the nuclear shape is oblate and the rotation is around the symmetry axis (i.e., single particle excitations), the original shell gaps disappear at relatively small ω values. On the contrary, for a prolate shape with rotation around an axis perpendicular to the symmetry axis (collective rotation), the single particle orbitals are much less mixed and the shell effects calculated at spin zero (see Fig. 11) are expected to survive

[1] Sometimes a small term $\Delta E^{\omega(I)}_{shell} = \hbar(\omega(I) - \tilde{\omega}(I))I$ is added to the expression of E^{ω}_{shell}, where $\tilde{\omega}$ is determined so that the smoothed angular momentum $\langle \sum_i j^i_x \rangle = I$ [115].

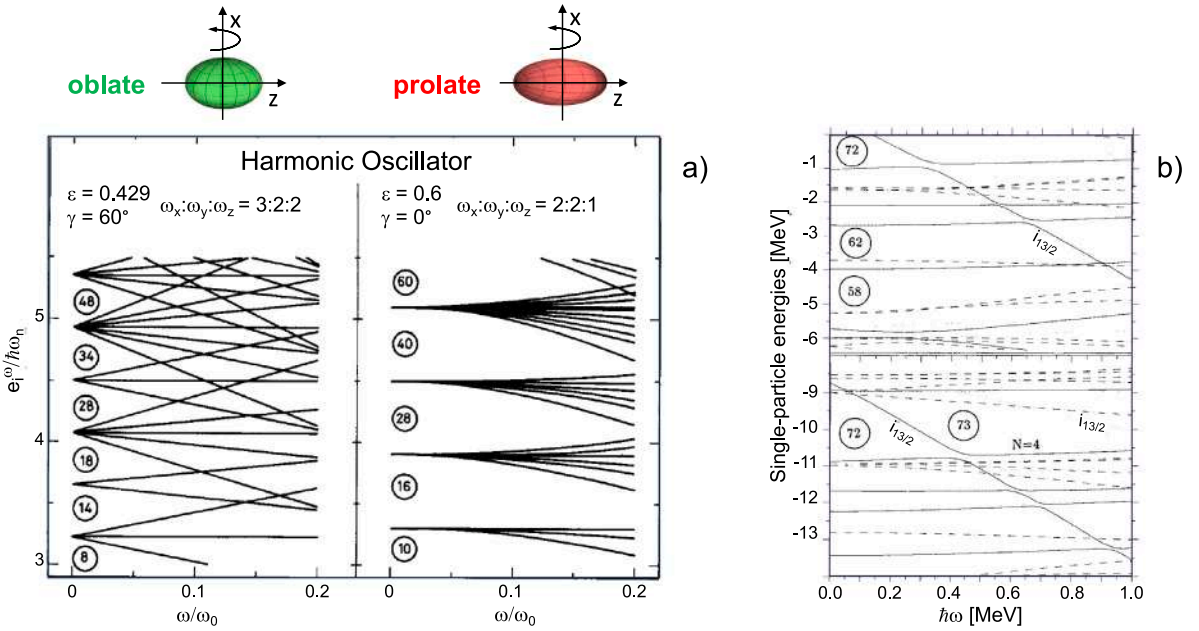

Fig. 16. Panel (a): Single-particle energies in the cranked harmonic oscillator, as a function of the rotational frequency ω (named Routhians) [125]. Left: the nuclear shape is oblate, with axis ratio $a_x : a_z = 2{:}3$, and the rotation is around the x-axis, i.e., around the symmetry axis (single-particle excitations). Single-particle energies are found to mix rather quickly, leading to the disappearance of the shell gaps found at zero frequency. Right: the nuclear shape is prolate, with axis ratio $a_x : a_z = 1{:}2$., and the rotation is around a perpendicular axis (collective rotation). Here, the original shell gaps, at $\omega = 0$, survive up to high ω values. Panel (b): single-particle Routhians for protons (top) and neutrons (bottom) for A ∼ 130–160 prolate nuclei, calculated using a Wood–Saxon potential including a monopole pairing force. The deformation parameters are $\beta \sim 0.38$ and $\gamma \sim 3°$, which are representative for a highly deformed configuration in ^{132}Ce, based on the occupancy of the lowest $i_{13/2}$ neutron level (intruder) crossing the N = 72 gap in the frequency range 0.1–0.4 MeV [135].
Source: Adapted from [125,135].

up to quite high ω values. This is clearly shown in Fig. 17, where the total shell correction energy is calculated from a Woods–Saxon potential and for spin values $I = 0$, 40 and 80, as a function of proton number Z (with fixed number of neutrons $N = 100$) and deformation β. In the case of negative β-values (corresponding to oblate shape and rotation around the symmetry axis) the shell energy is strongly dependent on I, while for positive β-values (i.e., prolate shape and collective rotation around an axis perpendicular to the symmetry axis) shell corrections very weakly depend on spin, with quite stable valleys (negative-values) and ridges (positive-values). For high-spin states, only the so-called "intruder orbitals", from higher oscillator shells, are greatly lowered in energy and reach the Fermi surface at large deformation. Such intruder orbitals are strongly deformation driving, therefore, the deformation of the nucleus at high spin is expected to depend on the number of intruder orbitals occupied in the given configuration (see Fig. 16(b) and Refs. [133,134]).

Total energy surfaces have been calculated as a function of angular momentum I and (β, γ) deformation parameters for a number of deformed nuclei, as well as for several light p and sd-shell nuclei [42,125,131,136,137]. Particularly stable and strongly elongated shapes, with axes ratio 2:1:1 (corresponding to axial symmetry) were predicted, in particular, in the regions of A ∼ 150 and A ∼ 190. Above a certain value of angular momentum (e.g., ∼ 50 $\hbar$ in ^{152}Dy and ∼ 40 $\hbar$ in ^{194}Hg), such strongly deformed shapes were found to become energetically favored over less deformed shapes (see Fig. 18).

In Section 3.2.1, we review the early experimental developments in the field of superdeformation, while in Section 3.2.2 we give a survey of superdeformed bands for which large hindrances in the γ-decay toward lower-deformed shapes, have been measured. As discussed in Section 2, hindrances in the electromagnetic decay are fingerprints of extreme shape coexistence phenomena.

3.2.1. Early experimental developments

Following the observation of fission isomers, in the '60s, there was a gap of about 25 years before the discovery of a superdeformed shape in the ^{152}Dy nucleus at high spin, made in 1986 by Twin and coworkers [138]. This delay was caused by the time needed for the development of high-energy resolution multi-detector γ-ray spectrometers, which were absolutely necessary to reach the requested sensitivity level (of the order of few %) in gamma-coincidence measurements. Starting with several rather small arrays of Germanium detectors at various laboratories worldwide [139], large international collaborations led to the construction of large arrays such as EUROBALL [35–37] and GAMMASPHERE [38,39]. These are the precursors of the present state-of-the-art γ-tracking arrays AGATA [140–144] and GRETA [145,146].

To date, more than 350 superdeformed rotational bands have been observed and studied throughout the entire nuclear chart [127]. As shown in Fig. 19, SD nuclei appear in specific regions of the nuclear chart, with mass numbers around 40, 60,

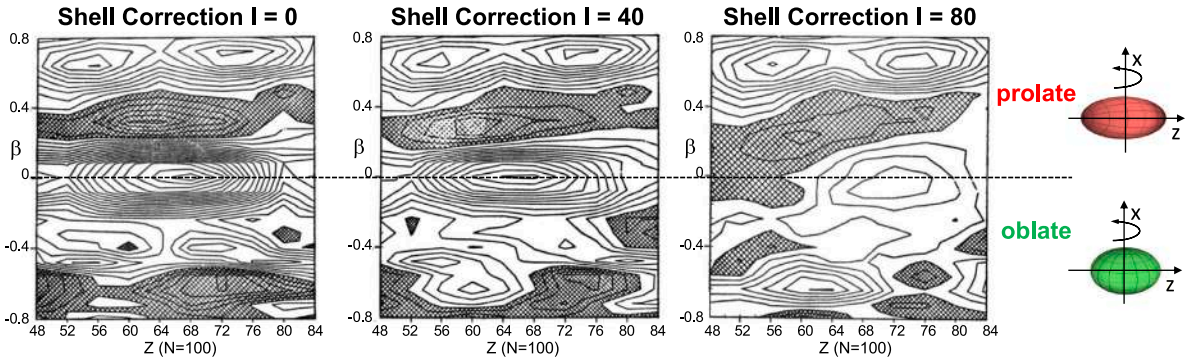

Fig. 17. Total shell-correction energies calculated from a Woods–Saxon potential and for spin values I = 0, 40, and 80, as a function of proton number Z (with neutron number $N = 100$) and deformation β. Positive β values correspond to prolate shape with rotation around the perpendicular axis ($\gamma = 0°$), negative β values to oblate shapes with non-collective rotation around the symmetry axis ($\gamma = 60°$), as indicated by cartoons on the right of the figure. The two cases of Fig. 16 correspond to $\beta = 0.79$ and $\beta = -0.40$,respectively. Shaded areas represent regions of negative shell energy. The spacing between the contours is 1 MeV.
Source: Adapted from [125].

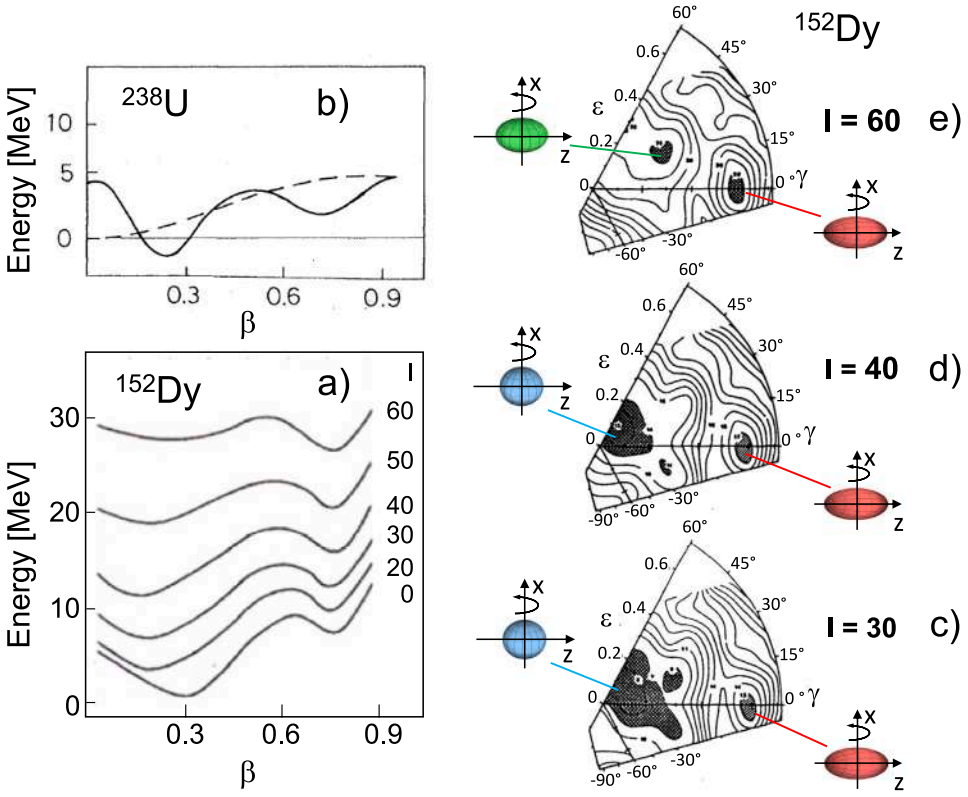

Fig. 18. Panel (a): Potential Energy curves of ^{152}Dy as a function of the quadrupole deformation parameters β and different angular momentum values ($I = 0$, 20, 30, 40, 50 and 60). Panel (b): similar calculation performed at $I = 0$ for ^{238}U (same as in Fig. 12(b)). Panels (c–d): corresponding two-dimensional plots in ϵ-γ coordinates for ^{152}Dy for $I = 30$, 40 and 60. Spherical, oblate and prolate shapes associated to the minima in the PES are represented by blue, green and red ellipsoids, respectively.
Source: Adapted from [12,125].

80, 130, 150, and 190, i.e., in correspondence with the large shell gaps expected to occur when the ratio of the long to short axes of the nuclear shape is a rational ratio, e.g., close to 2:1, as discussed in the previous section [3,125]. Up to now, superdeformation is considered one of the most extreme phenomena in nuclear physics, in terms of both deformation and electromagnetic decay. Being predicted 10 years before it was found, it was ranked among the top 10 most exciting physics discoveries along with high-T superconductivity, supernovae 1987 A and buckyballs, as reported by D. Kleppner in Ref. [147].

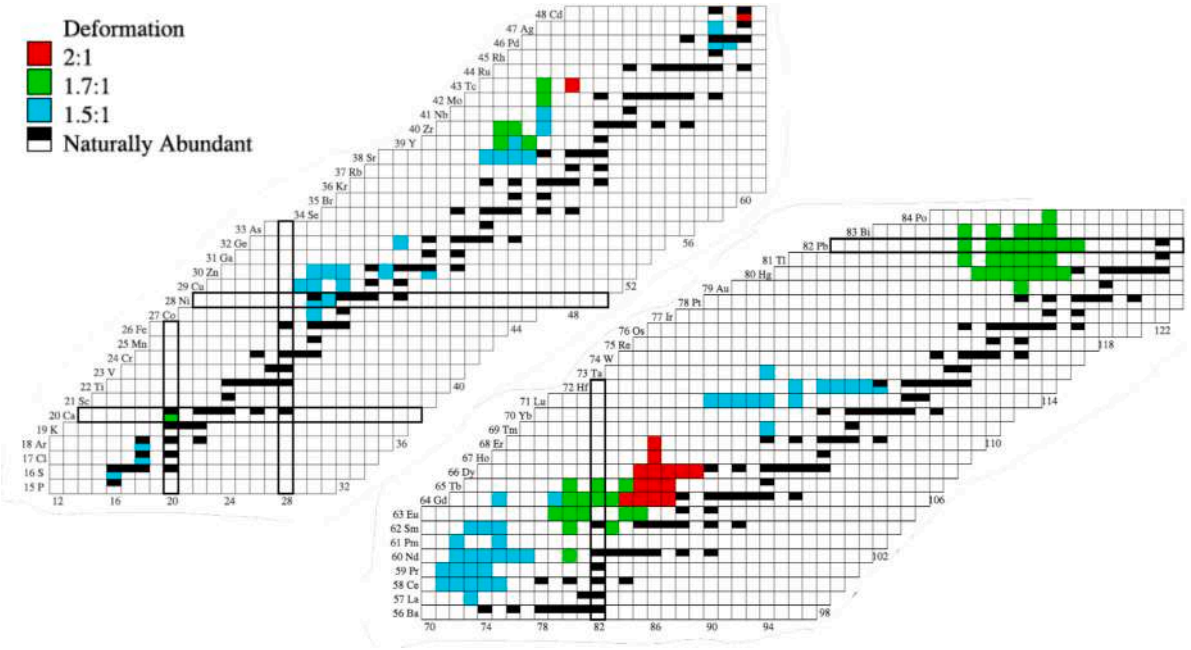

Fig. 19. Chart of nuclides, showing local regions of superdeformation in the A ∼ 40, 80, 130, 150, and 190. The region of fission shape isomers is given in Fig. 13.
Source: Adapted from [127].

Superdeformed bands are populated at the highest spins, and close to the fission barrier, by employing fusion-evaporation reactions, where a compound nucleus is formed by the fusion of a heavy-ion projectile and a target nucleus [148]. After the hot compound nucleus evaporates several light particles (typically neutrons, protons or charged particles like alphas, deuterons, etc.), the decay flow populates the final nucleus, with a distribution of excitation energies comprised between the yrast line and the neutron separation energy. From this entry distribution in energy and spin, the nucleus cools down via a cascade of gamma rays, reaching the yrast line and then ending in the ground state. In all studied cases, evidences for very large deformation come from (i) large values of the dynamic moment of inertia $\mathfrak{I}^{(2)}$ [149][2], significantly enhanced with respect to ND nuclei (Fig. 20(a)), and (ii) large electric quadrupole moments Q (which are proportional to the quadrupole deformation obtained from B(E2) values, see Section 2.2.3) – they deviate strongly from the $1/A^{1/3}$ dependence typical of the ground-state deformations (Fig. 20(b)).

Fig. 21(a) shows, in a schematic way, the decay scenario of superdeformed nuclei, characterised by the presence of two minima in the nuclear potential energy surface, corresponding to the coexistence of normal (ND) and superdeformed (SD) shapes, over a wide range of spins and excitation energies. At the highest spins, the minimum associated with the strongly elongated shape is energetically favored (inset 1): at the spin and excitation energies associated with the entry distribution, the coupling of excited SD and ND states allows the transition between excited states on either side of the barrier. Finally, few % of the population reaches the ground state in the deformed well at a given spin. The nucleus is now well separated from the ND states by the barrier and decays by long series of almost equi-spaced (picket-fence) highly-collective E2 transitions (with very high transition probability, up to ∼2000 W.u.). These transitions connect members of strongly deformed rotational bands of prolate nature, as shown in panels (b) and (c) for the yrast bands of ^{152}Dy and ^{191}Hg nuclei, respectively, the first discovered superdeformed bands in the A = 150 and A = 190 mass regions.

As shown in Fig. 21(a), as spin decreases during the decay, the energy of the two minima becomes closer and closer (inset 2), until the states trapped in the SD minimum arrive to lie at energies well above the ND yrast line by several MeV (inset 3). Even being in such unfavored conditions, i.e., embedded, from the energy point of view, in a region of closely spaced ND states, with progressively increasing level density while the spin decreases (inset 3), the nucleus does not decay out of the SD minimum. For some time it remains isolated by the barrier separating it from levels outside the SD well. Eventually, however, the SD state comes close enough in energy to a ND level that a small coupling between the two types of states occurs, leading to the rapid depopulation of the SD structures over few spin units (see Fig. 22). Two extreme scenarios of barrier penetration can here appear, as schematically

[2] In high-spin physics, two kinds of moment of inertia can be defined: (i) the *kinematic* moment of inertia $\mathfrak{I}^{(1)}$, related to the overall motion of the nucleus and defined via the first derivative of the rotational energy with respect to spin, $dE/dI = \hbar^2 I/\mathfrak{I}^{(1)} = E_\gamma/2 = \hbar\omega$, and (ii) the *dynamic* moment of inertia $\mathfrak{I}^{(2)}$, describing the response of the nucleus to a torque and defined in terms of the second derivative of the rotational energy, $dE^2/dI^2 = \hbar^2/\mathfrak{I}^{(2)} = \hbar d\omega/dI$. The two moments of inertia are identical for a perfect rotor. In the case of the nucleus, changes in the internal structure (e.g., alignment of single-particle angular momentum) will result in different values for I/ω and $dI/d\omega$, reflecting the fact that the rotation of a nucleus is not the simple rotation of a rigid body [149].

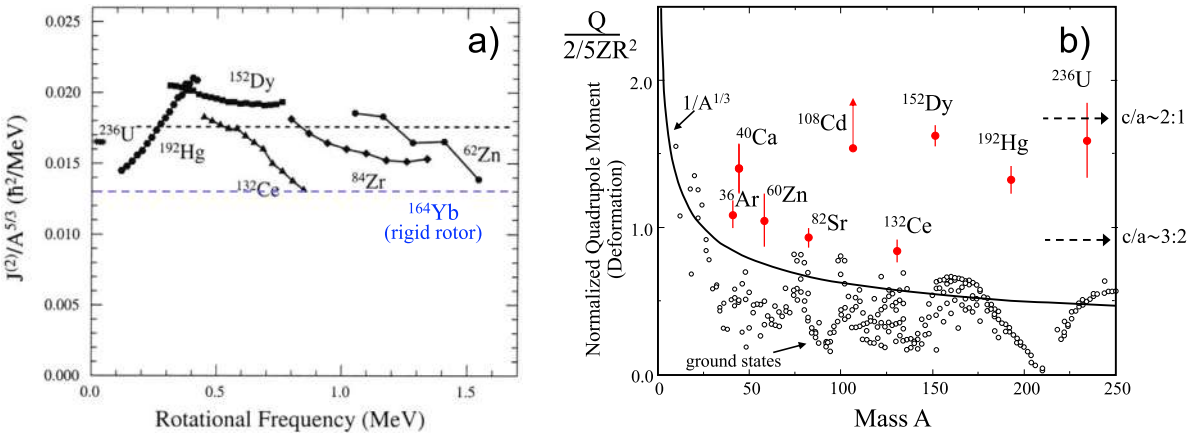

Fig. 20. Panel (a): Dynamical moments of inertia $\mathfrak{I}^{(2)}$ [149], scaled by a factor $A^{5/3}$, for superdeformed bands in the various mass regions. Panel (b): Measured intrinsic quadrupole moments Q scaled to remove the Z dependence for both normal deformed (open circles), and selected cases of superdeformed nuclei (full circles) [67]. The solid line represents the $A^{-1/3}$ dependence typical of ground state deformation. On the right, approximate prolate deformations are given for the superdeformed nuclei of interest, in terms of major:minor axis ratios of 3:2 and 2:1. See text for details.
Source: Adapted from [41].

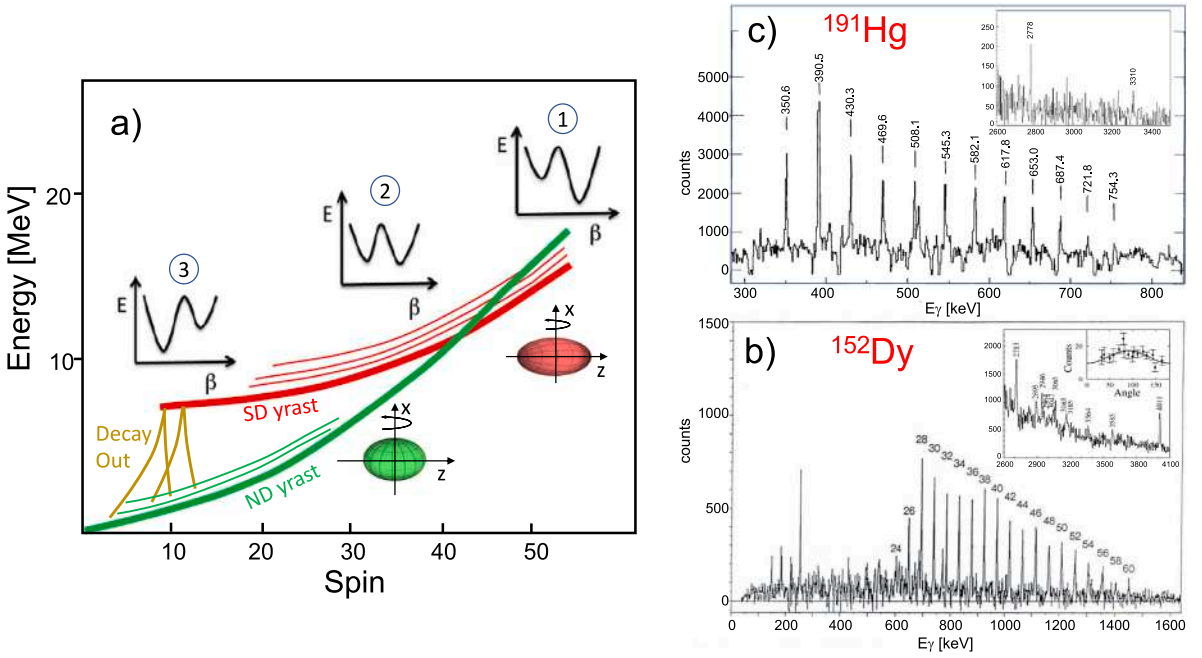

Fig. 21. Panel (a): Schematic depiction of the γ-decay flux along the ND and SD yrast lines, with sketches of the ND and SD minima at different spins. γ-ray spectra showing the first discovered superdeformed yrast bands in the A = 150 and A = 190 mass regions, i.e., in ^{152}Dy and ^{191}Hg, are shown in panels (b) and (c), respectively (original data from the TESSA3 [138] and Argonne-Notre Dame arrays [150]). The inset in each panel gives a zoom on the high-energy region, both measured in high-statistics experiments later performed with GAMMASPHERE [151,152], where γ transitions directly linking superdeformed and normal states are observed. In the case of ^{152}Dy, the angular distribution of the most intense 4011-keV linking transition, connecting the 28^+ SD state (at 11893 keV) to the 27^- SD state (at 7882 keV) is also shown, clearly pointing to its dipole (E1) character (see also Figs. 30 and 31).
Source: Adapted from [138,150–152].

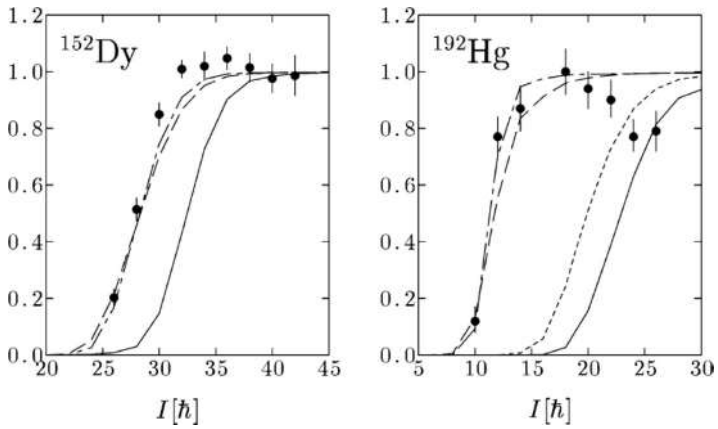

Fig. 22. The experimental γ-ray intensity pattern at the decay-out of the yrast SD band in ^{152}Dy (left) and^{192}Hg (right). The lines denote the results of decay-out calculations, following the model of Ref. [153], without any adjustment (solid), with modification of the level density in the ND well (dashed and dotted), and with modification of the mass parameter related to pairing correlations (dot-dashed) which enters into the calculation of the barrier penetration between the SD and ND well.
Source: Adapted from [154].

illustrated in Fig. 23. In panel (a), the SD state is coupled through a barrier only to a few "doorway" states in the ND well, and a sudden decay out into the minimum at lower deformation proceeds via a rather limited number of γ cascades, to a large extent fully identified experimentally (panels (c) and (d)). This situation typically can be observed in light/medium mass nuclei, where the density of states in the ND well is rather low at the excitation energy at which the decay-out occurs. Panel (b) shows an alternative situation which usually occurs in mass regions of A $\sim$ 150 and 180, where the "doorway" state in the ND well is further spread over many excited ND states, and it is the coupling to these states which eventually leads to a highly-fragmented γ cascades. In such a case, only a few discrete high-energy γ transitions, directly linking the SD yrast to the discrete states in the ND well, have been identified. Their intensities account for few % only of the SD yrast population (insets of Fig. 21(b) and (c)), while the largest fraction forms an unresolved quasi-continuum distribution, at lower γ-transition energies (Fig. 23 panels (d) and (f)). The final stage of the decay proceeds in the ND well via cascades connecting states characterized by spherical or weakly deformed shapes (rotational bands of oblate nature are often observed).

One must recognize that current nuclear theory does not offer a comprehensive, reliable microscopic description of a complex phenomenon like the decay from an SD band into ND states. Furthermore, the density of ND states may be quite high, and a detailed study requires a statistical treatment of this phenomenon, including estimates of the electromagnetic widths on ND and SD states [154,155]. Therefore, in the present review, we limit ourselves to discuss the connection between the decay through a barrier in the Potential Energy Surface, commonly referred to as "tunneling", and the experimental hindrance of the γ decay (see Eq. (3) in Section 2.2.2).

The tunneling process between SD and ND states has been extensively studied in various regions of the nuclear chart. For heavy nuclei with mass A = 150–180, it provides a remarkable example of transition from a quantum mechanical ordered system, characterized by good quantum numbers (i.e., the SD nucleus), toward final excited states (at 4–5 MeV above the ground state), which display characteristics of quantum chaos [156,157], where quantum numbers are largely lost – apart from energy, spin and parity. A review on this topic was given in 2016 by Lopez-Martens et al. [148].

In the following subsection we present a survey of SD bands for which detailed experimental information on the properties of decay-out is available, focusing on cases in which discrete (and fragmented) γ-decays linking transitions have been observed and hindrances in the γ-decay toward lower-deformed shapes have been measured. This will allow to quantitatively discuss the decay-out process in terms of a tunneling through a barrier in the potential energy surface, between superdeformed and normal deformed shapes (see Fig. 21), an approach which is also applied in the discussion of selected cases of shape coexistence at zero spin, e.g., the fission shape isomers (Section 3.1) and shape-isomer-like nuclei (Section 4), as also discussed in connection with Fig. 9.

3.2.2. Survey of decay-out of superdeformed bands with hindrance due to shape change

The decay of superdeformed bands shows similarities with the phenomenon of γ-decay of fission shape isomers in the actinides, here discussed in Section 3.1. In both cases, a potential energy barrier isolates the strongly deformed states from the states with normal deformation, what results in a scenario of shape coexistence. The decay of superdeformed bands is, however, a more complex phenomenon compared to the decay of fission shape isomers, where the electromagnetic decay to normal deformed configurations competes only against fission. In the case of SD bands, the decay competes against the collective $E2$ decay along the superdeformed band itself for several consecutive in-band transitions, thus providing important information on the mixing and on the transmission coefficients through the barrier, as a function of angular momentum and internal excitation energy (i.e., "temperature"). The

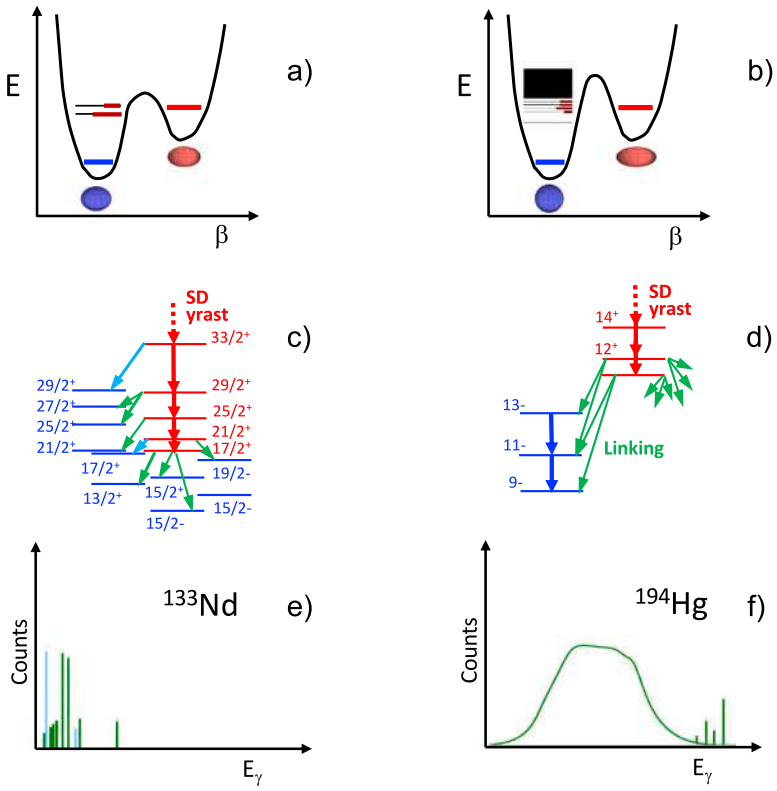

Fig. 23. Illustration of the two extreme scenarios occurring at the angular momentum where the SD yrast band decays out into the ND well, via the coupling to doorway states in the ND well. Panel (a): the SD yrast state is connected to a few doorway states on the ND side. Panel (b): the doorway state is spread over many excited ND states. The corresponding decay-out schemes and γ-ray energy spectra are shown in panels (c)–(e) and (d)–(f), respectively, with reference examples to the cases of ^{133}Nd and ^{194}Hg. Red (blue) transitions indicate SD (ND) transitions, while green transitions show the decay-out transitions. Red (blue) lines indicate states of predominant SD(ND) nature.
Source: Adapted from [148].

results can be used to benchmark nuclear models predicting barriers and inertial mass parameters which are key ingredients in the description of the large amplitude motion connecting superdeformed and normal shapes [148,155]. In particular, the probability to tunnel through the barrier depends on the interactions coupling the different states along the way, with the pairing interaction and the K-quantum number both playing a role. As a result, large hindrances on the transmission coefficient might be expected.

In this review we focus on the shape change phenomenon at the angular momentum where the decay-out of the SD yrast band occurs. A survey of SD bands is presented for which quantitative experimental information on the decay-out properties is available in terms of measured discrete γ transitions linking SD and ND states (the so called "linking" transitions). Such transitions correspond to less than 30 cases (less than 10% of the total number of SD nuclei presently known), as a consequence of the experimental difficulties in observing weak (high-energy) γ transitions with intensities as low as 10^{-4}. From the observed linking transitions, essential spectroscopic observables can be extracted, such as excitation energy, spin and parity for SD states, as well as information on the decay mechanism itself, responsible for the rapid depopulation of the SD structures (see Ref. [148] for a detailed discussion). Information on linking transitions for SD nuclei (i.e., initial and final state energies and spins, γ-transition energy, decay branching, and reduced transition probabilities, when available) is summarized in Tables 2 and 3 for mass A ~ 190 (i.e., ^{192,194,196}Pb and ^{190,191,194}Hg), in Table 4 for mass A ~ 150 (i.e., ^{152}Dy, ^{149}Gd and ^{151}Tb), in Table 5 for mass A ~ 80 (i.e., ^{84}Zr), in Table 6 for mass A ~ 60 (i.e., ^{60}Zn, ^{58,59}Cu and ^{56,58}Ni) e in Table 7 for mass A ~ 40 (i.e., ^{40,42}Ca and ^{36,40}Ar). The latter is the lightest mass region considered in this review. Figs. 29, 30, 31, 32, and 33 display partial decay schemes for the decay of the SD bands for which full information is available for the discrete decay-out transitions, i.e., ^{192,194}Pb, ^{194}Hg, ^{152}Dy, ^{84}Zr, ^{60}Zn, ^{58}Cu, ^{58}Ni, ^{40,42}Ca and ^{36,40}Ar. Similar information on decay-out transitions is also available for the cases of $^{132-137}$Nd (Z = 60, A ~ 130) [158–163] and ^{163,164}Lu (Z = 71, A ~ 160) [164,165], which present rather specific features, as later briefly discussed.

From the data presented above, different features emerge for the decay out of SD bands in the various mass regions. For the heavy-mass systems with A ~ 150 and 190, the superdeformed bands are characterized by intrinsic quadrupole moments derived from B(E2) values (see Section 2.2.3) Q_t ~ 17–20 eb, corresponding to deformation parameters β_2 ~ 0.5–0.7, comparable with the values for fission isomers in the actinides region (i.e., Q_t ~ 30 eb and β_2 ~ 0.7), as shown in Figs. 18 and 20 (see also Ref. [127]. The decay out into the states at lower deformation, which occurs at spin ~10 in mass A ~ 190 and ~30 in mass 150, is a statistical process which proceeds via a few discrete γ rays collecting typically less then ~10% intensity, mainly of E1 type

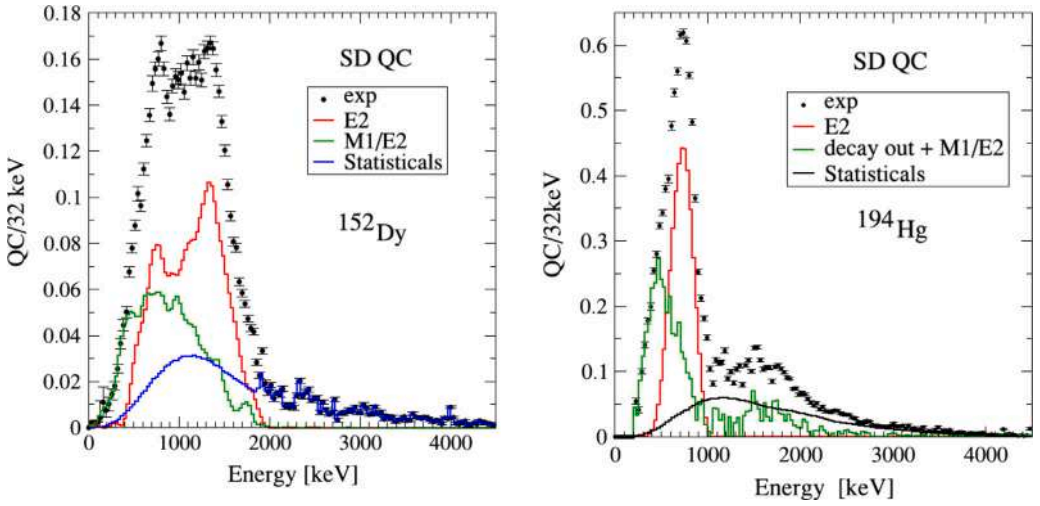

Fig. 24. Decomposition of the SD quasi-continuum (QC) spectra observed in coincidence with the SD yrast bands of ^{152}Dy (left) and ^{194}Hg (right) nuclei. The blue/black lines represent the statistical E1 component (often parametrized as the tail of the Giant Dipole Resonance), while the E2 QC component, originating from γ rays feeding of the SD yrast from the region of excited rotational bands (rotational damping regime [172,173]), is given by red lines (see Refs. [174,175]). The decay-out spectrum from the SD yrast band is shown by green lines. In ^{152}Dy, it is mostly composed of M1/E2 γ rays, and it cannot be easily separated from the pure E2 QC. In ^{194}Hg it is also made up of statistical E1 γ rays which appear as an excess of strength above the statistical E1 spectrum, beyond 1 MeV ([148] and Refs. therein).
Source: Taken from [148].

and all characterized by large hindrances in their decay, as later discussed. The largest fraction of the decay of the band, up to 100% for the lowest measured spin state, is instead fragmented into short γ cascades (~2 steps long) of E1 and E2 character which form a quasi-continuum (QC) distribution well identified in the γ spectrum of ^{192,194}Pb and ^{191,192,194}Hg in the 1–2 MeV region (see Fig. 24(left) [152,166–168]. A statistical fluctuation analysis of the decay-out QC spectrum measured in ^{192}Hg, following the method developed in Refs. [169,170], has revealed that ~10^4 transitions are sampled in the decay out of the SD band [171], explaining the experimental difficulties in identifying discrete γ transitions connecting SD and ND states. Such a large number of paths is also in agreement with predictions from a schematic model based on equidistant single-particle levels (with pairing treated using the BCS method), from which information on a substantial reduction of the Δ_0 pairing gap in the ND well, as a function of spin (from Δ_0 = 0.9 to 0.7 MeV), was also deduced. In the case of ^{152}Dy, the QC decay-out distribution, located below 1 MeV in the γ spectrum, is merged together with the QC distribution of transitions feeding the SD band, therefore, the decay-out out spectrum can only be extracted through a model simulation (Fig. 24 (b)) [148].

Moving down in mass number, the decay properties of the SD bands gradually change. The typical quadrupole moments become smaller (Q_t ~ 2–6 eb, for A ~ 40 to 80), with corresponding deformation parameters β_2 ~ 0.4–0.6 (see Fig. 20 and Ref. [127]). For mass A ~ 80 (^{84}Zr), the decay out still occurs at high spins, around 25 $\hbar$, with only a small fraction of the SD intensity taken by linking transitions of typical E1 character, as in the heavier 150 and 190 mass regions. In contrast, in mass A ~ 40 and 60, due to the lower density of final ND states, the decay out becomes less fragmented, and the highly deformed bands are more easily connected to the structures with lower deformation. Experimentally, rather intense discrete linking transitions of E2 character, moderately hindered, are here observed, collecting a sizeable fraction of the SD band decay (individual decay branches can reach more than 30% of the SD band intensity). In mass A ~ 60, other decay modes are also observed, such as prompt-particle decay out of the SD well (e.g., p and α in ^{56,58}Ni and p in ^{58,59}Cu [176–180]). While in mass 60 the superdeformed bands still decay out at rather high spin, around 10–15 $\hbar$, in the lightest region of ^{40,42}Ca and ^{36,40}Ar nuclei, the SD bands can be followed down to the 0^+ band head [181–185]. In ^{38}Ar, an additional highly deformed non-yrast band has also been observed over a wide spin range, connected to the low-lying structure of lower deformation [186]. Such observations provide extended experimental information to be compared with most advanced theory predictions, either based on large-scale shell model calculations (in the $sd-fp$ space) [187–189], beyond mean field [190,191], and molecular dynamics approaches [192–194]. As a result, microscopic aspects of deformation and shape changes in these lighter mass regions, including the degrees of mixing into specific lower deformation states, can be addressed. In both Ar and Ca cases, the bands are interpreted as arising from multiparticle–multihole excitation across the sd–fp shell gap (see also Fig. 37), a mechanism which could be at the origin of strongly deformed ground states in and near the N = 20 magic nuclei in the Z ≈ 12 region (i.e., in the so-called "island of inversion" [195]).

The coexistence of shapes in the mass region A ~ 40 has also been clearly demonstrated by a Coulomb-excitation experiment of ^{42}Ca, performed with the AGATA tracking array [182,196]. The data has provided magnitudes and relative signs of several E2 matrix elements coupling the low-lying states in ^{42}Ca, from which the spectroscopic quadrupole moment of the 2_2^+ state of the SD band was extracted confirming a large deformation (β_2 = 0.48(16)), with a small deviation from an axially symmetric shape (γ = 13(5)°). This is in contrast with a weakly deformed, γ-soft character of the 0_1^+ ground state. As reported in Table 7, the large B(E2)

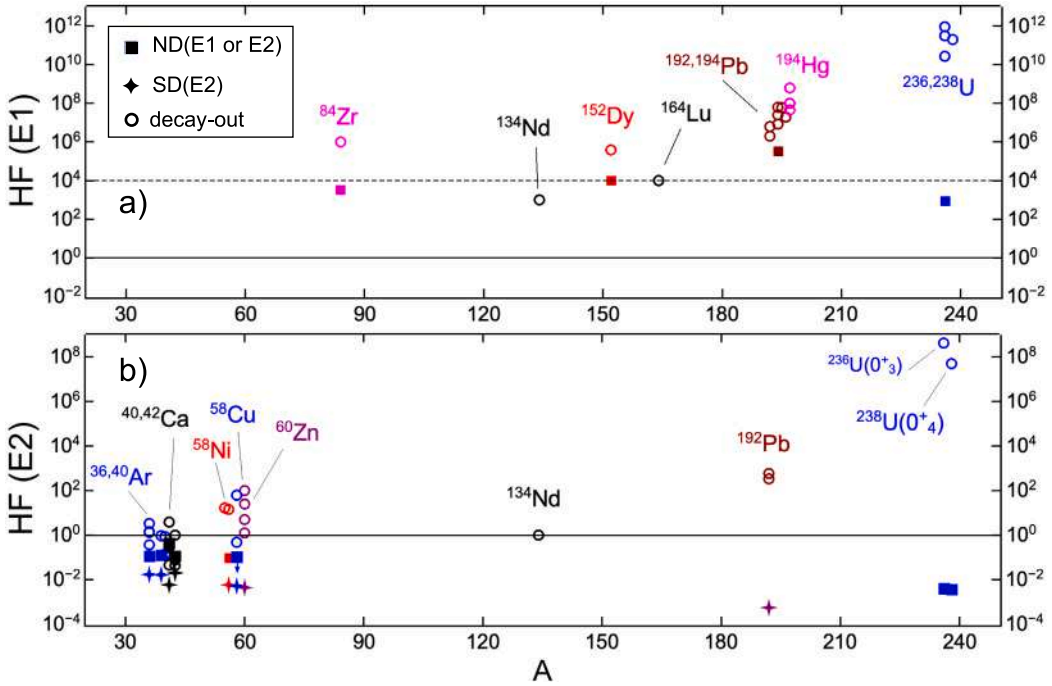

Fig. 25. Hindrance factors (HF) extracted from the experimental B(E1) (panel (a)) and B(E2) (panel (b)) reduced transition probabilities available for discrete γ transitions linking SD yrast bands to lower deformation states, in the mass regions A $\sim$ 40, 60, 130, 150, and 190. Hindrances for E1 and E2 decays from the 0^+ shape isomers states in ^{236,238}U are also shown as a reference. See Eq. (3) and text for details.

value extracted for the $0_2^+ \rightarrow 2_1^+$ decay confirms a strong mixing between the SD and ND structures, as also observed in ^{40}Ar and ^{40}Ca.

In the attempt of formulating a comprehensive picture that applies to SD bands in general, a rather difficult task due to the variety of decay modes discussed above, we now focus on the experimental B(E/Mλ) reduced transition probabilities available for the discrete linking transitions (see Tables 2 and 7). From such values, hindrance factors (HF) relative to the Weisskopf estimates [69] can be extracted, according to Eq. (3).

Experimental hindrance factors are reported in Fig. 25(a) and (b), with open circles, for E1 and E2 multipolarities of the decay-out transitions, respectively. As a comparison, available HF values for E2 transitions along the SD band and E1 and E2 transitions among ND states, in the same nucleus, are also shown using stars and full squares. In panel (a), the dashed line at 10^4 indicates the average hindrance factor, HF_{ND}(E1), observed for E1 transitions with $\Delta K = 0$, while for E2 transition the reference value (HF_{ND}(E2)) is 1, as reported in [69]. In general, for masses A $\geq$ 80, a dominance of E1 decay is observed, with large relative hindrances $HF_{rel} = HF_{SD}/HF_{ND}$, of the order of 10^2 to 10^4, with respect to the corresponding average estimates for E1 and E2, respectively. In this context, Lu and Nd isotopes are specific. In Lu nuclei, the SD bands are characterized by a considerable degree of triaxiality ($\gamma \sim 20°$), which makes the decay out ~400 times faster as compared to axially symmetric systems in the A=190 region [164,165]. In turn, in Nd nuclei, the highly-deformed bands ($\beta = 0.30$–0.35) decay into normal deformed states which do not differ significantly in deformation ($\beta = 0.20$–0.25), leading to a fast decay out, proceeding via a few transitions collecting a very large fraction of the entire flux [158–163]. For smaller masses, A $\sim$ 40 and 60, the decay is governed by E2 transitions with smaller hindrance, in particular in the Ar and Ca nuclei. In the figure, the exceptionally large HF values measured for E1 and E2 transitions from the 0^+ shape-isomer states in ^{236,238}U are also reported, as a reference.

As discussed in Section 3.2.1, the hindrance of the γ decay for the decay-out transitions can be associated, in first place, with the gross feature of the barrier separating the SD and ND states. For example, HF_{rel} values can be used for a qualitative test of the trend, as a function of the barrier height, of the transmission coefficient T $\sim 1/HF_{rel}$, being T a measure of the ease or hindrance to tunnel through the potential energy barrier in the deformation coordinate space – a comparison on absolute scale would require an accurate estimate, case by case, of the level density in the ND well, at the excitation energy of the decay-out, and of the transition probability (E1 or E2) at the decay-out [199]. For elaborated calculations of T we refer to Ref. [148], while here we consider a schematic expression of T, widely used in fission as well as SD decay-out studies, taking into account two parameters only, namely *(i)* the barrier height V_B and *(ii)* the effective frequency at the barrier ω_B. These two parameters refer to the simplest approximation of the potential energy and mass parameter around the top of the barrier. For an inverted parabola parametrizing the potential energy barrier and a constant mass parameter, the transmission coefficient becomes:

$$T = \frac{1}{1 + exp(2\pi \frac{V_B - E}{\hbar\omega_B})} \tag{27}$$

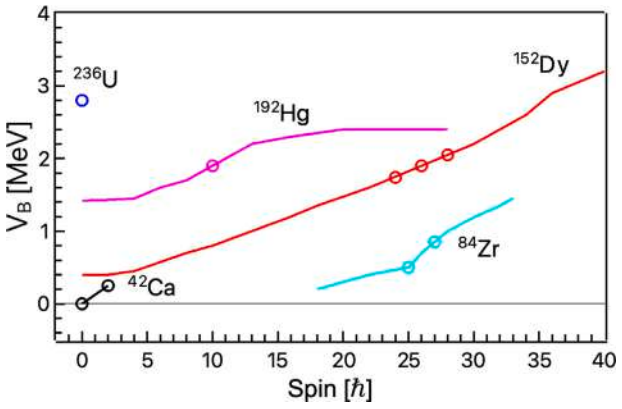

Fig. 26. Barriers heights relative to the SD minimum along the tunneling path, as a function of spin, in representative nuclei in the A ~ 40, 80, 150 and 190 mass regions [153,154,196,197]. The barrier toward the lower deformed minimum is also given for the 0^+ fission isomer in ^{236}U, for comparison purposes [122] (see Fig. 14). Circles correspond to barrier values at the decay-out spins.

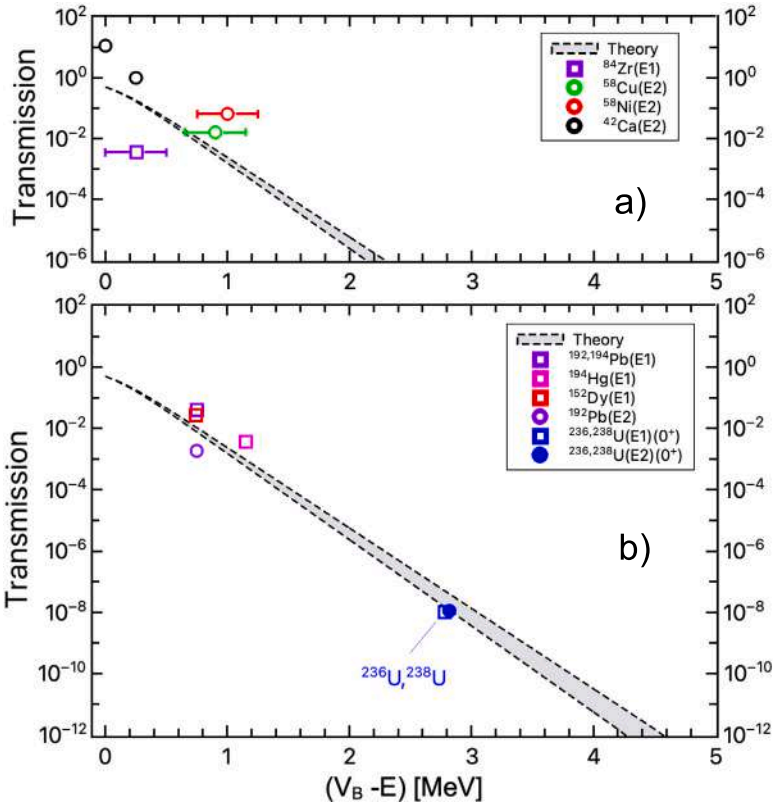

Fig. 27. Experimental transmission coefficients, estimated from the hindrance factors available for SD bands for light/medium mass nuclei (panel (a)) and in heavy systems (panel (b)) (Fig. 25) for cases where calculated barrier heights above the SD state ($V_B - E$) are available [55,122,153,154,196–198]. Schematic model predictions (Eq. (27)) are given for barrier frequency $\hbar\omega_B$ = 0.97–1.04 MeV (gray region).

where E is the energy of the SD state, $V_B - E$ measures the barrier height above the SD state, and ω_B is the effective barrier frequency. Typical values for $\hbar\omega_B$ are of the order of 1 MeV (e.g., 0.97 and 1.04 MeV for ^{152}Dy and ^{192}Hg, at the decay-out spins of 30 and 10 $\hbar$, respectively [154]. Barrier heights, above the SD state, may vary instead between 0.25–2 MeV for SD nuclei [148,154],

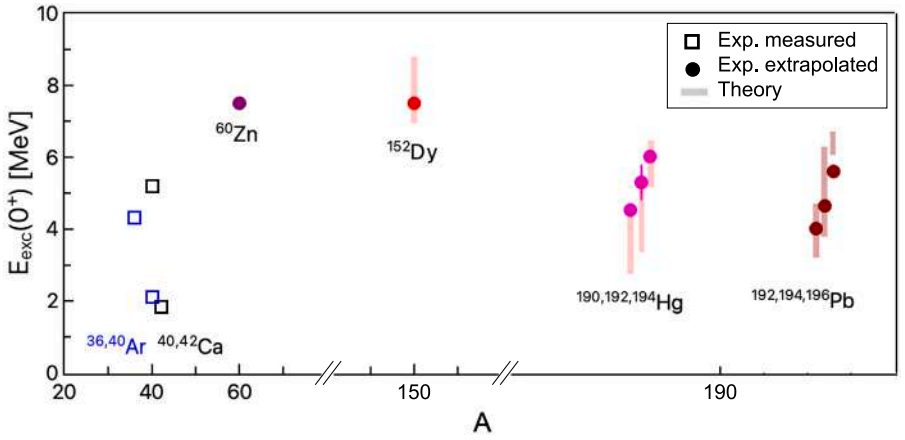

Fig. 28. Excitation energies of the $I^\pi = 0^+$ band heads of selected SD bands: open squares refer to measured values (mass region A ∼ 40), filled circles show estimates based on extrapolation from observed linking transitions and quasi-continuum analyses (mass region A ∼ 150 and 190). The extrapolations are performed using a functional form of the excitation energy written as $E^{SD}(I) = E^{SD}(0^+) + a[I(I+1)] + b[I(I+1)]^2$, where $E^{SD}(I)$ is the energy of the SD level at spin I (see, e.g., Ref. [151]). Shaded bars give the range of calculated values for $E^{SD}(0^+)$ from different theory approaches (e.g., relativistic mean field, Strutinsky and Hartree–Fock Bogoliubov with different interactions) [151,204,204–208]. For Hg and Pb, see also discussion in connection with (Fig. 68).

up to more than 2.5 MeV for the extreme case of fission-shape isomers [12] (see Fig. 14). Fig. 26 shows examples of barrier height calculations relative to the SD minimum for Zr, Dy and Hg, as a function of spin, according to the model of Refs. [153,154,197]. Circles indicate barrier values at the decay-out spins. We note that sizeable barriers are still expected at I = 0 in heavy systems, such as ^{192}Hg. The barrier height for the 0^+ fission isomer in ^{236}U is also shown (see Fig. 14), as well as barriers for superdeformed 0^+ and 2^+ states in ^{42}Ca, where the decay out occurs. The latter are obtained from beyond-mean-field model approaches using the Gogny interaction [196]. It is evident that the barrier heights, at the decay, are considerably smaller in ^{84}Zr than in the other heavier systems, and in ^{42}Ca vanish, as also shown by the Potential Energy Surfaces of ^{42}Ca discussed in Section 4.1 (see Fig. 40(a) and (b) and related discussion).

Fig. 27 shows the prediction of the transmission coefficient T from Eq. (27) (gray region), as a function of the barrier height ($V_B - E$) and assuming $\hbar\omega_B$ values between 0.97 and 1.04 MeV. Symbols give qualitative experimental estimates (i.e., T ∼ 1/HF$_{rel}$) obtained from the hindrance factors available for SD bands in light/medium mass nuclei (panel (a)) and in heavy systems (panel (b)) (see Fig. 25 and Tables 2 and 7), assuming barrier heights from corresponding calculations [55,122,153,154,196–198]. For heavy systems, the data follow rather well the expected trend, for both E1 and E2 transitions, thus providing support to the barrier penetration interpretation in describing the gross decay properties of nuclei with highly-elongated shapes and at the angular momenta where the decay-out into lower-deformed structures occurs. In this case, the decay out can be described as statistical process into a chaotic environment of ND states [148]. It is also found that experimental values of transmission coefficients for the 0^+ decay of the ^{236,238}U fission shape isomers (Table 1) are also in approximate agreement with the predictions from Eq. (27), suggesting a validity of the barrier penetration interpretation for selected cases of 0^+ states, where a sizeable barrier is expected to be present between the shape coexisting structures with significantly different shapes. In general, it is found that, in light mass nuclei, data appear rather scattered with respect to the predicted trend (panel (a)), indicating that additional factors related to the microscopy of the system may contribute to modify the γ-decay hindrances. We refer, in particular, to a direct coupling of SD states to a small number of doorway states, owing to a possibly reduced size of the barrier and a reduced level density in the ND well (see, e.g., Ref. [200] and Fig. 23).

In heavy nuclei, the decay out of SD bands occurs at high angular momenta, from I ∼ 10 to 30, depending on the mass region, what prevents the observation of the 0^+ SD band heads as an end point of the cascade (see Tables 2, 3, 4, 5, 6 and Figs. 29, 30, 31 and 32). As shown in Fig. 28, the excitation energy of the SD yrast band heads for ^{60}Zn, ^{190,192,194}Hg and ^{192,194,196}Pb can be inferred by extrapolating the SD band to zero rotational frequency, knowing the excitation energy and spin of the SD band at the decay out, from linking transitions. Band heads energies between 4 and 8 MeV, relative to the ground state, are found, with corresponding theory predictions differing by 1–2 MeV among different models. It follows that other experimental techniques are needed to get direct access to zero/low spin states of such highly elongated shapes, as for example multinucleon transfer reactions with heavy ions [201–203]. We note, however, that the high density of states in the low-spin region of interest might hamper this approach, resulting in a serious limitation in terms of comparison with theory predictions, what prevents to achieve a coherent picture of shape coexistence from zero to high spins in heavy systems. The situation can be different in lighter systems, where the SD decay cascade reaches its 0^+ bandhead (in Section 3.2.2, cfr. Fig. 28).

Some insight into the characteristics discussed above is provided by Fig. 26 where the heights of the theoretical barrier separating the SD bandheads from ND excitations are shown for Hg, Dy, Zn and Ca nuclei. While the hypothetical SD 0^+ state for Hg nuclei is expected to be separated from the ND structures by a rather high barrier of ∼1.4 MeV, in analogy to shape isomers in U nuclei, such

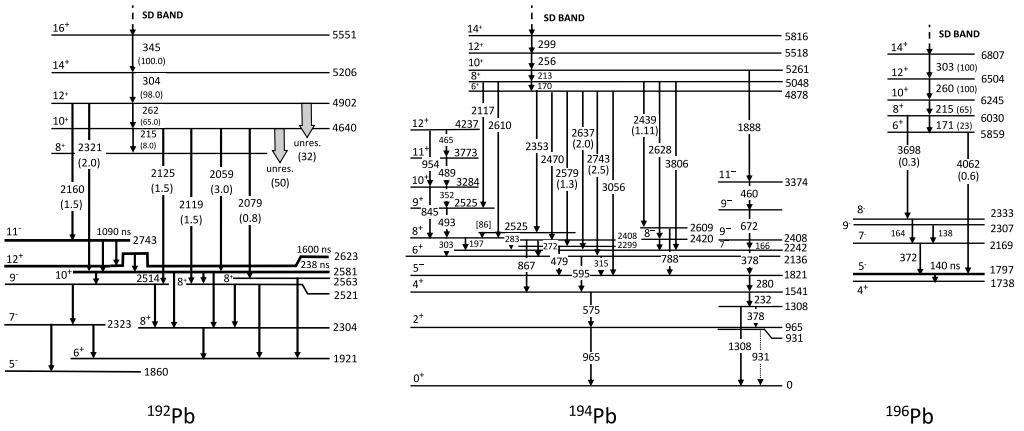

Fig. 29. Partial decay schemes of ^{192}Pb, ^{194}Pb and ^{196}Pb showing the lowest part of the superdeformed yrast band and the normal deformed states to which the SD band mainly decays. The intensities of the linking transitions (if available) are given in brackets (in % of the SD band intensity). Dashed arrows indicate extension of the SD band to higher spins or tentative placement of the transitions (see also Table 2).
Source: Data from [207–209].

Table 2
Characteristics of the SD yrast band at the decay-out spins, as observed in ^{192}Pb, ^{194}Pb and ^{196}Pb: E_i, E_f and I_i^π, I_f^π are the initial and final excitation energies and spin-parities, respectively; U is the excitation energy above yrast; $T_{1/2}$ is the half life; E_γ are the energies of the discrete γ transitions linking the SD band to ND states, with branching BR (central value from [67]) and multipolarity $E/M\lambda$ (in round brackets if uncertain, in squared brackets if deduced from the spins and parities of the initial and final levels); $B(E/M\lambda)$ are the corresponding reduced transition probabilities in Weisskopf units. The fraction of electromagnetic decay which is unresolved is indicated by γ(unres.). References to specific papers are given in the last column.

Nucleus	E_i [MeV]	I_i^π	U [MeV]	$T_{1/2}$ [ps]	E_f [MeV]	I_f^π	E_γ [MeV]	BR [%]	E/Mλ	B(E/Mλ) [W.u.]	Refs.
^{192}Pb (SD yrast)	4.425	8^+	2.121				γ(unres.)	100	E/M		[207]
	4.640	10^+	2.059		4.425	8^+	0.215	12.3	E2	1800[a,b]	
					2.581	10^+	2.059	4.6	M1	7.4(27) 10^{-5}	
					2.562	8^+	2.079	1.2	E2	1.7(9) 10^{-3}	
					2.119	8^+	2.119	2.3	E2	3.0(12) 10^{-3}	
					2.514	9^-	2.125	2.3	E1	5.0(19) 10^{-7}	
							γ(unres.)	77.2	E/M		
	4.902	12^+	2.278		4.639	10^+	0.262	66.3	E2	1800[a,b]	
					2.160	11^-	2.160	1.0	E1	1.6(10) 10^{-7}	
					2.321	10^+	2.321	2.0	E2	8.6(32) 10^{-4}	
							γ(unres.)	30.6	E/M		
	5.206	14^+	1.707		4.902	12^+	0.304	98	E2	1800[a,b]	
							γ(unres.)	2	E/M		
^{194}Pb (SD yrast)	4.878	(6^+)	2.743		2.525		2.353	5.0			[209–211]
					2.408		2.470	2.7			
					2.299		2.579	5.4			
					2.242	(7^-)	2.637	3.2	(E1)	$\geq$12(5) 10^{-8}	
					2.136	(6^+)	2.743	5.9	(M1)	$\geq$22(7) 10^{-6}	
					1.821	(5^-)	3.056	1.4	(E1)	$\geq$4(2) 10^{-8}	
							γ(unres.)	76.4	E/M		
	5.047	(8^+)	2.438	14	4.878	(6^+)	0.170	62.2	(E2)	1500[a]	
					2.931	(9^+)	2.117	1.0	(M1/E2)		
					2.608		2.439	1.0			
					2.438	$(8)^+$	2.610	1.9	(M1)	2.3(9) 10^{-6}	
					2.420	(8^-)	2.628	1.4	(E1)	1.6(8) 10^{-8}	
					2.241	$(7)^-$	2.806	1.9	(E1)	1.67(6) 10^{-8}	
							γ(unres.)	30.6	E/M		
	5.261	(10^+)	2.680	5.8	5.047	(8^+)	0.213	90	E2	[a]	
					3.373	(11^-)	1.888	1.0	(E1)	5(2) 10^{-8}	
							γ(unres.)	9.0	E/M		
^{196}Pb (SD yrast)	5.859	6^+	3.436		1.797	5^-	4.062	2.6	E1		[208]
							γ(unres.)	97.4	E/M		
	6.030	8^+	3.440		5.859	6^+	0.171	35.4	E2	[a]	
					2.333	(8^-)	3.698	0.5	(E1)		
							γ(unres.)	64.2	E/M		

[a] Transition within the SD band.
[b] From quadrupole moment Q_0.

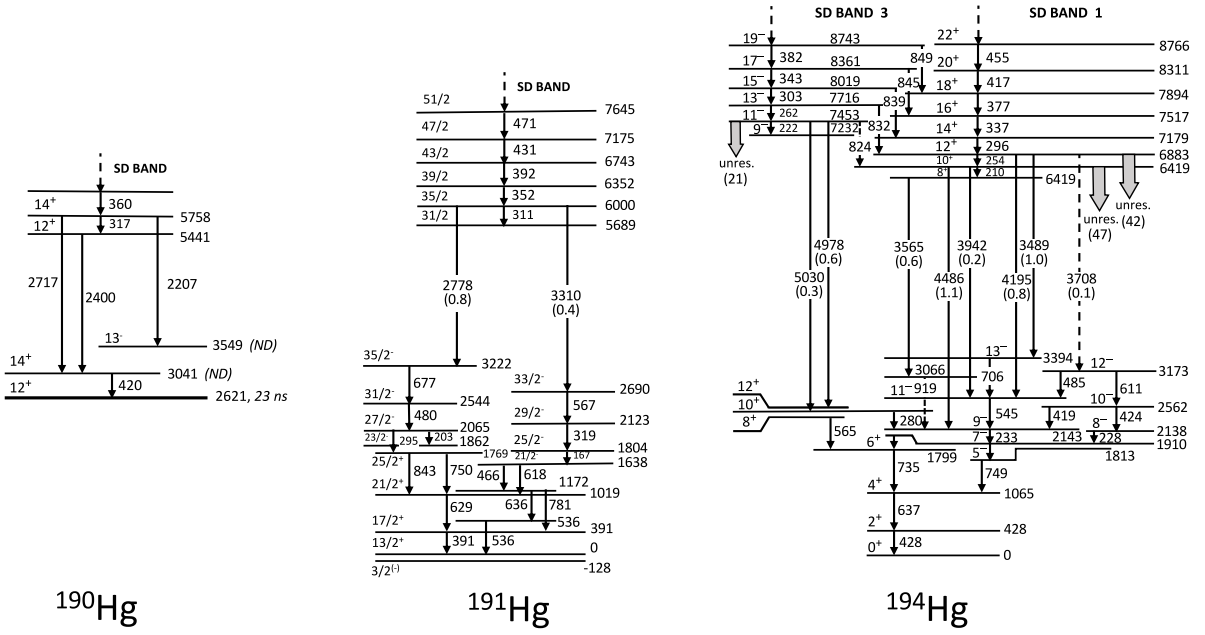

Fig. 30. Partial decay schemes of ^{190}Hg, ^{191}Hg and ^{194}Hg, showing the lowest part of the superdeformed yrast band and the normal deformed states to which the SD band mainly decays. In ^{194}Hg, the decay of an excited SD band (SD3) is also shown. The intensities of the linking transitions (if available) are given in brackets (in % of the SD band intensity). Dashed arrows indicate extension of the SD band to higher spins or tentative placement of the transition, thick arrows give the intensity going into unresolved, fragmented γ decays (see also Table 3).
Source: Data from [152,205,212].

Table 3
Characteristics of the SD yrast band at the decay-out spins, as observed in ^{190}Hg, ^{191}Hg and ^{194}Hg (in this case the excited band SD3 is also reported). See Table 2 caption for detailed explanations.

Nucleus	E_i [MeV]	I_i^π	U [MeV]	$T_{1/2}$ [ps]	E_f [MeV]	I_f^π	E_γ [MeV]	BR [%]	E/Mλ	B(E/Mλ) [W.u.]	Refs.
^{190}Hg (SD yrast)	5.441	(12^+)	2.820		3.041	(14^+)	2.400				[205]
	5.758	(14^+)	2.717		5.440	(12^+)	0.317				
					3.549	(13^-)	2.207				
					3.041	(14^+)	2.717				
^{191}Hg (SD yrast)	5.689	(31/2)	3.145				γ(unres.)	100	E/M		[67,152]
	6.000	(35/2)	2.778		5.689	(31/2)	0.311	16.9	E2	[a]	
					3.222	$35/2^-$	2.778	1.0			
					2.690	$33/2^-$	3.310	0.5			
							γ(unres.)	81.7	E/M		
^{194}Hg (SD yrast)	6.419	(8^+)	4.055		3.066		3.565	60.0			[206,212]
							γ(unres.)	40.0	E/M		
	6.629	(10^+)	4.205		6.419	(8^+)	0.210	2.0	E2	1670[a]	
					2.688	(11^-)	3.942	0.4	(E1)		
					2.143	9^-	4.486	2.2	(E1)		
							γ(unres.)	95.3	(E/M)		
	6.883	(12^+)	4.407	2.4	6.629	(10^+)	0.254	53.2	E2	1786	
					3.173	(12^-)	3.710	0.1	(E1)	$1.6\ 10^{-9}$	
					3.394	(13^-)	3.489	1.1	(E1)	$2.2\ 10^{-8}$	
					2.688	(11^-)	4.195	0.9	(E1)	$1.0\ 10^{-8}$	
							γ(unres.)	44.7	(E/M)		
^{194}Hg (exc. SD3)	7.232	(9^-)	5.089				γ(unres.)	100	E/M		[212]
	7.453	(11^-)	4.765		7.232	(9^-)	0.222	2.2	E2	[a]	
					6.629	(10^+)	0.824				
					2.476	(12^+)	4.978	2.7			
					2.424	(10^+)	5.030	1.3			
							γ(unres.)	93.8	E/M		

[a] Transition within the SD band.

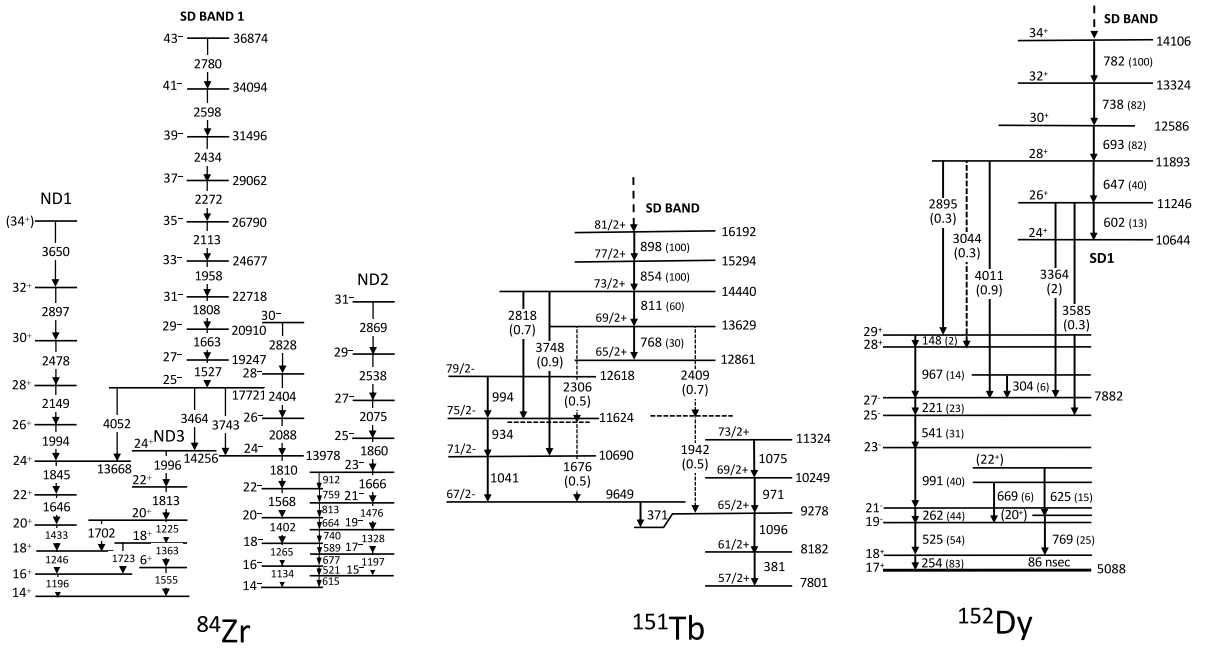

Fig. 31. Partial decay schemes of ^{152}Dy, ^{151}Tb and ^{84}Zr, showing the lowest part of the superdeformed yrast band and the normal deformed states to which the SD band mainly decays. The intensities of the linking transitions (if available) are given in brackets (in % of the SD band intensity). Dashed arrows indicate extensions of the SD band to higher spins or tentative placements of the transition. In the case of ^{151}Tb, excitation energies of the SD yrast band are not certain and the ones reported correspond to the most likely decay-out scenario proposed by Robin et al. [213] (see also Tables 4 and 5).
Source: Data from [151,213,214].

Table 4
Characteristics of the SD yrast band at the decay-out spins, as observed in ^{152}Dy, ^{149}Gd and ^{151}Tb. In the case of ^{151}Tb, excitation energies are taken from Ref. [213], and correspond to the most likely decay-out scenario. See Table 2 caption for detailed explanations.

Nucleus	E_i [MeV]	I_i^π	U [MeV]	$T_{1/2}$ [ps]	E_f [MeV]	I_f^π	E_γ [MeV]	BR [%]	E/Mλ	B(E/Mλ) [W.u.]	Refs.
^{152}Dy (SD yrast)	10.644	24^+	3.417				γ(unres.)	100.0	E/M		[151]
	11.245	26^+	2.616		10.644	24^+	0.602	32.5	E2	2520[a,b]	
					7.882	27^-	3.364	0.5			
					7.661	25^-	3.585	0.8			
							γ(unres.)	66.3	E/M		
	11.893	28^+	3.044		11.245	26^+	0.648	48.8	E2	2520[a,b]	
					8.996	29^-	2.895	0.4			
					8.849	28^+	3.044	0.4			
					7.882	27^-	4.011	1.1	E1	2.6 10^{-6}	
							γ(unres.)	49.4	E/M		
^{149}Gd (SD yrast)	10.625	$(47/2^-)$	4.121				γ(unres.)	100.0	E/M		[215]
	11.243	$(51/2^-)$	3.502		10.625	$(47/2^-)$	0.618	23.5	E2	[a]	
					9.055	$(49/2^-)$	2.188	3.5			
					8.465	$(47/2^-)$	2.778	0.7			
					8.458	$(51/2^-)$	2.785	0.7			
							γ(unres.)	71.5	E/M		
^{151}Tb (SD yrast)	12.861	$(65/2^+)$	3.583				γ(unres.)	100.0	E/M		[213]
	13.629	$(69/2^+)$	3.380		12.861	$(65/2^+)$	0.768	50.0	E2	[a]	
					10.963		2.306	0.8			
					10.860		2.409	1.2			
							γ(unres.)	48.0	E/M		
	14.44	$(73/2^+)$	3.116		13.629	$(69/2^+)$	0.811	60.0	E2	[a]	
					11.624	$(75/2^-)$	2.818	0.7			
					10.690	$(71/2^-)$	3.748	0.9			
							γ(unres.)	38.4	E/M		

[a] Transition within the SD band.
[b] From quadrupole moment Q_0.

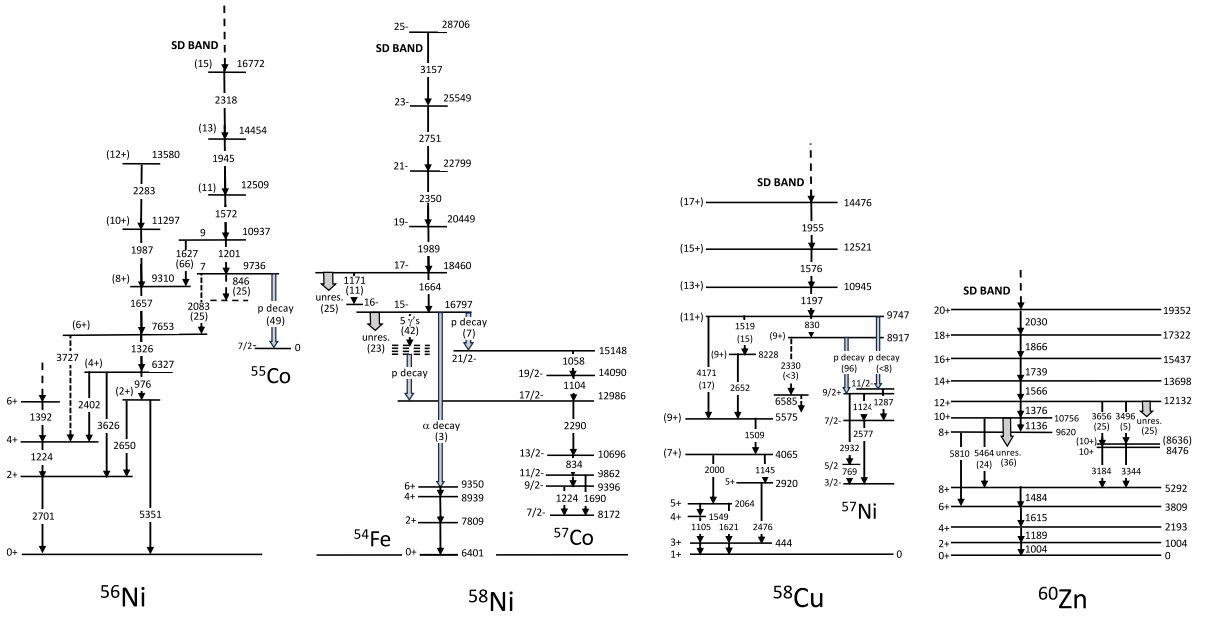

Fig. 32. Partial decay schemes of ^{60}Zn, ^{58}Cu, ^{58}Ni and ^{56}Ni, showing the lowest part of the superdeformed yrast band and the normal deformed states to which the SD band mainly decays. The intensities of the linking transitions (if available) are given in brackets (as decay branches, in %). Dashed arrows indicate extension of the SD band to higher spins or tentative placement of the transitions, thick arrows give the intensity going into unresolved, fragmented γ decays, or p and α particle decay (see also Table 6).
Source: Data from [176–179,204].

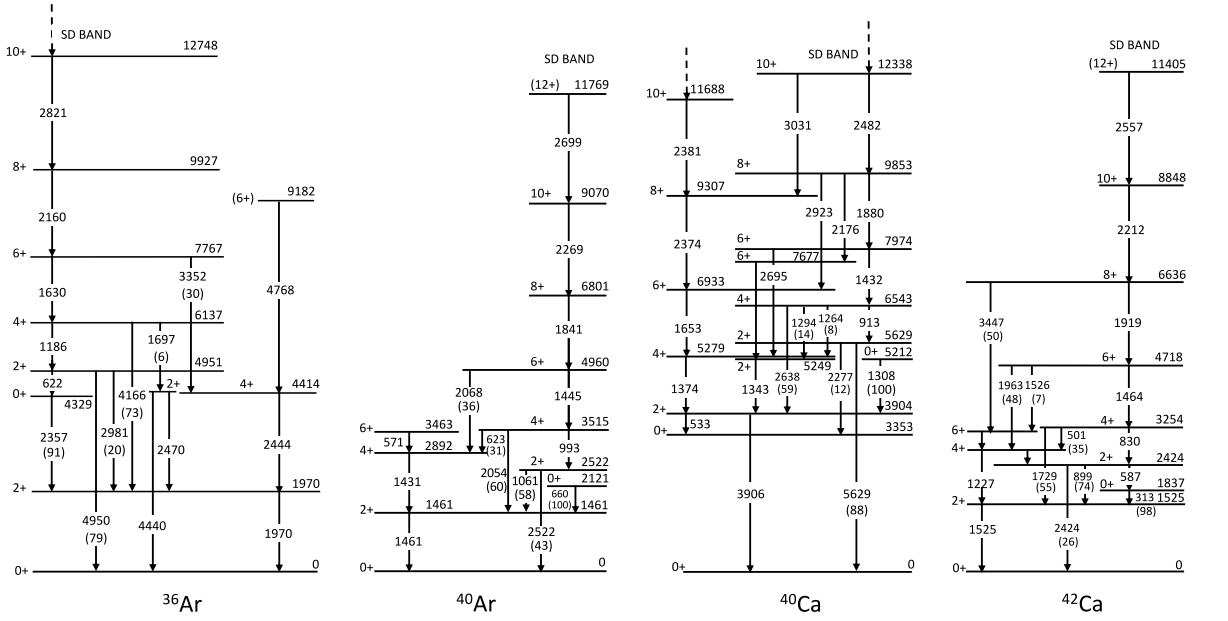

Fig. 33. Partial decay schemes of ^{40}Ca, ^{42}Ca, ^{36}Ar and ^{40}Ar, showing the lowest part of the superdeformed yrast band and the normal deformed states to which the SD band mainly decays. The intensities of the linking transitions (if available) are given in brackets (as decay branches, in %). Dashed arrows indicate extensions of the SD band to higher spins or tentative placement of the transitions (see also Table 7).
Source: Data from [181,182,184,185].

Table 5
Characteristics of the SD yrast band at the decay-out spins, as observed in ^{84}Zr. See Table 2 caption for detailed explanations.

Nucleus	E_i [MeV]	I_i^π	U [MeV]	$T_{1/2}$ [ps]	E_f [MeV]	I_f^π	E_γ [MeV]	BR [%]	E/Mλ	B(E/Mλ) [W.u.]	Refs.
^{84}Zr (SD yrast)	17.721	25^-	2.783	0.014^{40}_{-10}	14.254	(24^+)	3.464	0.4	(E1)	$\sim 10^{-6}$	[214]
						24^-	3.743	0.7	(M1 + E2)	$\lesssim 10^{-4}$[b]	
						24^+	4.052	0.9	(E1)	$\lesssim 10^{-6}$	
							γ(unres.)	98%			
	19.247	27^-	2.234		17.721	(25^-)	1.527	0.65	E2	[a]	
							γ(unres.)	0.35			

[a] Transition within the SD band.
[b] Upper limit for B(M1).

barrier is only of ~0.4 MeV for Dy nuclei and almost vanishes for light Zn and Ca species. This last feature is in agreement with mentioned above experimental data on the 0^+ SD bandheads, which could be identified in light nuclei. In all known cases, the 0^+ SD bandhead, which is populated in the SD decay, seems to be separated from the ND states by a very low barrier or such a barrier is not present at all – the decay is not hindered. The fact that the known 0^+ members of SD bands in light nuclei do not seem to be separated from ND states by a high barrier does not imply that such a barrier cannot exist between other 0^+ excitations and ND states. More generally, in a way similar to 0^+ shape isomers in actinides, some of the 0^+ states in any nucleus may correspond to the first excitation in a deformed PES minimum and can manifest significant hindrance in their decay toward ND states.

Table 6
Characteristics of the SD yrast band at the decay-out spins, as observed in ^{60}Zr, ^{58,59}Cu and ^{56,58}Ni. See Table 2 caption for detailed explanations.

Nucleus	E_i [MeV]	I_i^π	U [MeV]	$T_{1/2}$ [ps]	E_f [MeV]	I_f^π	E_γ [MeV]	BR [%]	E/Mλ	B(E/Mλ) [W.u.]	Refs.
^{60}Zn (SD yrast)	9.620	(8^+)	4.328		3.809	(6^+)	5.810		(E2)	$\geq$0.01	[67,204]
						(6^+)	γ(unres.)	$\leq$4	(E2)	[a]	
	10.756	(10^+)	2.280		9.620	(8^+)	1.136	40[c]	(E2)	225[a,b]	
					5.292	8^+	5.464	24	(E2)	0.04(2)	
							γ(unres.)	36			
	12.132	(12^+)			10.756	(10^+)	1.376	45[c]	(E2)	225[a,b]	
					8.636	(10^+)	3.496	5	(E2)	0.2(1)	
					8.476	10^+	3.656	25	E2	0.8(2)	
							γ(unres.)	25			
^{58}Cu (SD yrast)	8.917	(9^+)	3.569	0.22	6.585		2.330	<3			[67,176,179]
					^{57}Ni(3.702)	(9/2)	2.301(5)(E_p)	96(4)	p decay		
	9.747	(11^+)	2.354	0.38	8.917	(9^+)	0.830	65	E2	190(35)[a]	
					8.228	(9^+)	1.519	15	E2	2.1(8)	
					5.575	(9^+)	4.171	17	E2	0.016(6)	
					^{57}Ni(3.866)	$11/2^-$	3.008(E_p)	<8	p decay		
^{59}Cu (SD yrast)	13.351	$29/2^+$	1.102		12.243	$25/2^+$	1.108	4.1	E2		[180,200,216]
					12.039	$25/2^+$	1.313	18.1	E2		
					11.917	$25/2^+$	1.434	62.7	E2		
					11.838	$25/2^+$	1.514	15.1	E2		
^{56}Ni (SD yrast)	9.736	7	2.135		8.891	5	0.845	25	(E2)	124[a,b]	[177]
					7.653	6^+	2.083	25			
					^{55}Cu(g.s.)	$7/2^-$		49(14)	p decay		
	10.937	9	1.927		9.736	7	1.201	34.0	(E2)	124[a,b]	
						8^+	1.627	66.0	(D)		
^{58}Ni (SD yrast)	16.797(3)	(15^-)	1.945	17(11)	15.434	(13^-)	1.364	12.5	(E2)	0.07	[67,178,217]
					15.413	(13^-)	1.385	12.5	(E2)	0.06	
					12.83–15.32	(13^-),(14^+)	5 γ's	42	Q,D		
							γ(unres.)	23			
					^{57}Co(15.148(1))	$21/2^-$	1.62(6)(E_p)	7(2)	p decay		
					^{54}Fe(9.350(1))	6^+	6.90(6)(E_α)	2.6(3)	α decay		
	18.461	(17^-)	1.102		17.290	(16^+)	1.171	10.9	D + Q		
					16.798	(15^-)	1.663	64.1	Q	170[a,b]	
							γ(unres.)	25.0			

[a] Transition within the SD band.
[b] From quadrupole moment Q_0.
[c] Assuming for the 1.376 and 1.136 MeV transitions intensities of 45 and 18% of the SD yrast, respectively.

Table 7
Characteristics of the SD yrast band at the decay-out spins, as observed in ^{36,40}Ar and ^{40,42}Ca. See Table 2 caption for detailed explanations.

Nucleus	E_i [MeV]	I_i^π	U [MeV]	$T_{1/2}$ [ps]	E_f [MeV]	I_f^π	E_γ or E_{e^-} [MeV]	BR [%]	E/Mλ	B(E/Mλ)/ρ^2(E0) [W.u.]/[m.u.]	Refs.
^{36}Ar (SD yrast)	4.329	(0_2^+)	4.329	>0.485	1.970	2_1^+	2.357	90.9	[E2]	<2.1	[67,184,218]
					0.0	0_1^+	4.329	<9.1			
	4.951	2_3^+	2.981	0.033(17)	4.329	(0_2^+)	0.622	<0.8			
					1.970	2_1^+	2.981	20.0			
					0.0	0_1^+	4.950	79.2	(E2)	0.7(3)	
	6.137	(4_2^+)	1.723	0.132(21)	4.951	2_3^+	1.186	20.3	E2	52(8)[a]	
					4.440	2_2^+	1.697	6.3	E2	2.7(4)	
					1.970	2_1^+	4.166	73.4	E2	0.3(1)	
	7.767	(6^+)		0.076(11)	6.137	4_2^+	1.630	70.0	E2	64(9)[a]	
					4.414	4_1^+	3.353	30.0	E2	0.75(12)	
^{40}Ar (SD yrast)	2.121	0_2^+	2.121	104(14)	1.461	2_1^+	0.660	100.0	[E2]	5.3(8)	[67,185]
	2.522	2_2^+	1.061	0.23(4)	1.461	2_1^+	1.061	57.5	M1+E2	0.037(6);18(5)	
					0.0	0_1^+	2.522	42.5	E2	1.19(18)	
	3.515	4_2^+	0.622	1.95(28)	2.892	4_1^+	0.623	31.1	M1+(E2)	0.20(5)	
					2.522	2_2^+	0.993	9.0	[E2]	50(30)[a]	
					1.461	2_1^+	2.054	59.9	[E2]	8.2(18)	
	4.960	6_2^+	1.495	0.10(4)	3.515	4_2^+	1.445	64.1	E2	70(30)[a]	
					2.892	4_1^+	2.068	35.9	E2	7(3)	
^{40}Ca (SD yrast)	5.212	0_3^+	5.212	1.02(21)	3.904	2_1^+	1.308	100.0	E2	$17(^{+4}_{-3})$	[67,82,181,219]
					3.353	0_2^+	1.859	<0.002	E0	<45	
					0.0	0_1^+	5.212	0.046	E0	2.3(5)	
	5.629	2_3^+	1.725	0.040(15)	3.353	0_2^+	2.277	12.3	[E2]	$3.3(^{+2}_{-11})$	[181]
					0.0	0_1^+	5.629	87.7		$0.26(^{+15}_{-7})$	
	6.543	4_3^+	1.263	0.121(21)	5.629	2_3^+	0.913	18.8	E2	$170(^{+70}_{-50})$[a]	
					5.279	4_1^+	1.264	8.2			
					5.249	2_2^+	1.294	14.1	(E2)	$22(^{10}_{-7})$	
					3.904	2_1^+	2.638	58.8	E2(+M3)	$2.6(^{+8}_{-6})$	
	7.974	(6^+)	1.044		6.543	4_3^+	1.432		(Q)		
					5.279	4_1^+	2.695		(Q)		
	9.854	(8^+)	1.753		7.974	(6_3^+)	1.880		(Q)		
					7.677	(6_2^+)	2.176		(Q)		
					6.930	6_1^+	2.921		(Q)		
	12.335	(10^+)	1.332		9.854	(8_3^+)	2.481		(Q)		
					9.305	(8_2^+)	3.030		(Q)		
^{42}Ca (SD yrast)	1.837	0_2^+	1.837	387(6)	1.525	2_1^+	0.313	98.0	E2	57(6)	[33,67,182,196]
					0.0	0_1^+	1.837	2.0	E0	145(14)	
	2.424	2_2^+	0.909	0.140(40)	1.837	0_2^+	0.587	0.5	[E2]	$15(^{+6}_{-4})$[a]	[67,182,196,220]
					1.525	2_1^+	0.899	73.7	M1+E2	0.11;12.9(25)	
					0.0	0_1^+	2.424	25.8	E2	1.0(1)	
	3.254	4_2^+	0.502	0.123(21)	2.752	4_1^+	0.501	35.2	[M1]	0.5(11)	[67,182,196,220]
					2.424	2_2^+	0.830	9.9	[E2]	$27(^{+4}_{-6})$[a]	
					1.525	2_1^+	1.729	54.9	E2(+M3)	$23(^{+3}_{-4})$	
	4.718	6_2^+	1.529	0.083(32)	3.254	4_2^+	1.464	45.0	[E2]	50[a]	
					3.189	6_1^+	1.526	7.2			
					2.752	4_1^+	1.963	47.8	[E2]	$12(^{+7}_{-3})$	
	6.636	8_1^+	1.529	0.036(15)	4.718	6_2^+	1.919	50			
					3.189	6_1^+	3.447	50			

[a] Transition within the SD band.

The following Section 4 is devoted to a survey of 0^+ states decay properties in regions of the nuclear chart well known for shape coexistence phenomena. We will focus, in particular, on even–even isotopes around Z = 20, 28, 50, 82 proton shell closures (±2 protons) and along Z = 36 (Kr), Z = 38 (Sr) and Z = 40 (Zr) isotopic chains. The aim is to delineate common features in the decay pattern of 0^+ excitations, in order to identify candidates for highly deformed shapes which could provide additional examples of shape isomers, in medium/heavy mass regions.

4. Shape coexistence through 0^+ states

The existence of deep secondary minima in the nuclear PES, which would lead to the appearance of shape isomers in systems lighter than actinides, has been addressed by some theoretical approaches for a long time. Already in the '70s, deformation energy calculations predicted the existence of secondary minima in Hg isotopes, near the magic proton shell Z = 82 (e.g., [221–224]). Few years later, in the '80s, a study based on Hartree–Fock plus BCS calculations, in which a large number of nuclei was surveyed,

pointed to ten isotopes in which a deformed 0^+ state is separated from a spherical structure by a significantly high barrier: ^{66}Ni and ^{68}Ni, ^{190,192}Pt, ^{206,208,210}Os, and ^{194,196,214}Hg [225]. Other investigations [56,226], which used a nonaxial Hartree–Fock–Bogoliubov approach, selected a rather restricted number of candidates, among which the lightest were ^{66,68}Ni, ^{74,76}Kr, ^{78,80,98}Sr, ^{80,82,100}Zr, and ^{86}Mo. Also, in more recent years, Möller et al. [59,227] presented a global study of potential energy surfaces in 7206 nuclei from A = 31 to A = 290 by employing a well-benchmarked macroscopic–microscopic finite-range liquid-drop model [228]. Here, secondary PES minima at spin 0 were found in a few tens of nuclei. In spite of finding many nuclei lighter than actinides, in which 0^+ shape isomers could be expected on the basis of theoretical calculations, such states had not univocally been identified experimentally.

In order to search for 0^+ states predicted by theory to be deformed, the decay of which is hindered by a high potential barrier, we have performed an extensive survey of the properties of observed 0^+ excitations in regions of the nuclear chart pointed by calculations or in the areas well known for shape coexistence phenomena. We focus, in particular, on even–even isotopes around Z = 20, 28, 50, 82 proton shell closures (± 2 protons) and along Z = 36 (Kr), Z = 38 (Sr) and Z = 40 (Zr) isotopic chains. The aim is to delineate common features in the decay pattern of 0^+ excitations, in order to identify candidates for highly deformed shapes which could provide additional examples of shape isomers, in medium/heavy mass regions.

Fig. 34(a) shows experimentally established hindrance factors (HF) for 0^+ excitations (open circles), calculated from Eq. (3) using experimental B(E2) values available in literature [67,220]. The exceptionally large HF values measured for E2 transitions from the 0^+ shape-isomer states in ^{236,238}U are also reported. In panel (b), full square symbols give corresponding HF values for transition from the first excited 2^+_1 state to the 0^+_{gs}, for comparison. The solid line at HF = 1 corresponds to B(E2) = 1 W.u., which is the reference value for E2 transition [69]. Dashed lines at HF = 0.1 and HF = 10 define the HF values associated to enhancement or moderate suppression of B(E2) values, as explained in Fig. 9. Candidates for shape isomerism should be searched for in the upper part of panel (a), i.e., for HF > 10. Fig. 35 gives the same picture, with boxes covering the intervals of low hindrance factors (HF < 10) for the excited 0^+ E2 decays shown in Fig. 34. As can be seen, only a small part of 0^+ states decay demonstrates hindrance higher than 10 (27 cases out of a total of 207 examined excitations, i.e., ∼13%). With the inclusion of 0^+_3 in ^{50}Cr (Z = 24) (at 3895(1) keV), 0^+_3 in ^{172}Yb (Z = 70) (at 1405 keV), and 0^+_2 in ^{186}Os and 0^+_3 in ^{192}Os (Z = 76) (located at 1061(1) and 1206 keV, respectively), not discussed here, the survey exhausts all cases of significantly retarded E2 decays from 0^+ states between Ar (Z = 16) and U (Z = 92), reported in the literature [67]. This covers also mass regions which were not considered in this review, where shape coexistence has been traditionally found [24], as, for example, Ge (Z = 32) and Se (Z = 34) isotopes close to N = Z [229–234] and on the neutron rich side [235–240], as neutron-rich Mo (Z = 42), Ru (Z = 44) and Pd (Z = 46), extensively studied in Coulomb excitation and fission reactions [18,241–246]. In these cases, shape coexistence has often been discussed in connection with triaxiality (see Refs. [24,104,247] and references therein).

In the following paragraphs, each nucleus having 0^+ excitation with strongly hindered decay (HF > 10), will be discussed in the context of the nuclear chart region to which it belongs (Fig. 35).

4.1. The Z = 20 region: Ar, Ca and Ti

The A ∼ 40 region, being characterized by a relatively small number of nucleons, is considered an excellent testing ground for different theoretical approaches, such as, large-scale shell model (SM) [188,189], beyond-mean-field models (BMF) [190,191,248], and antisymmetrized molecular dynamics (AMD) [192–194]. It follows that a microscopic understanding of the origin of a shape-coexistence scenario might be easier to achieve in this mass region, provided comprehensive experimental data is available.

According to mean-field based predictions, as for example the one provided by the macroscopic–microscopic model of Moeller et al. [59], or the Hartree–Fock–Bogoliubov calculations based on the Gogny force, by S. Hilaire and M. Girod [198,249], the closed-shell Ca isotopes from A = 38 to 50 should be characterized by rather structureless Potential Energy Surfaces (PES), all dominated by a pronounced spherical minimum. In contrast, in Ar (Z = 18) (Fig. 36) a deformed oblate ground state is expected for A = 32–36 in the otherwise spherical isotopic chain. The Ti (Z = 22) isotopic chain is also predicted to be characterized by a spherical ground state, with a possible spherical-prolate shape coexistence scenario at A = 44.

Experimentally, as already anticipated in Section 3.2.2, a much more complex picture is found, which is evidenced in Fig. 37 by the sequence of excited 0^+ states (here shown up to 0^+_4) observed in Ar, Ca and Ti nuclei, and by the corresponding level schemes given in Figs. 38, 39 and 41. In ^{36,38,40}Ar [184–186,218], ^{40,42,44}Ca [67,82,181–183,196,219] and ^{44}Ti [251], 0^+ states which are bandheads of rotational structures (normally deformed (ND) or superdeformed (SD)), originally identified in transfer reaction studies [67], have been interpreted in terms of multiparticle–multihole (mp–mh) configurations on basis of the most recent SM and BMF approaches (labels in the figure). In the case of Ca isotopes, a parabolic trend as a function of neutron number seems to be followed by the 0^+ excitation arising from 2p-2h proton excitations across the Z = 20 shell gap (symbols connected by blue dashed line). The minimum is reached at ^{44}Ca, the neutron mid-shell (N = 24), which is the typical fingerprint of shape-coexisting intruder configurations in the vicinity of closed shells. The deformation of such structures is not fully known experimentally, since extended spectroscopic investigations are available only for ^{40}Ca and ^{42}Ca (see Refs. [82,181,182,196] and references therein).

As evidenced in Fig. 35, in the A ∼ 40 region there is only one possible candidate for a significantly retarded decay, i.e., the 0^+_3 in ^{42}Ca, located at 3.300 MeV with HF = 16, for which a lower lifetime limit has been reported in a (p,p′γ) Doppler-shift attenuation method measurement from 1969 [252], on the basis of a measured upper limit of decay branchings. No information on this state is instead available from the most recent Coulomb excitation experiment performed with the AGATA array at LNL [182,196]. It is very likely that the decay hindrance in this case arises not from the wave function separation in the deformation space but from cancellations between E2 matrix elements connecting the initial and final states. Similar situation occurs in ^{58}Ni and ^{66}Ni and will be discussed in detail in the next section. In all other 0^+ cases reported in Ar, Ca and Ti isotopes, rather fast E2 decay branches

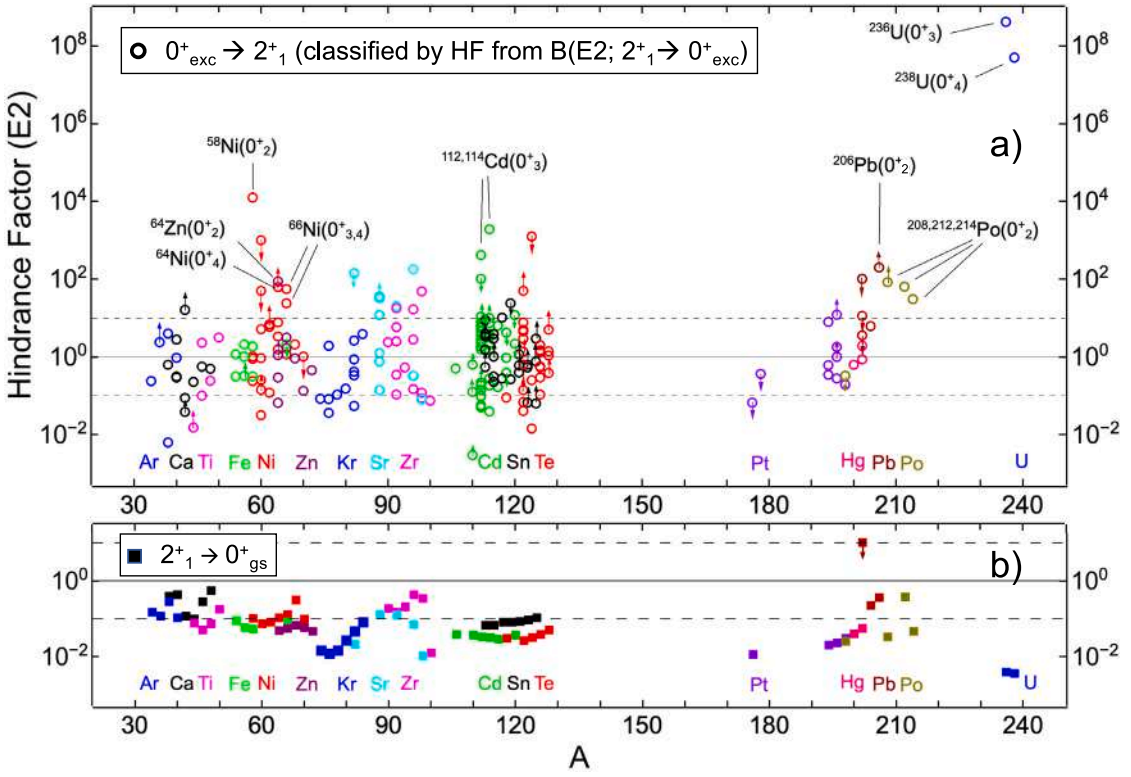

Fig. 34. Panel (a): Hindrance factors (HF) for even–even nuclei, extracted from the experimental B(E2) reduced transition probabilities available for excited 0^+ states (open circles) in regions of the nuclear chart well known for shape coexistence phenomena, i.e., around Z = 20, 28, 50, 82 proton shell closures (±2 protons) and along Z = 36 (Kr), Z = 38 (Sr) and Z = 40 (Zr) isotopic chains. The exceptionally large HF values measured for E2 transitions from the 0^+ shape-isomer states in ^{236,238}U are also reported. Panel (b): Corresponding HF values for transition from the first excited 2^+_1 state to the 0^+_{gs} (full square symbols). The solid line at HF = 1 corresponds to B(E2) = 1 W.u., which is the reference value for E2 transition [69]. Dashed lines at HF = 0.1 and HF = 10 define the HF values associated to enhancement or moderate suppression of the B(E2) transition probability. See Fig. 9, Eq. (3) and related text for details.

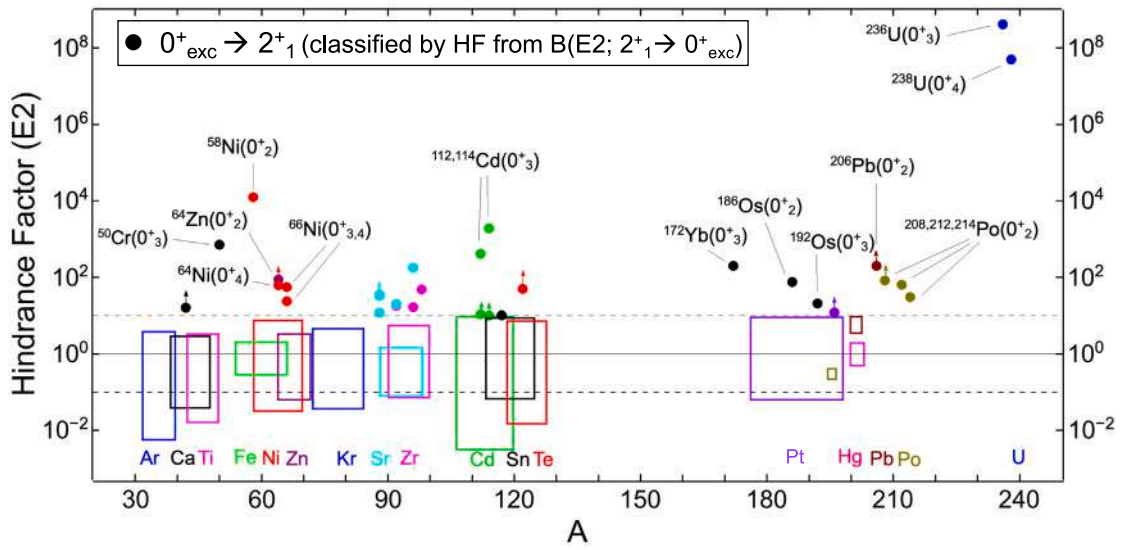

Fig. 35. Same as Fig. 34, highlighting the 0^+ states with significantly hindered E2 decay (HF > 10). The remaining cases of ^{50}Cr, ^{172}Yb, ^{186}Os and ^{192}Os, reported in literature and not discussed in this review, are also included. Boxes cover the intervals of low hindrance factors (HF < 10) for excited 0^+ E2 decays, as shown in Fig. 34.

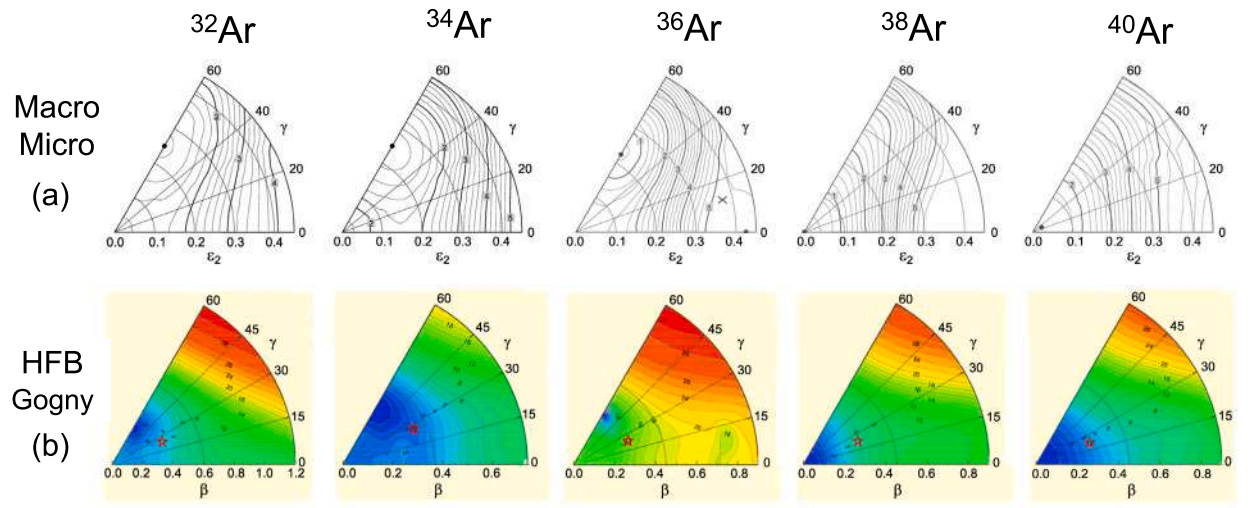

Fig. 36. Potential energy surfaces for $^{32-40}$Ar obtained from different type of calculations: (a) macroscopic–microscopic mean field model of Moeller et al. [59] and (b) Hartree–Fock–Bogoliubov calculations based on the Gogny force, by S. Hilaire and M. Girod [198,249]. Energies (in MeV) are given on the contour plots.
Source: Adapted from [59,250].

Table 8
Experimental information available on 0^+ excitations in even–even Ar isotopes (A = 34 − 40) (see also Fig. 37). E_i, E_f and I_i^π, I_f^π are the initial and final excitation energies and spin-parities, respectively; $T_{1/2}$ is the half life; E_γ or E_{e^-} are γ- or E0-transition energies, with branching BR (central value from [67]) and multipolarity $E/M\lambda$ (in round brackets if uncertain, in squared brackets if deduced from the spins and parities of the initial and final levels); $B(E/M\lambda)$ and ρ^2(E0) are the corresponding reduced transition probabilities and monopole strength in Weisskopf units (W.u.) and milliunits (m.u.), respectively. Hindrance factors (HF) for E2 transitions are calculated according to Eq. (3), taking always decay from high to low spin (i.e., B(E2;$2^+ \rightarrow 0^+$) = 1/5 B(E2;$0^+ \rightarrow 2^+$)). References to specific papers are given in the last column.

Nucleus	E_i [MeV]	I_i^π	$T_{1/2}$ [ps]	E_f [MeV]	I_f^π	E_γ or E_{e^-} [MeV]	BR [%]	$E/M\lambda$	$B(E/M\lambda)/\rho^2$(E0) [W.u.]/[m.u.]	HF	Refs.
^{34}Ar	3.876(1)	0_2^+	>0.187	2.091	2_1^+	1.785	100.0	[E2]	<26	>0.20	[67,253]
	4.964(1)	0_3^+		4.132	1_1^+	0.832	100.0				
^{36}Ar	4.329	(0_2^+)	>0.485	1.970	2_1^+	2.359	90.9	[E2]	<2.1	>2.4	[67,184,218]
				0.0	0_1^+	4.329	<9.1				
^{38}Ar	3.377	0_2^+	22.8(15)	2.167	2_1^+	1.209	99.3	E2	1.26(8)	4.0	[33,67]
				0.0	0_1^+	3.377	0.7(1)	E0	16.1(28)		
	4.709(1)	0_3^+	$1.7(^{+21}_{-7})$	3.937	2_2^+	0.773	100.0	[E2]	$160(^{+110}_{-90})$	0.0063	
^{40}Ar	2.121	0_2^+	104(14)	1.461	2_1^+	0.660	100.0	[E2]	5.3(8)	0.9	[67]

Additional 0^+ states [67]:
^{34}Ar; 0_4^+: 5.909(12) MeV from (^{3}He,n) studies (no γ branch reported);
^{36}Ar; $0_{3,4}^+$: 9.700(30) MeV (no γ branch reported), 10.854(2) MeV resonance with γ branch, from (p,t), (p,p'), (p,α), (p,γ) studies;
^{38}Ar; $0_{4,7}^+$: 7.060(15), 18.784(30) MeV, from (t,p) and (p,t) studies (no γ branch reported); $(0_{5,6}^+)$: 10.516(5), 10.547(5) MeV, resonances from (α,γ) studies.

are instead found to connect the rotational structures to the low-spin states, indicating a strong mixing between configurations built on different deformations. This goes together with the sizeable B(E2;$0^+_{exc} \rightarrow 2^+$) measured values, which correspond to the absence of significant hindrance (HF < 10), as reported in Fig. 34. In case of Ca isotopes, the appreciable mixing between different configurations is also confirmed by the significant monopole strength (ρ^2(E0)) values experimentally available, with the exception of the unusually small ρ^2(E0; $0_3^+ \rightarrow 0_1^+$) value in ^{40}Ca (see also Fig. 8). The latter is interpreted, by a state-of-the-art large-scale-shell-model calculation, as due to destructive interference in the mixing of shape-coexisting structures which are based on several different multiparticle–multihole excitations [82].

One can then conclude that the available experimental results in the A ∼ 40 region indicate, in general, the absence of a significant barrier in the potential energy landscape (PES), which could isolate the structures based on different deformations, as also suggested by the BMF calculations discussed in Section 3.2.2 and shown in Fig. 40 for ^{42}Ca. It follows that the shape coexistence scenario in the mass region A ∼ 40 is of the type named "No/Weak Barrier, No Hindrance", as reported in Fig. 9(e).

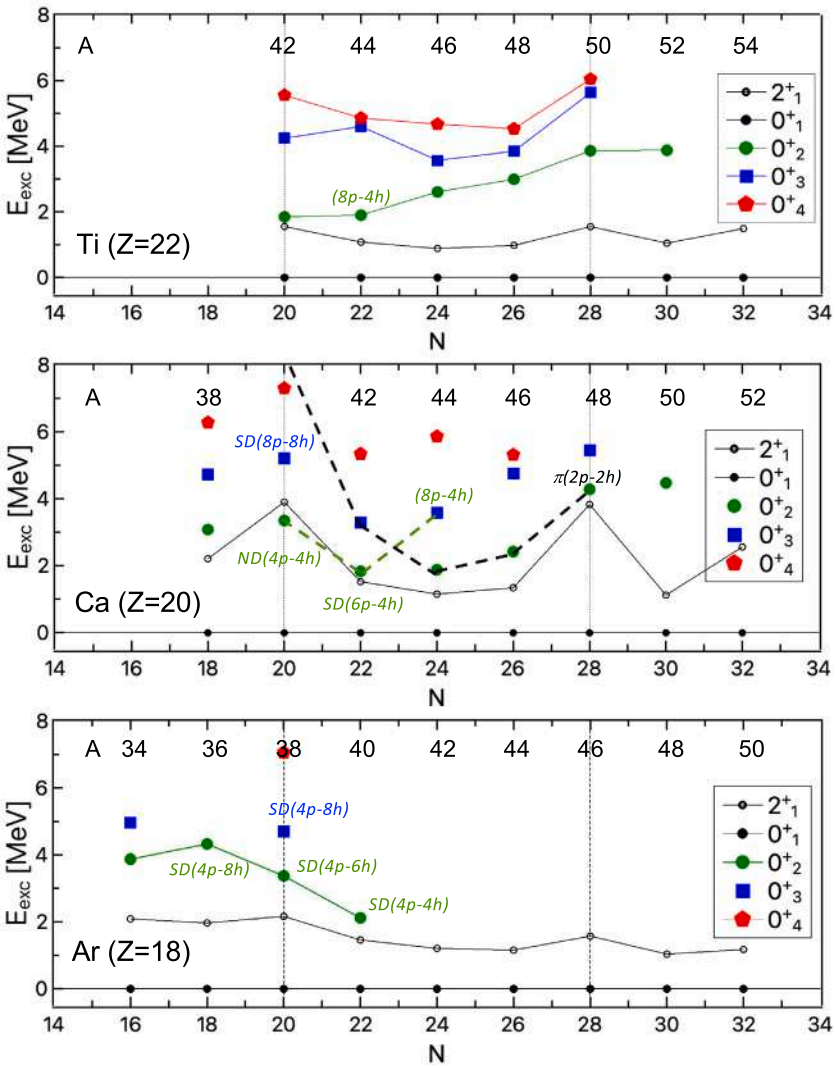

Fig. 37. Survey of 0^+ states (up to 0^+_4) observed in the Z = 20 ± 2 nuclei of Ar, Ca and Ti. Labels give multiparticle–multihole configuration assignments for ND and SD states, as follows from large-scale shell model calculations and/or mean field approaches. In Ca isotopes, dashed lines connect states interpreted as arising from similar types of mp-mh, on the basis of nucleon transfer experiments, as originally discussed in Ref. [30] (see Tables 8, 9, and 10 for details).

4.2. The Z = 28 region: Fe, Ni and Zn

As in the case of the A ∼ 40 mass region, the rather limited number of valence nucleons makes the A ∼ 60 region computationally accessible by different theoretical calculations, from large-scale shell model (SM) [55,64,258–260] to beyond-mean-field approaches (BMF) [261–264].

Fig. 42 shows the excited 0^+ states located experimentally in Fe, Ni and Zn nuclei, for which γ decays have also been reported. The decay properties of these states are summarized in Tables 11, 12, and 13.

4.2.1. The Ni isotopes

The Ni isotopic chain (Z = 28) form a particularly excellent laboratory to study a variety of nuclear structure phenomena, including shape coexistence. As anticipated in Section 3.2.2, this feature is visible already in case of the doubly magic ^{56}Ni, in which two well-deformed rotational bands were located, extending to high spins [177] (one of these bands partially decays via prompt proton emission into the ground state of ^{55}Co, see Fig. 32). Also, in the neighboring ^{58}Ni nucleus more than twenty deformed rotational bands were observed [178,217,265]. To this, one may add two highly deformed bands identified in ^{62}Ni [266]. The β_2 values extracted from the experimental data for the rotational structures mentioned above, all collected in a series of experiments with GAMMASPHERE, are in the range of 0.3–0.45 [267]. The deformed rotational bands in Ni nuclei, in contrast to Ca nuclei, do not extend from high spins down to the 0^+ bandheads – the majority of them decay out already at I ∼ 10. As mentioned earlier, the

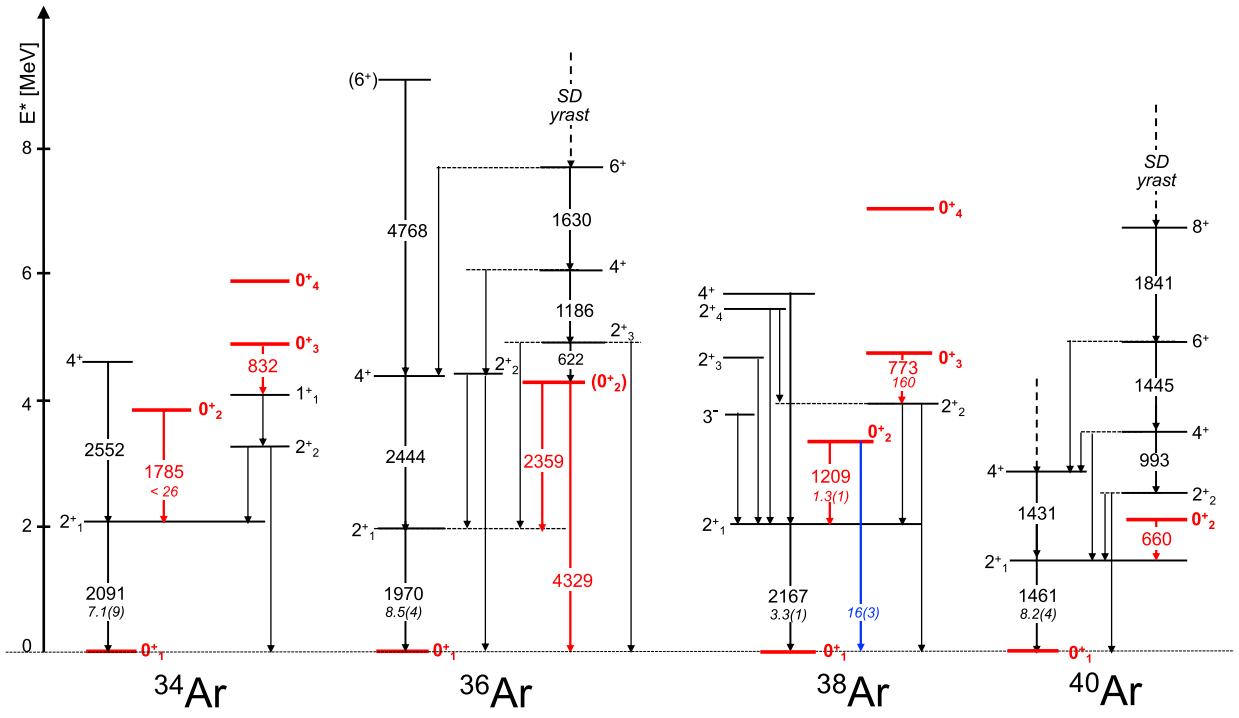

Fig. 38. Partial level schemes of ^{34,36,38,40}Ar [67]. The γ decay of 0^+ states is highlighted in red, with energies in keV and B(E2) values in W.u. (in italic). Blue arrows indicate the E0 decay, when measured, with ρ^2(E0) values in m.u. (in italic). Dashed arrows indicate continuation of band structures to higher spins (see Table 8 for details).

identification of the 0^+ bandheads of these rotational bands is rather difficult, as they are expected to lie at relatively high excitation energy and cannot be easily accessed for spectroscopic studies. Instead, accessible for experimental investigations are lower lying 0^+ states with certain deformation – they still can provide rich information on shape coexistence, even though no band-like structures have been observed on top of them yet. The systematics of the lowest 0^+ states (up to five) which are known in $^{56-70}$Ni is shown in Fig. 42, and their properties are listed in Table 11. In the Ni isotopes, a highly hindered E2 decay was measured for four 0^+ states: 0^+_2 in ^{58}Ni, with HF = 1.25×10^4, 0^+_4 in ^{64}Ni, with HF > 63 [21,268], 0^+_3 and 0^+_4 in ^{66}Ni with HF = 50 and 24 [68], respectively. The information on ^{64,66}Ni was obtained from complementary experimental campaigns at IFIN-HH (Bucharest), ILL (Grenoble), ANL (Argonne) and TUNL (Duke Univ.), exploiting transfer reactions, neutron capture, Coulomb excitation, and nuclear resonance fluorescence.

First, we turn our attention to ^{66}Ni, which has been a candidate for decades to possess a deep secondary prolate minimum in the PES at sizeable deformation. As a matter of fact, starting from the '80s, various theoretical models, i.e., Hartree–Fock plus BCS [225], Hartree–Fock–Bogoliubov (HFB) [56,226], and macroscopic–microscopic finite-range liquid-drop model [227,228], suggested in this nucleus the existence of a pronounced secondary PES minimum which may give rise to a shape-isomer-like 0^+ state. Very similar results came also from recent calculations based on the HFB approach with the Gogny interaction [198] and HFB calculations with the A3DA-m interaction, as well as from recent HFB calculations with the D1S Gogny force [264]. Fig. 43 shows two-dimensional PES surfaces for Ni isotopes resulting from the macro–micro (a), HFB with Gogny (b), and HFB with the A3DA-m interaction (c) calculations, where the pronounced prolate minimum in the PES of ^{66}Ni is clearly visible. In view of the theoretical results mentioned above, it is natural to assume that for one of, or both, 0^+_3 and 0^+_4 states in ^{66}Ni, which demonstrate hindered decay via a E2 transition, the hindrance originates from the potential barrier separating the secondary minimum from the main minimum. Unfortunately, this expectation could not be verified experimentally, since measuring nuclear deformation in these states has been out of reach until now. Help for assessing the nature of 0^+ excitations in ^{66}Ni came instead from ISOLDE data on β decay of the ^{66}Co ground state [100].

Out of four known low-lying 0^+ states in ^{66}Ni, only two are populated in the β^- decay of ^{66}Co – these are 0^+_1 (g.s.) and 0^+_3 (see Fig. 44). The selectivity in β decay is warranted by similarities of the structure of the states involved. Since the 1^+ ground state in ^{66}Co is spherical, it is very likely that the 0^+_1 and 0^+_3 states, fed in β decay, will also be spherical. Instead, the 0^+_2 and 0^+_4 excitations, being not populated directly in the β decay, are likely to be deformed. At this point, the 0^+_4 excitation, decaying via a transition which is hindered, is the best candidate for a state in the secondary prolate minimum, separated by a significant potential barrier from the main, spherical minimum.

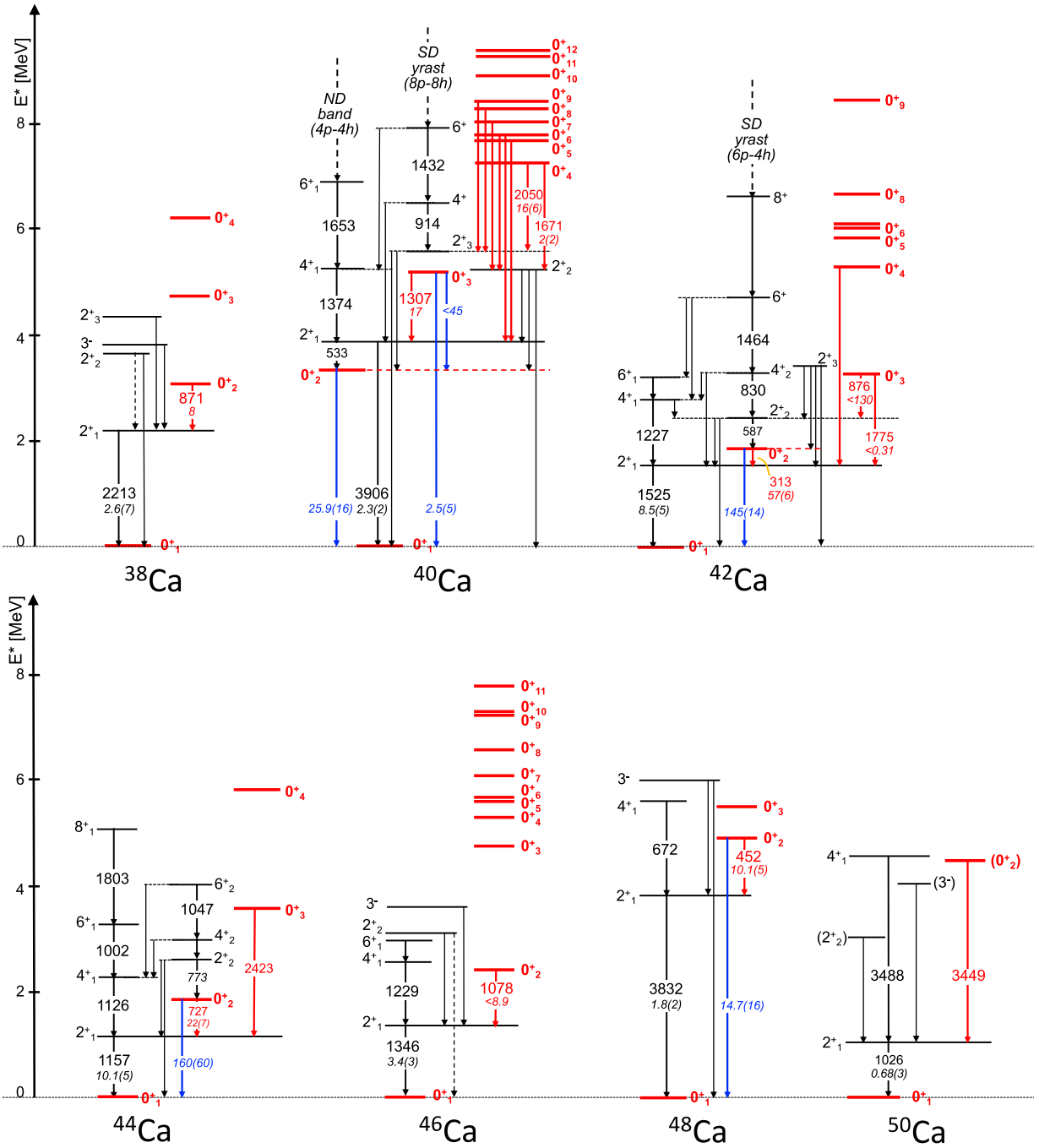

Fig. 39. Partial level schemes of even–even Ca isotopes with A = 38–50 [67]. The γ decay of 0^+ states is highlighted in red, with energies in keV and B(E2) values in W.u. (in italic); blue arrows indicate measured E0 decays, with ρ^2(E0) values in m.u. (in italic); dashed arrows give uncertain transitions or continuation of band structures to higher spins (see Table 9 for details).

To shed more light on the nature of the 0^+ states in ^{66}Ni, one has to rely on theory, which in recent years made an enormous progress in calculating shape coexistence in nuclei with masses A = 60–100 [55,64,107,258,259,271]. In particular, by using state-of-the-art Monte Carlo shell model (MCSM) [51,52,272,273] it became possible to assess transition probabilities between states of different shapes for heavy nuclei, and to examine the origin of retarded decays in the cases where such decays are calculated. One of the subjects of MCSM studies were the $^{62-70}$Ni isotopes [55,64]. In all these cases, the calculations predict coexistence of

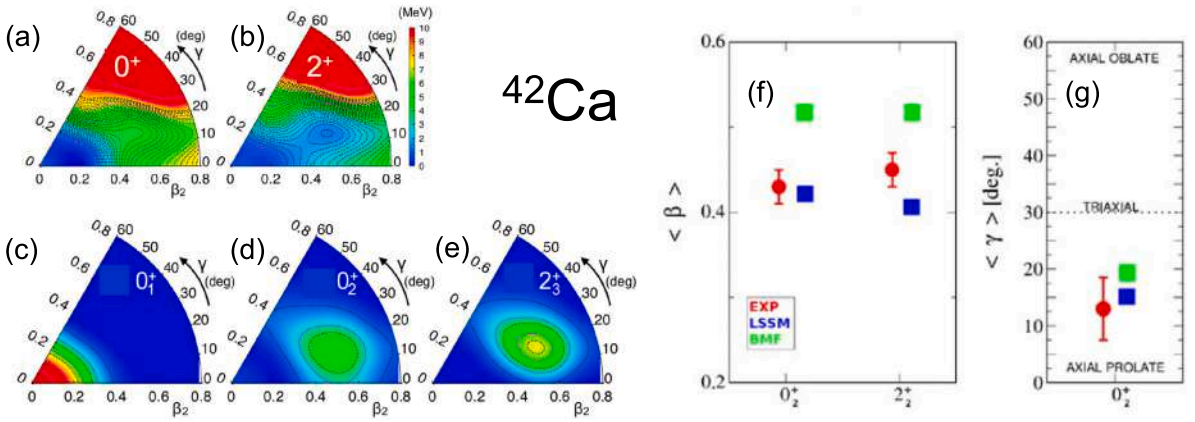

Fig. 40. Potential-energy surfaces for ^{42}Ca computed with the Gogny D1S interaction and particle number and angular momentum projection with I = 0 (a) and I = 2 (b), respectively. Energies in each plot are normalized to the one in the corresponding minimum. Contour lines are separated by 0.25 MeV (dashed lines) and 2 MeV (solid lines). Panels (c), (d) and (e): collective wave functions for the band head states predicted by the calculations, with red (blue) regions representing large (small) contributions to the wave functions. Panels (f) and (g): experimental deformation parameters, β and γ, for the 0_2^+ and 2_2^+ states of the SD band of ^{42}Ca, compared with predictions from Large Scale Shell Model (LSSM) and Beyond Mean Field (BMF) approaches [196]. See also Fig. 39 and Table 9.
Source: Adapted from [196].

Table 9
Experimental information available on 0^+ excitations in Ca isotopes (A = 38–50), see also Fig. 37 and Table 8 for detailed explanations.

Nucleus	E_i [MeV]	I_i^π	$T_{1/2}$ [ps]	E_f [MeV]	I_f^π	E_γ or E_{e^-} [MeV]	BR [%]	E/Mλ	B(E/Mλ)/ρ^2(E0) [W.u.]/[m.u.]	HF	Refs.
^{38}Ca	3.084	0_2^+	$19(^{+10}_{-7})$	2.213	2_1^+	0.871	100.0	[E2]	$8(^{+3}_{-5})$	0.63	[67]
^{40}Ca	3.353	0_2^+	2170(80)	0.0	0_1^+	3.353	100.0	E0	25.9(16)		[33,67,82]
	5.212	0_3^+	1.02(21)	3.904	2_1^+	1.308	100.0	E2	$17(^{+4}_{-3})$	0.29	
				3.353	0_2^+	1.859	<0.002	E0	<45		
				0.0	0_1^+	5.212	0.046	E0	2.3(5)		
	7.301	0_4^+	0.118(35)	5.629	2_3^+	1.671	5.0	[E2]	$1.8(^{+18}_{-10})$	2.8	
				5.249	2_2^+	2.050	95.0	[E2]	$16(^{+8}_{-4})$	0.31	
	7.702	0_5^+		3.904	2_1^+	3.797	100.0	[E2]			
	7.815	0_6^+		5.249	2_2^+	2.565	30.1	[E2]			
				3.904	2_1^+	3.908	69.9	[E2]			
	8.019	0_7^+		5.249	2_2^+	2.770	100.0	[E2]			
	8.276	0_8^+		5.629	2_3^+	2.646	100.0	[E2]			
	8.439	0_9^+		5.629	2_3^+	2.810	100.0	[E2]			
^{42}Ca	1.837	0_2^+	387(6)	1.525	2_1^+	0.313	97.9	E2	57(6)	0.088	[33,67,182,196]
				0	0_1^+	1.837	2.1	E0	145(14)		
	3.300	0_3^+	>0.9	2.424	2_2^+	0.876	92.6	E2	<130	>0.038	[67,252]
				1.525	2_1^+	1.775	7.4	E2	<0.31	>16	
	5.345	0_4^+		1.525	2_1^+	3.820	100.0	[E2]			
^{44}Ca	1.884	0_2^+	13.9(42)	1.157	2_1^+	0.727	100.0	E2	$22(^{+9}_{-5})$	0.23	[33,67]
				0.0	0_1^+	1.884	0.012	E0	16(6)×10		
	3.581	0_3^+		1.157	2_1^+	2.426(3)	100.0	(E2)			
^{46}Ca	2.423	0_2^+	>4.5	1.346	2_1^+	1.078	100.0	[E2]	<8.9	>0.56	[67]
^{48}Ca	4.284	0_2^+	223(11)	3.832	2_1^+	0.452	77.5	[E2]	10.1(5)	0.50	[33,67]
				0.0	0_1^+	4.284	22.5	E0	14.7(16)		
^{50}Ca	4.476	(0_2^+)		1.027	2_1^+	3.449	100.0				[67]

Additional 0^+ states from (^{3}He,n), (p,t), (t,p) studies (no γ branch reported or resonance states) [67,254]:
^{38}Ca; $0^+_{3,4}$: 4.748(5), 6.277(3) MeV;
^{40}Ca (up to 11 MeV); $0^+_{10,11,12}$, $0^{(+)}_{13}$, $0^+_{14,15,16}$, $0^{(+)}_{17}$, 0^+_{18}, $0^{(+)}_{19}$: 8.939, 9.304(5), 9.406, 10.608, 10.622, 10.701, 10.749, 10.803, 10.870, 10.954 MeV;
^{42}Ca; 0^+_{5-11}: 5.860(10), 6.016(5), 6.080, 6.720(8), 8.450, 12.280, 14.700(50) MeV;
^{44}Ca; 0^+_4: 5.864(20) MeV;
^{46}Ca; 0^+_{3-7}, (0^+_{8-10}), 0^+_{11}, (0^+_{12}): 4.758(3), 5.317(3), 5.600(4), 5.628(10), 6.047(15), 6.555(15), 7.233(15), 7.267(15), ~7.830, 16.155(30) MeV;
^{48}Ca; 0^+_3, (0^+_4): 5.461(7), 12.869(12) MeV.

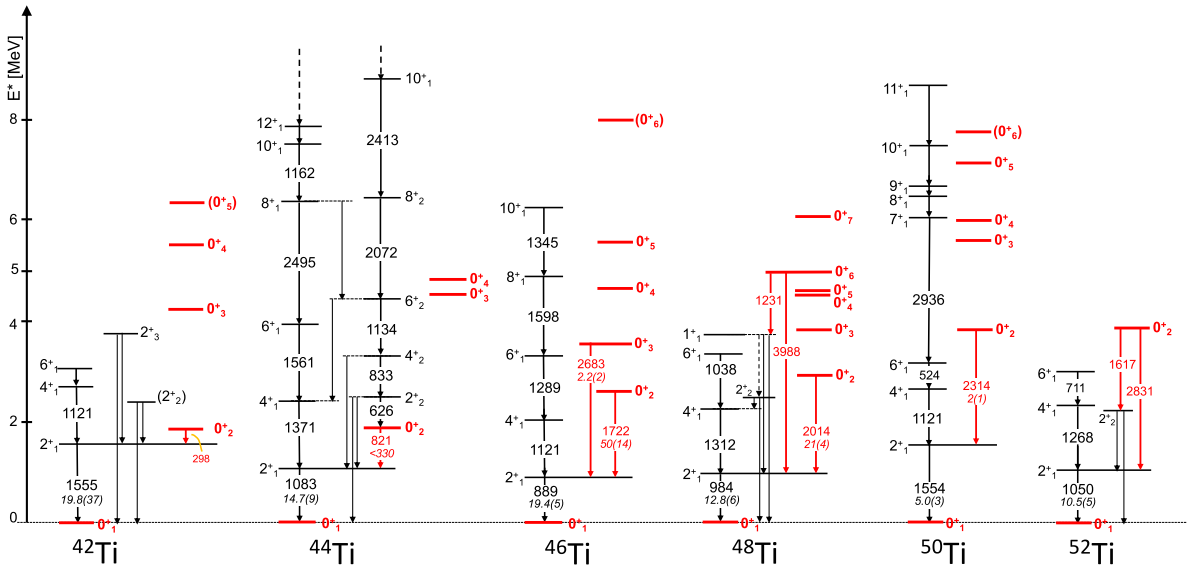

Fig. 41. Partial level schemes of even–even Ti isotopes with A = 42–52 [67]. The γ decay of 0^+ states is highlighted in red, with energies in keV and B(E2) values in W.u. (in italic). Dashed arrows indicate uncertain transitions or continuation of a structure to higher spins. See Table 10 for details.

Table 10
Experimental information available on 0^+ excitations in Ti isotopes (A = 42–52), see also Fig. 37 and Table 8 for detailed explanations.

Nucleus	E_i [MeV]	I_i^π	$T_{1/2}$ [ps]	E_f [MeV]	I_f^π	E_γ or E_{e^-} [MeV]	BR [%]	E/Mλ	B(E/Mλ)/ρ^2(E0) [W.u.]/[m.u.]	HF	Refs.
^{42}Ti	1.854	0_2^+	>0.14	1.555	2_1^+	0.298	100.0	[E2]	[a]		[67]
^{44}Ti	1.904	0_2^+	>0.5	1.083	2_1^+	0.821	100.0	[E2]	<330	>0.015	[67,255]
^{46}Ti	2.611	0_2^+	0.076(21)	0.889	2_1^+	1.722	100.0	[E2]	50(14)	0.10	[67]
	3.572	0_3^+	0.192($^{+16}_{-13}$)	0.889	2_1^+	2.683	100.0	[E2]	2.17(18)	2.3	
^{48}Ti	2.997	0_2^+	0.080(14)	0.984	2_1^+	2.014	100.0	(E2)	20.6($^{+44}_{-32}$)	0.24	[67]
	4.971	0_6^+		3.739	1_1^+	1.231	54.9	[M1]			
				0.984	2_1^+	3.988	45.1	[E2]			
^{50}Ti	3.868	0_2^+	0.50(23)	1.554	2_1^+	2.314	100.0	(E2)	1.6($^{+14}_{-5}$)	3.1	[67]
^{52}Ti	3.882(1)	0_2^+		2.264	2_2^+	1.617(1)	59.9	[E2]			[67]
				1.050	2_1^+	2.831(3)	40.1	[E2]			

[a] B(E2)<20 × 10^4 W.u., from $T_{1/2}$ lower limit.
Additional 0^+ states from (^{3}He,n), (t,p), (e,e′) reaction studies (no γ branch reported) [67,256,257]:
^{42}Ti; $0^+_{3,4}$, (0^+_5): 4.245(25), 5.555(20), 6.370(30) MeV;
^{44}Ti; $0^+_{3,4}$: 4.605(5), 4.860(30) MeV; several 0^+ resonances above 9.2 MeV;
^{46}Ti; $0^+_{4,5}$, (0^+_6), $0^+_{7,8}$, (0^+_9): 4.675(10), 5.610(30), 8.020(30), 12.460(30), 14.153(6), 14.300(60) MeV;
^{48}Ti; $0^+_{3,4,5,7}$: 3.851(1), 4.535(3), 4.589(3), 6.122 MeV;
^{50}Ti; $0^+_{3,4,5}$, ($0^+_{6,7}$), 0^+_8: 5.633(15), 6.045(15), 7.190(60), 7.808(15), 16.010(60), 16.580(60).

low-lying spherical, oblate, and strongly deformed prolate shapes. Fig. 43 (d) and (e) show potential energy surfaces for $^{62-70}$Ni obtained from constraint Hartree–Fock method for the A3DA-m Hamiltonian (used in the MCSM approach), together with the main components of the 0_4^+ states (prolate) and 2_1^+ states (spherical) wavefunctions displayed as circles. In turn, Fig. 45 displays partial experimental decay schemes of $^{56-70}$Ni, and, for $^{64-70}$Ni, their comparison with MCSM predictions (up to 0_4^+). One can see that in all cases the predicted excitation energy pattern of the 0^+ excitations is in accord with the experimental sequence. In addition, a significant hindrance of the E2 transition deexciting prolate deformed 0^+ states in the $^{64-68}$Ni isotopes is given by calculations.

Coming back to ^{66}Ni, as earlier discussed in Section 2.1, MCSM calculations predict a spherical structure for the 0_1^+, 0_3^+ and 2_1^+ states, with major components of the wave function localized in the main, spherical minimum of the PES (see Figs. 3 and 43). In contrast, 0_2^+ and 0_4^+ are found to be well localized in secondary minima of oblate and prolate nature, respectively, with wave functions characterized by sizeable excitations of protons across the Z = 28 shell gap (from $f_{7/2}$ to $f_{5/2}$ and $p_{3/2;1/2}$), as well as neutrons across the N = 40 subshell gap (from $f_{5/2}$ and $p_{3/2;1/2}$ to $g_{9/2}$ and $d_{5/2}$), what facilitates the development of deformation (see Fig. 6, left). Such a mechanism has been named *Type II shell evolution* and was described in more detailed way in Section 2.1 [64].

The MCSM approach was also used to calculate the β^- decay of the ^{66}Co ground state into ^{66}Ni – comparison between theory and experiment is shown in Fig. 44. The selective population of the 0_1^+, 0_3^+ and two 2^+ states in ^{66}Ni, which all are spherical, was

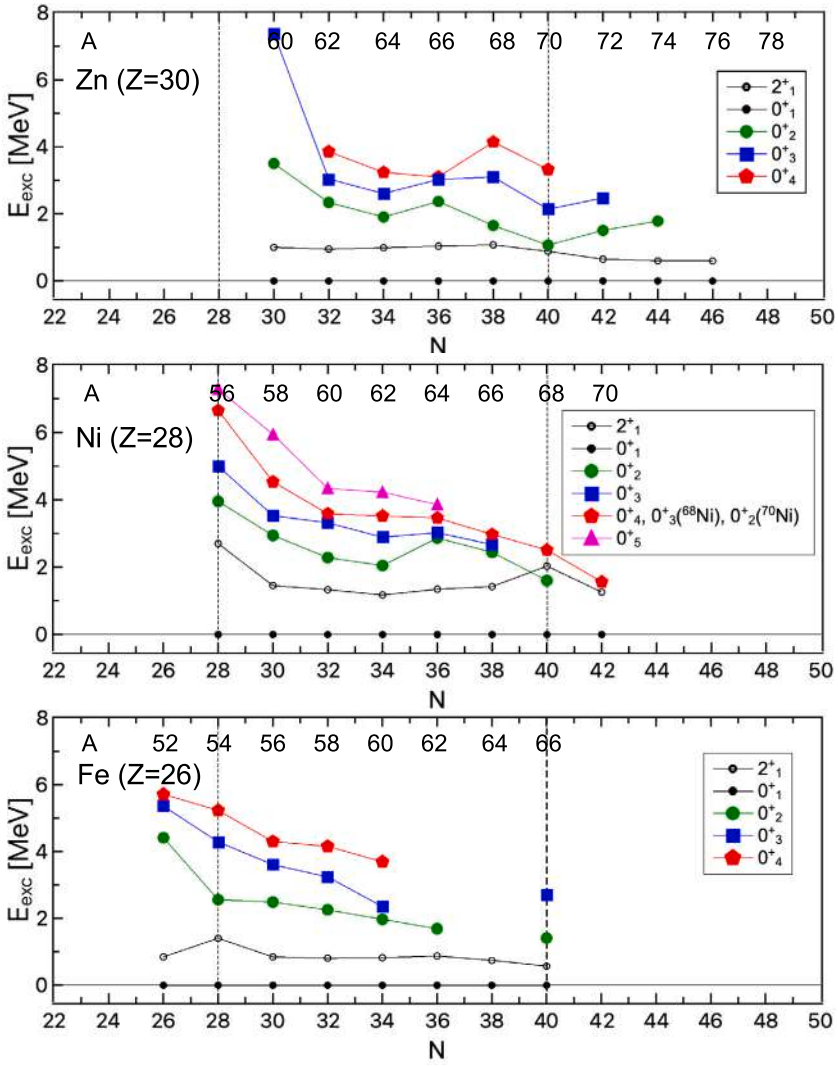

Fig. 42. Survey of 0^+ states observed in the Z = 28 ± 2 nuclei of Fe, Ni and Zn (up to 0^+_4 in Fe and Zn, up to 0^+_5 in Ni isotopes). The first 2^+ excitation is also given as a reference (open circles). Dashed lines mark the Z = 28 and 40 neutron shell closures (see Tables 11–13 for details).

well reproduced. The calculations did also very well in predicting very weak (not measurable) feeding of the 0^+_2 and 0^+_4 states, which are deformed and to which no direct population was observed [100]. In view of the above considerations, there is no doubt that the 0^+_4 state, experimentally identified at 2974 keV and decaying via a hindered E2 transition, HF = 25, corresponds to the calculated 0^+_4 prolate excitation, which is predicted to decay via a retarded E2 transition with HF = 833. This hindrance arises from a sizeable potential barrier separating the prolate (secondary) and spherical ground state minima, which makes the 0^+_4 state wave function much concentrated in the secondary minimum, i.e., with very small admixtures of the spherical components, as shown in Fig. 43(d). The MCSM results are obtained by diagonalizing the Hamiltonian with a finite number of basis vectors. Reasonably good approximation can be achieved for energies and enhanced transitions with certain numbers of such selected basis vectors. For weak transitions including those with high HF values, more basis vectors are needed, as such transitions are also due to minor components in the wave functions. This is the main reason why the HF values obtained by MCSM often appear to be larger than experimental ones, but the "largeness" of the HF is correctly reproduced. Of special interest is also the hindrance measured for the E2 transitions originating from the 0^+_3 state of HF = 50, which, according to MCSM calculations, is spherical. The calculations predict a retardation of the 0^+_3state decay as well with HF = 500, however, its origin is very different from the 0^+_4 case – by analyzing computed wave functions one could assess that the hindrance arises from cancellations among E2 matrix elements for the $0^+_3 \rightarrow 2^+_1$ transition. Similar conclusion on the decay of the spherical 0^+_3 state in ^{66}Ni was obtained from the study presented in Ref. [275], where large scale Shell Model calculations [258] were used to interpret the characteristics of the 0^+_2 and 0^+_3 excitations in ^{66}Ni.

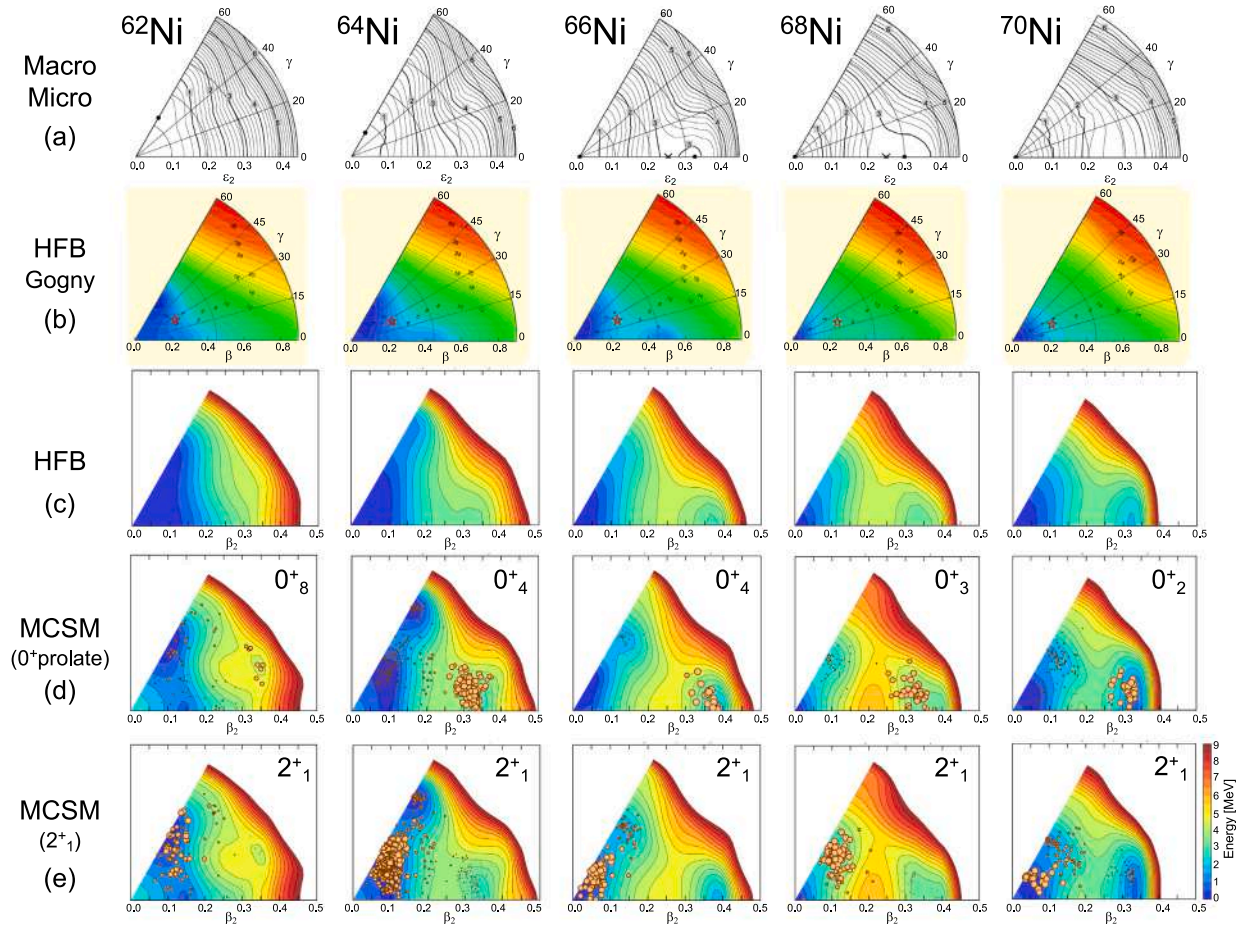

Fig. 43. Potential energy surfaces for $^{62-70}$Ni obtained from different type of calculations: (a) macroscopic–microscopic mean field model of Moeller et al. [59], (b) Hartree–Fock–Bogoliubov calculations based on the Gogny force, by S. Hilaire and M. Girod [198,249], (c) Hartree–Fock–Bogoliubov calculations with the A3DA-m interaction, (d) constraint Hartree–Fock method for the A3DA-m Hamiltonian [55], with circles showing the main components of the 0^+ prolate state wavefunction, and (e) same as (d), with circles showing the main components of the 2^+_1 state (spherical) wavefunction. Energies (in MeV) are given on the contour plots in (a)–(b), and by common color scale in (c)–(e).
Source: Adapted from [59,250].

In ^{64}Ni, the situation is similar to the ^{66}Ni case. The three lowest 0^+ excited states closely resemble the sequence of 0^+ excitations in ^{66}Ni, with the highest one, 0^+_4, located at 3463 keV, which demonstrates a hindered E2 decay to the 2^+_1 state, with HF > 63 [21,268] (see Fig. 45). As in ^{66}Ni, this 0^+_4 excitation is a candidate for the prolate deformed state lying in the prolate PES minimum (see discussion below). The support for such a hypothesis comes again from two sources: (i) from β^- decay of the spherical 1^+ ground state of ^{64}Co measured at ISOLDE [99], which strongly feeds the supposedly spherical 0^+_1 ground state in ^{64}Ni and, to much lesser extent, the 0^+_2 and 0^+_3 states, but not the 0^+_4 one, (ii) from the MCSM calculations which predict the 0^+_4 state as an excitation located in the deep prolate PES minimum, of which decay is hindered by a large factor, HF = 10000. Calculations of the Potential Energy Surface in deformation space for ^{64}Ni require a special mention. While the earlier mean-field approaches [56,198,225–228,264] predicted in ^{64}Ni only a single, spherical minimum (see Fig. 43(a,b) where the PESs from Ref. [59,198,227,249] are shown), a very different results came from constraint-HFB calculations with the A3DA-m Hamiltonian, which was used in the MCSM scheme [55,64] – see Fig. 43(c,d,e). Here, the PES of ^{64}Ni shows unexpectedly two secondary minima: one oblate and one prolate. These isolated, deformed local minima in the PES are stabilized by extra binding provided largely by the strong monopole tensor part of the nucleon–nucleon force acting between neutrons promoted to the neutron $g_{9/2}$ unique-parity orbital from the pf shell and protons excited to the $f_{5/2}$ orbital, across the Z = 28 shell gap, which, in turn, is reduced due to this interaction (the proton-$f_{5/2}$ – neutron-$g_{9/2}$ tensor interaction reduces the proton $f_{5/2} - f_{7/2}$ spin–orbit splitting). Such additional binding also deepens the secondary PES minima in ^{66}Ni, which were discussed in Section 2.1 from the viewpoint of *Type II shell evolution*.

In terms of the low-lying, low-spin excitations in ^{64}Ni, the MCSM predicts coexistence of spherical 0^+_1 and 0^+_3, oblate deformed 0^+_2 and prolate-deformed 0^+_4 states. Fig. 43(d) displays, with circles, the main components of the 0^+_4 state, which are mainly concentrated

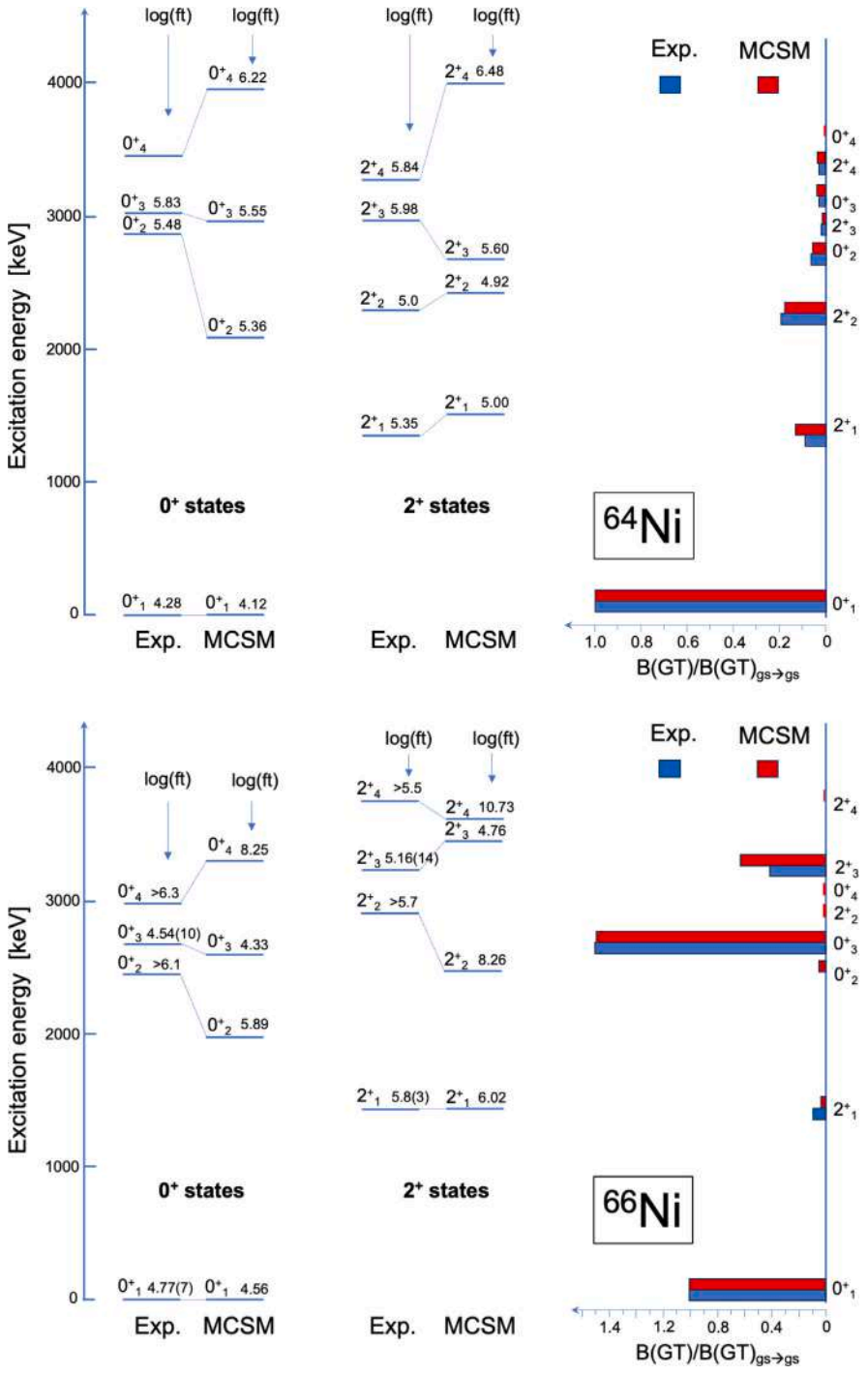

Fig. 44. Comparison of the states in ^{64}Ni (top) and ^{66}Ni (bottom) observed in the β^- decay of ^{64}Co and ^{66}Co, respectively, with experimental and predicted MCSM values of log(ft). In the calculations, the formula $ft = K(g_A^2 q^2 B_{GT})^{-1}$ was used, where k/g_V^2 = 6147 s, g_A/g_V = −1.2772 [269], and q = 0.744 is a standard quenching factor [270]. States up to 4 MeV are presented. On the right side of each panel, the experimental and calculated B(GT) values, normalized to the corresponding $B(GT)_{g.s.}$ value are shown for each considered state, at the approximate experimental excitation energy [99,100].

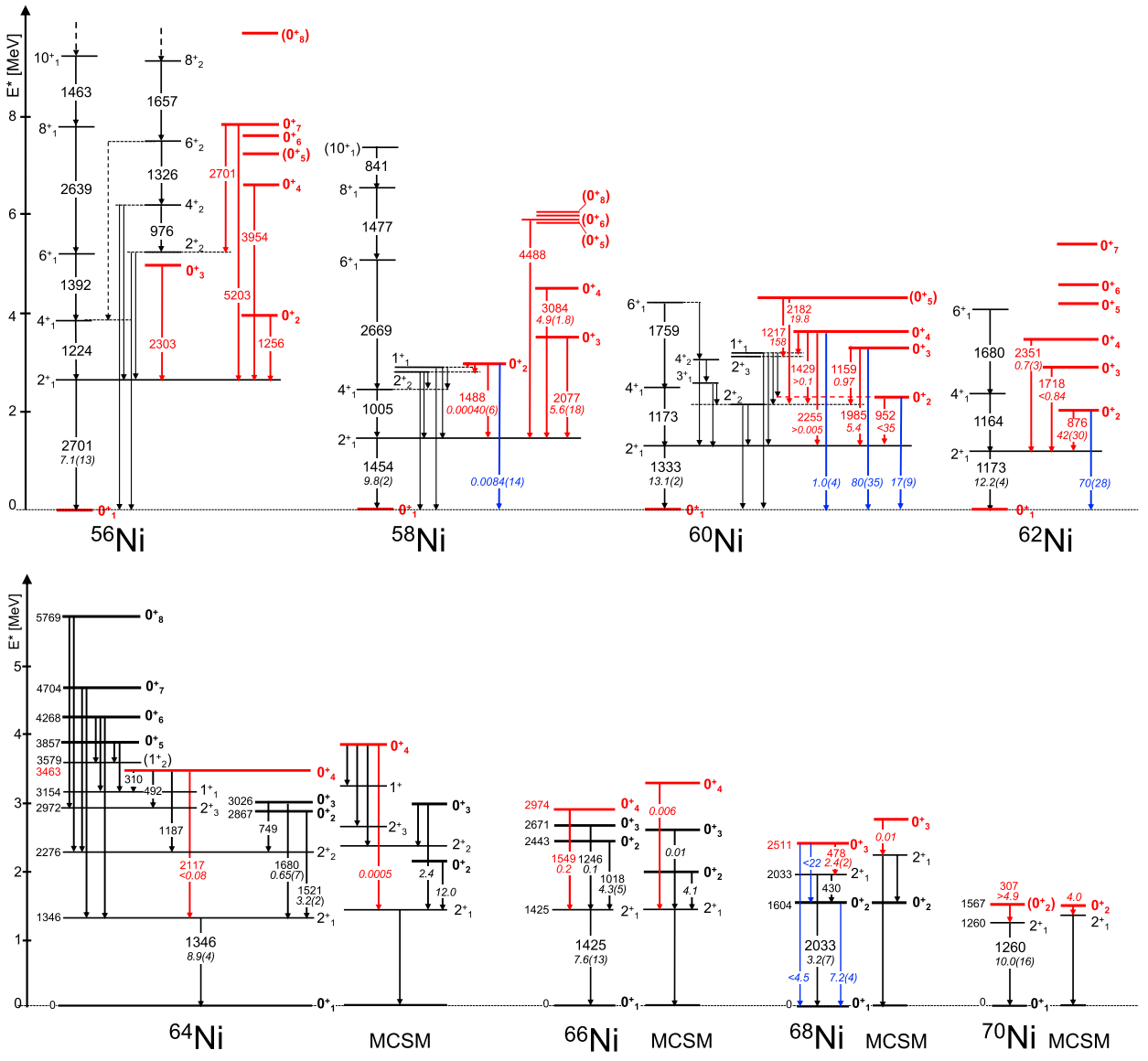

Fig. 45. Top row: Partial level schemes of even–even Ni isotopes with A = 56–62, with the γ decay of 0^+ states highlighted in red. Bottom: Partial level schemes of even–even Ni isotopes with A = 64–70, with red lines/arrows indicating the prolate 0^+ excitations and their direct decay to the 2^+_1 state. Predictions from MCSM calculations are also shown, limited to the decay of $0^+_{2,3,4}$. In all panels, γ-ray energies are in keV and B(E2) values in W.u. (in italic); blue arrows indicate measured E0 decays, with ρ^2(E0) values in m.u. (in italic); dashed arrows give uncertain transitions or continuation of a structure to higher spins (see Table 11 for details).
Source: Data from [21,67,68,274].

in the prolate PES minimum and are rather well isolated from the spherical 2^+_1 state components, illustrated in 43(e). This separation results in a hindrance of the $0^+_4 \rightarrow 2^+_1$ transition calculated to be HF = 10000, which is consistent with the experimentally determined lower hindrance limit of HF > 63 for this transition. When examining the PES of ^{64}Ni obtained from MCSM Hamiltonian shown in Fig. 43(c), one finds that the secondary prolate minimum in ^{64}Ni is shallower with respect to the corresponding minimum in ^{66}Ni and, in consequence, the barrier separating the 0^+_4 state from spherical 2^+_1 is lower. The fact that the prolate deformed 0^+_4 excitation in ^{64}Ni exhibits higher hindrance of its decay to 2^+_1 than the corresponding decay of 0^+_4 in ^{66}Ni, requires some explanation. Analysis of the wave functions of 0^+_4 and 2^+_1 in ^{64}Ni showed that not only the barrier separating the PES minima is responsible for the retarded E2 $0^+_4 \rightarrow 2^+_1$ decay. A significant contribution to the retardation of this decay arises from cancellation effects among E2 matrix elements, similarly to the case of 0^+_3 in ^{66}Ni. This result, as well as the origin of hindrance in the decay of the spherical 0^+_3 excitation in ^{66}Ni discussed earlier, clearly demonstrate that the retardation of the decay of the 0^+ states, in relatively light nuclei, can originate from the localization of the wave functions of initial and final states in different regions of the (β, γ) plane of the PES, well separated by a potential barrier, or matrix elements cancellations or both.

Table 11

Experimental information available on 0^+ excitations in Ni isotopes (A = 56–70), see also Fig. 42 and caption of Table 8 for detailed explanations.

Nucleus	E_i [MeV]	I_i^π	$T_{1/2}$ [ps]	E_f [MeV]	I_f^π	E_γ or E_{e^-} [MeV]	BR [%]	E/Mλ	B(E/Mλ)/ρ^2(E0) [W.u.]/[m.u.]	HF	Refs.
^{56}Ni	3.957	0_2^+		2.701	2_1^+	1.256		[E2]			[67]
	5.004	0_3^+		2.701	2_1^+	2.303		[E2]			
	6.655	0_4^+		2.701	2_1^+	3.954		[E2]			
	7.904	0_7^+		5.353	2_2^+	2.551	9.9	[E2]			
				2.701	2_1^+	5.203	90.1	[E2]			
^{58}Ni	2.943	0_2^+	1460(140)	2.902	1_1^+	0.040	72.1	[M1]	0.116(14)		[33,67]
				2.775	2_2^+	0.167	13.3	[E2]	21(3)	0.24	
				2.459	4_1^+ [a]	0.483	<0.29				
				1.454	2_1^+	1.488	14.3	[E2]	0.00040(6)	12 500	
				0	0^+	2.942	0.042	E0	0.0084(14)		
	3.531	0_3^+	0.19(6)	3.038	2_3^+	0.493	<0.9	[E2]	<69	>0.072	
				2.943	0_2^+	0.589		[E0]			
				2.902	1_1^+	0.629	<1.0	[M1]	<0.0047		
				2.775	2_2^+	0.756	<1.7	[E2]	<15	>0.32	
				2.459	4_1^+ [a]	1.072	<2.7				
				1.454	2_1^+	2.077	93.6	[E2]	5.6(18)	0.89	
				0.0	0_1^+	3.531	0.064	E0	$90(^{+30}_{-40})$		
	4.538	0_4^+	0.031(11)	1.454	2_1^+	3.084	100.0	[E2]	4.9(18)	1.0	
	5.942	(0_6^+)		1.454	2_1^+	4.488	100.0				
^{60}Ni	2.285	0_2^+	>1.5	1.333	2_1^+	0.952	100.0	[E2]	<35	>0.14	[33,67,276]
				0.0	0_1^+	2.285	0.016	E0	$17(^{+5}_{-13})$		
	3.318	0_3^+	$0.24(^{+28}_{-11})$	2.159	2_2^+	1.159	1.2	[E2]	0.97	5.2	
				1.333	2_1^+	1.985	98.8	[E2]	5.4	0.93	
				0.0	0_1^+	3.319	0.064	E0	$80(^{+20}_{-50})$		
	3.588	0_4^+	<40	3.194	1_1^+	0.394	18.2	[M1]	>0.002		
				2.159	2_2^+	1.429	55.8	[E2]	>0.1	<50	
				1.333	2_1^+	2.255	25.9	[E2]	>0.005	<1000	
				0.0	0_1^+	3.588	0.1	E0	$1.0(^{+7}_{-6})$		
	4.341	(0_5^+)	$0.029(^{+31}_{-21})$	3.124	2_3^+	1.217	30.1	[E2]	158	0.032	
				2.159	2_2^+	2.182	69.9	[E2]	19.8	0.25	
^{62}Ni	2.049	0_2^+	$1.8(^{+19}_{-6})$	1.173	2_1^+	0.876	100.0	E2	$42(^{+22}_{-7})$	0.12	[33,67,220]
				0.0	0_1^+	2.048		E0	70(28)		
	2.891	0_3^+	>3.1	1.173	2_1^+	1.718	100.0	E2	<0.84	>5.95	
	3.524	0_4^+	$0.74(^{+46}_{-22})$	1.173	2_1^+	2.351	100.0	E2	0.73(34)	6.8	
^{64}Ni	2.867	0_2^+	1.45(10)	1.346	2_1^+	1.522	100.0	E2	$3.15(^{+23}_{-21})$	1.6	[21,67,268]
	3.026	0_3^+	3.6(12)	2.277	2_2^+	0.749	3.5	E2	$1.5(^{+8}_{-4})$	3.3	
				1.346	2_1^+	1.680	96.5	E2	0.65(7)	7.7	
	3.463	0_4^+	>2 [b]	3.154	1_1^+	0.310	3.6	M1			
				2.972	2_3^+	0.492	0.8	E2			
				2.277	2_2^+	1.187	77.8	E2			
				1.346	2_1^+	2.117	17.9	E2	<0.08	> 63	[21,67,268]
	3.857	0_5^+		3.579	(1_2^+)	0.279	9.1				
				3.154	1_1^+	0.702	90.9	[M1]			
	4.268	0_6^+		3.579	(1_2^+)	0.688	16.6				
				3.154	1_1^+	1.115	75.3	[M1]			
				1.346	2_1^+	2.922	8.1	[E2]			
	4.704	0_7^+		2.277	2_2^+	2.428	38.7	[E2]			
				1.346	2_1^+	3.358	61.3	[E2]			
	5.769	0_8^+		2.277	2_2^+	3.492	45.1	[E2]			
				1.346	2_1^+	4.423	54.9	[E2]			
^{66}Ni	2.443	0_2^+	7.6(8)	1.425	2_1^+	1.018	100.0	[E2]	4.3(5)	1.2	[67,68]
	2.671	0_3^+	134(9)	1.425	2_1^+	1.246	100.0	[E2]	0.09(1)	56	
	2.974	0_4^+	$19.6(^{+75}_{-66})$	1.425	2_1^+	1.549	100.0	[E2]	0.21(7)	24	
^{68}Ni	1.604	0_2^+	268(5)	0.0	0_1^+	1.604	100.0	E0	7.2(4)		[33,67,274]
	2.511	0_3^+	570(50)	2.033	2_1^+	0.478	98.1	[E2]	2.4(2)	2.1	
				1.604	0_2^+	0.907	<0.18	E0	<22		
				0.0	0_1^+	2.511	<1.73	E0	<4.5		
^{70}Ni	1.567	(0_2^+)	$1.65(^{+30}_{-25})\times10^3$	1.260	2_1^+	0.308	>66	[E2]	>4.9	<0.98	[67,274]
				0.0	0_1^+	1.567	<33	E0	<540		

[a] Unreasonable decay.

[b] From B(E2), Coulomb excitation study [268];

Additional 0^+ states from β decay, (p,t), (^{3}He,n), (n,n′) and (p,p′) reaction studies (no γ branch reported) [67]:

^{56}Ni; (0_5^+), 0_6^+, (0_8^+), 0_{9-13}^+: 7.289(25), 7.670(8), 9.756(5), 9.943(4), 9.994(3), 10.011(6), 10.041(6), 10.250(6) MeV;

^{58}Ni; $(0_{5,7,8}^+)$, 0_9^+, (0_{10}^+), : 5.924(10), 5.963(10), 5.982(10), 10.590(50), 14.470(40) MeV;

^{62}Ni; $0_{5,6,7}^+$: 4.230(1), 4.623(5), 5.447(5) MeV.

The β^- decay of the ^{64}Co ground state 1^+ into ^{64}Ni was also modeled by the MCSM approach – comparison between theory and experiment is shown in Fig. 44. The calculations reproduce very well the strong feeding of the ^{64}Ni 0^+ g.s. and a weak/medium population of the 0^+_2, 0^+_3, 0^+_5 and 0^+_6 states as well as 2^+_1 - 2^+_6 states. The lack of measurable feeding to the prolate 0^+_4 excitation predicted by MCSM provides additional argument for assigning the calculated prolate deformed 0^+_4 state to the 0^+_4 excitation located at 3463 keV, as it is very much in line with the experimental observation.

When moving toward lighter Ni isotopes, the extra binding for prolate configurations caused by tensor interaction is reduced as there are progressively fewer neutrons which can be excited to the $g_{9/2}$ orbital. As a result, the prolate deformed minimum rises in excitation energy, moves toward triaxiality and becomes very shallow – see Fig. 43 for ^{62}Ni. As mentioned earlier, two rotational bands were identified in ^{62}Ni characterized by the quadrupole deformation parameter β_2 of around 0.4, assuming prolate deformation [266]. Even though they are surely based on the low-spin level structure of ^{62}Ni, they decay out already at spin 8 and 10, respectively, and one cannot trace their low-spin members down to spin 0. The MCSM calculations predict many 0^+ excitations located in the energy range where bandhead of the lower-lying positive-parity deformed band is expected. It is very likely that the 0^+ state calculated in the prolate-triaxial deformed minimum will be a bandhead of the rotational structure. However, one should not expect any significant hindrance of its decay as the minimum is rather shallow. Of particular interest in ^{62}Ni is also a very high value of the E0 strength for the $0^+_2 \rightarrow 0^+_1$ transition, $10^3 \times \rho^2(0^+_2 \rightarrow 0^+_1) = 70(28)$, which contradicts the hypothesis of vibrational character of the 0^+_2 excitation. It points to a rather significant mixing of the two structures each associated with significantly different shapes. Existence of such mixing is further supported by a fast E2 transition $0^+_2 \rightarrow 2^+_1$, for which B(E2) = 41.9 W.u., and a high E(0) strength for the $2^+_2 \rightarrow 2^+_1$ transition, as obtained in proton- and neutron-inelastic-scattering measurements performed at the Australian National University (ANU) and the University of Kentucky [276,277]. This picture is very much in line with MCSM calculations, according to which the 0^+_2 and 2^+_1 wave functions demonstrate broad distributions in the PES.

In ^{60}Ni, similarly, very strong E0 transition to the ground state was measured for the decay of the 0^+_3 state, with $10^3 \times \rho^2$ value of $80(^{+20}_{-50})$. Again, this can be a sign of a strong mixing between spherical and deformed structures in this nucleus. Such hypothesis is further supported by strongly enhanced ρ^2(E0) value established for the $2^+_2 \rightarrow 2^+_1$ transition in this nucleus [276,277].

The nucleus ^{58}Ni also shows some features pointing to shape coexistence already at low excitation energy in this otherwise spherical nucleus. Here, the 0^+_2 state has a very hindered E2 decay to 2^+_1 with HF = 12500, and a very low value for the E0 $0^+_2 \rightarrow 0^+_1$ g.s. transition strength of $10^3 \times \rho^2 = 0.0084(14)$. This low value of the E0 strength can be explained by the fact that the 0^+_2 state is spherical and there is no significant difference of mean-square charge radii between 0^+_1 and 0^+_2. In turn, hindrance of the E2 $0^+_2 \rightarrow 2^+_1$ transition in ^{58}Ni probably arises from cancellation effects among E2 matrix elements, in analogy to the decay of the spherical 0^+_3 state in ^{66}Ni. There is even some resemblance between the two isotopes: ^{58}Ni can be viewed as a ^{56}Ni core with two additional neutrons in the $p_{3/2}f_{5/2}p_{1/2}$ orbitals while ^{66}Ni would be a ^{68}Ni core minus two neutrons in the same orbitals. In contrary to 0^+_2, the 0^+_3 excitation in ^{58}Ni is connected with 2^+_1 by a relatively fast E2 transition with B(E2) = 5.6(18) W.u. and the E0 branch to the 0^+_1 ground state has a high value of $10^3 \times \rho^2 = 90(^{30}_{-40})$. This characteristics points to a significant difference in mean-square charge radii of 0^+_3 and 0^+_1 g.s. and/or to a substantial mixing of configurations associated with different shapes. A microscopic model for electric monopole (E0) transition matrix elements, that uses orbital occupations obtained from shell model calculations and EDF calculations constrained by these occupations, was applied to shed light on the origin of the observed E0 transitions strength [81]. The model, in spite of providing a good overall description of the E0 transitions properties in the Ni region, fails in predicting the E0 strength for the $0^+_2 \rightarrow 0^+_1$ decay in ^{58}Ni – the calculated value is much larger than the experimental number. Also, the calculated E2 matrix element for the $0^+_2 \rightarrow 2^+_2$ transition of 13.0 efm^2 is much larger than the experimental value of 1.4(5) efm^2. A solution for both problems was proposed by requiring a mixing between 0^+_2 and 0^+_3, however, the results were still not satisfactory. What regards description of the strength of E2 transitions deexciting the 0^+s states by shell model, the calculations with the GXPF1 interaction did rather well, with one notable exception – the calculated B(E2; $0^+_2 \rightarrow 2^+_1$) was by more than three orders of magnitude larger than the experimental value [278]. It remains to be seen if the MCSM calculations can properly describe these strengths.

The doubly magic ^{56}Ni nucleus, being spherical in the ground state, develops deformed structures at relatively low excitation energy as well. Two well-deformed rotational bands were located in this nucleus encompassing spin ranges 2–12, and (7)-17 [177], as shown in Section 3.2.2 (see Fig. 32). They were later extended to higher spins of 13 and 18, respectively. These bands were successfully reproduced with simultaneous description of spherical states by the Monte Carlo Shell Model calculations with full pf plus $g_{9/2}$ model space [279]. Within this approach, the structure located at lower energy and beginning at spin 2 is composed mainly of the 4-p 4-h excitations within the pf shell model space, while to interpret the second deformed band, the model space had to be extended by including the $g_{9/2}$ orbital. This second band was found to be formed predominantly of configurations in which one nucleon from those promoted above the Z = 28 shell gap, occupies the $g_{9/2}$ single particle state. Calculations place the 0^+ band head of the first band only about 300 keV below its 2^+ member. It could be that the 0^+_3 level, experimentally located at 5004 keV, belongs to band but the E2 transition deexciting the 2^+ band member is too weak to compete with the 2003 keV decay-out gamma ray connecting this 2^+ state with 2^+_1.

In Ni isotopes with A > 66, the high-spin structures could not be explored due to the lack of suitable stable projectile–target combination, but in these nuclei, similarly to ^{64}Ni and ^{66}Ni, already the low-energy, low-spin states exhibit shape coexistence. In the context of the effects caused by the monopole tensor force discussed above, it is worthwhile to focus first on the 0^+_1 ground state and the two excited 0^+s, 0^+_2 and 0^+_3, in ^{68}Ni, which were located at 1604 and 2511 keV, respectively, in measurements performed at NSCL (MSU), ISOLDE and Louvain-la-Neuve [274,280–283].

The large shell model calculations, including MCSM approach, reproduce the energy of these three states quite well and predict for them spherical, oblate and prolate deformation, respectively [55,280,282,284]. In Fig. 43, it can be seen that the existence of a secondary minimum, of prolate nature, in the PES of ^{68}Ni is predicted already by the macroscopic–microscopic finite-range

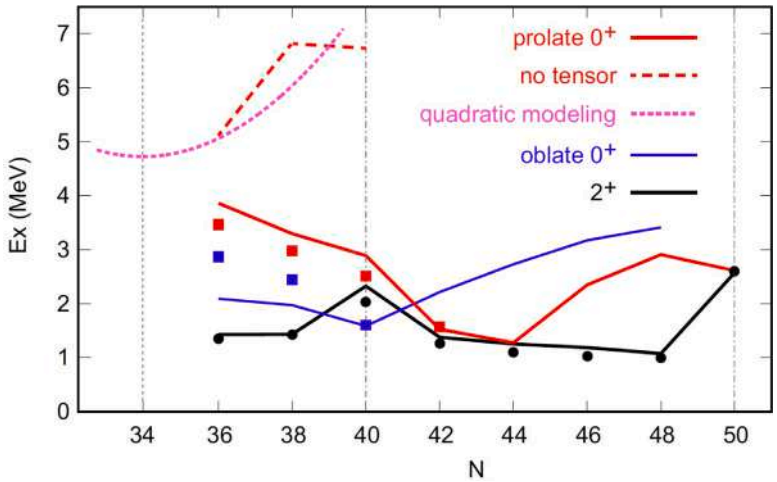

Fig. 46. Excitation energies for $^{64-78}$Ni. Symbols are experimental data. Lines are theoretical calculations. The excitation energies of strongly prolate deformed states are shown by red squares and line. Those of moderately oblate deformed states are shown by blue squares and line. Black circles and line indicate the excitation energies of the 2^+_1 states. The estimated excitation energies of strongly prolate deformed states calculated without major monopole contributions of the tensor force are shown by red dashed line. Pink dotted line indicates the simple modeling of deformed intruder states (see the text), with parameters fitted to the estimated values without the tensor-force effect.
Source: Taken from [50].

liquid-drop model as well as by the HFB with the Gogny force approach. This minimum is significantly deepened by the additional binding produced by the monopole tensor interaction (*Type II shell evolution*) discussed above in the case of ^{64}Ni and ^{66}Ni – see Fig. 43(c,d,e). The interaction contributes also to the development of an oblate minimum what is visible in the same figures.

In comparison of ^{68}Ni with ^{66}Ni, the height of the barrier between the prolate and spherical minima is larger in ^{68}Ni but, at the same time, the prolate minimum in ^{66}Ni is lower due to stronger p–n interaction coming from larger number of neutron holes in the N = 40 closed shell. As the result, the barrier that should be overcome when decaying from prolate deformed 0^+ to a spherical 2^+ state should be of similar size. However, there is other substantial difference: in ^{66}Ni, the prolate 0^+_4 excitation decays to the 2^+_1 state which, according to MCSM calculations, is spherical, while in ^{68}Ni an E2 transition connects the prolate 0^+_3 excitation with the 2^+_1 state which is oblate – note that the spherical 2^+ state is too high in energy for ^{68}Ni because of its doubly closed-shell structure. The barrier between prolate and oblate minima in ^{68}Ni is much lower than the prolate-spherical one in ^{68}Ni. All these characteristics of the PES structure are nicely reflected in the wave function components distribution in the deformation space, calculated for the considered states. For the prolate 0^+_3 state, the components are located mostly in the prolate minimum, with some of them lying in the oblate well (Fig. 43(d)). For the 2^+_1 state in ^{68}Ni, the wave function components are mostly concentrated in the oblate minimum, but this is in contrast with 2^+_1 in ^{66}Ni, the wave function of which resides in the spherical PES minimum. Consequently, a larger hindrance of the decay from the prolate 0^+_4 excitation to 2^+_1 is expected in ^{66}Ni when comparing with ^{68}Ni. The MCSM calculations for ^{66}Ni predict HF = 833 while for ^{68}Ni HF = 500 (Fig. 45). In terms of qualitative relative difference, these results are in line with the experiment which yields the hindrance factors of 24 for ^{66}Ni and 2.1 for ^{68}Ni. Similar description of the properties of the first three 0^+ states in ^{68}Ni was also provided by the large-scale shell model calculations with the LNPS interactions [258,284]. For the $0^+_3 \rightarrow 2^+_1$ transition, which is of particular interest here, they predict hindrance of ∼7, which has a correct order of magnitude.

Upon addition of two neutrons to ^{68}Ni, leading to ^{70}Ni, the expectations related to shapes associated with the 0^+ states change substantially. The MCSM model predicts spherical-prolate shape coexistence [55,280,282], assigning spherical and prolate deformation to the 0^+_1 ground state and 0^+_2 state, respectively. From the experimental point of view, the 0^+_2 in ^{70}Ni was located at energy of 1567 keV and its lifetime of 7.2 ns was measured. A significant population of this excitation observed in β-decay of the prolate deformed ^{70}Co ground state, measured at RIKEN [285], provides strong indication of its prolate character. These results point to a drop in excitation energy of the prolate potential minimum, in line with theoretical expectations (Fig. 43(d,e)), and to a relatively fast E2 $0^+_2 \rightarrow 2^+_1$ transition with B(E2) = 3.6 W.u., in spite of a rather high potential barrier separating the two minima. This can be interpreted in terms of a significant overlap of the 0^+_2 and 2^+_1 wave functions components lying in the oblate region of the PES. In the case of ^{70}Ni, the MCSM framework better reproduces the $0^+_2 \rightarrow 2^+_1$ transition probability yielding B(E2) = 4.0 W.u.

Low lying 0^+ states have not so far been observed in Ni isotopes with A > 70, but on the basis of the MCSM calculations one may expect that they exist and that some of them are deformed [55]. Indeed, a piece of experimental information which points to shape coexistence in the neutron-rich ^{78}Ni isotope came recently from the identification in RIKEN of a few low-lying excited states in this nucleus, including two 2^+ states [286]. With the help of MCSM calculations it was concluded that the higher lying 2^+ excitation demonstrates prolate deformed characteristics, while the 0^+ ground state and the first 2^+_1 state are of spherical nature. It is worth noticing that according to this MCSM model, ^{78}Ni is the last in the chain having spherical shape. In heavier isotopes prolate deformation may prevail in the ground states.

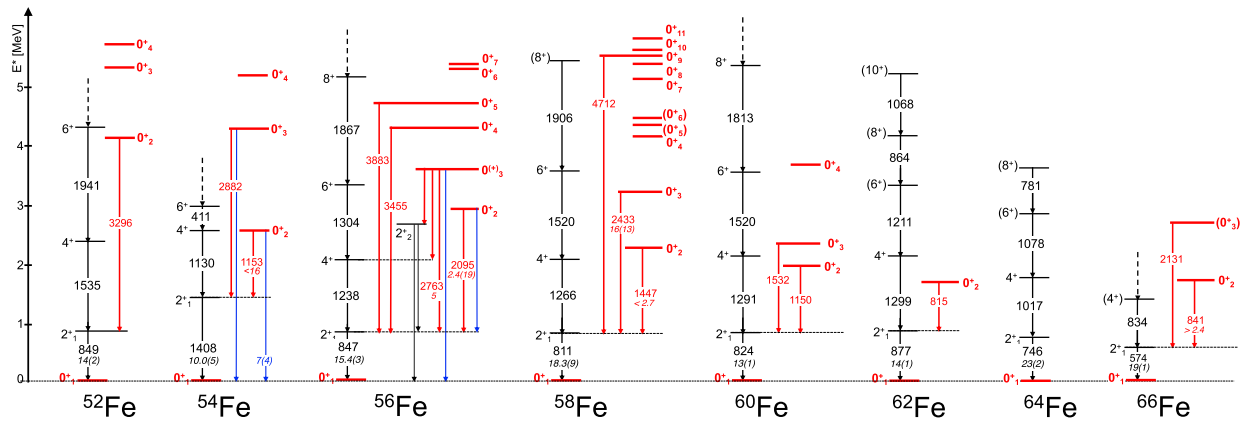

Fig. 47. Partial level schemes of even–even $^{52-66}$Fe nuclei [67]. The γ decay of 0^+ states is highlighted in red, with energies in keV and B(E2) values in W.u. (in italic). Blue arrows indicate measured E0 decays, with ρ^2(E0) values in m.u. (in italic). Dashed arrows give continuation of a structure to higher spins (see Table 12 for details).

As discussed earlier in this chapter, prolate deformed local minima in the PES (Fig. 43) are stabilized by extra binding, provided largely by the tensor monopole interaction of the NN interaction: the additional binding creates a prolate minimum in ^{64}Ni and deepens the ones in $^{66-70}$Ni. When moving toward lighter Ni isotopes, the effect is reduced as there are progressively fewer neutrons in $g_{9/2}$ excited across the N = 40 subshell gap. As a result, the deformed minimum rises in excitation energy. The action of tensor force is clearly reflected in the systematics of 0^+ excitations in Ni isotopes, which is displayed in Fig. 46. Instead of following a parabolic behavior with a minimum energy in the middle of the fp subshell, i.e., at N = 34, the energy of the prolate 0^+ states is raised with decreasing number of neutrons from N = 42 in ^{70}Ni to N = 34 in ^{62}Ni.

4.2.2. The Fe isotopes

According to macroscopic–microscopic mean-field calculations [59] and HFB calculations based on the Gogny force, by S. Hilaire and M. Girod [198,249], no clear secondary minima appear in the Potential Energy Surfaces of Fe isotopes with A ∼ 54–70, of interest here. The most probable shape is found to be either spherical/weakly-deformed or weakly deformed, as in $^{56-60}$Fe, with deformation parameters $\beta_2 \sim 0.1$–0.2. Only in ^{66}Fe, a clear secondary prolate minimum appears around $\beta_2 \sim 0.3$ in the calculations of Moller et al. [59].

Experimentally, in Fe isotopes a number of low-lying 0^+ states has been observed (see Figs. 42 and 47), in particular from a series of β-decay studies mainly performed at ISOLDE and MSU [100,287–290]. None of these states has appreciable hindrance, i.e., HF < 10 for each of them, as shown in Figs. 34 and 35 and in Table 12, thus suggesting a scenario of significant mixing between different configurations. The nature of all these excitations has not yet been established experimentally, however, they might be associated with deformed structures which become yrast when moving toward N = 40. In fact, a rapid development of collectivity has been reported in the neutron-rich Fe isotopes. This is reflected by the downward trend of the 2^+_1 energies in ^{64,66}Fe, and by an increase in the transition rates for the 2^+_1 states in ^{62,64,66}Fe, as measured in multinucleon transfer and Coulomb excitation reactions [291,292]. The measured B(E2) values around 20 W.u. correspond to a rather large deformation parameter $\beta_2 \sim 0.28$, in agreement with large-scale shell-model calculations in the $fpgd$ valence space [292]. These calculations also show that the ground state wave function of ^{62}Fe contains a 60% probability of excitations to the upper gd orbitals, which increases to 90% in ^{64}Fe and to almost 99% in ^{66}Fe [292], in line with the enhanced collectivity observed experimentally. In the case of ^{66}Fe, the shell-model calculations reported in Ref. [289] also confirm that the second 0^+ state, located experimentally at 1.414 MeV, is of spherical nature, being associated with a closed shell configuration, while most recent MCSM calculations [100] show a rather fragmented wave function for the 0^+_1 ground state, with components spread over a broad, deformed prolate minimum, what suggests a transitional nature of this nucleus. ^{66}Fe lies, in fact, in between the spherical ^{68}Ni and the well deformed ^{64}Cr ($\beta_2 \sim 0.3$), which exhibits features of a rotational nucleus [258].

A possible shape-coexistence scenario in Fe isotopes could also be qualitatively viewed from the perspective of the correspondence between the deformed ground states in the Fe nuclei and the deformed excited states in the Ni isotopes, as well as between possibly weakly deformed excited states in Fe and the close-to-spherical ground states in Ni isotopes. At higher spins, a number of rotational bands, including some associated with large deformation, has been found in Fe isotopes with assigned configurations including at least one $g_{9/2}$ neutron, as in the case of deformed structures in the Ni's. Additional support to shape coexistence in Fe isotopes comes also from the large "backbending" behavior observed, in particular, in the yrast sequence of ^{60}Fe (see Fig. 48). Similarly to the Hg case, discussed in Section 4.5, such a pattern has been interpreted as resulting from the crossing of the weakly-deformed (shell-model type) ground-state sequence by a prolate-deformed rotational band based on a $(g_{9/2})^2$ configuration and associated with an axial symmetric shape with $\beta_2 \sim 0.2$ deformation [293]. Indeed, the yrast band sequence in ^{62,64,66,68}Fe can be also reproduced

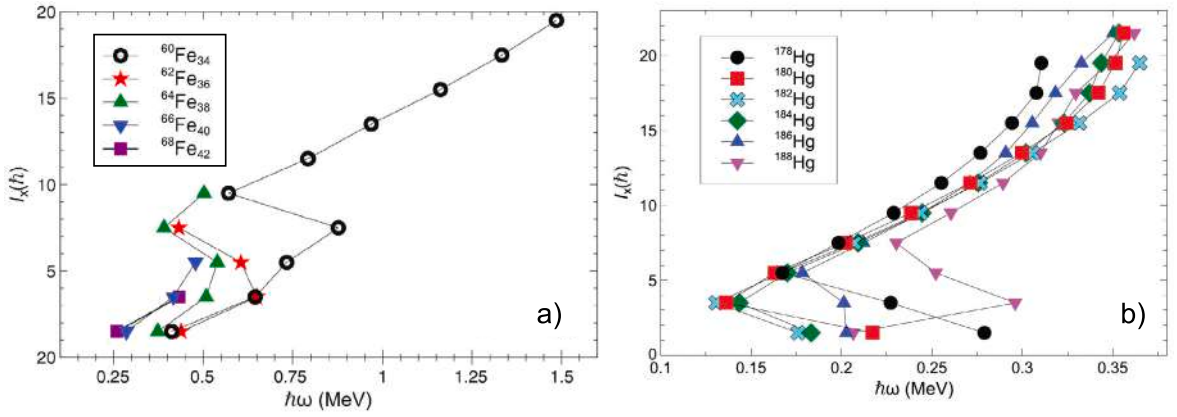

Fig. 48. Panel (a): Spin along the rotational axis, I_x, as a function of the rotational frequency, $\hbar\omega$, for the yrast sequences of $^{60-68}$Fe isotopes. Panel (b) similar to (a), for $^{178-188}$Hg isotopes. In both cases, the backbending pattern is attributed to a strong interaction between weakly-deformed (shell-model type) and prolate-deformed rotational sequences.
Source: Adapted from [293]

Table 12
Experimental information available on 0^+ excitations in Fe isotopes (A = 52–66), see also Fig. 42 and caption of Table 8 for detailed explanations.

Nucleus	E_i [MeV]	I_i^π	$T_{1/2}$ [ps]	E_f [MeV]	I_f^π	E_γ or E_{e^-} [MeV]	BR [%]	E/Mλ	B(E/Mλ)/ρ^2(E0) [W.u.]/[m.u.]	HF	Refs.
^{52}Fe	4.146	0_2^+		0.849	2_1^+	3.296	100.0	[E2]			[67]
^{54}Fe	2.561	0_2^+	≥1.4	1.408	2_1^+	1.153	98.8	E2	<16	>0.31	[33,67]
				0.0	0_1^+	2.561	0.2	E0	$7(^{+2}_{-6})$		
	4.291	0_3^+	$0.055(^{+17}_{-14})$	1.408	2_1^+	2.882	100.0	E2	$4.3(^{+11}_{-14})$	1.2	
				0.0	0_1^+	(4.291)		E0			
^{56}Fe	2.942	0_2^+	$0.45(^{+21}_{-12})$	0.847	2_1^+	2.095	100.0	[E2]	$2.4(^{+7}_{-12})$	2.1	[67]
				0.0	0_1^+	(2.941)		[E0]			
	3.610	$0_3^{(+)}$	0.052(21)	2.658	2_2^+	0.952	<1.4	[E2]	<15.4	>0.32	
				2.085	4_1^+[a]	1.525	<0.6				
				0.847	2_1^+	2.763	91.6	[E2]	5	1.0	
				0.0	0_1^+	3.610	<6.4				
	4.302(1)	0_4^+		0.847	2_1^+	3.455	100.0	[E2]			
	4.730(1)	0_5^+		0.847	2_1^+	3.883	100.0	[E2]			
^{58}Fe	2.258	0_2^+	>2.5	0.811	2_1^+	1.447	100.0	[E2]	<2.7	>1.9	[67]
	3.244	0_3^+	$0.031(^{+67}_{-14})$	0.811	2_1^+	2.433	100.0	[E2]	$16(^{+8}_{-16})$	0.31	
	5.523(2)	0_9^+		0.811	2_1^+	4.712(3)	100.0	[E2]			
^{60}Fe	1.974	0_2^+		0.824	2_1^+	1.150	100.0	[E2]			[67,287]
	2.356	0_3^+		0.824	2_1^+	1.532	100.0	[E2]			
^{62}Fe	1.692(2)	(0_2^+)		0.877	2_1^+	0.815(2)					[67]
^{66}Fe	1.414	0_2^+	<35	0.574	2_1^+	0.841	100.0	[E2]	>2.4	<12	[100,289,290]
	2.704	(0_3^+)		0.574	2_1^+	2.131	100.0				[290]

[a] Unreasonable decay.
Additional 0^+ states from β decay and (p,t), (^{3}He,n) reaction studies (no γ-decay reported) [67]:
^{52}Fe; $0_{3,4}^+$, (0_5^+), 0_{6-10}^+: 5.363(5), 5.718(8), 6.634(10), 6.927(15), 8.037(12), 8.561(5), 10.332(5), 10.990(20) MeV;
^{54}Fe; 0_{4-11}^+: 5.233(10), 6.400(10), 7.560(20), 10.250(20), 10.700(10), 12.040(20), 13.520(20), 14.870(20) MeV;
^{56}Fe; 0_{6-16}^+: 5.296(5), 5.386(7), 6.512, 6.567, 6.700(12), 6.800(15), 7.124(15), 7.220, 7.254, 8.110(30), 9.200(30) MeV;
^{58}Fe; 0_4^+, $(0_{5,6}^+)$, $0_{7,8,10,11}^+$, (0_{12}^+), 0_{13-16}^+: 4.158(10), 4.350(20), 4.450(20), 5.138(10), 5.406(10), 5.620(10), 5.830(20), 6.168(10), 6.450(10), 6.650(20), 6.760(20), 7.124(10) MeV;
^{60}Fe; 0_4^+: 3.698(5) MeV.

by a schematic two-band mixing model in which the unperturbed spherical and deformed levels are mixed by a $V_{int} \sim 100$ keV interaction matrix element [293].

As already anticipated, a scenario of strongly mixed spherical and deformed configurations is realized in the Fe isotopes, in agreement with the very limited hindrance measured for 0^+ excitations.

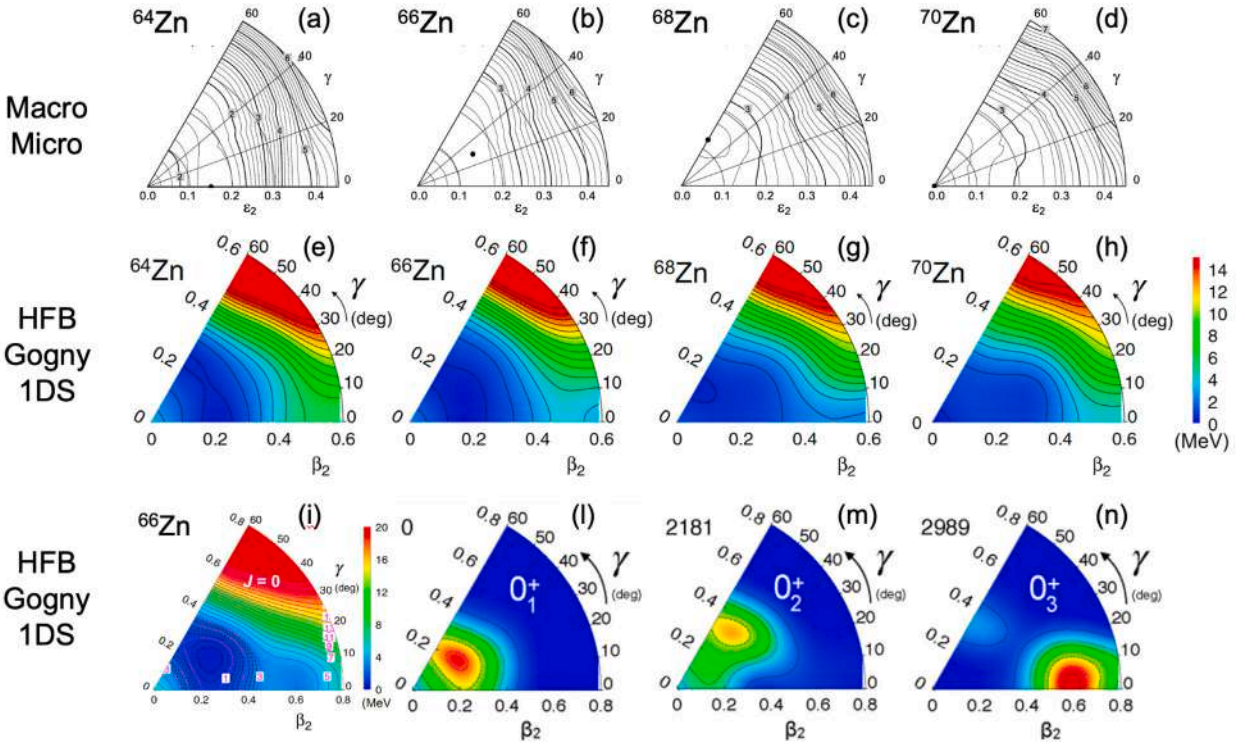

Fig. 49. Potential Energy Surfaces (PES) for stable even–even $^{64-70}$Zn isotopes, obtained from mean-field calculations by Moller et al. [59] (panels (a)–(d)), and deformation-constrained Hartree–Fock calculations with the particle number projection method (PN-VAP) and Gogny D1S interaction (panels (e)–(h)). Panel (i): PES for ^{66}Zn after projecting onto angular momentum J = 0, showing a more defined triaxial-shape minimum and the development of a second prolate minimum. Panels (l)–(n): corresponding collective wave functions for 0^+_1, 0^+_2 and 0^+_3 of ^{66}Zn obtained within the symmetry-conserving configuration mixing (SCCM) framework [261,296,297].
Source: Adapted from [59,263].

4.2.3. The Zn isotopes

According to HFB calculations based on the Gogny force, no local minima associated to different deformations appear in the Potential Energy Surfaces of Zn isotopes, which show instead a diffused γ-soft character, as displayed in Fig. 49 for A = 64–70 [263]. Similar results are obtained by self-consistent relativistic Hartree–Bogoliubov [294] and relativistic mean-field calculations [59,295]. For heavier Zn isotopes, with A = 72–78, recent large-scale shell-model calculations with the LNPS and JUN45 effective interactions and Monte Carlo shell-model calculations with the A3DA-m Hamiltonian confirm the persistence of a diffused γ-soft minimum, with no dominant shape and substantial shape fluctuations [260]. From a microscopic perspective, the absence of local (deformed) minima in the PES of Zn isotopes is attributed to the two extra protons beyond Z = 28, suppressing the excitation from the $f_{7/2}$ proton shell which are instead responsible for the appearance of prolate local minima in the neighboring Ni isotopes. In heavy Zn nuclei, a clear deviation from sphericity is also predicted, at variance from the Ni, and in general agreement with the experimental findings, as reported in a series of measurements with various techniques (see Ref. [260] and references therein). Spectroscopic quadrupole moments of the 2^+_1 states were also experimentally determined in ^{72}Zn and ^{74}Zn in Coulomb excitation experiments at ISOLDE, leading to $Q_s = -24(4)$ efm^2 and $Q_s = -7(9)$ efm^2 (consistent with zero), respectively, thus pointing to triaxiality (or shape coexistence, in the latter case) [260,262].

Experimentally, low-lying 0^+ states in Zn nuclei have been observed in the mass range A = 60–76 and at A = 82 (the systematics is displayed in Figs. 42 and 50), with no significant hindrance for γ decays (i.e., HF < 10) (see Figs. 34, 35 and Table 13). The only exception is the 0^+_2 excitation in ^{64}Zn, with HF = 88 for the decay to the 2^+_1 state. An attempt to find an explanation for this delay was made using the Interacting Boson Model [298,299]. Within this framework, it was suggested that ^{64}Zn possesses E(5) symmetry and the 0^+_2 state is a member of the three-phonon multiplet, so called 0^+_τ, for which the probability of transition to the 2^+_1 excitation is rather low, while transition to the 2^+_2 state is favored. Indeed, the obtained value of the B(E2; $0^+_2 \rightarrow 2^+_2$)/B(E2; $0^+_2 \rightarrow 2^+_1$) ratio, 1054, is close to theoretical predictions for the 0^+_τ state. This definitely excludes the vibrational interpretation of the 0^+_2 excitation, which would imply the ratio equal to 0. The E(5) symmetry character of the low-lying 0^+ states in ^{64}Zn, however, is not supported by the E0 transition connecting 0^+_2 with the ground state, with a transition strength of $\rho^2(0^+_2 \rightarrow 0^+_1) = 3.7(4)$ m.u. – in this case the E(5) symmetry predicts a zero strengths value. In turn, the 0^+_3 state in ^{64}Zn shows a behavior similar to that of the 0^+_ξ state predicted by the E(5) symmetry [299]. It is an open question why, in ^{64}Zn, the 0^+_2 state identified as 0^+_τ lies at much lower energy than 0^+_3 which corresponds to 0^+_ξ, while, according to theory, this order should be reversed. Taking it together,

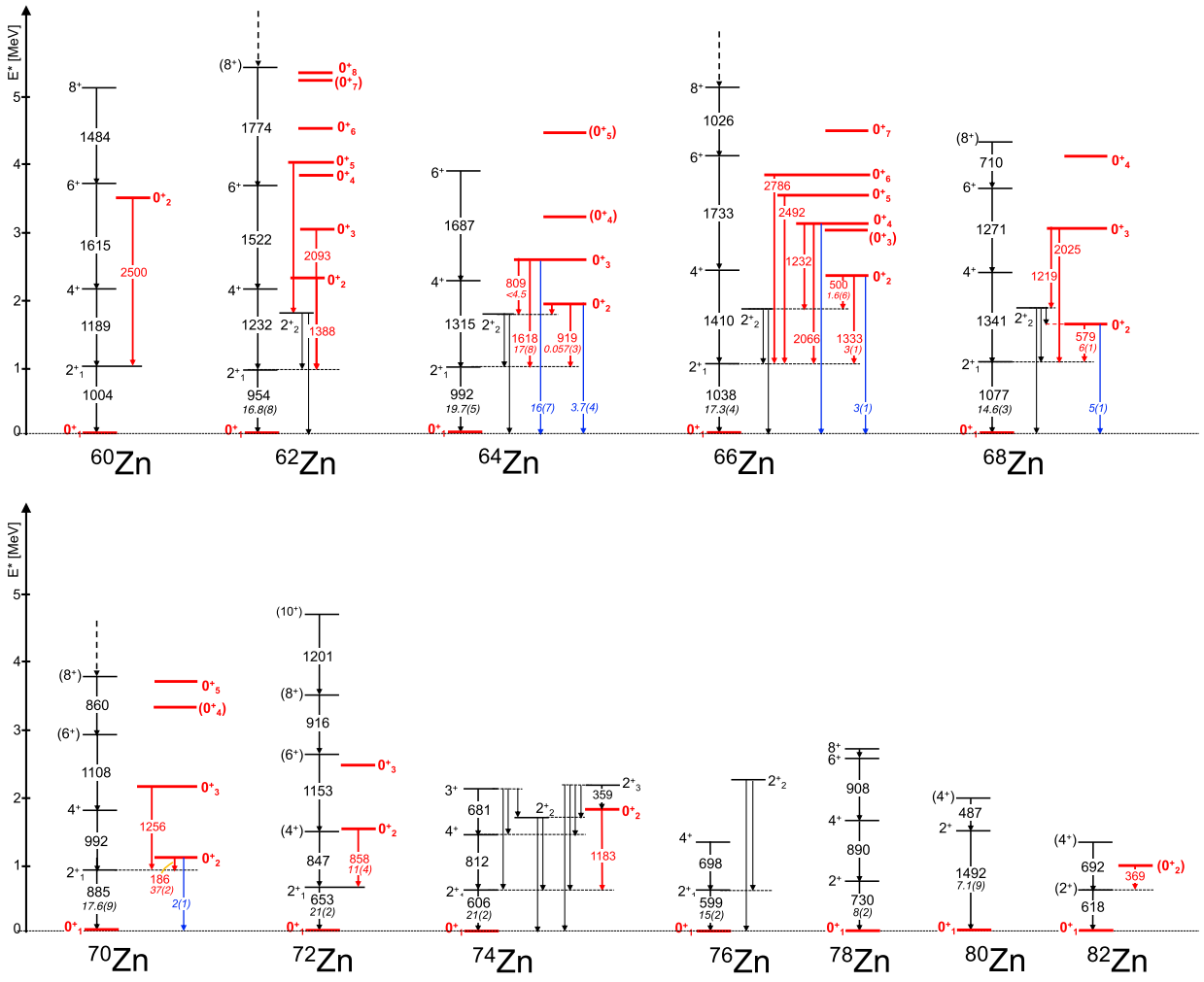

Fig. 50. Partial level schemes of even–even $^{60-82}$Zn [67]. The γ decay of 0^+ states is highlighted in red, with energies in keV and B(E2) values in W.u. (in italic). Blue arrows indicate measured E0 decays, with ρ^2(E0) values in m.u. (in italic). Dashed arrows give continuation of a structure to higher spins (see Table 13 for details).

the pattern of experimental quantities prevents drawing a consistent picture of the low-lying states in ^{64}Zn within geometrical approach. Other calculations, which were performed for ^{64}Zn within a deformed configuration mixing shell model (DCM) based on intrinsic Hartree–Fock states in the $(p_{3/2}f_{5/2}p_{1/2}g_{9/2})^n$ model space, were not successful in reproducing the hindrance of the $0^+_2 \rightarrow 2+_1$ transition [300]. These calculations, however, showed that the 0^+_2 excitation is to some extent specific having a large contribution from the intruder configuration $(1g_{9/2})^2_{I=0}$.

Also in ^{66}Zn, the properties of the lowest 0^+ excitations were tried to be interpreted in the frame of the E(5) symmetry [298,299]. Indeed, the 0^+_2 and 0^+_3 states show a behavior similar to that of the 0^+_ξ and 0^+_τ states predicted by the E(5) symmetry, but other observables do not support a picture based on the geometrical model. Much richer information on the lowest 0^+ excitations in ^{66}Zn came from the recent Coulomb excitation study performed with the GALILEO array at LNL [263,301], which yielded a set of reduced E2, E3, and M1 matrix elements, allowing the extraction of more than 10 reduced transition probabilities between low-spin states and the spectroscopic quadrupole moment of the 2^+_1 state. B(E2) values were obtained for transition depopulating the excited 0^+_2 state, as well as the $\rho^2(E0;0^+_2 \rightarrow 0^+_1)$ monopole transition strength, pointing to a triaxial deformation for the 0^+_1 ground state ($\gamma = 44(8)°$) and an almost spherical character for the 0^+_2 excitation. By combining the $\rho^2(E0; 0^+_2 \rightarrow 0^+_1)$ value with the deformation parameters for the 0^+_1 and 0^+_2 states, a very small mixing between these two states was determined, indicating almost pure configurations of the wave functions of the discussed two 0^+ states. In this context, the 0^+_2 excitation appears as a distinct and isolated structure having weak connection to other low-lying states. Extensive beyond-mean-field and large-scale shell-model calculations with various model spaces and interactions were performed. These calculations predict rather diffused shapes for most of the low-lying states in ^{66}Zn

and reproduce reasonably well the excitation energies of the low-lying states, however, they predict for the 0_2^+ state a deformation similar to that of the ground state, which is not consistent with experiment.

Moving to heavier Zn isotopes, it appears that the 0_2^+ state in ^{68}Zn, similarly as in the ^{66}Zn case, decays roughly like two-phonon-type 0^+ state, i.e., by an enhanced E2 transition to the 2_1^+ state and a strongly hindered E2 transition to 2_2^+, while the 0_3^+ excitation behaves like three-phonon-type 0^+ state, i.e., its decay to the 2_1^+ state is hindered and decay to 2_2^+ is enhanced – all this in agreement with the E(5) symmetry predictions. Other observables like the E0 transition strength, however, are not compatible with the spherical-vibrator picture. For example, the $\rho_0(0_2^+ \rightarrow 0_1^+)$ in ^{68}Zn exceeds the vibrational value by a factor of 5. Also, the behavior of the 0_2^+ state in the excitation energy is not compatible with what is expected for vibrational nuclei – in ^{68}Zn the energy of the 0_2^+ state significantly decreases (see Fig. 42) in contrast to the 2_1^+, 2_2^+ and 4_1^+ states. It turned out that it is more appropriate to interpret low-lying states of ^{68}Zn (and also Zn isotopes with lower masses) as members of quasi-rotational bands. For example, based on the Coulomb excitation data [302], in ^{68}Zn, the 0_2^+ state has been suggested to be the bandhead of a structure slightly more deformed than the excitations built on the ground state, being $B(E2;2_3^+ \rightarrow 0_2^+) = 17.4(14)$ W.u. and $B(E2;2_1^+ \rightarrow 0_1^+) = 15.6(10)$ W.u. Even further decrease of the 0_2^+ energy occurs in ^{70}Zn, bringing the 0_2^+ state close to the 2_1^+ excitation (Fig. 42). Using the intermediate energy Coulomb-excitation technique, reduced transition probabilities $B(E2; 0_{g.s.}^+ \rightarrow 2_1^+)$ of 1432(124) e^{2}fm^4 and $B(E2; 0_{g.s.}^+ \rightarrow 2_2^+)$ of 53(7) e^{2}fm^4 have been determined for ^{70}Zn [303] The nonzero $B(E2;0_{g.s.}^+ \rightarrow 2_2^+)$ value confirms that ^{70}Zn cannot be considered a good vibrational nucleus, as in such scenario the excitation of the second phonon would be forbidden in first order. The beyond-mean-field calculations as well as shell-model approach point rather to the development of a triaxial shape for the ground-state band of ^{70}Zn.

Going more neutron rich, the ^{72}Zn nucleus was recently studied using multiple safe Coulomb excitation in inverse kinematics at the ISOLDE with the Miniball+C-REX detection setup [262]. The 0^+ ground state of ^{72}Zn was found to have a high degree of triaxiality with overall deformation larger in comparison to Zn isotopes with $N < 40$ – this is in agreement with beyond mean-field GCM and the shell-model calculations. In contrast, a different structure of the 0_2^+ state was indicated by a low experimental $B(E2; 0_2^+ \rightarrow 2_1^+)$ strength. According to shell-model calculations, the 0_2^+ state features a larger fraction of the spherical configuration in its wave function than the 0_1^+ ground state.

In ^{74}Zn, the existence of a rotational band, with large in-band B(E2) values, built on the 0_2^+ state, was reported in the study performed at the TRIUMF-ISAC1 facility employing the GRIFFIN γ-ray spectrometer [304]. Together with a rotational ground-state band and a gamma band related to it, these structures point to a configuration-coexistence scenario with weak mixing. The large-scale-shell model calculations which consider the pf shell for protons and the $1p_{3/2}\ 0f_{5/2}\ 1p_{1/2}\ 0g_{9/2}\ 1d_{5/2}$ orbitals for neutrons confirm this shape-coexistence picture of a triaxially deformed 0_1^+ ground state coexisting with the slightly less deformed 0_2^+ state. This difference in deformation arises from the fact that the ground state of ^{74}Zn is suggested to involve more neutron excitations across the $N = 40$ gap than the 0_2^+ state.

The investigation of low-lying excitations in Zn isotopic chain were extended to neutron-rich $^{81-84}$Zn at the RIBF facility (RIKEN) by using the BigRIPS separator and DALI2 high-efficiency gamma-ray spectrometer [305] In ^{82}Zn, the 0_2^+ state was tentatively located 269(17) keV above the 2_1^+ excitation placed at 618(15) keV. This finding, together with information on the 2^+ and 4^+ states and the comparison with shell model calculations, show that ^{78}Ni core-breaking configurations provide a significant contribution to the structure of low-lying states in the considered neutron-rich Zn nuclei.

4.3. The Z = 40 region: Kr, Sr and Zr

Fig. 51 shows the excited 0^+ states (up to 0_4^+) located experimentally in Zr, Sr and Kr nuclei. The decay properties of these states are discussed in the next Sections 4.3.1 and 4.3.2, and are summarized in Tables 14, 15, and 16.

4.3.1. The Zr and Sr isotopes

The Sr and Zr isotopes have been at the center of extensive investigations in recent years, employing a variety of experimental techniques, including detailed γ-spectroscopy studies of fission fragments, also based on isomer and β-decay spectroscopy [241]. It was found that only few excited 0^+ states exhibit a hindered E2 gamma decay in this region of nuclear chart. The list of these excitations include three states in Zr isotopes: 0_3^+ in ^{92}Zr with HF = 18, 0_4^+ in ^{96}Zr with HF = 17, and 0_4^+ in ^{98}Zr with HF = 49, as well as two states in the Sr chain: 0_4^+ in ^{88}Sr with HF = 33 and 0_3^+in ^{96}Sr with HF = 179. Three of them are located near the N = 60 isotone line, where an abrupt shape transition occurs from spherical ground states for $N < 60$, to deformed ground states in isotopes with $N \geq 60$. It has been known for quite some time that this shape transition is associated with coexistence of well isolated structures corresponding to different deformations: one is based on a spherical shape while others are constructed on deformed configurations. One can then expect that also the observed hindrance of 0^+ decays in Sr and Zr nuclei may be related to transitions between different structures that are inhibited.

The systematics of 0^+ excitations in Sr and Zr, including up to four lowest lying states, is shown in Fig. 51. For $^{88-98}$Zr and $^{90-96}$Sr nuclei, i.e., with $N < 60$, the ground states are spherical, whereas 0_2^+ and 0_3^+ excitations are believed to be oblate/triaxial and prolate, respectively. The situation changes drastically in ^{98}Sr and ^{100}Zr, where the prolate 0^+ state becomes the ground state and a strong deformation in the ground state remains in heavier Sr and Zr isotopes. A strong support for this scenario comes from various experiments, including the measurements of transition probabilities in coexisting rotational bands and spherical structures by employing the lifetime and the Coulomb excitation technique [309–311], as well as electron-scattering on ^{96}Zr [271] and a neutron scattering on ^{94}Zr [312] nuclei.

Several theory approaches were applied to describe the phenomenon of rapid change from spherical into a deformed shape at N = 60 in Sr and Zr nuclei (see Fig. 52 and Fig. 55). The quest started from mean-field calculations and went over early shell-model, up to interacting boson model and large-scale shell-model calculations [18,313–324]. Most of these models, however, could not describe the rapid shape transition satisfactorily.

Table 13
Experimental information available for 0^+ excitations in Zn isotopes (A = 62–76). See also Fig. 37 and caption of Table 8 for detailed explanations.

Nucleus	E_i [MeV]	I_i^π	$T_{1/2}$ [ps]	E_f [MeV]	I_f^π	E_γ or E_{e^-} [MeV]	BR [%]	E/Mλ	B(E/Mλ)/ρ^2(E0) [W.u.]/[m.u.]	HF	Refs.
^{60}Zn	3.504(1)	0_2^+		1.004	2_1^+	2.500	100.0	[E2]			[306]
^{62}Zn	2.342	0_2^+		0.954	2_1^+	1.388	100.0	[E2]			[67,220,307]
	3.046	0_3^+		0.954	2_1^+	2.093	100.0	[E2]			
	4.008[a]	0_5^+		1.805	2_2^+	2.204	100.0	[E2]			
^{64}Zn	1.910	0_2^+	$0.950(50)\times10^3$	1.799	2_2^+	0.111	3.3	[E2]	76(24)	0.066	[33,67,298]
				0.992	2_1^+	0.919	96.1	E2	0.057(3)	88	
				0.0	0_1^+	1.910	0.6	E0	3.7(4)		
	2.610	0_3^+	0.20(8)	1.799	2_2^+	0.809	<0.5	[E2]	<4.5	>1.1	
				0.992	2_1^+	1.618	99.5	E2	$17(^{+11}_{-5})$	0.29	
				0.0	0_1^+	2.610	0.003	E0	$16(^{+7}_{-6})$		
^{66}Zn	2.372	0_2^+	2.8(10)[b]	1.873	2_2^+	0.500	0.4	E2	1.6(6)	3.1	[33,67,263,298]
				1.039	2_1^+	1.333	99.6	E2	3.0(10)	1.7	
				0.0	0_1^+	2.372	0.01	E0	$2.5(^{+7}_{-19})$		
	3.105	0_4^+		1.873	2_2^+	1.232	94.1	[E2]			
				1.039	2_1^+	2.066	5.8	[E2]			
				0.0	0_1^+	3.105	0.02	E0			
	3.532	0_5^+		1.039	2_1^+	2.492	100.0	[E2]			
	3.825	0_6^+		1.039	2_1^+	2.786	100.0	[E2]			
^{68}Zn	1.656	0_2^+	96(16)	1.077	2_1^+	0.579	100.0	E2	5.5(10)	0.91	[33,67,298]
				0.0	0_1^+	1.659(7)	0.042	E0	5.1(13)		
	3.103	0_3^+		1.833	2_2^+	1.219	97.1	[E2]			
				1.077	2_1^+	2.025	≤2.9	[E2]			
^{70}Zn	1.071	0_2^+	$3.90(20)\times10^3$	0.885	2_1^+	0.186	99.7	[E2]	37.3(19)	0.13	[33,67]
				0.0	0_1^+	1.067	<0.3	E0	1.9(12)		
	2.141	0_3^+		0.885	2_1^+	1.256	100.0	[E2]			
^{72}Zn	1.511	0_2^+	$6.2(^{+39}_{-10})$[c]	0.653	2_1^+	0.858	100.0	[E2]	$11(^{+3}_{-5})$	0.45	[67,262]
^{74}Zn	1.789	0_2^+		0.606	2_1^+	1.183	100.0	E2			[67,304,308]
^{82}Zn	0.987(23)	(0_2^+)		0.618(15)	(2_1^+)	0.369(17)	100.0				[305]

[a] Reported at 3.936(6) MeV in (p,t) study of Ref. [307];
[b] From B(E2), Coulomb excitation study [263];
[c] From B(E2), Coulomb excitation study [262];
Additional 0^+ states from β decay and (^{3}He,n), (^{3}He,d), (d, ^{3}He), (p,t), (t,p) reaction studies (no γ-decay reported) [67,307]:
^{60}Zn; 0_3^+: 7.380(30) MeV;
^{62}Zn; $0_{4,6}^+$, (0_7^+), 0_8^+: 3.862(2), 4.552(9), 5.240(20), 5.340(30) MeV;
^{64}Zn; $(0_{4,5}^+)$: 3.240(20), 4.470(3) MeV;
^{66}Zn; (0_3^+), 0_7^+: 3.030, 4.511(5) MeV;
^{68}Zn; 0_4^+: 4.148(7) MeV;
^{70}Zn; (0_4^+), 0_5^+: 3.328(5), 3.680(5) MeV;
^{72}Zn; 0_3^+: 2.476(10) MeV.

4.3.1.1. Zr isotopes. In the Zr isotopes, a rapid change of nuclear structure, as a function of the number of neutrons, can be observed by inspecting the level schemes displayed in Fig. 53. A significant progress in describing these evolution came from the development of a new shell model calculation scheme, i.e., the advanced version of MCSM, which, recently, reached the capability of being applied to calculate the structure of Zr nuclei [52,273] (see Fig. 52). These new MCSM calculations, relying on the use of a very large configuration space, were able to reproduce correctly the evolution of nuclear structure in Zr isotopes with 50≤N≤70, including the abrupt change in deformation of the ground states when passing from ^{98}Zr to ^{100}Zr [107]. Fig. 54(a) taken from Togashi et al. [107] shows the properties of $0_{1,2}^+$ states. The 0_1^+ ground state remains spherical up to N = 58, and becomes prolate at N = 60. The nature of the second 0_2^+ state changes along the isotopic chain, being spherical in ^{90}Zr, oblate in ^{92,94}Zr, triaxial-deformed in ^{96}Zr, prolate in ^{98}Zr and oblate in ^{100}Zr. In ^{100}Zr, a spherical state, which was ground state at N < 60, appears as the 0_4^+ state. Fig. 54(b) displays B(E2; $2_1^+ \rightarrow 0_1^+$) values – they are small up to N = 58 and increase sharply at N = 60, what is consistent with experiment [325–327]. In addition, theoretical and experimental transition probabilities for the lowest transitions in rotational bands built on the 0_2^+, B(E2; $2_2^+ \rightarrow 0_2^+$), also nicely agree for ^{94}Zr and ^{96}Zr.

The analysis of details of the MCSM approach was instrumental in finding that responsible for the reorganization of the shell structure at N = 60 is so called *Type II shell evolution*, which relies here on a large energy lowering of configurations involving the excitation of protons to the $0g_{9/2}$ orbital and neutrons to the $0g_{7/2}$, due to the tensor and central forces acting coherently.

The advanced MCSM calculations explain a few specific experimental results which regard ^{96}Zr and ^{98}Zr and are of interest here. In ^{96}Zr, the first excited state is 0_2^+ at 1582 keV and it decays toward 0_1^+ via a well known E0 transition. In the work of Kremer et al. [271], performed at the S-DALINAC in Darmstadt with inelastic electron scattering, it was found that this 0_2^+ excitation is connected to the 2_2^+ state located just above it, at 2226 keV, via an E2 transition with large E2 transition probability B(E2) = 36(11)

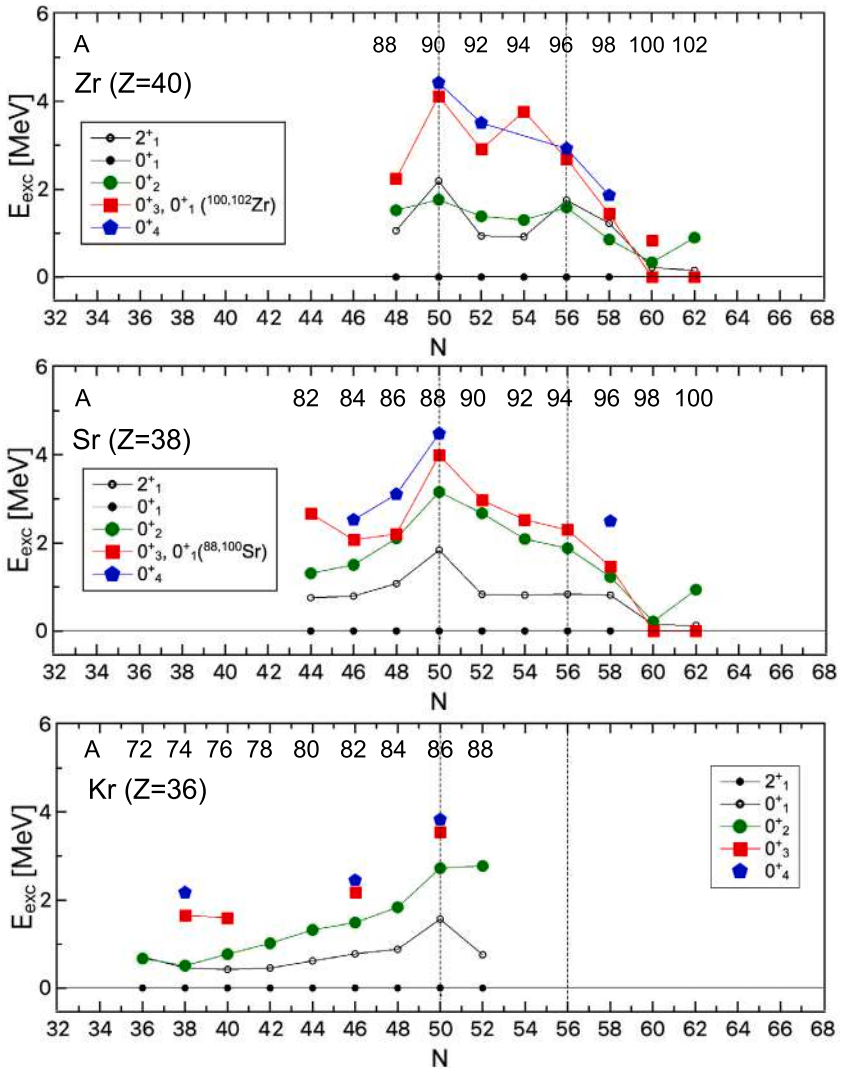

Fig. 51. Survey of 0^+ states (up to 0^+_4) observed in the Z = 36, 38 and 40 nuclei of Kr, Sr and Zr. The first 2^+ excitation is also given as a reference (open circles). Dashed lines mark the N = 50 and 56 neutron shell closures. In the case of Sr and Zr, the 0^+_3 excitation (red squares) is predicted to be prolate and becomes the ground state at N = 60 (see Tables 16, 15, 14 for details).

W.u. This is in contrast to the low value of probability for transition between 2^+_1 and 0^+_1, B(E2) = 2.3(3) W.u. A hypothesis was then put forward that 2^+_2 state is the second member of the collective rotational band built on the 0^+_2 band head, while the 0^+_1 ground state and 2^+_1 excitations are spherical.

Such a scenario is fully supported by MCSM: the wave function of both the 0^+_2 and 2^+_2 excitations are well localized in the triaxial minimum in the PES and the predicted B(E2;$2^+_2 \rightarrow 0^+_2$) = 36.7 W.u. agrees excellently with the experimental value. Further, the measured very low probability of the transition $2^+_2 \rightarrow 0^+_1$, B(E2) = 0.26(8) W.u. is in accord with the MCSM, what confirms that the 2^+_2 and 0^+_2 states, lying in a deformed PES minimum, are well isolated from the spherical minimum where the 0^+_1 and 2^+_1 states reside. Significant separation of the structures located in the two different PES minima is supported by the low experimental value of the E0 $0^+_2 \rightarrow 0^+_1$ transition strength, ρ^2(E0) = 7.5 m.u. Detailed microscopic calculations are needed to elucidate the observed hindrance of 0^+_4 decay, HF = 16.7.

In ^{98}Zr, the situation is very similar. The first excited state is again the 0^+_2 excitation which decays to 0^+_1 via an E0 transition with a small ρ^2(E0) = 11.2 m.u., suggesting that the wave functions of 0^+_1 and 0^+_2 are rather well separated and do not mix. Unlike ^{96}Zr, here the first excited state 2^+_1 is not related to the structure of the ground state 0^+_1, but belongs to the structure built on the 0^+_2 excitation.

This hypothesis is supported by the rather collective value of B(E2; $2^+_1 \rightarrow 0^+_2$) measured, using the plunger technique, by Singh et al. with EXOGAM+VAMOS in GANIL, as 28.3(64) W.u. [309], and by Karayonchev et al. at the Cologne Tandem, as $11(^{+3}_{-2})$ [328].

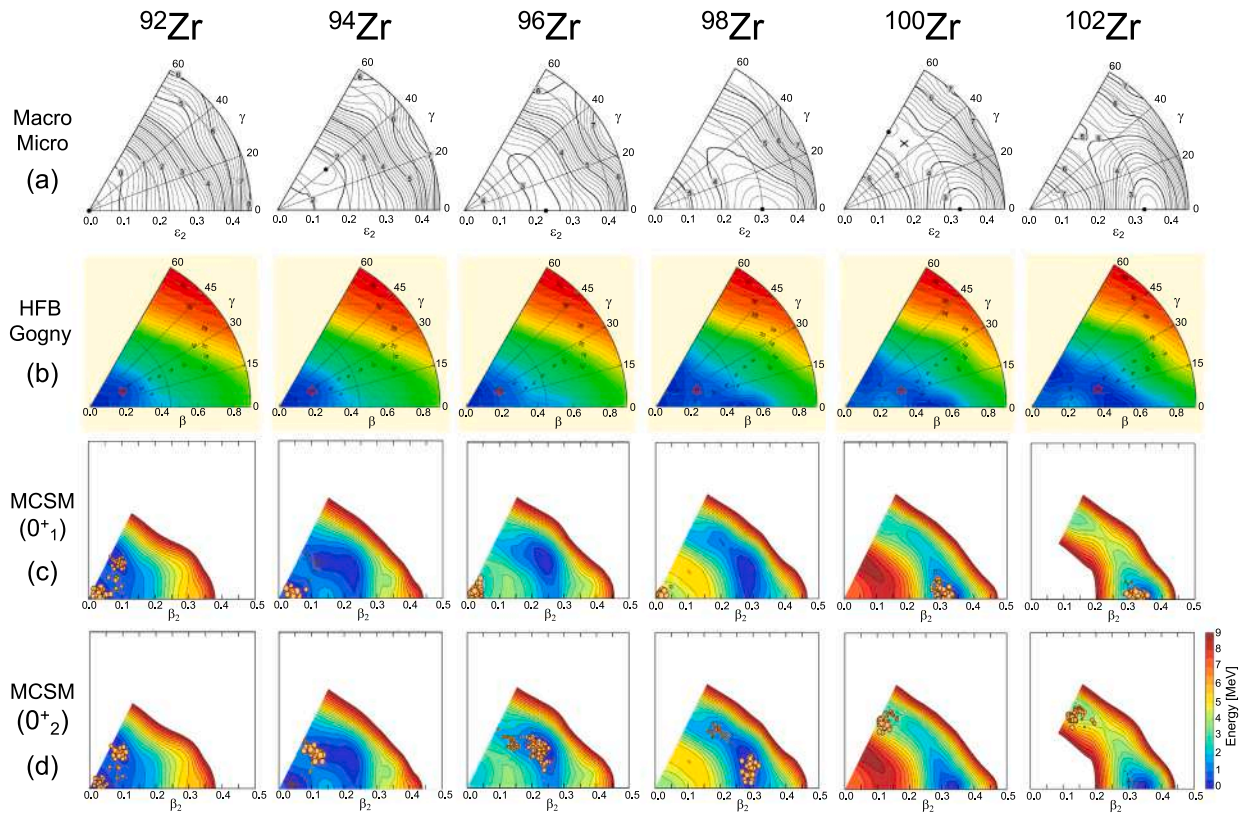

Fig. 52. Potential energy surfaces for even–even $^{98-102}$Zr obtained from different type of calculations: (a) macroscopic–microscopic mean field model of Moeller et al. [59], (b) Hartree–Fock–Bogoliubov calculations based on the Gogny force, by S. Hilaire and M. Girod [198,249], and (c) Monte Carlo Shell Model Hamiltonian by Togashi et al. [107], with circles showing the main component of the 0^+_1 state, and (d) with circles showing the main component of the 0^+_2 state wavefunction. Energies (in MeV) are given on the contour plots in (a)–(b), and by common color scale in (c)–(d).
Source: Adapted from [59,250].

The large B(E2) values of B(E2; $4^+_1 \rightarrow 2^+_1$) and B(E2;$4^+_1 \rightarrow 2^+_2$), which were measured by Singh et al. as 43.3(8.7) and 67.5(13.5) W.u., and by Karayonchev et al. as $25(^{+15}_{-7})$ and $38(^{+26}_{-13})$ W.u., respectively, as well as the results B(E2;$6^+_1 \rightarrow 4^+_1$) = 103(36) W.u. (Singh et al.) (Fig. 53), suggest the existence of a deformed, band-like structures in ^{98}Zr. Two scenarios were proposed to accommodate these experimental data:*(i)* the four states: 0^+_3, 2^+_2, 4^+_1 and 6^+_1 form a well-deformed rotational band based on the 0^+_3 state, while the 0^+_2 and 2^+_1 are the lowest members of another moderately deformed structure built on the 0^+_2. In such case, a large value of B(E2; $4^+_1 \rightarrow 2^+_1$) = 43.3 W.u. would indicate a significant mixing of the well-deformed structure with the deformed configuration based on the 0^+_2 excitation. *(ii)* The collective band consists of 0^+_2, 2^+_1, 4^+_1 and 6^+_1 states, while the 0^+_3 and 2^+_2 states are not involved.

The MCSM calculations fully support the proposed triple shape coexistence scenario in ^{98}Zr with a spherical 0^+_1 state, a prolate deformed 0^+_2 state, and a triaxial 0^+_3 state. The collectivity of the bands built on the 0^+_2 and 0^+_3 states is well reproduced: B(E2; $2^+_1 \rightarrow 0^+_2$) = 70 W.u. and B(E2; $4^+_1 \rightarrow 2^+_2$) = 76 W.u., B(E2; $6^+_1 \rightarrow 4^+_2$) = 87 W.u. However, the MCSM calculations do not predict correctly the strong mixing of the two bands, giving B(E2; $4^+_1 \rightarrow 2^+_1$) < 1 W.u. The E2 decay from the higher lying 0^+_4 state is hindered and to interpret this delay MCSM calculations for this state are needed.

The second scenario is more in line with a theoretical approach based on the interacting boson model with configuration mixing (IBM-CM) [329,330], which was recently used to describe the properties of low-lying structures in the even–even Zr chain of isotopes. In this model, the normal A-configuration is associated with only neutron boson pairs and no active protons above Z = 40 sub-shell gap (i.e, proton bosons number equals 0), while the intruder B-configuration corresponds to two-proton excitation from below to above this gap, creating (2p-2h) states, for which the proton bosons number is 1. In particular, for ^{98}Zr, most of the low-lying states, which are shown in Fig. 53, have an intruder character with the number of neutron and proton bosons of 4 and 1, respectively. Specifically, the experimental groups of states, (0^+_2), (2^+_1), (0^+_3, 2^+_2, 4^+_1), (0^+_4, 2^+_4, 3^+_1, 4^+_3, 6^+_1), correspond to calculated excitations

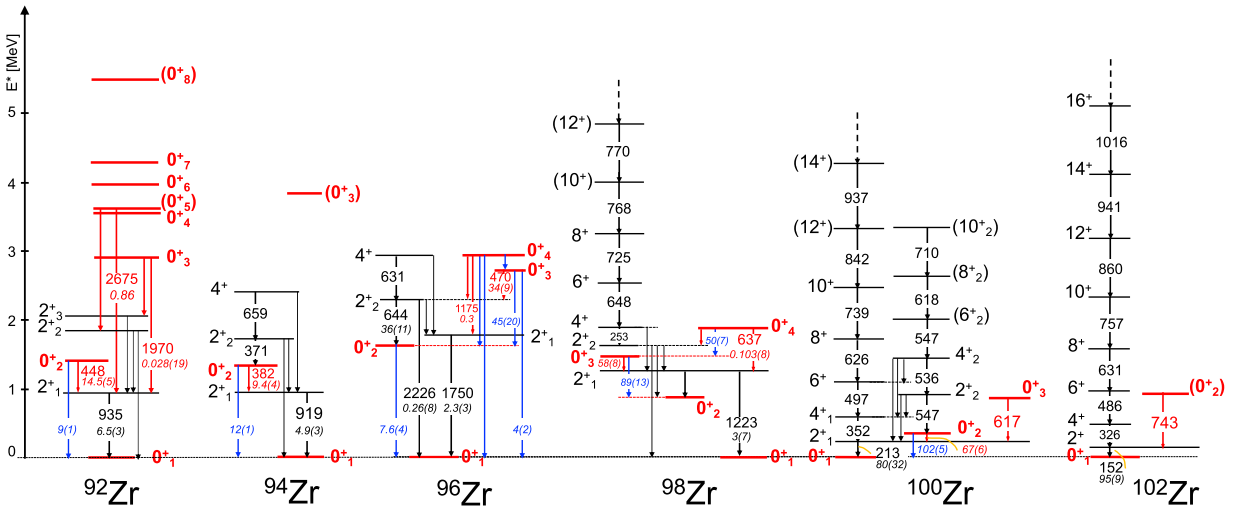

Fig. 53. Partial level schemes of ^{92,94,96,98,100}Zr [67]. The γ decay of 0^+ states is highlighted in red, with red and blue arrows indicating measured γ and E0 decay from 0^+ states, with energies in keV and B(E2) and ρ^2(E0) values in W.u. and m.u., respectively (in italic). Dashed arrows indicate the continuation of a band to higher spins (see Table 14 for details).

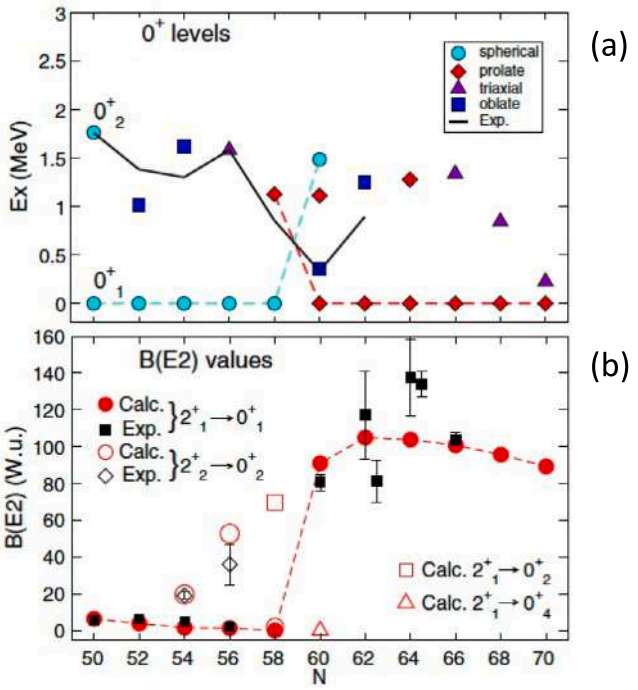

Fig. 54. Panel (a): 0^+ levels of Zr isotopes as a function of the neutron number N. Solid line for experimental data [67], symbols for theoretical results from MCSM calculations of Togashi et al. [107], with the shape classification as shown in the legend. Dashed lines connect relevant results to guide the eye. Panel (b): B(E2;$2^+ \to 0^+$) values as a function of N. Experimental data from [271] (and references therein [67,220]) are compared with MCSM results.
Source: Adapted from [107].

dominated by order parameters $n_d \sim 0$, 1, 2 and 3, respectively. Only the 0^+_1 and 2^+_3 states are calculated in the IBM-CM as single-particle excitations, which are mostly outside the IBM model space. In this approach, the band consisting of 0^+_2, 2^+_1, 4^+_1 and 6^+_1 states, is explained as a sequence of states associated with different order parameters n_d and, as such, connected with enhanced E2 transitions. The model reproduces well the measured low B(E2; $0^+_4 \to 2^+_1$) = 0.103(8) W.u., giving for it the value of 0.045 W.u. It fails, however, in predicting the experimental high strength of the $4^+_1 \to 2^+_2$ E2 transition, by providing for it a very small number B(E2; $4^+_1 \to 2^+_2$) = 1.67 W.u. One should note that another independent IBM-CM calculation on ^{98}Zr [331], that was recently carried

Table 14
Experimental information available on 0^+ excitations in Zr isotopes (A = 88–102), see also Figs. 51 and 53, and caption of Table 8 for detailed explanations.

Nucleus	E_i [MeV]	I_i^π	$T_{1/2}$ [ps]	E_f [MeV]	I_f^π	E_γ or E_{e^-} [MeV]	BR [%]	E/Mλ	B(E/Mλ)/ρ^2(E0) [W.u.]/[m.u.]	HF	Refs.
^{88}Zr	1.521	0_2^+		0.0	0_1^+		0.05	(E0)			[67]
				1.057	2_1^+	0.465	100.0	[E2]			
^{90}Zr	1.761	0_2^+	61.3(25) 10^3	0.0	0_1^+	1.761		E0	3.52(23)		[33,67]
	4.124	0_3^+		2.186	2_1^+	1.938	100.0	[E2]			
	4.426	0_4^+	0.20($^{+24}_{-8}$)	2.186	2_1^+	2.240	100.0	[E2]	2.1($^{+15}_{-11}$)	2.4	
^{92}Zr	1.383	0_2^+	88(3)	0.0	0_1^+	1.383	0.2	E0	8.5(10)		[33,67]
				0.935	2_1^+	0.448	99.8	E2	14.4(5)	0.35	
	2.904	0_3^+	0.83($^{+57}_{-24}$)	0.935	2_1^+	1.970	30.6	E2	0.28($^{+9}_{-20}$)	18	
				2.067	2_3^+	0.837	69.4	[E2]	47	0.11	
	3.610	(0_5^+)	0.151($^{+26}_{-23}$)	0.935	2_1^+	2.675	77.5	[E2]	0.9	5.8	
				1.847	2_2^+	1.762	22.5	[E2]	2	2.5	
^{94}Zr	1.300	0_2^+	291(11)	0.0	0_1^+	1.300	0.4	E0	11.7(14)		[33,67]
				0.919	2_1^+	0.382	99.6	[E2]	9.4(4)	0.53	
^{96}Zr	1.582	0_2^+	38.0(7) 10^3	0.0	0_1^+	1.582		E0	7.6(4)		[33,67]
	2.695	0_3^+	28(7)	0.0	0_1^+	2.695	0.0030	E0	4.3($^{+22}_{-24}$)		
				1.582	0_2^+	1.114	0.018	E0	45($^{+19}_{-20}$)		
				2.226	2_2^+	0.470	100.0	[E2]	34(9)	0.15	
	2.926	0_4^+	20(14)	0.0	0_1^+	2.926		E0			
				1.582	0_2^+	1.344		E0			
				1.750	2_1^+	1.175	71.4	(E2)	0.3	17	
				2.226	2_2^+	0.700	28.6	(E2)	1.8	2.8	
				2.695	0_3^+	0.230		E0			
^{98}Zr	0.854	0_2^+	64(7) 10^3	0.0	0_1^+	0.854	100.0	E0	11.1(13)		[33,67,332]
	1.436	0_3^+	0.72(8) 10^3	0.854	0_2^+	0.582	6.2	E0	89(13)		
				1.223	2_1^+	0.213	93.8	E2	58(8)	0.086	
	1.859	0_4^+	290(13)	1.223	2_1^+	0.637	15.1	E2	0.103(8)	49	
				1.436	0_3^+	0.423	1.3	E0	50(7)		
				1.591	2_2^+	0.269	83.6	E2	42(3)	0.12	
^{100}Zr	0.331	0_2^+	5.53(15) 10^3	0.0	0_1^+	0.331	43.2	E0	102(5)		[33,67]
				0.213	2_1^+	0.119	56.8	E2	67(6)	0.075	
	0.829	0_3^+		0.213	2_1^+	0.617	100.0	[E2]			
^{102}Zr	0.895	(0_2^+)		0.152	2_1^+	0.743	100.0				[67]

Additional 0^+ states from β-decay and (p,t), (t,p), (d,d′) reaction studies (no γ-decay reported) [67]:
^{88}Zr; 0_3^+, (0_4^+): 2.231, 3.430 MeV;
^{90}Zr; 0_5^+: 5.441(5) MeV;
^{92}Zr; 0_4^+, $0_{6,7}^+$, (0_8^+): 3.589(10), 3.992(10), 4.283(10), 5.490 MeV;
^{94}Zr; (0_3^+): 3.776(7) MeV.

out, managed to describe adequately the empirical B(E2; $4_1^+ \rightarrow 2_1^+$) and B(E2; $4_1^+ \rightarrow 2_2^+$) rates, but it leads to large discrepancies for other transition probabilities [328].

In view of the above considerations, it is of great interest to establish the rate of the $2_2^+ \rightarrow 0_3^+$ E2 transition as the two models predict very different values in this case. The MCSM, considering this transition as the lowest one in the well-deformed rotational band based on the 0_3^+ excitation, calculates for it the value of 49 W.u. The IBM-CM approach views this transition as the one connecting two states characterized by the same order parameter $n_d = 2$ (members of the two-quasiphonon triplet), what results in a low calculated value of 6.54 W.u.

4.3.1.2. Sr isotopes. An evolution of the nuclear structure as a function of the number of neutrons, similar to the one observed in the Zr nuclei, was found in the Sr isotope chain (see Fig. 55 and Fig. 56). First of all, an abrupt transition from spherical to deformed ground states occurs at N = 60, i.e., in ^{98}Sr [333]. This shape transition is accompanied by the presence of deformed low-lying 0^+ excited states for N < 60 which become the ground state at N > 60. On the contrary, the spherical ground-state configuration of the isotopes with N < 60 becomes higher lying for those with N ≥ 60. Of particular interest are the ^{96}Sr and ^{98}Sr nuclei adjacent to opposite sides of the sphere-deformation boundary.

In ^{96}Sr, two low-lying 0^+ states were located by Jung et al., [334] just above the 2_1^+, at 1229 and 1465 keV, and interpreted as candidates for a deformed band head. These two 0^+ excitations are connected with a highly enhanced electric monopole transition ρ^2(E0) = 185(50) m.u., which indicates mixing of the configurations with distinctly different deformations. In contrast, the E0 decays of the 0_2^+, and 0_3^+ states to the ground state have not been observed. The 0_3^+ state decays to the 2_1^+ excitation by a strongly hindered E2 transition, HF = 179.

In order to shed more light on nuclear shapes associated with the individual states and the corresponding wave functions, including, first of all, those of the 0^+ excitations, ^{96}Sr and ^{98}Sr isotopes were investigated by safe Coulomb excitation of radioactive beams with MINIBALL at ISOLDE [310,311]. Using the method of quadrupole invariants, a rather small quadrupole deformation

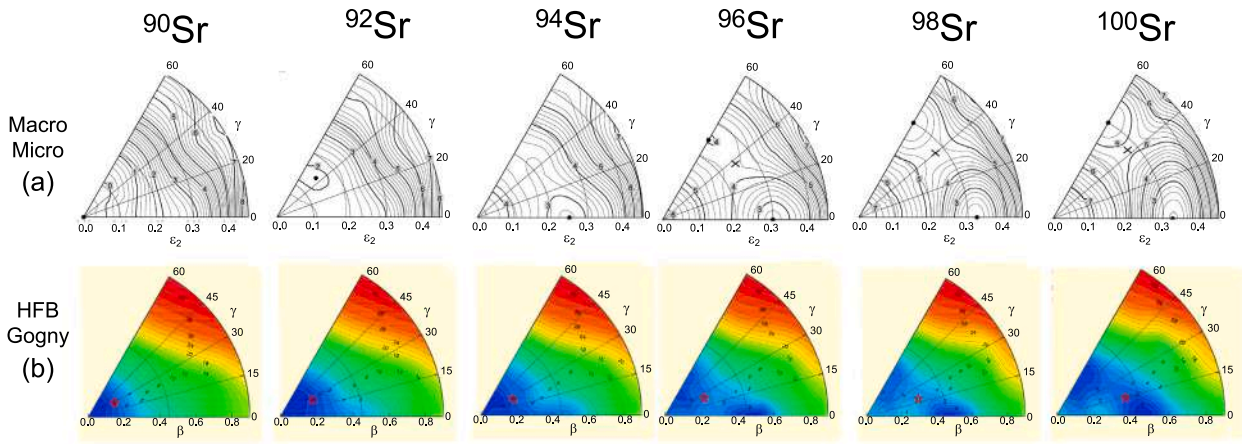

Fig. 55. Potential energy surfaces for even–even $^{90-100}$Sr obtained from different type of calculations: (a) macroscopic–microscopic mean field model of Moeller et al. [59], and (b) Hartree–Fock–Bogoliubov calculations based on the Gogny force, by S. Hilaire and M. Girod [198,249].
Source: Adapted from [59,250].

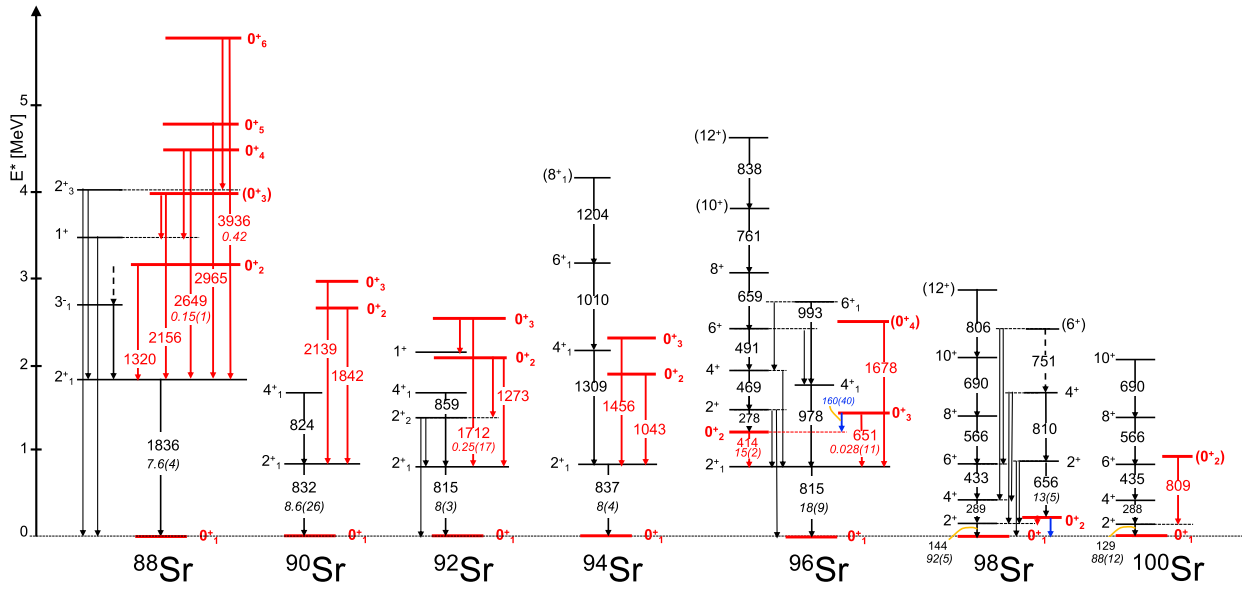

Fig. 56. Partial level schemes of ^{88,90,92,94,98}Sr [67,335]. Excited 0^+ states are highlighted in red, with red and blue arrows indicating measured γ and E0 decay from 0^+ states, with energies in keV and B(E2) and ρ^2(E0) values in W.u. and m.u., respectively (in italic). Dashed arrows give tentative transitions. See also Table 15 for details.

was deduced from the measurements for the ground state 0^+_1 in ^{96}Sr ($\langle Q^2 \rangle$ = 0.22(4) e^{2}b^2) – this indicates its close to spherical character. Also, the spectroscopic quadrupole moment obtained for the 2^+_1 state, $Q_s = -22(^{+33}_{-31})$ efm^2, is compatible with zero. In addition, analysis of the Coulomb data performed for ^{98}Sr, which is described further, showed that one may also expect significant triaxiality for the ground state of ^{96}Sr.

Recently, the 0^+ states in ^{96}Sr were studied at TRIUMF using the SHARC and TIGRESS arrays in a (d,p) reaction employing a ^{95}Sr radioactive beam [336]. The 0^+_1, 0^+_2, and 0^+_3 states were populated with spectroscopic factors of C^2S = 0.19(3), 0.22(3), and 0.33(12). Since the ground state of ^{95}Sr has a nearly spherical shape [337], it can be assumed that in this experiment there is a fairly strong direct population of spherical states and a rather small population of deformed configurations. The low value of C^2S for the 0^+_1 ground state was interpreted as possible evidence for its weakly oblate or triaxial shape. The larger transfer strength to the 0^+_2 and 0^+_3 states indicated that their wave functions can contain a sizeable amount of spherical configurations. To reconcile the transfer reaction data with the deformation of the excited 0^+ states evidenced through the presence of rotational bands, a two-level shape mixing model was applied. The 0^+_1 was not considered as a third partner in this analysis as its mixing with the 0^+_2 and 0^+_3 should be

negligible in agreement with nonobservation of the E0 transitions connecting the ground state with the higher lying ones. Assuming that the transfer reaction d(^{95}Sr,p)^{96}Sr populates only spherical components of the 0^+_2 and 0^+_3 wave functions, and considering that the E0 transition strength between those states is ρ^2(E0) = 185(50) m.u., it was calculated that the spherical component in the 0^+_2 state amounts to 40(14)% and the deformation parameter β_{def} for the deformed component is 0.31(3).

A picture of the ^{96}Sr nucleus which emerges seems to show a triple shape coexistence which is reflected in a weakly deformed triaxial 0^+ ground state and two excited 0^+ states arising from a strong mixing of a deformed and spherical configurations. The large mixing of deformed and spherical shapes evidenced for the 0^+_2 and 0^+_3 excitations would imply that both these states decay toward the 2^+_1 state via an E2 transition of similar strength. However, the corresponding transition probabilities are 15.3 W.u. and 0.028 W.u., which casts some doubts on the present understanding of the 0^+_2 and 0^+_3states character. In a recent paper, Urban et al. exploiting large data sets from neutron-induced fission on ^{235}U and spontaneous fission of ^{252}Cf, collected at ILL with EXILL and ANL with GAMMASPHERE, observed a 277.7-keV E2 decay from 2^+_2 into the 0^+_2 state in ^{96}Sr, which completes the deformed band based on this 0^+ excitation. A lower limit of B(E2) ≥ 38(8)W.u. is proposed for the rate of the 277.7-keV transition, which supports a moderate collectivity for the deformed band on top of the 0^+_2 level [338].

Turning now to ^{98}Sr, in this nucleus the ground-state band has a rotational character what is consistent with a deformed shape of the ground state. The first excited 0^+ state, was identified at very low excitation energy of 215 keV [339] and suggested to be the lowest member of the spherical structure, which just interchanged with the deformed one when moving from ^{96}Sr to ^{98}Sr.

As mentioned earlier, the nature of the low-lying states in ^{98}Sr, including all those of the 0^+ excitations, was investigated by safe Coulomb excitation of radioactive beams at ISOLDE [310,311]. First of all, in these investigations, a large change in spectroscopic quadrupole moments between the ground state ($\langle Q^2\rangle$ = 1.30(4) e^{2}b^2) and the low-lying 0^+_2 state ($\langle Q^2\rangle$ = 0.33(3) e^{2}b^2) was found, consistent with the large deformation established for the 2^+_1 state (a member of the ground state rotational band) and a small one observed for the 2^+_2 excitation (belonging to the spherical structure). In addition, one can note that the deformation of the ground state in ^{96}Sr and that of the 0^+_2 state in ^{98}Sr are similar, supporting the scenario in which these two configurations exchange with each other at $N = 60$.

The triaxiality parameter was also extracted from the Coulomb excitation data for both 0^+_1 and 0^+_2 states in ^{98}Sr, independent of the large difference between the quadrupole deformation between them. It suggests a non-axially symmetric prolate shape, with the deformation parameter γ equals to 21° and 23° respectively. In view of the similarity between the 0^+_2 state in ^{98}Sr and the 0^+_1 ground state in ^{96}Sr, one might also expect significant triaxiality for the ground state in ^{96}Sr. Since triaxiality often leads to the mixing of wave functions, an attempt was made to assess the mixing between deformed and spherical configurations present in the lowest states of ^{98}Sr. A phenomenological two band mixing model was applied and measured E2 matrix elements were used [311]. The results support the weak mixing scenario (of ∼10%) between prolate and spherical configurations in the wave functions of the 0^+ states in ^{98}Sr, in spite of their proximity in energy. This scenario is also supported by independent measurements of E0 monopole strength, performed at TRIUMF, which point to a mixing of approximately 8.6% and 1.3% between the two low-lying 0^+ states and, separately, 2^+ lowest excitations, corresponding to deformation parameters β_2 = 0.38(1) and −0.23(2), respectively, for the deformed prolate and the spherical/oblate structure [340]. A band-like structure built on 0^+_2 has been also observed in ^{98}Sr data from spontaneous fission of ^{248}Cm and ^{252}Cf, measured with the EUROGAM2 and GAMMASPHERE arrays [335]. The band is clearly of non-rotational nature, and very different from the ground state band. The situation is very similar to what observed in ^{100}Zr, where all levels from the side band built on 0^+_2 decay to states of the ground-state band, although the mixing is not very strong, thus pointing to a similarity of these two structures in ^{98}Sr and ^{100}Zr.

In order to interpret the experimental results for the ^{96}Sr and ^{98}Sr isotopes, beyond-mean-field calculations using the Gogny D1S interaction in a five-dimensional collective Hamiltonian (5DCH) formalism [249,341–343] were performed. The very small value of spectroscopic quadrupole moment Q_s = −5.6 e fm^2, calculated for the 2^+_1 state in ^{96}Sr, is in agreement with experimental value of $-22(^{+33}_{-31})$ e fm^2. However, the calculated B(E2; $2^+_1 \rightarrow 0^+_1$) = 32 W.u. and B(E2; $0^+_2 \rightarrow 2^+_1$) = 58 W.u. are significantly higher than the experimental values of 17.1 and 15.3 W.u., respectively. No model prediction was presented for the reduced $0^+_3 \rightarrow 2^+_1$ transition probability, which is very low, B(E2;$0^+_3 \rightarrow 2^+_1$) = 0.028.

4.3.2. The Kr isotopes

Even though in neutron deficient Kr isotopes no excited 0^+ states exhibiting a hindered E2 γ decay were found, these species demonstrate very interesting properties related to the fact that oblate and prolate shapes coexist within a narrow energy range of a few hundred keV and the corresponding states are very strongly mixed – the case corresponds to the scheme illustrated in Fig. 9(f). This shape-coexistence and shape-mixing scenario was inferred from: *(i)* the moments of inertia of the ground-state bands in $^{72-76}$Kr which were observed to be perturbed at low spin, (ii) the reduced collectivity of transition probabilities at low spin, (iii) the energies of the 0^+_2 states, which, after decreasing in energy from ^{78}Kr, become isomeric, low-lying states in ^{74}Kr [19,20] and ^{72}Kr [346], as measured at the Vivitron in Strasbourg and at LISE in GANIL, *(iv)* the E0 strengths for transitions to the ground states having a maximum of 96(9) m.u. in ^{74}Kr, *(v)* the identification of the 0^+_2 state in ^{72}Kr as the band head of the known prolate rotational structure, which supports oblate-shape assignment to ground state in ^{72}Kr [346], (vi) the measurement of the absolute B(E2; $0^+_1 \rightarrow 2^+_1$) excitation strength in ^{72}Kr, performed at MSU, which is consistent with the oblate ground state deformation [347] (^{72}Kr is one of the very few nuclei having oblate ground state), *(vii)* Coulomb excitation experiments, performed at GANIL, from which for ^{76}Kr a purely prolate shape for the 0^+_1 state and a triaxial-oblate shape for the 0^+_2 state were established, while for ^{74}Kr a triaxial-prolate shape for the 0^+_1 state and maximum triaxiality for the 0^+_2 state were indicated [348]. A picture has then emerged of the shape transition from a prolate ground state, that coexists with an excited oblate configuration in the $^{74-78}$Kr isotopes, to an oblate ground state in ^{72}Kr coexisting, in turn, with a prolate excited structure.

Table 15
Experimental information available on 0^+ excitations in Sr isotopes (A = 82–100), see also Figs. 51 and 56, and caption of Table 8 for detailed explanations.

Nucleus	E_i [MeV]	I_i^π	$T_{1/2}$ [ps]	E_f [MeV]	I_f^π	E_γ or E_{e^-} [MeV]	BR [%]	E/Mλ	B(E/Mλ)/ρ^2(E0) [W.u.]/[m.u.]	HF	Refs.
^{82}Sr	1.311	0_2^+	<3.5 10^3	0.574	2_1^+	0.737	100.0	[E2]	>0.035	<142	[67]
^{84}Sr	1.504(1)	0_2^+		0.793	2_1^+	0.709	100.0	E2			[67,344]
	2.072	0_3^+		0.793	2_1^+	1.278	100.0	E2			
				1.454	2_2^+	0.671[a]		[E2]			
^{86}Sr	2.103	0_2^+		1.077	2_1^+	1.027	100.0	E2			[67,344]
	2.202	0_3^+		1.077	2_1^+	1.125	100.0	E2			
^{88}Sr	3.156	0_2^+	1.5($^{+8}_{-4}$)	1.836	2_1^+	1.320	100.0	E2	4.0($^{+15}_{-14}$)	1.3	[67]
	3.992	(0_3^+)	>0.48	1.836	2_1^+	2.156	13.3	[E2]	<0.14	>36	
				3.487	1_1^+	0.506	86.7	M1	<0.31		
	4.484	0_4^+	0.097(7)	1.836	2_1^+	2.649	7.9	[E2]	0.152(13)	33	
				3.487	1_1^+	0.998	92.1				
	4.801	0_5^+	0.016(5)	1.836	2_1^+	2.965	100.0	[E2]	6.6(21)	0.76	
	5.772	0_6^+	0.025(11)	4.036	2_4^+	1.737	59.2	[E2]	36(18)	0.14	
				1.836	2_1^+	3.936	40.8	[E2]	0.42(21)	12	
^{90}Sr	2.674	0_2^+		0.832	2_1^+	1.842	100.0	[E2]			[67,338]
	2.971	0_3^+		0.832	2_1^+	2.139	100.0	E2			
^{92}Sr	2.088	$0_2^{(+)}$		0.815	2_1^+	1.273	68	(E2)			[67,338]
				1.385	2_2^+	0.704	32	(E2)			
	2.527	0_3^+	6(4)	0.815	2_1^+	1.712	94.5	E2	0.25(17)	20	
				2.141	1_1^+	0.386	5.5	(M1)	0.0035(25)		
^{94}Sr	1.880	0_2^+		0.837	2_1^+	1.043		[E2]			[345]
	2.293	0_3^+		0.837	2_1^+	1.456		[E2]			
^{96}Sr	1.229	0_2^+	115(12)	0.815	2_1^+	0.414	100.0	E2	15.3(16)	0.33	[33,67,310,338]
	1.465	0_3^+	6.7(19) 10^3	0.815	2_1^+	0.651	99.4	E2	0.028(11)	179	
				1.229	0_2^+	0.235	0.6	E0	16(4)×10		
	2.493	(0_4^+)		0.815	2_1^+	1.678		(E2)			[338]
^{98}Sr	0.216	0_2^+	22.9(17) 10^3	0.0	0_1^+	0.216	44.8[b]	E0	69(7)		[33,67,310,340]
				0.145	2_1^+	0.071	55.2[b]	E2	62($^{+7}_{-6}$)	0.08	
^{100}Sr	0.938	(0_2^+)		0.129	2_1^+	0.809	100.0				[67]

[a] Reported in ^{84}Y ϵ decay (4.6(2) s) [67];

[b] From total intensity of γ and conversion electrons [67];

Additional 0^+ states from β-decay and (p,t), (t,p), (^{3}He,n), (p,p′), (d,d′) reaction studies (no γ-decay reported) [67]:
^{82}Sr; 0_3^+: 2.665(5) MeV;
^{84}Sr; (0_4^+), 0_5^+: 2.525(5), 3.330(30) MeV;
^{86}Sr; (0_4^+): 3.104(6) MeV.

By using the excitation energies of low-spin members of the ground-state rotational bands as compared to energies extrapolated from their high-spin members [346], the oblate–prolate configuration mixing was quantified, within the two-state mixing model, yielding a maximum admixture of 50% in ^{74}Kr. This result coincides well with a maximum value of $\rho^2(E0; 0^+2 \rightarrow 0_1^+) = 96(9)$ m.u. and minimum excitation energy of the 0_2^+ state observed in ^{74}Kr. In addition, the parabolic behavior of the 0_2^+ excitation energies in the Kr isotopic chains (see in Fig. 58), showing a minimum in ^{74}Kr, suggests that the oblate and prolate configurations cross just at ^{74}Kr.

Several theoretical approaches were applied to describe shape coexistence at low excitation energy in the light krypton isotopes. The list includes methods based on: the shell model [349,350], self-consistent triaxial mean-field models [351,352], or beyond-mean-field models [353–355]. It turned out that in order to reproduce the experimentally observed shape coexistence and transition from a prolate ground-state shape in ^{76}Kr and ^{74}Kr to oblate in ^{72}Kr with beyond-mean-field calculations, the inclusion of triaxial degree of freedom is required. This was shown in Ref. [354], where Hartree–Fock–Bogoliubov (HFB) based configuration-mixing calculations using the Generator Coordinate Method (GCM) with Gaussian Overlap Approximation (GOA) for the low-lying states in ^{72}Kr, ^{74}Kr, and ^{76}Kr with the finite-range, density-dependent Gogny D1S, including axial and triaxial quadrupole deformations were presented. Another beyond-self-consistent mean-field method based on HFB and the Gogny D1S interaction, which successfully and in a unified manner describes shape transitions and shape coexistence in the $^{70-78}$Kr region [355], used the so-called symmetry-conserving configuration mixing (SCCM) method. This framework is based on the GCM and includes quantum number restorations (particle number and angular momentum) and shape mixing of axial and triaxial intrinsic states. Fig. 57(b) displays potential energy surfaces (PES) for even–even $^{72-82}$Kr isotopes obtained with the method mentioned above [355]. Also, the PES obtained from macroscopic–microscopic mean field model of Moeller et al. [356] is shown for comparison in Fig. 57(a). In $^{72-78}$Kr nuclei, two minima are clearly visible in both types of approaches, an oblate and a prolate-triaxial one, whose relative depths evolve with the number of neutrons – they are quite degenerate in ^{74}Kr. To have a deeper insight into the predicted shape evolution along the isotopic chain, collective wave functions related to the PES for 0_1^+ (ground state) as well as to the 0_2^+, 2_1^+ and 2_2^+ excited states,

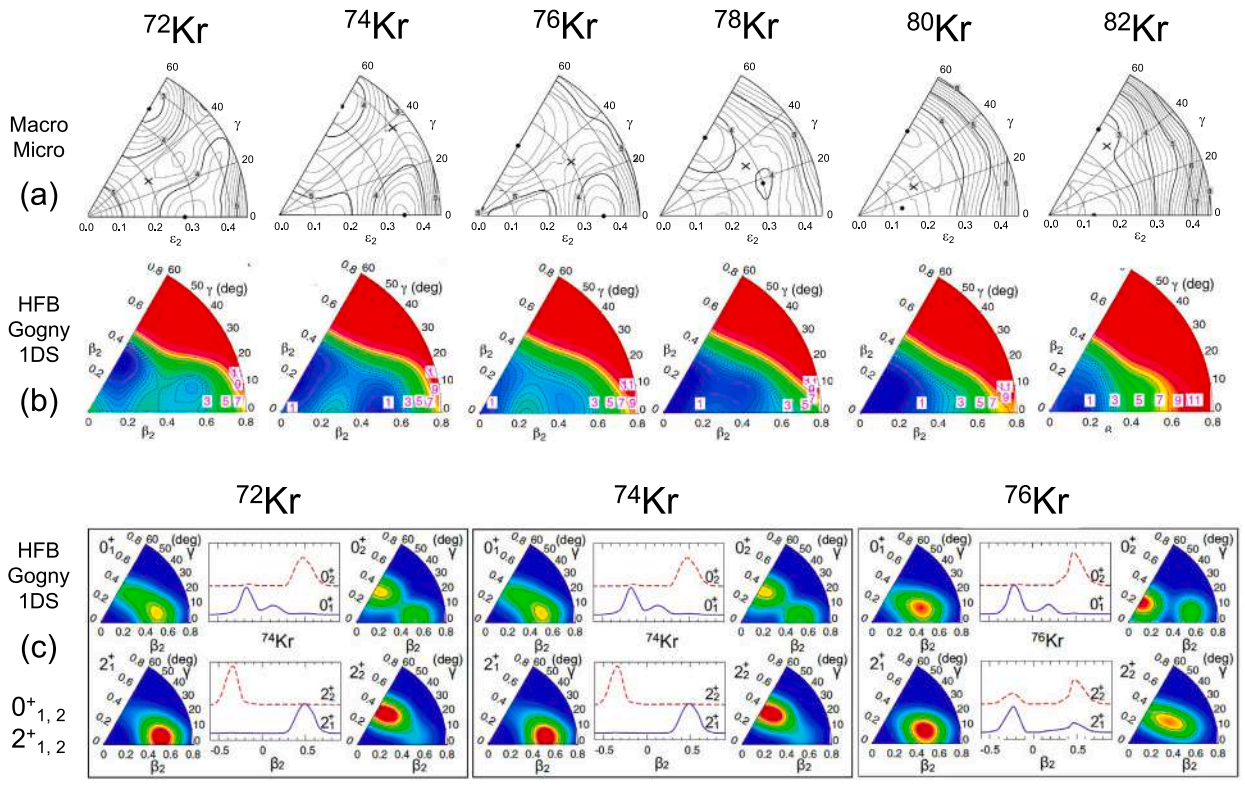

Fig. 57. Potential energy surfaces (PES) for even–even $^{72-82}$Kr obtained from different type of calculations: (a) macroscopic–microscopic mean field model of Moeller et al. [59], and (b) Hartree–Fock–Bogoliubov calculations based on the Gogny force, by Rodriguez [355]. Energies (in MeV) are given on the contour plots. (c): Collective wave functions related to the PES of (b) for 0^+_1 (ground state) and 0^+_2, and for 2^+_1, 2^+_2 excited states, calculated with the symmetry-conserving configuration mixing (SCCM) method for ^{72}Kr, ^{74}Kr and ^{76}Kr isotopes. One-dimensional plots represent axial calculations while "pie-like" plots represent full triaxial results (color scale: red and blue mean large and small height, respectively).
Source: Adapted from [59,355].

calculated with the SCCM method for ^{72}Kr, ^{74}Kr and ^{76}Kr isotopes, are shown in Fig. 57(c). Here, one dimensional plots represent axial calculations, while two-dimensional plots correspond to full triaxial results. Starting from ^{72}Kr and concentrating on the full triaxial calculations, the 0^+_1 and 2^+_1 states are predicted as axial oblate while 0^+_2 and 2^+_2 are of triaxial/prolate nature. For ^{74}Kr, the ground state wave function is quite extended in the γ direction and the 2^+_1 state shows a similar distribution in the (β_2, γ) deformation plane, although its wave function is more concentrated on the prolate side. Further, the 0^+_2 excited state shows a clear mixing of oblate and prolate shapes, whereas the wave function of the 2^+_2 state has a maximum in the oblate part of the (β_2, γ) plane. It is then clear that the calculated 0^+ states in ^{74}Kr demonstrate the mixing (through the γ direction) of shapes associated with the two minima observed in the PES (Fig. 57(b), while the 2^+ states are less mixed and more constrained inside the potential wells. Similar observations can be made for $^{76-78}$Kr isotopes, where the mixing between oblate and prolate shapes is assured by the softness in the γ direction. All this is fully in line with the shape coexistence and shape mixing scenarios observed in experiments for the $^{72-78}$Kr nuclei. In case of the axial calculations, the impossibility of shape mixing through the triaxial degree of freedom does not allow for a complete description of the properties of low-lying states in the neutron deficient Kr isotopes. This again emphasizes the need to consider the triaxial degree of freedom in the description of the properties of neutron-deficient Kr isotopes.

4.4. The Z = 50 region: Cd, Sn and Te

In the Z = 50, A ∼ 100 region, the increased number of nucleons, with respect to the Ca (Z = 20) and Ni (Z = 28) regions, makes microscopic calculations computationally challenging [365], therefore predictions for excited states are mainly based, thus far, on mean-field and beyond-mean-field approaches [59,105,198,264,366].

Fig. 59 shows the excited 0^+ states (up to 0^+_4) located experimentally in Cd, Sn and Te nuclei. The decay properties of these states are summarized in Tables 17, 18, 19, 20 and 21. In all three isotopic chains, a parabolic behavior is observed with a characteristic minimum around the neutron mid-shell at N = 66, which is a typical signature of shape coexistence (see discussion in Section 2.2). This is the region where some 0^+ excitations were interpreted in terms of phonons, although such interpretation has been critically questioned in view of recent experimental and theoretical investigations [367]. As shown in Figs. 34 and 35, the Z = 50 region

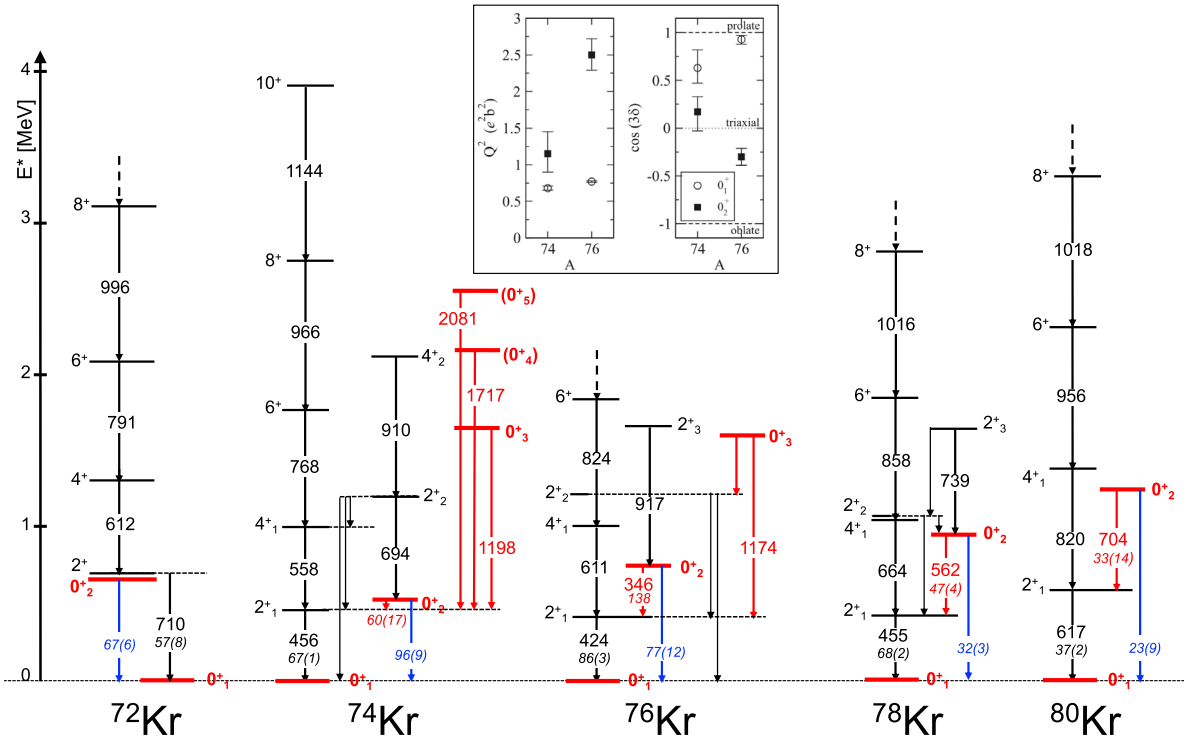

Fig. 58. Partial level schemes of ^{72,74,76,78,80}Kr [67]. The γ decay of 0^+ states is highlighted in red with red and blue arrows indicating measured γ and E0 decay from 0^+ states, with energies in keV and B(E2) and ρ^2(E0) values in W.u. and m.u., respectively (in italic). Dashed arrows indicate the continuation of a band to higher spins (see Table 16 for details). The inset shows the quadrupole deformation parameters obtained for the 0^+ states in ^{74}Kr and ^{76}Kr in the Coulomb excitation experiment of Clement et al. [348].

shows the largest number of significantly retarded E2 decays from excited 0^+ states (HF > 10) mostly located in Cd isotopes, which could be associated with local minima in Potential Energy Surfaces, at different deformations. Indeed, the appearance of relatively deep and well separated secondary PES minima was predicted in the Te, Sn, Cd and Pd region around N = 66 by the microscopic–macroscopic-model and beyond mean-field calculations [59,198], as well as relativistic energy density functional [106] and large-scale shell model calculations [365].

4.4.1. The Sn isotopes

In Sn isotopes, Hartree–Fock–Bogoliubov calculations of the PES, performed with the interaction of Togashi et al. [365], predict a main spherical minimum, accompanied by the appearance of a prolate one in ^{112,114,116}Sn. The prolate minimum almost disappears in ^{118}Sn and is not present in ^{120}Sn and heavier isotopes. It does not exist in Sn nuclei lighter than A = 110, either. This shape coexisting scenario also appears, less pronounced, in Hartree–Fock–Bogoliubov calculations based on the Gogny force [198,249,264], while it is not expected by macroscopic–microscopic mean field calculations of Moeller et al. [59], which predict a main spherical minimum only. Fig. 60 shows the PES calculated for A = 110–120 Sn isotopes for the different theory approaches.

From a microscopic point of view, in the context of *Type II shell evolution* (see Section 2.1), in the $^{112-116}$Sn isotopes, in analogy to Ni isotopes, a mechanisms for spontaneous symmetry breaking induced by the proton–neutron interaction might occur, leading to deep prolate minima. As shown in Fig. 6, in Sn isotopes neutron excitations to the $h_{11/2,}$ unique-parity orbital could play the same role as the $g_{9/2}$ neutron excitations in the Ni nuclei, inducing the reduction of the proton $g_{7/2}$-$g_{9/2}$ spin–orbit splitting (similarly to the proton $f_{5/2}$-$f_{7/2}$ splitting in Ni). We note that in terms of shell filling, ^{114}Sn corresponds to ^{66}Ni, while ^{112}Sn corresponds to ^{64}Ni (half-shell filling in Sn occurs at N = 116, and at N = 39 in Ni).

As shown in Figs. 61, 62 and Tables 17, 18, Sn isotopes are characterized by a large number 0^+ excitations (up to 15 in ^{114}Sn), firmly established in a series of high-resolution transfer studies, mainly (t,p) and (p,t) performed in the last two decades at Munich Q3D spectrograph [91–95,369–371]. Moreover, in the '70s, the two-proton transfer reaction (^{3}He,n) on ^{106,110,112,114,116}Cd targets was also found to populate strongly and selectively 0^+ states in A = 108, 112, 114, 116 and 118 Sn isotopes [90], thus indicating sizeable proton components in their wave functions. The histograms of Fig. 63 clearly demonstrate the large differences in population cross sections of 0^+ states in Sn isotopes, between (^{3}He,n) and two-neutron transfer processes [24], which might suggest the existence of excited structures of deformed (prolate) nature among the 0^+ states strongly populated in (^{3}He,n) processes. This is the case, for example, of 0^+_2 and 0^+_5 located at 2.191 and 3.570 MeV in ^{112}Sn, which appear, in contrast, to be weakly populated in two-neutron transfer studies [92]. A similar weak population pattern in two-neutron transfer was also observed for the shape-isomer-like

Table 16
Experimental information available on 0^+ excitations in Kr isotopes (A = 72–82) (see also Fig. 51 and caption of Table 8 for detailed explanations).

Nucleus	E_i [MeV]	I_i^π	$T_{1/2}$ [ps]	E_f [MeV]	I_f^π	E_γ or E_{e^-} [MeV]	BR [%]	E/Mλ	B(E/Mλ)/ρ^2(E0) [W.u.]/[m.u.]	HF	Refs.
^{72}Kr	0.671	0_2^+	26.3(21) 10^3	0.0	0_1^+	0.671	100.0	E0	67(6)		[33,67,346]
^{74}Kr	0.509	0_2^+	13.0(7) 10^3	0.0	0_1^+	0.509	59.9	E0	96(9)		[33,67,348]
				0.456	2_1^+	0.053	40.1	[E2]	60(17)	0.083	
	1.654	0_3^+		0.456	2_1^+	1.198	100.0	[E2]			[67,357]
	2.173	(0_4^+)		0.456	2_1^+	1.717	100.0				[357]
	2.537	(0_5^+)		0.456	2_1^+	2.081	100.0				[357]
^{76}Kr	0.770	0_2^+	42(6)	0.424	2_1^+	0.346	99.7	E2	138	0.036	[33,67,358]
				0.0	0_1^+	0.770	0.3	E0	77(12)		
	1.598	0_3^+	<4.7	0.424	2_1^+	1.174	92	E2	>2.6	<1.9	
				0.770	0_2^+	0.828		E0	<600		
				1.222	2_2^+	0.376	8	E2	>61	<0.082	
^{78}Kr	1.017	0_2^+	10.8(9)	0.0	0_1^+	1.017		E0	31.9(34)		[33,67,359]
				0.455	2_1^+	0.562	100.0	E2	47(4)	0.11	
^{80}Kr	1.321	0_2^+	4.9(21)	0.0	0_1^+	1.321		E0	23(9)		[33,67,360,361]
				0.617	2_1^+	0.704	100.0	E2	33(14)	0.15	
^{82}Kr	1.488	0_2^+	10(3)	0.0	0_1^+	1.488		E0	9.1($^{+27}_{-30}$)		[33,67,362,363]
				0.777	2_1^+	0.711	100.0	[E2]	15(5)	0.33	
	2.172	0_3^+	0.42(7)	1.957	2_3^+	0.215[a]		[E2]			[67,364]
				1.475	2_2^+	0.697	0.5	E2	1.9($^{+6}_{-5}$)	2.6	
				0.777	2_1^+	1.395	99.5	E2	12.0($^{+24}_{-18}$)	0.42	
				0.0	0_1^+	2.172		E0			
	2.450	0_4^+	~0.17	1.475	2_2^+	0.975	51.6	E2	92	0.054	
				0.777	2_1^+	1.674	48.4	E2	5.8	0.86	
	3.187	0_5^+		1.957	2_3^+	1.230	7.0	[E2]			
				1.475	2_2^+	1.712	6.8	[E2]			
				0.777	2_1^+	2.411	86.2	[E2]			
	3.234	0_6^+		2.480	2_4^+	0.754	33.8	[E2]			
				1.957	2_3^+	1.276	32.4	[E2]			
				0.777	2_1^+	2.458	33.8	[E2]			
	3.565	0_7^+		2.656	2_5^+	0.909	10.5	[E2]			
				2.480	2_4^+	1.085	8.4	[E2]			
				1.957	2_3^+	1.608	50.9	[E2]			
				1.475	2_2^+	2.090	11.5	[E2]			
				0.777	2_1^+	2.789	18.6	[E2]			
	3.716	0_8^+		2.547	(3^-)	1.168	9.2				
				2.094	3^+	1.622	5.7				
				1.957	2_3^+	1.759	7.5	[E2]			
				0.777	2_1^+	2.940	77.6	[E2]			
^{84}Kr	1.837	0_2^+	25(10)	0.882	2_1^+	0.956	100.0	[E2]	1.3(5)	3.8	[67]
^{86}Kr	2.726	0_2^+		2.349	2_2^+	0.377	41.2	[E2]			[67]
				1.565	2_1^+	1.162	58.8	[E2]			
	3.541	0_3^+		2.349	2_2^+	1.192	66.7	[E2]			
				1.565	2_1^+	1.977	33.3	[E2]			
^{88}Kr	2.776	0_2^+		1.577	2_2^+	1.198	64.5	[E2]			[67]
				0.775	2_1^+	2.000	35.5	[E2]			

[a] Uncertain placement [67]
Additional 0^+ states from ϵ decay, (t,p), (p,p′) reaction studies (no γ-decay reported) [67]:
^{86}Kr: 0_4^+: 3.832(10) MeV.

structures in ^{64}Ni and ^{66}Ni [21,68]. Additional examples are the 0_2^+ and 0_3^+ excitations in ^{114,116,118}Sn which seem to be built on different configurations, with 0_2^+ strongly dominated by protons (2p−2h) excitations.

In even Sn nuclei with A = 110–118, supports to the existence of secondary minima in the PES comes from the experimental observation, in (α, 2nγ) reactions, of positive-parity deformed rotational bands, extending to spins higher than 20^+ [16,67]. Their partial level schemes are reported in the top part of Figs. 61 and 62. Such bands were interpreted as two-particle-two-hole (2p−2h) $\pi g_{7/2}^2$-$\pi g_{9/2}^{-2}$ proton excitations across the Z = 50 shell gap, which drive the deformation of the nucleus to a prolate shape. Deformation parameters $\beta \sim 0.18$ and ~0.26 were deduced for the bands in ^{112}Sn and ^{114}Sn, respectively, via lifetime measurements [372,373]. While in ^{110}Sn the deformed band decays into lower deformed structures at spin 12^+ and has not been traced down to its 0^+ band head [374], in ^{112,114,116,118}Sn the deformed bands start to decay out at 6^+, with a small fraction of the intensity feeding down to the 0_2^+ band head. Moreover, in ^{118}Sn, the 0_2^+ band head decays to the spherical 2_1^+ level by a rather fast E2 transition with B(E2) = 19 W.u., pointing to a significant admixture of deformed and spherical components in the 0_2^+ wave function. In ^{116}Sn the picture is much less clear. Both 0_2^+ and 0_3^+ excitations at 1757 and 2027 keV, respectively, could be the band head of the deformed structure,

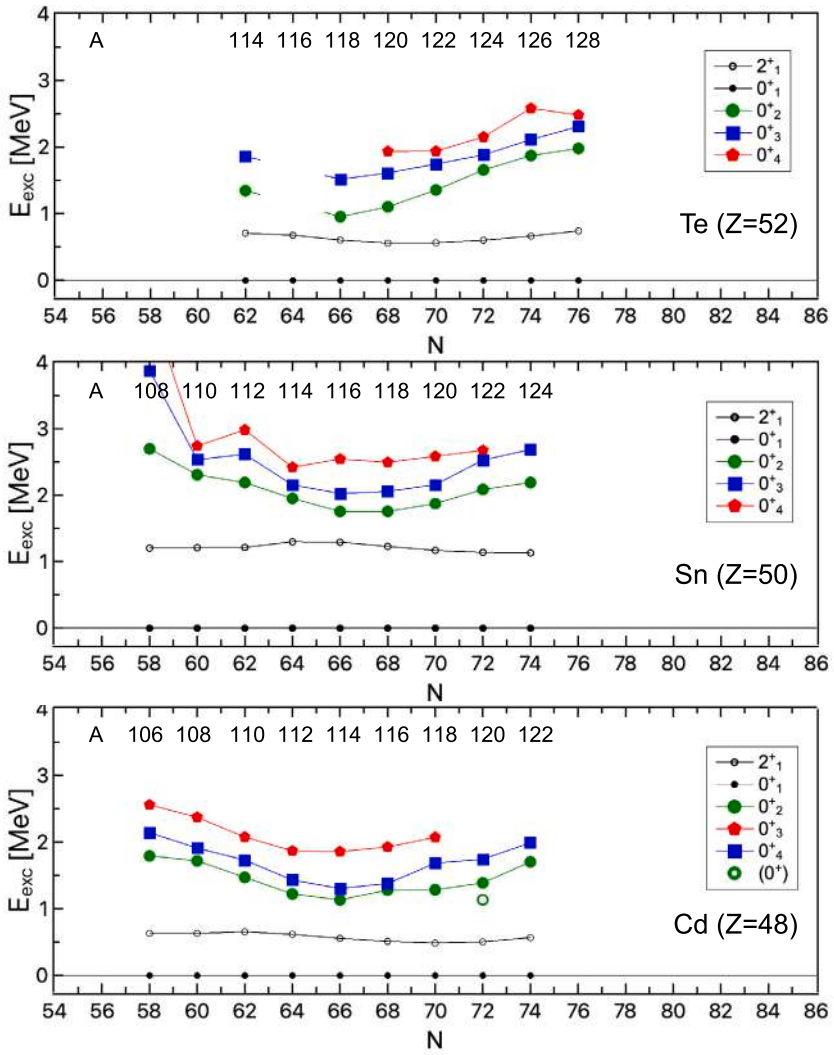

Fig. 59. Systematics of the energies of the $0^+_{1,2,3,4}$ states observed in the Z = 50 ± 2 nuclei of Cd, Sn and Te. The first 2^+ excitation is also given as a reference (open circles)(see Tables 19, 20, 17, 18, and 21 for details). For ^{120}Cd, the green circle symbol indicates the newly observed state at 1136 keV, proposed as 0^+_2 by Batchelder et al., [368].

as follows from the enhanced B(E2) values reported from the 2^+_2 state at 2112 keV to both 0^+_2 and 0^+_3 [375]. An indication for considering 0^+_2 as band head comes from the sizeable population of this state in the two-proton-transfer, (^{3}He,n) reaction [90]. However, recent β-decay and (n, γ) studies, performed at TRIUMF with the 8π spectrometer [376] and at ILL with FIPPS [375], seem to favor 0^+_3 as the head of the rotational band. From the (n, γ) investigation, a slightly delayed transition from 0^+_3 to 2^+_1 is also found (B(E2) = 0.49(7) W.u.; HF = 10.2), while the 0^+_2 to 2^+_1 decay is observed to be faster (B(E2) = 18(3) W.u.; HF = 0.28), in agreement with predictions from the Interacting Boson Model [375]. In ^{112,114}Sn, similar B(E2) information from the 0^+_2 band head is not available.

To achieve a more profound understanding of the shape coexistence phenomenon in Sn isotopes around A = 100, detailed studies of the properties of excited 0^+ states are needed, as for example in terms of state lifetimes. As given in Tables 17, 18, very limited information on lifetimes exists, mainly deduced from Coulomb excitation experiments performed in the '80s by Backlin et al. [377] and from recent (p,p'γ) studies in ^{112,114}Sn performed at the Cologne Tandem [378]. This leaves open the possibility of finding shape-isomer-like structures among excited 0^+ states, with significant hindrance in their decay toward the spherical 2^+_1 state caused by initial and final state wave functions localized in different regions of the PES (β, γ) plane, well separated by a potential barrier.

4.4.2. The Cd isotopes

According to macroscopic–microscopic calculations of Moller et al. [59], Cd isotopes with A = 104–112, exhibit potential-energy surfaces with a well defined prolate minimum around β_2 = 0.1–0.2, accompanied by an oblate minimum, of similar size, for A =

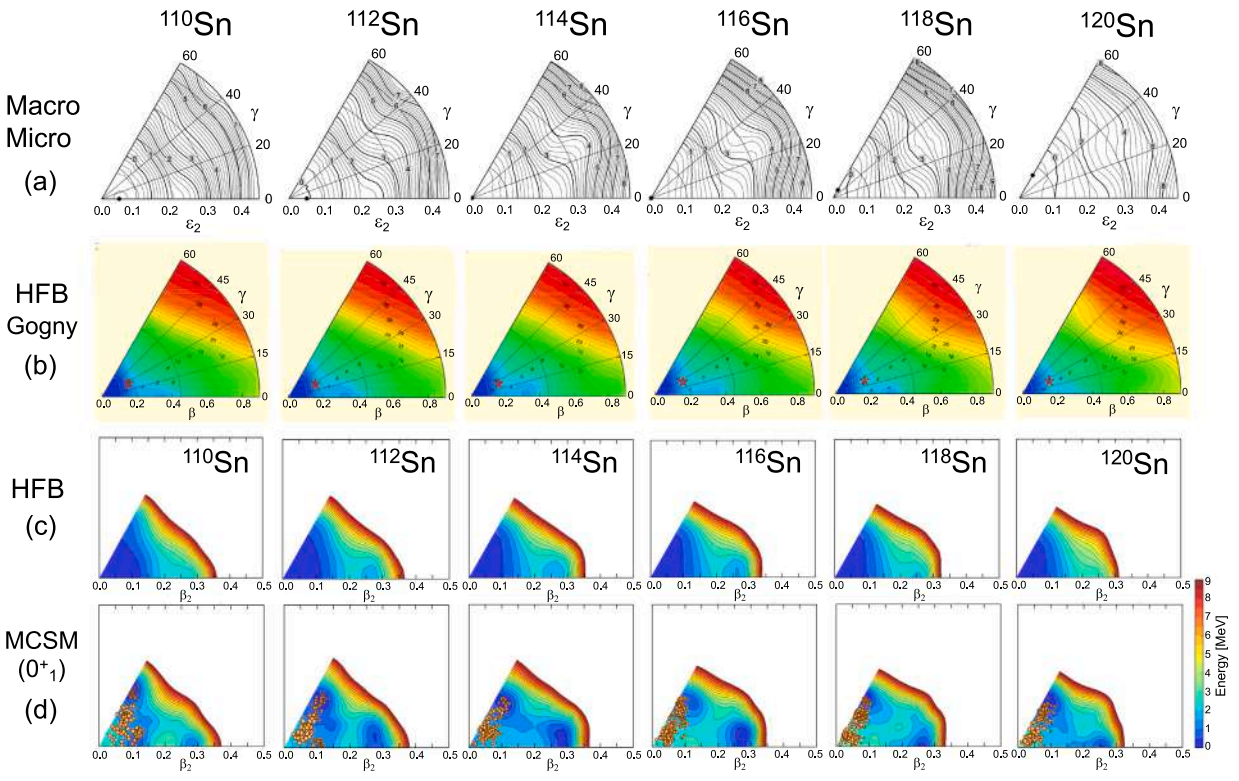

Fig. 60. Potential energy surfaces for even–even $^{110-120}$Sn obtained from different type of calculations: (a) macroscopic–microscopic mean field model of Moeller et al. [59], (b) Hartree–Fock–Bogoliubov calculations based on the Gogny force, by S. Hilaire and M. Girod [198,249], (c) Hartree–Fock–Bogoliubov calculations with the interaction of Togashi et al. [365], and (d) Monte Carlo Shell Model Hamiltonian by Togashi et al. [365], with circles showing the main component of the 0^+_1 state. Energies (in MeV) are given on the contours in (a)–(b), and by common color scale in (c)–(d).
Source: Adapted from [59,250].

114–118, which both vanish in heavier systems, while approaching the N = 82 shell closure. A slightly different scenario is predicted by Hartree–Fock–Bogoliubov calculations based on the Gogny DIS interaction [105,355,366], according to which a well defined prolate minimum (β_2 = 0.1–0.2), and a shallow second triaxial-prolate minimum with (β_2, γ) = (0.3, 20°) exist for A = 110–118 isotopes. Again, heavier systems, e.g., $^{128-130}$Cd, exhibit only almost spherical minima. All these features are shown in Fig. 64.

Experimentally, similarly to Sn isotopes, Cd nuclei display a characteristic parabolic-shaped pattern for the energy of excited states (including 0^+ excitations), as a function of the neutron number, reaching a minimum near the middle of the shell (i.e., at ^{114}Cd with N = 66, see Fig. 59). This is a typical scenario for shape coexistence, which was already suggested in the '70s by the observation of a deformed band in ^{110}Cd, built on the 0^+_2 level at 1473 keV [380]. Such a state, together with 0^+_2 in ^{112}Cd, located at 1224 keV, was also found to be strongly populated in two-proton transfer (^{3}He, n) studies [90], while weakly excited in two-neutron pick-up (p,t) studies [381], similarly to what was observed in ^{112,118}Sn isotopes (see Fig. 63 and related text). The strong difference in state population, in favor of (^{3}He, n) processes, indicate a significant (2p–4h) proton components in the 0^+_2 state wave function (e.g., $\pi(g_{9/2})^{-4}(d_{5/2})^2$ or $\pi(g_{9/2})^{-4}(g_{7/2})^2$) which can drive the system to a deformed configuration.

These shape-coexisting states, named "intruder excitations" were systematically studied in even–even Cd isotopes and originally considered as prototype examples of vibrational structures, within the Interactive Boson Model approach [382,383]. However, in recent years, more precise experimental works in terms of lifetime and branching ratio measurements, also in comparison with state-of-the-art calculations (e.g., the beyond Mean Field model with the Gogny DIS interaction shown in Fig. 64), strongly suggest that Cd isotopes exhibit multiple shape coexistence, contrary to the original picture of nuclear vibrations, as later discussed [384,385].

Similarly to Sn isotopes, in Cd nuclei a number of low-lying excited 0^+ states have been reported, as shown in Fig. 34, 35 and 65, and in Tables 19 and 20. In the majority of the cases, firmly established B(E2) values for the decay to the first excited 2^+_1 state do not show significant retardation (i.e., B(E2) > 1 and HF < 10), thus pointing to large mixing with the ground state wave function. Two specific cases display instead remarkably retarded E2 decays. They are 0^+_3 at 1433 keV in ^{112}Cd (B(E2) = 0.0121(17) W.u., HF = 413) and 0^+_3 at 1306 keV in ^{114}Cd (B(E2) = 0.0026(4) W.u., HF = 1923). We note that a similar additional case could be the 0^+_4 state located at 2079 keV in ^{110}Cd, for which only a relative B(E2) value exists (see Table 20). Such 0^+ excitations could be interpreted as bandheads of deformed structures located in local minima of the PES, possibly separated by a sizeable barrier toward the ground state, as predicted by the macroscopic–microscopic-model calculation of Moller et al. [59] in ^{114,116}Cd, for example (see Fig. 64).

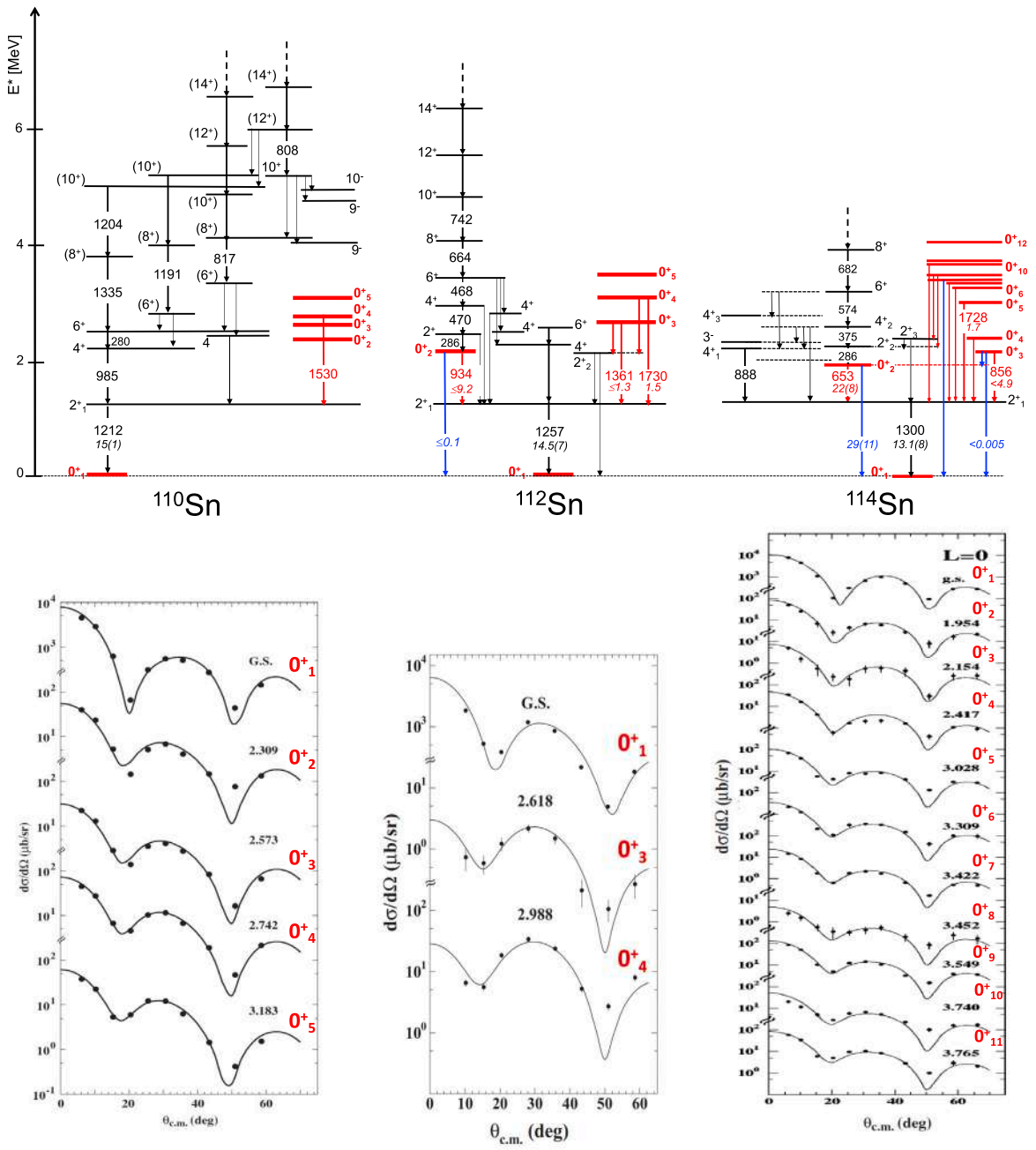

Fig. 61. Top panels: partial level schemes of ^{110,112,114}Sn, with 0^+ states highlighted in red [67]. Red and blue arrows indicate measured γ and E0 decay from 0^+ states, with energies in keV and B(E2) and ρ^2(E0) values in W.u. and m.u., respectively (in italic). Dashed arrows give continuation of structures to higher spins. Bottom panels: corresponding angular distributions of all 0^+ states observed in most recent (p,t) reaction studies [67,91–93] (see Table 17, for details). *Source:* Adapted from [91–93].

Indeed, a series of rotational bands have been discovered in Cd isotopes, from A = 106 to 110 [67,386–388]. In ^{106}Cd, three collective bands extending to spin more than 20 were observed, decaying out around spin 6–9 [386]. Moreover, in a recent Coulomb excitation experiment with the GRETINA array, the properties of low-lying states were investigated, and matrix elements were deduced supporting more a deformed rather than vibrational character for 2^+_1 in ^{106}Cd [389]. In ^{108}Cd, a short band structure, up to spin-parity 4^+, was observed built on the 0^+_2 state [390] (see Fig. 65) which was interpreted as a two-particle-two-hole proton excitation, similarly to the prolate ("intruder") bands found in neighboring Sn isotopes. The decay out from the 2^+ and 4^+ members of the band was found to be moderately hindered (with B(E2) ~ 0.2 W.u.), suggesting a rather high purity for the

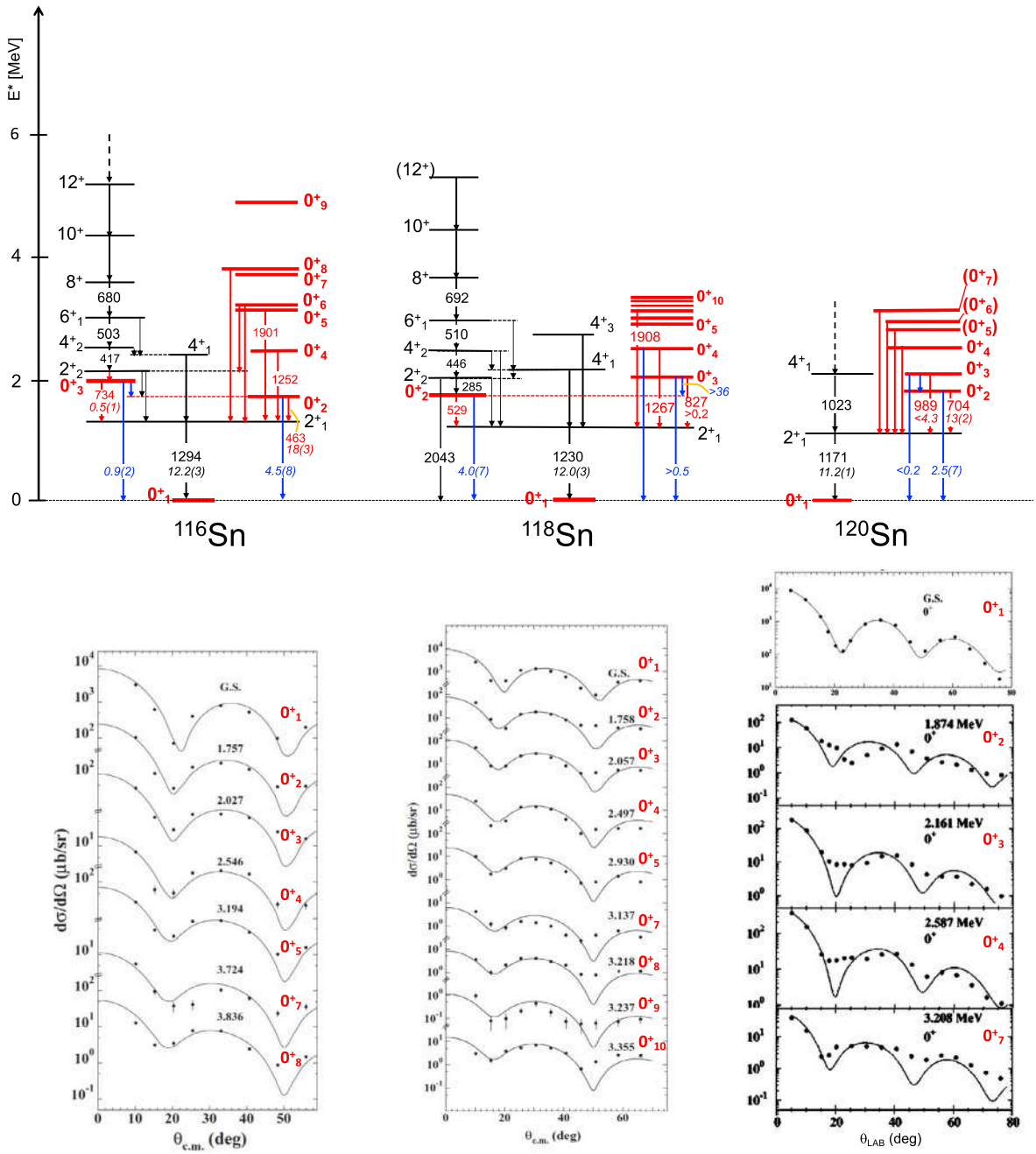

Fig. 62. Top panels: partial level schemes of ^{116,118,120}Sn, with 0^+ states highlighted in red [67]. Red and blue arrows indicate measured γ and E0 decay from 0^+ states, with energies in keV and B(E2) and ρ^2(E0) values in W.u. and m.u., respectively (in italic). Dashed arrows give continuation of structures to higher spins. Bottom panels: corresponding angular distributions of all 0^+ states observed in most recent (p,t) reaction studies [67,94,95,371] (see Table 18, for details). *Source:* Adapted from [94,95,371].

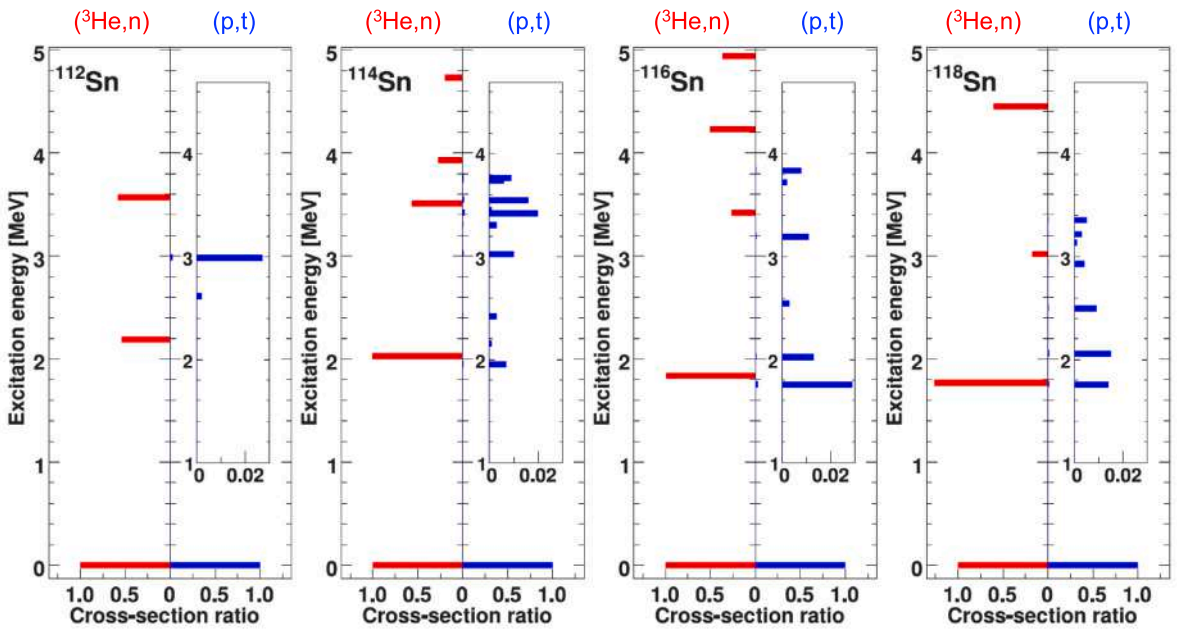

Fig. 63. Population cross sections for excited 0^+ states in ^{112,114,116,118}Sn, normalized to those of the ground state. In each plot, red and blue histograms represent the ratios observed in the (^{3}He, n) and (p,t) reaction, respectively. The insets on the right-hand sides of the plots display a ratio scale expanded to 0.03 to make the (p,t) data more clearly observable (they rarely exceed a few percent).
Source: Taken from [24].

Table 17
Experimental information available on 0^+ excitations in Sn isotopes (A = 108–114), see also Fig. 59 and caption of Table 8 for detailed explanations.

Nucleus	E_i [MeV]	I_i^π	$T_{1/2}$ [ps]	E_f [MeV]	I_f^π	E_γ or E_{e^-} [MeV]	BR [%]	E/Mλ	B(E/Mλ)/ρ^2(E0) [W.u.]/[m.u.]	HF	Refs.
^{110}Sn	2.742	0_4^+		1.212	2_1^+	1.530	100.0	[E2]			[67,91]
^{112}Sn	2.191	0_2^+	≥2.7	1.257	2_1^+	0.934	99.9	E2	≤9.2	≥0.54	[33,67,92,378]
				0.0	0_1^+	2.191	0.15	E0	≤0.1		
	2.618	0_3^+	≥2.910	1.257	2_1^+	1.361	98.8	E2	≤1.29	≥3.9	
				2.151	2_2^+	0.467	1.2	E2	≤3.3	≥1.5	
	2.986	0_4^+	0.762(131)	1.257	2_1^+	1.729	99.0	E2	1.49	3.4	
				2.151	2_2^+	0.835	1.0	E2	0.57	8.8	
^{114}Sn	1.953	0_2^+	6.5(23)	1.299	2_1^+	0.653	99.7	E2	22(8)	0.23	[33,67,378]
				0.0	0_1^+	1.953	0.3	E0	29(11)		
	2.156	0_3^+	>7.6	1.299	2_1^+	0.856	100.0	E2	<4.9	>1.0	
				0.0	0_1^+	2.156		E0	<0.005		
				1.953	0_2^+	0.203		E0	<0.9		
	2.421	0_4^+		1.299	2_1^+	1.121	100.0	E2			
	3.028	0_5^+	0.624(280)	1.299	2_1^+	1.728	95.2	E2	1.7	2.9	
				2.239	2_2^+	0.789	1.5	E2	1.3	3.8	
				2.454	2_3^+	0.574	3.6	E2	16	3.2	
	3.309	0_6^+		1.299	2_1^+	2.009	100.0	E2			
	3.422	0_7^+		1.299	2_1^+	2.122	61.7	E2			
				2.239	2_2^+	1.183	25.3	E2			
				2.454	2_3^+	0.968	13.0	E2			
	3.548	0_9^+		2.239	2_2^+	1.309	47.9	E2			
				2.454	2_3^+	1.094	52.1	E2			
	3.740	0_{10}^+		1.299	2_1^+	2.440	100.0	[E2]			

Additional 0^+ states from reaction studies (no γ-decay reported):
^{108}Sn: ($0^+_{2,3,4}$): ~2.7×10^3, ~3.88×10^3, ~4.90×10^3 MeV, from (^{3}He,n) [90];
^{110}Sn: $0^+_{2,3,5}$: 2.309(3), 2.573(3), 3.183(3) MeV, from (p,t) [91];
^{112}Sn: $(0_5)^+$: 3.570 MeV from (^{3}He,n) [90];
^{114}Sn: $0^+_{8,11,12}$: 3.452, 3.765(3), 4.413(6) MeV, from (p,t) [67,93].

Table 18
Experimental information available on 0^+ excitations in Sn isotopes (A = 116–124), see also Fig. 59 and caption of Table 8 for detailed explanations.

Nucleus	E_i [MeV]	I_i^π	$T_{1/2}$ [ps]	E_f [MeV]	I_f^π	E_γ or E_{e^-} [MeV]	BR [%]	E/Mλ	B(E/Mλ)/ρ^2(E0) [W.u.]/[m.u.]	HF	Refs.
^{116}Sn	1.757	0_2^+	44(6)	1.294	2_1^+	0.463	99.7	[E2]	18(3)	0.28	[33,67,94,375]
				0.0	0_1^+	1.757	0.3	E0	4.5(8)		
	2.027	0_3^+	164(10)	1.294	2_1^+	0.734	100.0	[E2]	0.49(7)	10.2	
				0.0	0_1^+	2.027		E0	0.85(16)		
				1.757	0_2^+	0.271		E0	86(16)		
	2.546	0_4^+		2.112	2_2^+	0.434	2.9	[E2]			
				1.294	2_1^+	1.252	97.1	[E2]			
	3.194	0_5^+		1.294	2_1^+	1.901	100.0	[E2]			
	3.236	0_6^+		2.112	2_2^+	1.124	78.7	[E2]			
				1.294	2_1^+	1.943	21.3	[E2]			
	3.837	0_8^+		1.294	2_1^+	2.543	100.0	[E2]			
^{118}Sn	1.758	0_2^+	21(3)	1.230	2_1^+	0.529	100.0	E2	19(3)	0.26	[33,67]
				0.0	0_1^+	1.758		E0	4.0(7)		
	2.057	0_3^+	<200	1.758	0_2^+	0.299		E0	>36		
				1.230	2_1^+	0.827	100.0	E2	>0.21	<24	
				0.0	0_1^+	2.057		E0	>0.48		
	2.497	0_4^+		1.230	2_1^+	1.267	100.0	E2			
				0.0	0_1^+	2.497		E0			
	3.137	0_7^+		1.230	2_1^+	1.908	100.0	[E2]			
^{120}Sn	1.875	0_2^+	7.4(10)	1.171	2_1^+	0.704	100.0	[E2]	12.6(17)	0.40	[33,67,95]
				0.0	0_1^+	1.875		E0	2.5(7)		
	2.160	0_3^+	>4	1.171	2_1^+	0.989	100.0	[E2]	<4.3	>1.2	
				0.0	0_1^+	2.160		[E0]	<0.17		
				1.875	0_2^+	0.285		[E0]	<7		
	2.587	0_4^+	>0.34	1.171	2_1^+	1.416	100.0	[E2]	<8.3	>0.60	
	2.858	(0_5^+)		1.171	2_1^+	1.686	100.0				
	3.035	(0_6^+)		1.171	2_1^+	1.864	100.0				
	3.209	0_7^+		1.171	2_1^+	2.037	100.0	[E2]			
^{122}Sn	2.088	0_2^+	>0.277	1.141	2_1^+	0.947	100.0	E2	<75	>0.067	[67,94]
	2.530	0_3^+		2.154	2_2^+	0.377	7.3	[E2]			
				1.141	2_1^+	1.390	92.7	E2			
	2.676	0_4^+	>0.2	1.141	2_1^+	1.535	100.0	[E2]	<9.3	>0.54	
	2.868	0_5^+	$0.13(^{+20}_{-6})$	1.141	2_1^+	1.727	100.0	[E2]	8(6)	0.63	
	3.206	0_6^+		1.141	2_1^+	2.066	100.0	[E2]			
^{124}Sn	2.192	0_2^+	>1.38	1.132	2_1^+	1.060	100.0	E2	<6.5	>0.77	[67,379]
	2.689	0_3^+	>0.79	2.130	2_2^+	0.559	22.0	E2	<79	>0.063	
				1.132	2_1^+	1.557	78.0	E2	<1.7	>2.9	

Additional 0^+ states from reaction studies (no γ-decay reported):
^{116}Sn: 0_7^+: 3.724(3), from (p,t) [94]; 0_9^+: 4.940 MeV, from (^{3}He,n) [90];
^{118}Sn: $0^+_{5,8,9,10}$: 2.930, 3.218(3), 3.237(3), 3.355(3) MeV, from (p,t) [371]; 0_6^+: 3.020(3), from (^{3}He,n) [90].
^{120}Sn: 0_8^+: 16.9(4) × 10^3, from (p,p′) [67].

band, as is the case of deformed structure well isolated from the main minimum by a potential energy barrier in the deformation space. Furthermore, deformed structures have been clearly identified in ^{108}Cd at high spins with GAMMASPHERE: a superdeformed (SD) prolate band, not linked to the main minimum, has been observed, with a major-to-minor axis ratio larger than 1.8:1, i.e., one of the most deformed structures identified in any nucleus, to date [387]. An additional SD band was also reported, as well as a number of rotational structures of lower deformation [67,388]. It is likely that some of the 0^+ states in ^{108}Cd are band heads of these high-spin structures.

Moving to heavier Cd isotopes, "intruder" bands are here observed up to spin 6^+ in ^{110}Cd and ^{112}Cd, (see Fig. 65). In these nuclei, extensive experimental information is also available on decay branches, including very weak ones from non-yrast states, following in particular the recent β^+/EC decay of ^{110,112}In and β^- decay of ^{112}Ag studies at TRIUMF, and lifetime determinations from (n, n'γ) reactions at University of Kentucky, from Garrett et al. [384,385,392] and reference therein). Band-like structures have been identified built on 0^+ and 2^+ excitations, in several cases with B(E2) values for the in-band transitions poiting to a highly-collective nature of these structures. The results were compared with beyond-mean-field calculations by Rodriguez et al. [296] which qualitatively reproduce the observed excitation spectrum and decay schemes, and indicate that the $0^+_{1,2,3,4}$ states, and corresponding excitations built on them, are characterized by different deformations, and no vibrational character in their wave functions. As shown in Fig. 66(b) and (c), in both ^{110,112}Cd, the 0_1^+ ground states are predicted to be prolate deformed (with $\beta_2 \sim 0.2$), while the 0_2^+ states possess triaxial shapes, with wave-function distributions having mean values of (β_2, γ)~(0.4, 20°). The 0_3^+ excitations in these nuclei are suggested instead to be oblate deformed. Yet another characteristics demonstrates the nature of the 0_4^+ states – the theory calculates them as the heads of prolate bands, strongly connected with the "intruder" bands built on 0_2^+ (with B(E2; $2_5^+ \rightarrow 0_4^+$) = 34(15) W.u. and B(E2; $4_6^+ \rightarrow 2_5^+$) = 77(30) W.u.). In fact, a short band up to spin 4^+ was experimentally observed to develop on top of 0_4^+ in ^{112}Cd.

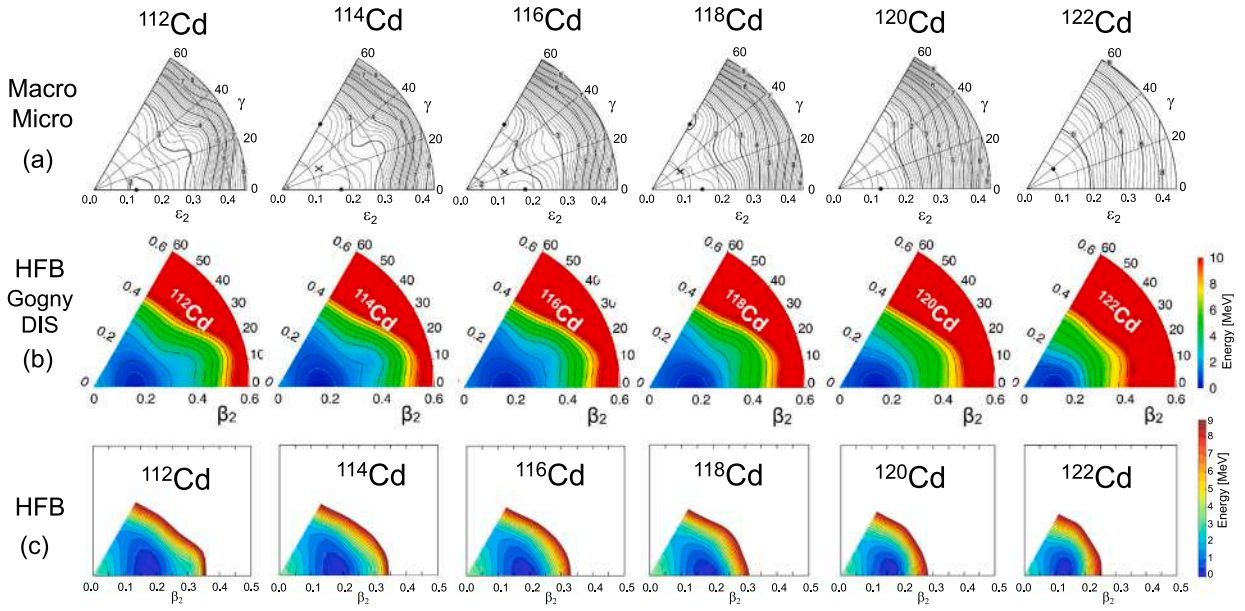

Fig. 64. Potential energy surfaces for even–even $^{112-122}$Cd obtained from different type of calculations: (a) macroscopic–microscopic mean field model of Moeller et al. [59], (b) Hartree–Fock–Bogoliubov calculations based on the Gogny DIS interaction [249,261], within the symmetry-conserving configuration mixing (SCCM) method [105,355,366], and (c) Hartree–Fock–Bogoliubov calculations with the interaction of Togashi et al. [365]. Energies (in MeV) are given on the contour plots in (a), and by color scale in (b)–(c).
Source: Adapted from [59,391].

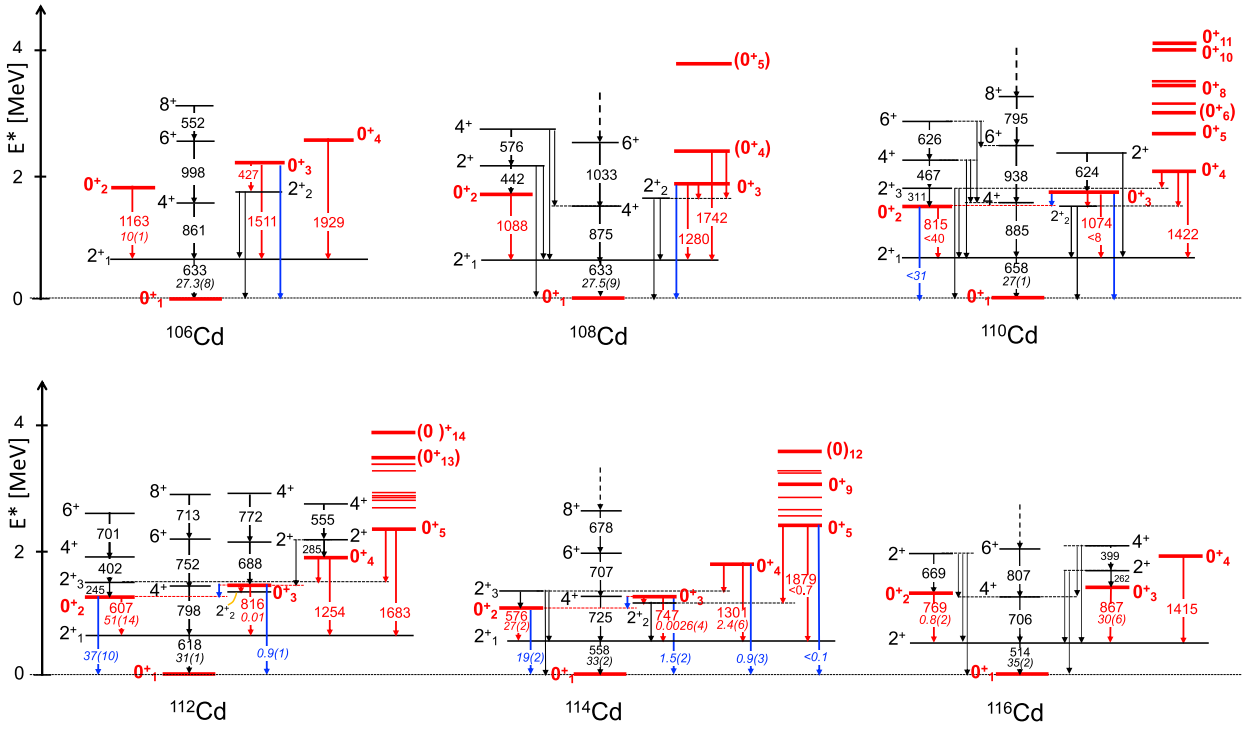

Fig. 65. Partial level schemes of even–even $^{106-116}$Cd isotopes, with 0^+ states highlighted in red [67]. Red and blue arrows indicate measured γ and E0 decay from 0^+ states, up to 0^+_5 for the main E2 decay branches. Energies are in keV and B(E2) and ρ^2(E0) values in W.u. and m.u., respectively (in italic). Dashed arrows give continuation of structures to higher spins (see Tables 19 and 20 for details).

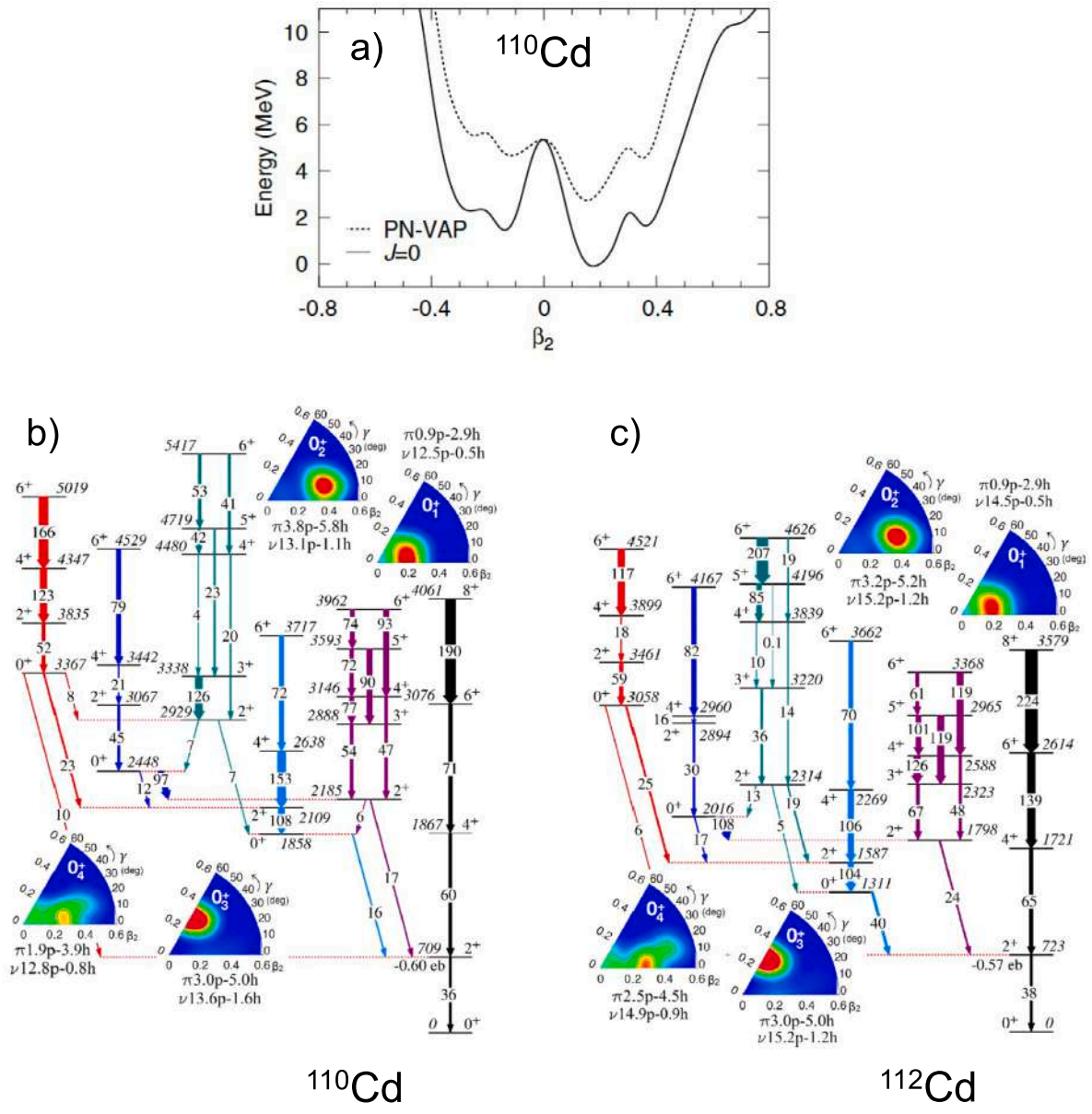

Fig. 66. Panel (a): One-dimensional potential energy surfaces of ^{110}Cd obtained by the Beyond Mean Field model and the Gogny D1S interaction [296] (PN-VAP, dotted line; see also 64), and corresponding projection of angular momentum J = 0 (solid line). Panels (b) and (c): Predicted excitation energy spectra(in keV) and B(E2) values (in W.u.) of collective, low-lying, positive-parity bands of ^{110}Cd (b) and ^{112}Cd (c). The collective wave functions of the band heads and their particle-hole structures are given in the insets in the (β_2, γ) plane. For corresponding partial experimental decay schemes we refer to Fig. 65 and Refs. [384,385]. *Source:* Adapted from [384].

It is interesting to note that the interpretation proposed by the BMF calculations, discussed above, might also explain the significantly retarded E2 decay (B(E2) ≪1 W.u.) from 0^+_3 to 2^+_1 measured in ^{112}Cd (and possibly also in ^{110}Cd), as in terms of a substantial shape change from oblate to prolate deformation, between states residing in well localized minima in the potential energy surfaces. This is displayed in Fig. 66(a), where the one dimensional potential energy surfaces of ^{110}Cd is given for the full calculations (dotted line) and for the corresponding projection on the J = 0 angular momentum. In the latter case, a pronounced barrier appears to separate the oblate and prolate minima, thus pointing to a shape-isomer-like character for 0^+_3 in ^{110}Cd (cfr. Fig. 9(a) and (b)). A similar interpretation might also hold for the retarded decay measured in ^{112,114}Cd for 0^+_3 toward 2^+_1.

As shown in Fig. 65, several additional excited 0^+ states have been observed in ^{112,114}Cd, for which incomplete experimental information is available. In particular, for a number of them, upper limits on the lifetime exist, which also point to possibly significantly retarded transitions (see Tables 19, 20). Very limited information is also available for heavier Cd systems, including a

Table 19
Experimental information available on 0^+ excitations in Cd isotopes (A = 106–112), see also Fig. 59 and caption of Table 8 for detailed explanations.

Nucleus	E_i [MeV]	I^π_i	$T_{1/2}$ [ps]	E_f [MeV]	I^π_f	E_γ or E_{e^-} [MeV]	BR [%]	E/Mλ	B(E/Mλ)/ρ^2(E0) [W.u.]/[m.u.]	HF	Refs.
^{106}Cd	1.795	0^+_2	0.90(7)	0.633	2^+_1	1.163	100.0	E2	9.96(77)	0.50	[67,220,389,391]
				1.717	2^+_2	0.079		[E2]			
	2.144	0^+_3		1.717	2^+_2	0.427	29.6	E2			
				0.633	2^+_1	1.511	70.4	E2			
				0.0	0^+_1	2.144		E0			
	2.561	0^+_4		0.633	2^+_1	1.929	100.0	E2			
^{108}Cd	1.721	0^+_2		0.633	2^+_1	1.088	100.0	E2			[67]
	1.913	0^+_3		1.602	2^+_2	0.312	49.0	E2			
				0.633	2^+_1	1.280	51.0	E2			
				0.0	0^+_1	1.913		E0			
	2.375	(0^+_4)		1.602	2^+_2	0.773[a]	<15.3				
				0.633	2^+_1	1.742	84.7	(E2)			
^{110}Cd	1.473	0^+_2	>1.25	0.658	2^+_1	0.815	100.0	E2	<40	>0.13	[33,67,220,392]
				0.0	0^+_1	1.473		E0	<31		
	1.731	0^+_3	>1.39	1.476	2^+_2	0.256	14.3	E2	<1680	>0.0030	
				0.658	2^+_1	1.074	85.7	E2	<7.9	>0.63	
				0.0	0^+_1	1.731		E0	<0.12		
				1.473	0^+_2	0.258		E0	<2.5		
	2.079	0^+_4		1.784	2^+_3	0.295	78.3	E2	[100][b]		[67,220,384]
				1.476	2^+_2	0.603	<18	E2	[<0.65][b]		
				0.658	2^+_1	1.422	21.7	E2	[0.011][b]		
				1.473	0^+_2	0.605		E0			
				0.0	0^+_1	2.078		E0			
^{112}Cd	1.224	0^+_2	4.2(11)	0.618	2^+_1	0.607	99.9	E2	51(14)	0.098	[33,67,393]
				0.0	0^+_1	1.224	0.1	E0	37^{+9}_{-11}		
	1.433	0^+_3	$1.9(1)\times10^3$	1.312	2^+_2	0.121	34.7	E2	99(16)	0.051	
				1.224	0^+_2	0.209	3.8	E0	10.6(16)		
				0.618	2^+_1	0.816	59.8	E2	0.0121(17)	413	
				0.0	0^+_1	1.433	1.6	E0	0.87(12)		
	1.871	0^+_4		1.469	2^+_3	0.403	9.8	E2			[67]
				1.312	2^+_2	0.559	3.1	E2			
				0.618	2^+_1	1.254	87.2	E2			
	2.301	0^+_5	>0.623	1.469	2^+_3	0.832	32.6	E2	<23	>0.22	
				0.618	2^+_1	1.683	67.4	E2	<1.4	>3.6	
	2.650	0^+_6	$0.23(^{+12}_{-6})$	1.312	2^+_2	1.338	12.4	E2	$2.2(^{+7}_{-12})$	2.3	[67]
				0.618	2^+_1	2.033	87.6	E2	$1.9(^{+5}_{-11})$	2.6	
	2.773	$(0)^+_7$	>0.693	2.231	2^+_6	0.542	16.1	E2	<88	>0.057	[67]
				1.312	2^+_2	1.461	83.9	E2	<3.2	>1.6	
	2.834	0^+_8	>0.347	2.122	2^+_4	0.713	13.1	E2	<36	>0.14	[67]
				1.312	2^+_2	1.522	18.0	E2	<1.1	>4.5	
				0.618	2^+_1	2.217	68.9	E2	<0.65	>7.7	
	2.883	0^+_9	>0.693	2.156	2^+_5	0.727	21.9	E2	<27	>0.19	[67]
				1.469	2^+_3	1.414	60.8	E2	<2.7	>1.9	
				1.312	2^+_2	1.571	17.3	E2	<0.46	>11	
	3.252	0^+_{11}	$0.17(^{+58}_{-8})$	0.618	2^+_1	2.634	100.0	E2	$0.80(^{+74}_{-62})$	6.3	[67,394,395]
	3.353	0^+_{12}	0.13(4)	0.618	2^+_1	2.736	100.0	E2	0.9(3)	5.6	[67]
	3.452	(0^+_{13})		2.507	1^-_1	0.945	100.0	E1			[67]
	3.929	$(0)^+_{14}$	≤0.9	0.618	2^+_1	3.312	100.0	[E2]	>0.049	<102	[67]

[a] E_γ from level energy difference [67].
[b] Relative B(E2) values [384].
Additional 0^+ states from β-decay and (^{3}He,n), (d,p), (n,n′), (p,p′), (d,d′) reaction studies (no γ-decay reported) [67]:
^{108}Cd: (0^+_5): ~3.800 MeV;
^{110}Cd: 0^+_5, (0^+_6), 0^+_7, 0^+_8, (0^+_9), $0^+_{10,11}$: 2.662, 2.993, 3.148(3), 3.427(3), 3.489(3), 4.024(4), 4.128(4) MeV;
^{112}Cd: 0^+_{10}: 2.924(29) MeV.

rather uncertain assignment of the 0^+_2 in ^{120}Cd – the β-decay work of Batchelder et al., performed in Oak Ridge [368], proposes a new level at 1136 keV, previously unobserved, as the 0^+_2 state (circle symbol in Section 4.4(a)).

4.4.3. The Te isotopes

According to macroscopic–microscopic mean field calculations of Moeller et al. [59], an oblate–prolate shape coexistence scenario is expected in Te isotopes for A = 116 and 118, i.e., around the neutron mid-shell at N = 66. For lighter Te systems, a prolate deformed minimum with β_2 = 0.1–0.2 is predicted, while heavier systems show an oblate deformation. Similar features appear in Hartree–Fock–Bogoliubov calculations based on the Gogny force of Hilaire and Girod [198,249], as shown in Fig. 67. These

Table 20
Experimental information available on 0^+ excitations in Cd isotopes (A = 114–122), see also Fig. 59 and caption of Table 8 for detailed explanations. In ^{120}Cd, the state located at 1.136 MeV has been proposed as a (0^+) state by Batchelder et al. [368], and interpreted as a possible band head of an excited band structure.

Nucleus	E_i [MeV]	I_i^π	$T_{1/2}$ [ps]	E_f [MeV]	I_f^π	E_γ or E_{e^-} [MeV]	BR [%]	E/Mλ	B(E/Mλ)/ρ^2(E0) [W.u.]/[m.u.]	HF	Refs.
^{114}Cd	1.135	0_2^+	9.9(6)	0.558	2_1^+	0.576	99.9	E2	27.4(17)	0.18	[33,67]
				0.0	0_1^+	1.135	0.1	E0	19.0(20)		
	1.306	0_3^+	$4.7(3)\times10^3$	1.210	2_2^+	0.096	55.5	E2	127(16)	0.039	[67,396]
				1.135	0_2^+	0.171	0.8	E0	0.52(8)		
				0.558	2_1^+	0.747	32.2	E2	0.0026(4)	1923	
				0.0	0_1^+	1.306	11.5	E0	1.50(22)		
	1.860	0_4^+	1.8(4)	1.364	2_3^+	0.495	5.7	E2	18(6)	0.28	[33,67]
				0.558	2_1^+	1.301	94.3	E2	2.4(6)	2.1	
				0.0	0_1^+	1.860		E0	$0.91(^{+33}_{-35})$		
	2.438	0_5^+	>0.90	1.210	2_2^+	1.228	7.0	E2	<0.5	>10	[33,67,220,397]
				0.558	2_1^+	1.879	81.6	E2	<0.67	>7.5	
				0.0	0_1^+	2.438	11.4	E0	<0.1		
	2.554	0_6^+	$0.32(^{+12}_{-7})$	1.860	0_4^+	0.695		E0	85(32)		[33,67,220,397]
				1.364	2_3^+	1.189	15.3	E2	3.5	1.4	
				0.558	2_1^+	1.995	84.7	E2	1.5	3.3	
				0.0	0_1^+	2.554		E0	28(9)		
	2.637	0_7^+	$0.25(^{+6}_{-4})$	1.210	2_2^+	1.427	10.8	E2	1.3	3.8	[67,220,397]
				0.558	2_1^+	2.078	89.2	E2	1.6	3.1	
	3.053	0_9^+		2.820	4_7^+ [a]	0.233	0.1				[67]
				2.219	2_6^+	0.834	4.9	(E2)			
				2.048	2_5^+	1.005	6.9	[E2]			
				0.0	0_1^+	3.053	88.2	[E0]			
	3.222	0_{10}	$0.14(^{+9}_{-4})$	1.210	2_2^+	2.013	100				[67]
^{116}Cd	1.283	0_2^+	65(4)	1.213	2_2^+	0.069	18.0	[E2]	$3.0(8)\times10^4$ [b]		[67]
				0.513	2_1^+	0.769	82.0	[E2]	0.79(22)	6.3	
	1.380	0_3^+	1.15(23)	0.513	2_1^+	0.867	100.0	[E2]	30(6)	0.17	
	1.928	0_4^+		0.513	2_1^+	1.415	100.0	[E2]			
^{118}Cd	1.286	0_2^+	9.7(14)	0.488	2_1^+	0.798	100.0	[E2]	5.3(8)	0.94	[67]
	1.615	0_3^+	<7.1	1.270	2_2^+	0.346	<4.9	[E2]	>13	<0.38	
				0.488	2_1^+	1.127	95.1	[E2]	>1.2	<4.2	
	2.074	0_4^+		0.488	2_1^+	1.586	100.0	[E2]			
^{120}Cd	1.136	(0^+)		0.506	2_1^+	0.630	100.0				[67,368]
	1.389	0_2^+	<13	0.506	2_1^+	0.883	100.0	[E2]	>2.3	<2.2	
	1.745	0_3^+	<13	0.506	2_1^+	1.239	100.0	[E2]	>0.42	<12	
^{122}Cd	1.705	$0_2^{(+)}$		0.569	2_1^+	1.135	100.0	Q			[67]
	1.992	$0_3^{(+)}$		0.569	2_1^+	1.422	100.0	Q			

[a] Unreasonable decay.
[b] Unreasonably large value.
Additional 0^+ states from (t,p) reaction studies (no γ-decay reported) [67,398]:
^{114}Cd: $0^+_{8,11}$, $(0)_{12}$: 2.832(2), 3.253(3), 3.604(7) MeV.

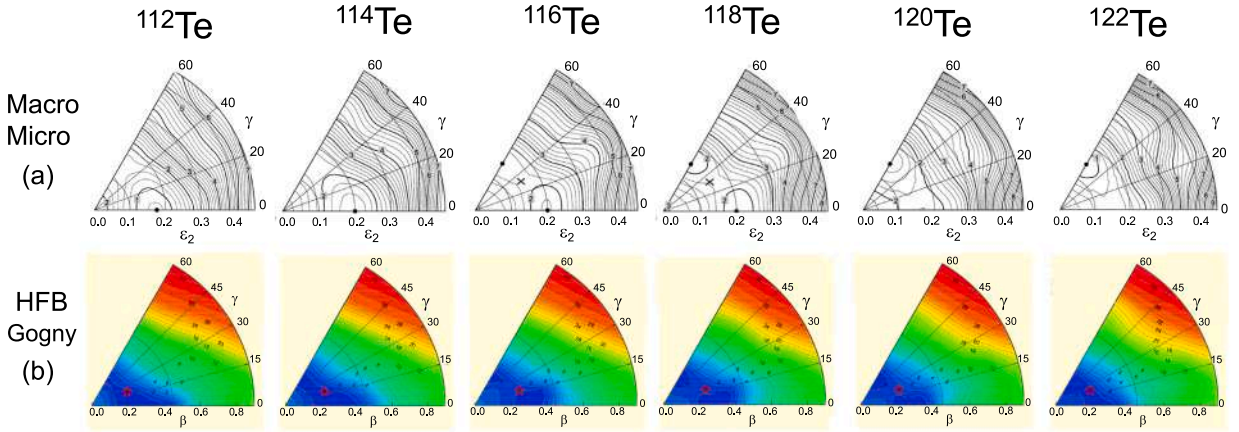

Fig. 67. Potential energy surfaces for even–even $^{112-122}$Te obtained from different type of calculations: (a) macroscopic–microscopic mean field model of Moeller et al. [59], (b) Hartree–Fock–Bogoliubov calculations based on the Gogny force, by S. Hilaire and M. Girod [198,249]. Energies (in MeV) are given on the contour plots.
Source: Adapted from [59,250].

Table 21
Experimental information available on 0^+ excitations in Te isotopes (A = 114–128). In ^{116}Te, no firm experimental evidence for excited 0^+ is present in the literature (a 0^+ state at 1060 keV, proposed by Kumpulainenet al., [399] has not been confirmed [67]). See also Fig. 34, 35 and caption of Table 8 for detailed explanations.

Nucleus	E_i [MeV]	I_i^π	$T_{1/2}$ [ps]	E_f [MeV]	I_f^π	E_γ or E_{e^-} [MeV]	BR [%]	E/Mλ	B(E/Mλ)/ρ^2(E0) [W.u.]/[m.u.]	HF	Refs.
^{114}Te	1.348	(0_2^+)		0.709	2_1^+	0.639	100.0				[67]
	1.861	(0_3^+)		0.709	2_1^+	1.152	100.0				
^{118}Te	0.957	0_2^+	55(45)	0.606	2_1^+	0.352	99.1	(E2)	56	0.089	[33,67]
				0.0	0_1^+	0.957	0.9	E0	16(9)		
	1.517	0_3^+		1.151	2_2^+	0.367	43.0	(E2)			
				0.957	0_2^+	0.560	1.7	E0			
				0.606	2_1^+	0.912	55.1	[E2]			
				0.0	0_1^+	1.517	0.2	E0			
^{120}Te	1.103	0_2^+		0.560	2_1^+	0.543	100.0	E2			[67,220]
				0.0	0_1^+	1.103		E0			
	1.613	0_3^+		1.103	0_2^+	0.511		E0			
				0.560	2_1^+	1.053	100.0	[E2]			
				0.0	0_1^+	1.614		E0			
	1.937	0_4^+		1.535	2_3^+	0.402	14.0	E2			[67,400]
				1.201	2_2^+	0.735	81.0	E2			
				0.560	2_1^+	1.375	5.0	E2			
^{122}Te	1.357	0_2^+	>1.39	0.564	2_1^+	0.793	100.0	[E2]	<36	>0.14	[33,67,220]
				0.0	0_1^+	1.357	0.027	E0	<0.08		
	1.747	0_3^+	>1.32	1.257	2_2^+	0.490	29.1	[E2]	<123	>0.041	
				0.564	2_1^+	1.183	70.9	[E2]	<3.7	>1.4	
	1.940	0_4^+	>1.39	1.357	0_2^+	0.583	0.15	E0	<0.9		
				1.257	2_2^+	0.683	95.3	[E2]	<73	>0.068	
				0.564	2_1^+	1.376	4.5	[E2]	<0.1	> 50	
				0.0	0_1^+	1.941	0.095	E0	<0.2		
	2.297	0_5^+	$0.9(^{+6}_{-3})$	0.564	2_1^+	1.733	100.0	[E2]	1.12	4.5	
	2.499	0_6^+	$0.7(^{+8}_{-3})$	1.257	2_2^+	1.242	22.2	[E2]	1.7	2.9	
				0.564	2_1^+	1.936	77.8	[E2]	0.65	7.7	
	2.756	0_7^+	$0.143(^{+34}_{-24})$	1.257	2_2^+	1.499	53.8	[E2]	7.9	0.63	
				0.564	2_1^+	2.192	46.2	[E2]	1	5	
^{124}Te	1.657	0_2^+	$0.55(^{+14}_{-7})$	0.603	2_1^+	1.055	100.0	E2	20(4)	0.25	[33,67]
				0.0	0_1^+	1.658	0.016	E0	8.3(26)		
	1.883	0_3^+	$0.76(^{+21}_{-14})$	1.657	0_2^+	0.226	0.1	E0	22(6)×10		
				1.326	2_2^+	0.557	99.6	E2	$350(^{+7}_{-10})$	0.014	
				0.0	0_1^+	1.883	0.3	E0	142(32)		
	2.153	0_4^+		1.326	2_2^+	0.828	80.7	E2			
				0.603	2_1^+	1.550	19.3	[E2]			
	2.308	0_5^+	<0.25 ns	1.883	0_3^+	0.426	0.036	E0	0.7(5)		
				1.657	0_2^+	0.652	<0.007	E0	<0.0011		
				0.603	2_1^+	1.706	99.95	E2	>0.004	<1250	
				0.0	0_1^+	2.310	<0.007	E0	<0.0024		
^{126}Te	1.873	0_2^+	$0.67(^{+8}_{-6})$	0.666	2_1^+	1.207	100.0	E2	$8.8(^{+8}_{-11})$	0.57	[67,401]
	2.114	0_3^+	$0.52(^{+7}_{-6})$	1.420	2_2^+	0.693	25.9	E2	$47(^{+7}_{-8})$	0.11	
				0.666	2_1^+	1.447	74.1	E2	3.4(5)	1.47	
	2.640	(0_5^+)	0.152(14)	1.420	2_2^+	1.220	25.0	E2	2.5(2)	2.0	
				0.666	2_1^+	1.973	75.0	E2	$9.2(^{+7}_{-6})$	0.54	
	2.681	(0_6^+)	$0.085(^{+5}_{-4})$	1.420	2_2^+	1.259	30.0	E2	17(1)	0.29	
				0.666	2_1^+	2.016	70.0	E2	3.8(2)	1.3	
^{128}Te	1.979	0_2^+	$1.4(^{+12}_{-8})$	0.743	2_1^+	1.236	100.0	[E2]	3.6(17)	1.4	[67,402]
	2.308	0_3^+	>1.2	1.520	2_2^+	0.788	28.1	[E2]	<13	>0.38	
				0.743	2_1^+	1.565	71.9	(E2)	<1.0	>5.0	
	2.482	0_4^+	$0.201(^{+55}_{-35})$	0.743	2_1^+	1.739	100.0	[E2]	4.6(10)	1.09	[402]
	2.517	0_5^+		1.520	2_2^+	0.997	100.0	[E2]			[402]

Additional 0^+ states in Te isotopes:
^{124}Te, from double-β decay studies of ^{124}Sn (very uncertain identification) [403,404]: 1.157, 2.020 MeV;
^{126}Te, from (p,t) reaction studies (no γ-decay reported) [220,405,406]: 0_4^+: 2.582(4) MeV.

predictions are supported by the energy systematics of the first excited 0^+ states of Te isotopes, shown in Fig. 59, which displays the typical parabolic trend (a fingerprint of shape coexistence), as also observed in Sn and Cd chains.

Traditionally, Te isotopes have been considered among the best examples of near-harmonic quadrupole shape vibrators, as a consequence of a rather regular pattern of equally-spaced excitations built on a weakly-deformed ground state, particularly evident for Te isotopes with A = 108–124, (see figure of yrast-state pattern in Ref. [407]). However, lifetime measurements performed

for 2^+ and 4^+ states in these nuclei pointed toward a more complex scenario, with possible appearance of γ-soft and rotor-like behavior, when moving away from mid-shell. From a systematic analysis of low-lying states, in comparison with IBM2 calculations, Rikovska et al. [408] suggested that considerable mixing between two coexisting configurations (an intruder structure and a normal vibrational configuration) should exist in even–even Te, in analogy to Cd and Sn isotopes. Indeed, information on excited structures possibly built on 0^+ states have been obtained from γ-spectroscopy studies mainly based on (α,xn) reactions on Sn targets, and (n,γ) and (n,n'γ) studies, pointing to a significant degree of collectivity in Te isotopes with A = 118 to 124. In particular, in ^{118}Te, at the middle of the shell (N = 66), lifetime measurements provided a large value (B(E2) = 60^{+35}_{-17} W.u.) for the $2^+_3 \rightarrow 0^+_2$ transition, suggesting the existence of a band built on the 957-keV 0^+_2 state, with 4^+ and 6^+ states tentatively assigned at 1976 and 2517 keV (with no in-band decays observed) [409]. In ^{122}Te, lifetimes measurements by Hicks et al. [410] also reported and extremely large B(E2) value for the $2^+_3 \rightarrow 0^+_2$ transition (B(E2) = 194^{+26}_{-24} W.u.), which could point to a band structure built on the 0^+_2 state located at 1357 keV (with band members tentatively identified up to (14^+)). Such a large B(E2;$2^+_3 \rightarrow 0^+_2$) value is however difficult to be explained in the context of similar B(E2) values in this region. A significant collectivity was also reported for the $2^+_3 \rightarrow 0^+_2$ in ^{124}Te (B(E2) = 20(3) W.u.), as follows from different measurements (see Hicks et al. [411] and references therein).

As summarized in Fig. 34, 35 and in Table 21, several 0^+ excited states have been observed in Te isotopes (up to 6 in ^{122}Te). In some cases, a significant population has been reported in two proton transfer reactions (in particular for 0^+_3 states in ^{120,122,126}Te [412,413]), what supports a shape coexistence scenario [15]. Existing data point to a strong shape mixing situation, with no clear evidence for retarded decays from excited 0^+ states caused by a significant shape change (small HFs are reported for B(E2) decays from 0^+ states). This is also caused by the limited precision of the experimental measurements (most of the available lifetimes are only limits) and by the absence of a detailed comparison with state-of-the-art theory predictions.

4.5. The Z = 82 region: Pt, Hg, Pb and Po

The Z ~ 82 region, in particular on the neutron-deficient side (A ~ 190–210), has been historically indicated as one of the most interesting regions where shape isomerism might occur [221–225,414]. Extended, systematic theory investigations based on Hartree–Fock–Bogoliubov calculations, macroscopic–microscopic models, as well as Energy Density Functional approaches, predict in systems like Os, Pt, Hg, and Pb, potential energy surfaces characterized by complex pattern, all showing distinct principal and secondary minima with large axial deformation, e.g., $\beta_2 \sim$ 0.5–0.6 [56,59,106,225,414–416]. In a number of cases, the minima differ in energy by ~2–5 MeV, and are separated by barriers with heights ranging from ~2 to 4 MeV, which for heavier masses are also rather stiff in the direction of triaxiality. Fig. 68 illustrates one-dimensional potential energy surfaces for Pt, Hg and Pb isotopes with neutron number N = 104–114, as a function of the quadrupole deformation parameter β_2 (upper axis), as follows from macroscopic–microscopic calculations of Pomorski et al. [415], based on the Lublin-Strasbourg-Drop (LSD) macroscopic energy and shell plus pairing-energy corrections. In the figure, red dots correspond to the experimental 0^+ band-head energies (~4–6 MeV above the ground state), extrapolated from the study of superdeformed (SD) yrast bands (see Section 3.2.2 and Fig. 28). Very good agreement is found with theory predictions for the energy of the secondary minimum at large deformation, what supports the strong complementarity of theory searches for shape isomers at spin 0 and the study of superdeformation at high spins.

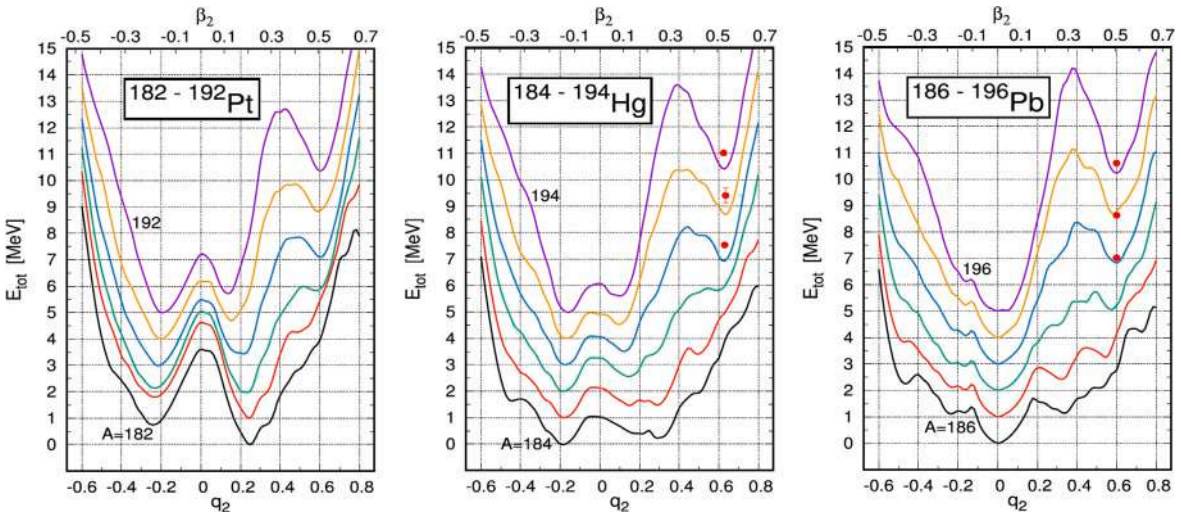

Fig. 68. Potential energies of Pt, Hg, and Pb isotopes with 104 ≤ N ≤ 114, as a function of the elongation parameter q_2 or quadrupole deformation β_2 (upper axis), as obtained from macroscopic–microscopic model of Pomorski et al. [415]. All local minima correspond to reflection symmetric shapes. Experimental energies of SD minima (red dots), extrapolated at spin 0^+, are taken from Ref. [148] (see also Fig. 28).
Source: Adapted from [415].

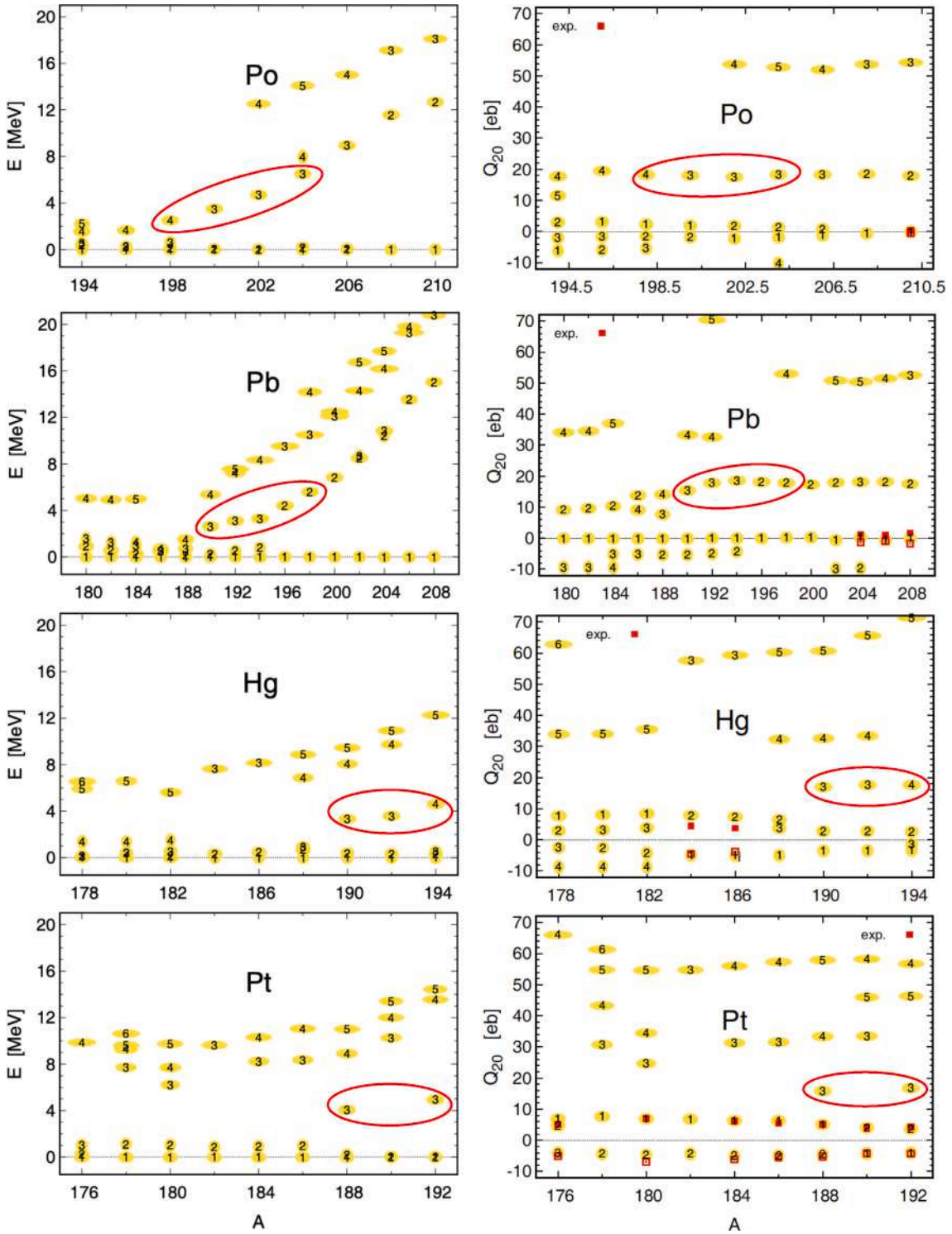

Fig. 69. Predictions from the macroscopic–microscopic model based on the Lublin-Strasbourg-Drop approach [417]. Left: Energies of ground state (label 1) and excited 0^+ states associated to local minima (labels 2, 3, . . .) for isotopic chains ranging from Pt to Po. Each label is surrounded by an ellipse the length of which corresponds to the elongation of the nucleus in that given state. Right: corresponding electric quadrupole moments obtained for the ground and the excited 0^+ states, with a comparison with available experimental data (boxes) [67].
Source: Adapted from [417].

While the observation of shape isomerism associated with very elongated (SD) shapes might require a significant experimental effort, at the limit or even beyond the present experimental capabilities due to the high density of states above 4 MeV excitation energy, theory generally supports the chance of observing a shape-coexistence scenario in this Z ∼ 82, A ∼ 200 region at lower excitations. Additional low-lying prolate or oblate minima with smaller deformation ($\beta_2 \sim \pm 0.2$), separated by modest barriers, are in fact appearing in the PES below 2 MeV. A number of yet unknown excited 0^+ states associated with different shapes (from moderately-deformed oblate and prolate to super- and hyper-deformed prolate shapes) is predicted to exist in even–even nuclei of the region between Pt and Ra, according to various theory approaches. As an example, the macroscopic–microscopic LSD model [417] predicts for Pt to Po isotopes, up to four excited 0^+ states of prolate and oblate nature (right column of Fig. 69) within a 2 MeV excitation-energy range (left column), while significantly elongated (prolate) shapes appear at higher excitation energies (typically above 4 MeV) – they correspond to the predicted candidates for shape isomers as discussed above. In the figure, shape-isomer structures which might be at reach in experimental investigations (e.g., with still accessible excitation energies, ∼4 MeV) are included in the red contours.

Experimentally, about 100 excited 0^+ states have been located in Pt, Hg, Pb and Po isotopes, as summarized in Tables 24, 25, 22, 23, and 26. As also shown in Fig. 34, in about 20 cases only, the information on B(E2) values is available, corresponding to hindrance factors concentrated below 10, what suggests a scenario of strong shape mixing. As evidenced in Fig. 35, in four cases, i.e., 0^+_2 in ^{206}Pb and ^{208,212,214}Po, the decay to 2^+_1 is firmly reported as hindered. In addition, in the case of ^{196}Pt, the decay from 0^+_3 to 2^+_2 also points to a very large hindrance value. While in the case of Pb and Po the structure of the 0^+_2 states is rather well interpreted within a shell model approach, with wave functions strongly dominated by neutron-hole components (see discussion in Sections 4.5.2 and 4.5.3), in the case of ^{196}Pt, as discussed in Section 4.5.3, the 0^+_3 state is seen as a strong candidate for a spherical or γ-soft vibration. Furthermore, two retarded decays are also identified in the neighboring Os isotopes (Z = 76), i.e., 0^+_2 in ^{186}Os (at 1.061 MeV, $T_{1/2} = 148(^{+83}_{-57})$ ps, B(E2) = 0.066 W.u., HF = 75.8) and 0^+_3 in ^{192}Os (at 1.206 MeV, $T_{1/2}$ = 35(13) ps, B(E2) = 0.24(9) W.u., HF = 20.8). A clear interpretation of these retardations in Os isotopes is missing – they lie in a region where several 0^+ states have been originally interpreted as phonon excitations [418], although their nature might be related to triaxiality, as recently proposed by Otsuka et al. [419] (see Section 5).

Fig. 70 shows the excited 0^+ states (up to 0^+_4) located experimentally in Pt to Po even–even isotopes. The parabolic behavior of 0^+_2 states, centered around N ∼ 104 (midshell), is the typical fingerprint for shape coexistence. A complete picture of this phenomenon emerges from the energy systematics of the positive parity excited states, which are members of the rotational bands built on these intruder 0^+_2 excitations (see, e.g., Fig. 7 and Sections 4.5.1 and 4.5.2).

4.5.1. The Hg isotopes

Fig. 71 shows the Potential Energy Surfaces for even–even $^{178-188}$Hg from different types of calculations, all predicting a complex scenario of oblate–prolate shape coexistence at moderate deformations, i.e., $\beta_2 \sim 0.1$–0.2 (see also Figs. 68 and 70). Experimentally, the first indication of shape coexistence in isotopes around Z = 82 came from studies at ISOLDE of the optical hyperfine structure in neutron-deficient Hg nuclei, which revealed in ^{185}Hg and ^{187}Hg a huge and unexpected isotope shift, corresponding to a large deformation change ($\Delta\beta_2^2 > 0.1$) [14]. An odd–even staggering of mean-square charge radii of Hg isotopes, later discovered in laser-spectroscopy studies [108,420,421], significantly contributed to establishing the idea of shape coexistence at low excitation energy, with its origin being related to the action of the monopole tensor term of the nuclear force [108].

Over the years, a substantial amount of information on Hg isotopes has been added using various experimental techniques, from decay studies to optical spectroscopy studies and in-beam γ-ray/electron spectroscopy (see, e.g., [24,422,423]). Microscopically, the "intruder" configurations giving rise to the striking parabolic pattern in the energy systematics of positive parity excited states of even–even isotopes (see Fig. 7) are located in secondary minima in the potential wells and arise from occupation of proton orbitals which lie above the Z = 82 closed shell. These orbitals can be accessed at a low cost in energy at large prolate or oblate deformations, leading to excited 0^+_2 states dominated by protons (2p-2h) excitations in both Hg and Pb.

As shown in Figs. 72 and 73, the structure of Hg isotopes with A = 180–190 is characterized by weakly deformed ($\beta_2 \sim 0.1$) ground-state bands which are crossed at low spin by more deformed configurations ($\beta_2 \sim 0.2$–0.3), as follows from moment of inertia estimates, lifetimes measurements and Coulomb excitation studies performed at various facilities (e.g., with MINIBALL at ISOLDE, GALILEO at LNL, GAMMASPHERE at Argonne) [424,425,428,429]. The analysis of experimental data points to near-degenerate nuclear states characterized by different shapes, with the ground state of $^{182-188}$Hg weakly deformed with oblate-like nature, while a prolate-like band is built on 0^+_2, the energy of which lowers when going toward neutron midshell $N = 104$. The admixture of the prolate deformed configurations into the ground state was estimated combining information from available $\rho^2(E0;0^+_2 \rightarrow 0^+_1)$ measurements, perturbation of energies in the rotational bands and hindrance factors for the α decay of Hg into Pt, yielding values scattered between few % and a maximum of ∼17% around N = 102–104 (see [24] and references therein). Similar analyses performed for the 2^+_1 states suggest an inversion of configurations between ^{182}Hg and ^{184}Hg, with a maximum mixing strength (∼50%) for the 2^+_1 in ^{184}Hg, at midshell. In the case of the most proton-rich nucleus ^{178}Hg, yrast-state lifetime measurements were obtained, up to spin 8^+, in an experiment performed at Jyväskylä with the JUROGAM array coupled to the RITU spectrometer [430]. Transition probability B(E2) for the measured quadrupole gamma-rays, absolute values of transition quadrupole moments Q_t and deformation parameters β_2, were deduced. The data point to a 2^+_1 deformation comparable with the ground state deformation, as also observed in heavier systems. A significantly larger value of $\beta_2 \sim 0.4$ (intermediate between normal and superdeformation) is instead deduced for higher spin states, as compared to excited states in heavier Hg isotopes, what indicates ^{178}Hg as a point where the nuclear structure significantly changes. Such structural change becomes also apparent from the kinematic moment of inertia behavior along the yrast line (see Fig. 73).

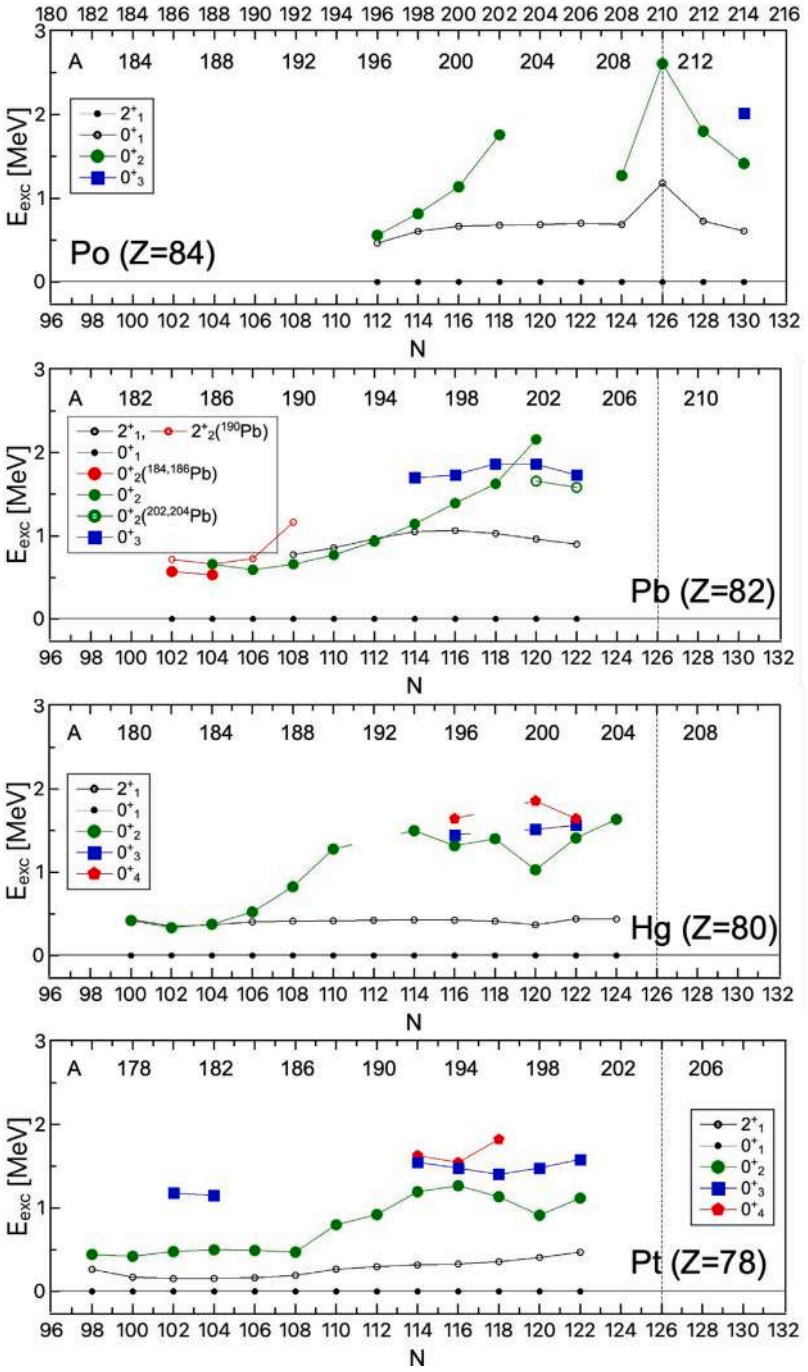

Fig. 70. Systematics of the energies of the $0^+_{1,2,3,4}$ states observed in the Z = 82 region of Pt, Hg, Pb and Po nuclei. The first 2^+ excitation is also given as a reference (open circles). The dashed vertical line marks the N = 126 neutron shell closure. In case of Pt and Hg isotopes, levels are connected according to their ordered appearance in energy, while in Pb 0^+_2 excitations are connected according to their configuration (red circles for prolate, green circles for oblate) (see also Fig. 7 and Tables 24, 25, 22, 23 and 26 for details).

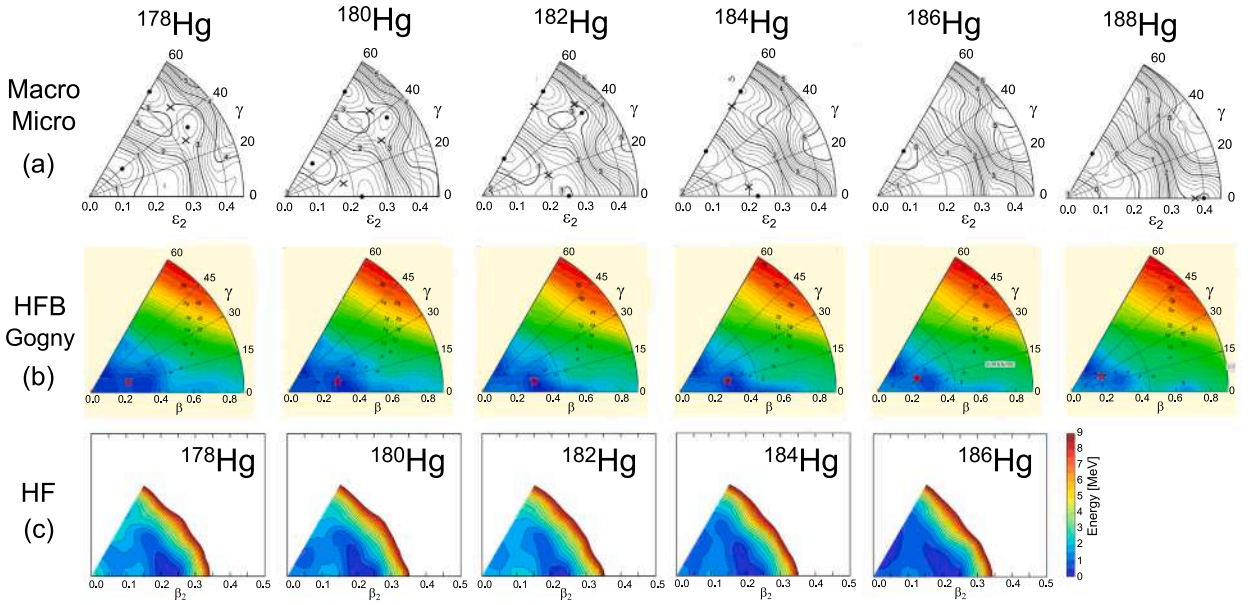

Fig. 71. Potential energy surfaces for even–even $^{178-188}$Hg obtained from different types of calculations: (a) macroscopic–microscopic mean field model of Moeller et al. [59], (b) Hartree–Fock–Bogoliubov calculations based on the Gogny force, by S. Hilaire and M. Girod [198,249], and (c) constrained Hartree–Fock calculations by Tsunoda et al. The Hamiltonian taken in Refs. [108,421] is used.
Source: Adapted from [59,250].

The experimental results for low-lying states in $^{182-188}$Hg are found to be well reproduced by the simple two-state mixing model described in detail in Ref. [31], thus supporting the underlying assumption of two unperturbed different configurations that mix when states with equal spin and parity are close in energy, as schematically depicted in Fig. 9(b'). This situation is similar to what observed in the lighter A ∼ 70 Kr region (see Section 4.3.2). In the case of ^{178}Hg, the schematic mixing model reproduces the data only assuming a much reduced mixing of the prolate structure into the 2_1^+ state (with 80% contribution of oblate deformed structure in the wave function similar to the ground state), while the 4_1^+ state wave function changes to an 80% portion of the prolate band, and the higher-lying states are described with an unperturbed prolate rotational band with a large deformation (e.g., $\beta_2 \sim 0.4$).

From a broader theory perspectives, the experimental results for excited states in Hg isotopes have been compared with several theoretical models based on state-of-the-art beyond mean-field, generalized Bohr Hamiltonian and interacting boson model with configuration mixing approaches [416,429,431–433]. In general, for very heavy nuclei like Hg, the currently available computational resources prevent systematic calculations including triaxial degrees of freedom, at variance from the extensive calculations performed in Kr isotopes (see Section 4.3.2). This might be the reason for only partial agreement obtained with experimental data, being the general behavior of both oblate and prolate structures rather well reproduced, although the relative positions of the two bands and their mixing is often not fully accounted for (see eg., [429]). We note that the peculiar phenomenon of shape staggering between the spherical ground states of even–even Hg's with A = 180,182, 184 and 186, and the deformed ground state of even–odd Hg's with A = 181, 183 and 185, was originally reproduced by minimizing the deformation energy calculated with the Strutinsky's shell correction method [223]. This shape staggering has also been recently obtained by microscopic Monte Carlo Shell Model calculations for Hg isotopes, which are computationally very demanding (see the PES in Fig. 71(c)) [108,421].

As shown in Fig. 70, in Hg isotopes heavier than A = 190, the parabolic trend followed by 0_2^+ interrupts and multiple 0^+ excitations appear, of unknown nature, with no indication of band structures built on these states.

4.5.2. The Pb isotopes

The situation in Pb nuclei, with a closed Z = 82 proton shell, has parallels with the Z = 80 (Hg) nuclei, in which shape coexistence was first observed in laser spectroscopy studies, and later confirmed by extensive investigations, in particular γ and electron in-beam spectroscopy, as discussed in Section 4.5.1. Compared to Hg, a more complex and richer situation is expected to occur at Z = 82, since deformed shapes like the ones observed in Hg isotopes are foreseen, but with the addition of a deep spherical minimum which naturally dominates the ground and excited state structures in Pb nuclei, near the N = 126 closed neutron shell. By removing a significative number of neutrons, calculations predict the appearance of three potential minima, i.e., spherical, oblate, and prolate, all at low energies, as shown, for example in Figs. 68 and 69 for ^{186}Pb and ^{188}Pb. According to Nilsson–Strutinsky calculations of potential energy surfaces, the prolate secondary minimum is expected to have a parabolic energy dependence on neutron number with its minimum near mid-shell, at N = 104 [224,434].

Experimentally, the investigation of such a complex spectroscopic situation has been made even harder by the fact that Pb nuclei around N = 104, as compared to Hg isotopes, are much more neutron deficient, therefore more difficult to populate, in particular for

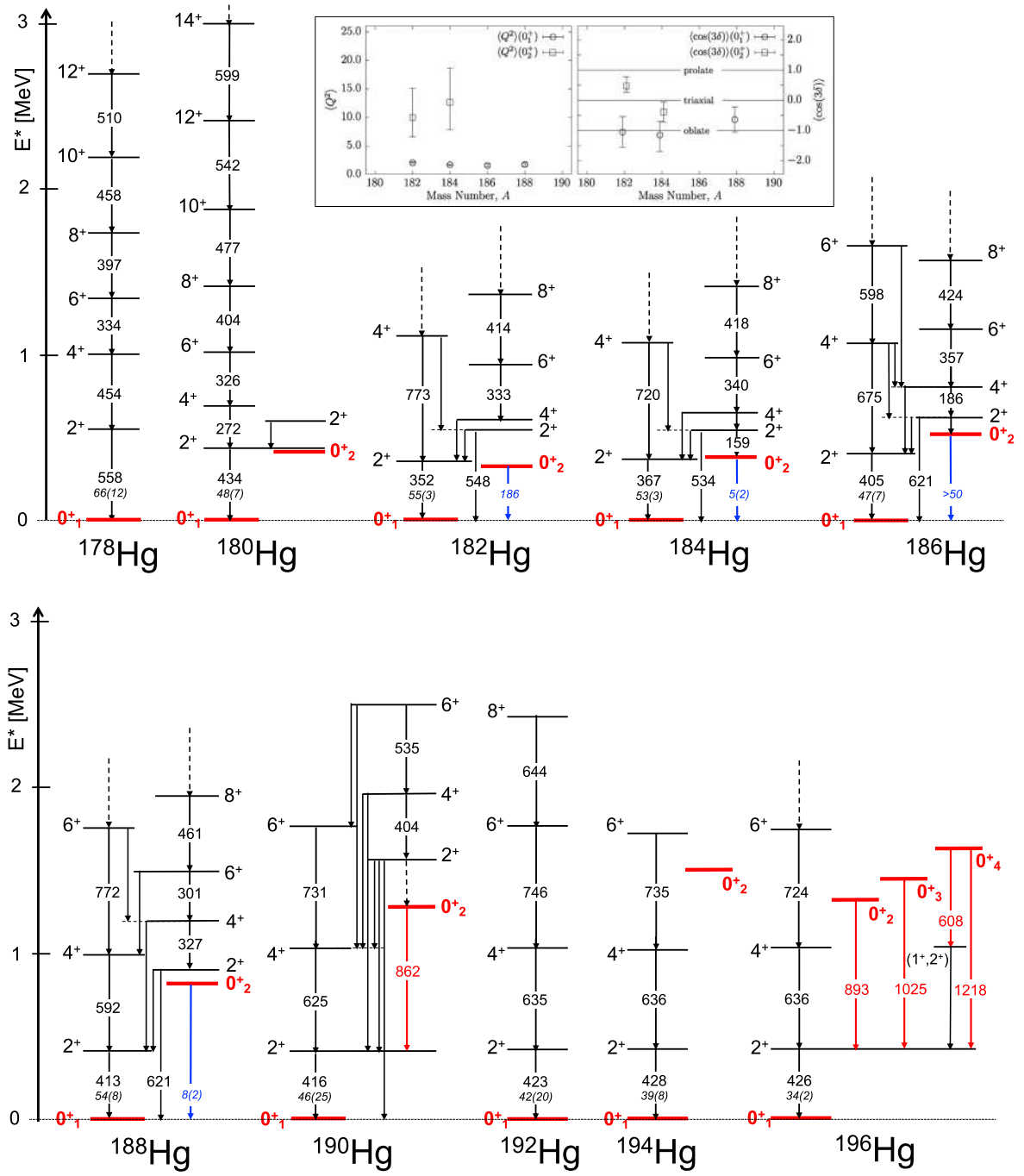

Fig. 72. Partial level schemes of even–even Hg isotopes with A = 180–196 [67]. Excited 0^+ states are highlighted in red, with red and blue arrows indicating measured γ and E0 decay from 0^+ states, with energies in keV and B(E2) and ρ^2(E0) values in W.u. and m.u., respectively (in italic). Dashed arrows indicate tentative transitions or the continuation of a band to higher spins (see Table 22 for details). The inset shows $\langle Q^2 \rangle$ and $cos(3\delta)$ values representing the overall deformation and the axial asymmetry, respectively, of the 0^+_1 (open circles) and 0^+_2 (open squares) states in $^{182-188}$Hg, as extracted from the matrix elements obtained by Bree et al. [424].
Source: Inset taken from Ref. [423].

Table 22
Experimental information available on 0^+ excitations in Hg isotopes (A = 186–204). In the case of ^{192}Hg, no excited 0^+ states are reported in literature [67]. See also Fig. 34, 35 and caption of Table 8 for detailed explanations.

Nucleus	E_i [MeV]	I_i^π	$T_{1/2}$ [ps]	E_f [MeV]	I_f^π	E_γ or E_{e^-} [MeV]	BR [%]	E/Mλ	B(E/Mλ)/ρ^2(E0) [W.u.]/[m.u.]	HF	Refs.
^{182}Hg	0.335	0_2^+		0.0	0_1^+	0.335		E0	186		[33,67,425]
^{184}Hg	0.375	0_2^+[a]	0.62(21) 10^3	0.0	0_1^+	0.375		E0	4.8(16)		[33,67,424]
^{186}Hg	0.523	0_2^+	<52	0.0	0_1^+	0.523		E0	>50		[33,67]
^{188}Hg	0.825	0_2^+	204(45)	0.0	0_1^+	0.825		E0	$8.0(^{+17}_{-19})$		[33,67]
^{190}Hg	1.279	0_2^+		0.0	0_1^+	1.279	3.1	E0			[67]
				0.416	2_1^+	0.862	96.9	[E2]			
^{196}Hg	1.319	0_2^+		0.0	0_1^+	1.319	≤16	E0			[67]
				0.426	2_1^+	0.893	84.0	(E2)			
	1.451	0_3^+		0.0	0_1^+	1.451		E0			
				0.426	2_1^+	1.025	100.0	(E2)			
	1.644	0_4^+		0.0	0_1^+	1.644		E0			
				0.426	2_1^+	1.218	81.3	(E2)			
				1.037	2^+	0.608	18.7	[E2]			
^{198}Hg	1.402	0_2^+		0.0	0_1^+	1.402	1.4(3)	E0			[67]
				0.412	2_1^+	0.990	100.0	E2			
^{200}Hg	1.029	0_2^+	8(4)	0.0	0_1^+	1.029		E0	$0.023(^{+13}_{-12})$		[33,67,426]
				0.368	2_1^+	0.661	100.0	E2	8(4)	0.63	
	1.515	0_3^+		1.029	0_2^+	0.486		E0			
				0.368	2_1^+	1.147	100.0	E2			
	1.857	0_4^+		1.718	1_3^+	0.138	3.5				
				1.631	1_2^+	0.226	5.8	M1			
				1.570	1_1^+	0.287	0.6				
				1.515	0_3^+	0.342[b]		E0			
				1.254	2_2^+	0.603	1.6	[E2]			
				1.029	0_2^+	0.827[b]		E0			
				0.368	2_1^+	1.489	88.5	E2			
				0.0	0_1^+	1.857[b]		E0			
	2.117	0_5^+		1.631	1_2^+	0.486	38.8	(M1)			
				1.641	2_5^+	0.475	1.6	[E2]			
				1.718	1_3^+	0.398	59.6	M1			
				0.0	0_1^+	2.117		E0			
^{202}Hg	1.411	0_2^+		0.440	2_1^+	0.972	100.0	(E2)			[67,427]
	1.565	0_3^+		0.440	2_1^+	1.125	100.0	E2	5.8(2)	0.86	
	1.644	0_4^+		0.440	2_1^+	1.204	100.0	E2	2.6(1)	1.92	
^{204}Hg	1.636	0_2^+		0.437	2_1^+	1.199	100.0	(E2)			[67]

[a] 8.6-keV E2 branch to 367-keV 2_1^+ state was suggested from β-decay and Coulomb excitation studies, B(E2)~80 W.u. [220,425].
[b] E_γ from level energy difference [67].
Additional 0^+ states from ϵ and α decay, fusion, Coulomb excitation, (p,t) and (^{3}He,n) reaction studies (no γ-decay reported) [67,220]:
^{180}Hg: 0_2^+: 0.420 MeV;
^{182}Hg: (0_2^+): 0.328(12) MeV;
^{194}Hg: 0_2^+: 1.500 MeV;
^{196}Hg: 0_5^+: 3.0(1)×10^3 MeV;
^{198}Hg: $0_{3,4}^+$: 1.550, 1.760(15) MeV;
^{200}Hg: 0_6^+, (0_7^+), 0_8^+ : 2.246, 2.332, 2.475 MeV;
^{202}Hg: ($0_{5,6}^+$), 0_7^+, ($0_{8,9}^+$), $0_{10,11}^+$: 1.656, 1.779, 1.901(1), 2.127, 2.571(1), 2.599, 2.686 MeV;
^{204}Hg: (0_3^+): 2.359(5) MeV.

what concerns excited off-yrast states. At first, low-lying 0_2^+ excitations have been observed in even–even neutron-deficient $^{190-194}$Pb isotopes, following β or α decay of Bi and Po isotopes, respectively, as well as (α,xn) reactions [441,442]. They were ascribed to shallow oblate minima in the potential energy surface, arising from (2p-2h) proton intruder states [57]. First evidence for the existence of prolate deformed rotational bands coexisting with the expected spherical configurations was given in ^{186,188}Pb by Hesse et al. [443], employing heavy ion induced fusion-evaporation reactions and experimental setup comprising a Compton suppressed germanium array equipped with a BGO γ-multiplicity filter (the OSIRIS spectrometer in Berlin), and a recoil filter detector (RFD) to select evaporation residua from a huge background of fission products. Since that time, extensive experimental activities have been performed in this difficult region of the nuclear chart, aided by the developments in spectroscopic techniques. A major breakthrough was achieved by combining a large Ge array with a high-transmission gas-filled recoil separator, such as JUROGAM at RITU at the Jyväskylä Laboratory in Finland, for recoil-decay tagging (RDT) measurements [422].

At present, in moderately neutron-deficient Pb isotopes, oblate- and prolate-deformed structures have been found to coexist with spherical states at low spin, as shown in Figs. 7, 74 and 75. Moreover, in the ^{186}Pb nucleus (with a spherical ground state), two excited 0^+ states have been observed in an α-decay fine-structure experiment performed at GSI with the SHIP separator [58].

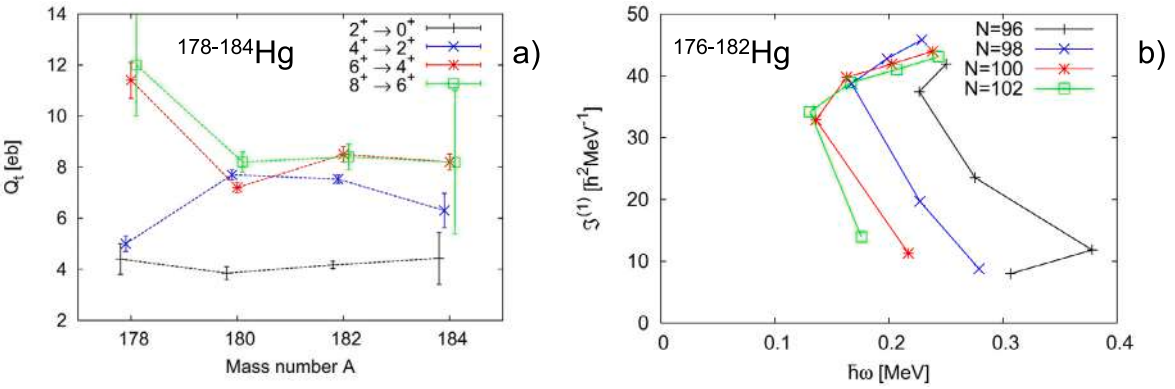

Fig. 73. Panel (a): Absolute values of transition quadrupole moments Q_t for the neutron-deficient $^{178-184}$Hg isotopes near midshell. Panel (b) Kinetic moments of inertia $\Im^{(1)}$ [149] for the $^{176-182}$Hg isotopes, as a function of frequency ω(I→I-2) for transitions along the yrast line, up to the 10^+ state.
Source: Adapted from Ref. [430].

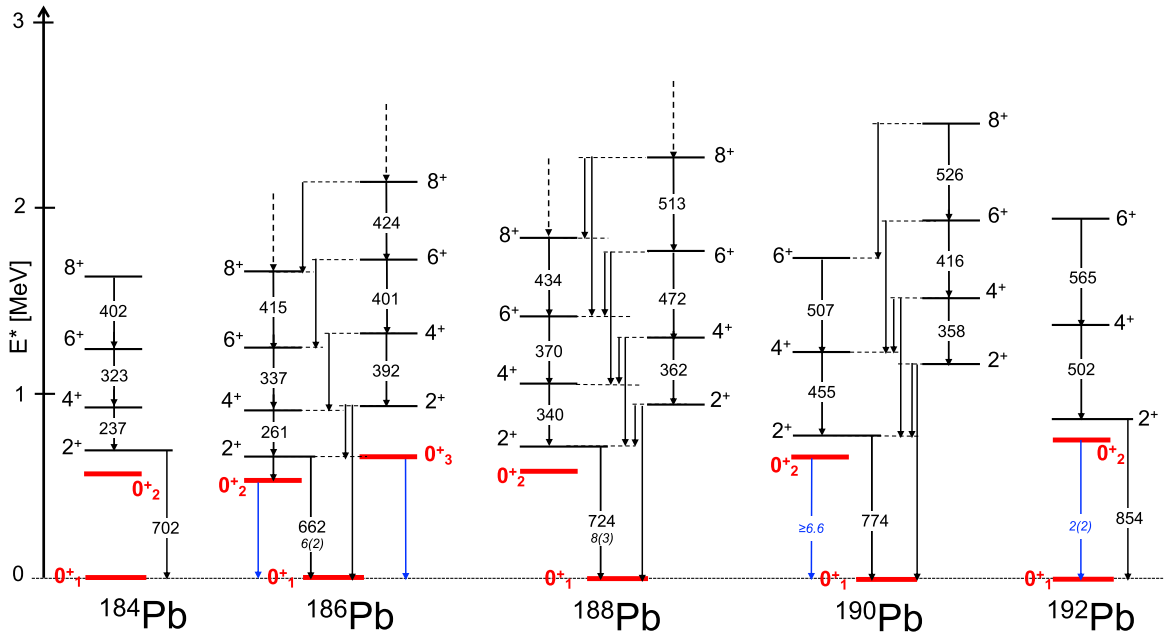

Fig. 74. Partial level schemes of even–even Pb isotopes with A = 184–192 [67]. Excited 0^+ states are highlighted in red, with red and blue arrows indicating measured γ and E0 decay from 0^+ states, with energies in keV and B(E2) and ρ^2(E0) values in W.u. and m.u., respectively (in italic). Dashed arrows indicate the continuation of a band to higher spins (see Table 23 for details).

They were associated with predominantly π(2p–2h) and π(4p–4h) excitations across the Z = 82 shell gap and assigned with deformed oblate and prolate shapes, respectively. Only very recently, an in-beam spectroscopic study at Jyväskylä, employing the electron conversion SAGE spectrometer and the recoil-decay tagging technique (RDT), firmly established the assignment of the 0^+_2 in ^{186}Pb as a state with predominantly prolate shape, and consequently, 0^+_3 as the band-head of the non-yrast band associated with predominantly oblate shape [66]. By analyzing conversion electron and γ-ray spectra obtained by gating on α particles emitted in the decay of the ^{186}Pb fusion reaction residua, a small mixing between the excited 0^+_2 and 0^+_3 states was extracted from the transition intensity balances between low-spin states. Also, the γ-ray feeding to 0^+_2 was observed to be solely coming from the 2^+_1 state, with a B(E2) transition probability of 190(80) W.u., in line with the sizeable collectivity measured for higher-spin transitions of the prolate bands in ^{186,188}Pb isotopes. In ^{186}Pb, the prolate minimum is therefore lower in energy than the oblate one [66]. As reported in Table 23, no sign of retarded decay is found from the prolate 2^+_1 excitation toward 0^+_1, in agreement with the picture of a rather reduced barrier between the prolate local minimum, at $\beta_2 \sim 0.3$, and the spherical ground state, as also shown in Fig. 68. Thus far, ^{186}Pb is the only known nucleus where the ground state and the two first excited states form a triplet of zero-spin states assigned with prolate, oblate and spherical shapes, although a similar scenario might occur in neighboring systems, as for example in ^{188}Pb.

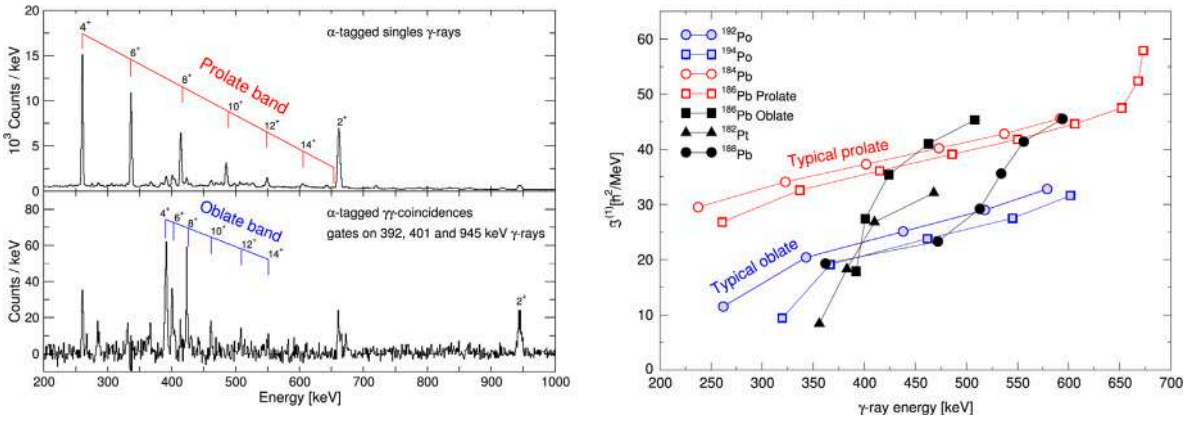

Fig. 75. Left panel: Gamma-ray energy spectra of the two rotational bands built upon different deformed minima (prolate and oblate) in ^{186}Pb. Transitions are labeled according to spin and parity of their initial state [422]. Right panel: Kinematic moments of inertia $\Im^{(1)}$ [149] as a function of γ-ray energy for the two collective bands in ^{186}Pb, together with those for known bands in nuclei close to ^{186}Pb. The similarities in the kinematic moments of inertia plots between the oblate bands in ^{186}Pb, and in ^{182}Pt, ^{188}Pb could be related to a shape change toward a more deformed oblate structure, as predicted by calculations [435–437]. *Source:* Taken from [422,438].

Table 23
Experimental information available on 0^+ excitations in Pb isotopes (A = 184–202). See also Fig. 34, 35 and caption of Table 8 for detailed explanations.

Nucleus	E_i [MeV]	I_i^π	$T_{1/2}$ [ps]	E_f [MeV]	I_f^π	E_γ or E_{e^-} [MeV]	BR [%]	E/Mλ	B(E/Mλ)/ρ^2(E0) [W.u.]/[m.u.]	HF	Refs.
^{186}Pb	0.535(2)	0_2^+		0.0	0_1^+	0.535(2)		E0			[58,66,67]
	0.659(4)	0_3^+		0.0	0_1^+	0.659(4)		E0			
^{190}Pb	0.658(4)	0_2^+	≤0.22 10^3	0.0	0_1^+	0.658		E0	≥6.6		[33,67]
^{192}Pb	0.769	0_2^+	0.75(10) 10^3	0.0	0_1^+	0.769		E0	1.66(24)		[33,67]
^{194}Pb	0.931	0_2^+	1.1(2) 10^3	0.0	0_1^+	0.931		E0	0.97(18)		[33,67]
^{202}Pb	1.658	0_2^+	<30	0.961	2_1^+	0.697	100.0	E2	>1.4	<3.6	[33,67]
				0.0	0_1^+	1.658		E0	8(5)		
	1.862	0_3^+	<30	0.961	2_1^+	0.901	100.0	E2	>0.44	<11.4	[33,67]
				0.0	0_1^+	1.862		E0	$1.8(^{+12}_{-10})$		
	2.159	0_4^+	<30	0.961	2_1^+	1.198	100.0	E2	>0.049	<102	[33,67]
				0.0	0_1^+	2.159		E0	$3.6(^{+24}_{-22})$		
^{204}Pb	1.583	0_2^+	65(20)	0.899	2_1^+	0.684	100.0	[E2]	0.81(25)	6.2	[33,67]
				0.0	0_1^+	1.583		E0	8.6(28)		
	1.730	0_3^+	<20	0.0	0_1^+	1.730		E0	$60(^{+40}_{-30})$		
^{206}Pb	1.166	0_2^+	0.75(4) 10^3	0.803	2_1^+	(0.363)[a]	≤0.24	[E2][a]	<0.025	>200	[33,67,439]
				0.0	0_1^+	1.166	100(13)	E0	1.07(8)		
^{208}Pb	4.868(2)	0_2^+	>0.312	4.086	2_1^+	0.782					[33,67]
				0.0	0_1^+	4.870(3)		E0	<233		
	5.241	0_3^+	>0.690	2.615	3^-	2.627	<400	[E3]	<635		[67,440]
				0.0	0_1^+	5.241(3)	100.0	E0			

[a] γ ray not seen, E_γ from level energies difference.
Additional 0^+ states from reaction studies (Po α decay, Bi ϵ decay, (p,t), (t,p) and (^{3}He,n) in particular, no γ-decay reported) [67]:
^{184}Pb: 0_2^+: 0.570(30) MeV;
^{188}Pb: 0_2^+: 0.591 MeV;
^{196}Pb: $0_{2,3}^+$: 1.143, 1.698 MeV;
^{198}Pb: $(0_{2,3}^+)$: 1.382(1), 1.735(1) MeV;
^{200}Pb: $0_{2,3}^+$: 1.626, 1.867 MeV;
^{206}Pb: $0_{3,4,5}^+$: 2.314(2), (4.1 × 10^3(1)), 5.637(10) MeV.

Moving away from the N = 104 mid-shell, in-beam studies of ^{182,184}Pb have shown that the prolate intruder configuration rises in energy, with no sign of the oblate (2p-2h) structure (see Fig. 7). In fact, the latter is expected to disappear, according to beyond-mean-field calculations [434,436,437]. Moving toward heavier isotopes, with N > 106, low-lying 0^+ states, appearing below the first excited 2_1^+ state, are also found in ^{190,192,194}Pb, with rather reduced monopole transition strength in ^{192,194}Pb (e.g., ρ^2(E0) ∼ 1 m.u., see Table 23). They can be associated to excited structures with lower (oblate) deformation, as show in Fig. 7. Additional 0^+ excitations are also reported in heavier Pb systems, with A ≥196 (see Fig. 70), where only a dominant spherical minimum and a secondary oblate minimum with $\beta_2 \sim 0.2$ are expected, according to mean-field and beyond mean-field predictions [415,434,436].

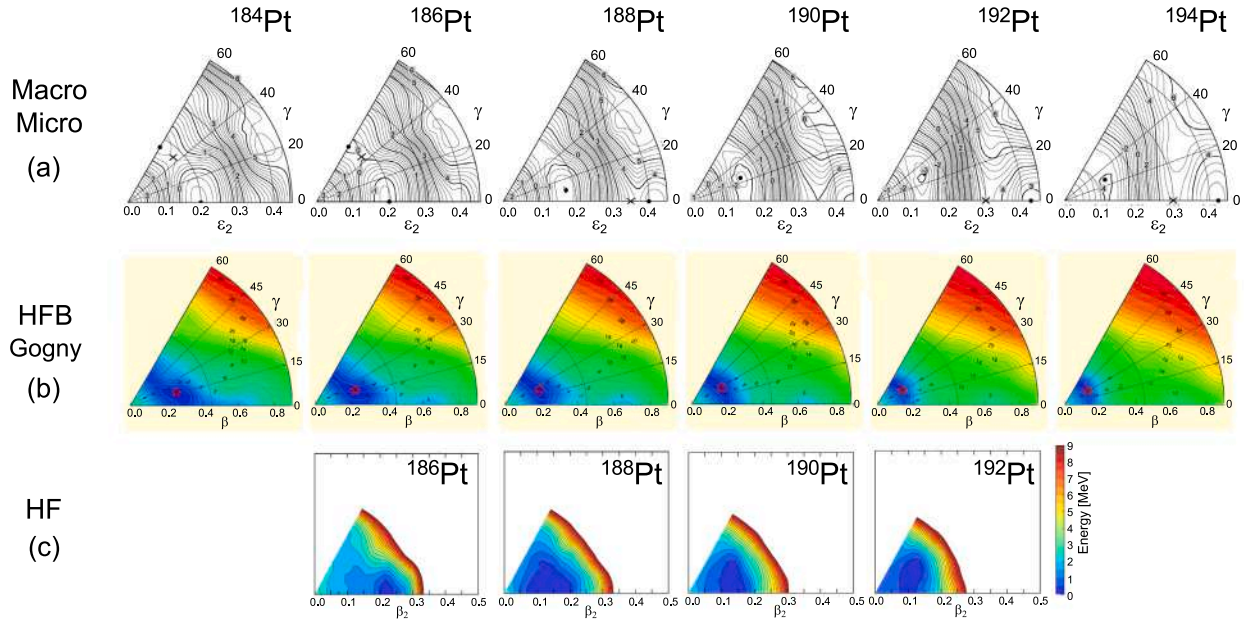

Fig. 76. Potential energy surfaces for even–even $^{184-194}$Pt obtained from different types of calculations: (a) macroscopic–microscopic mean field model of Moeller et al. [59], (b) Hartree–Fock–Bogoliubov calculations based on the Gogny force, by S. Hilaire and M. Girod [198,249], and (c) constrained Hartree–Fock calculations by Tsunoda et al. The Hamiltonian taken in Refs. [108,421] is used.
Source: Adapted from [59,250].

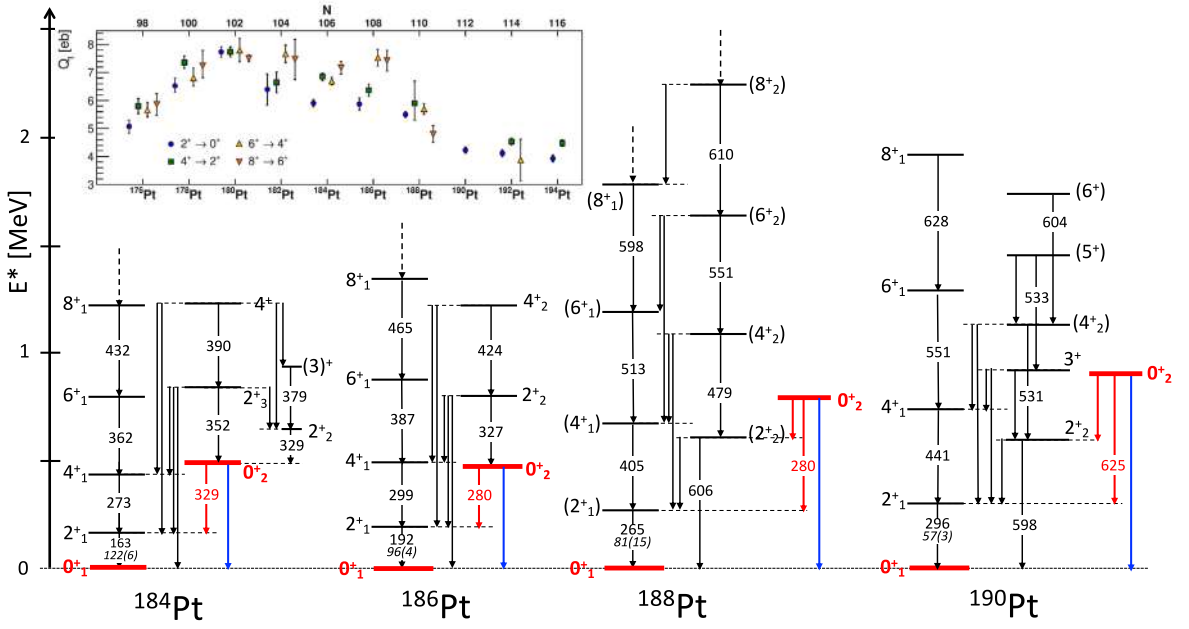

Fig. 77. Partial level schemes of even–even Pt isotopes with A = 184–190 [67]. Excited 0^+ states are highlighted in red, with red and blue arrows indicating measured γ and E0 decay from 0^+ states, with energies in keV and B(E2) and ρ^2(E0) values in W.u. and m.u., respectively (in italic). Dashed arrows indicate the continuation of a band to higher spins (see Tables 24 and 25 for details). The inset shows the transitional quadrupole moments Q_t calculated from lifetimes of 2^+ to 8^+ states in even–even $^{176-194}$Pt nuclei.
Source: Inset taken from Ref. [24].

Only one 0^+ excitation shows a significantly retarded E2 decay, i.e., 0_2^+ in ^{206}Pb, located at 1.166 MeV. This state is described as having a fairly pure $\nu(f_{5/2})^{-2}$ two-neutron-hole character, with a large hindrance arising from cancellation effects [439,444,445].

As in the case of the Hg isotopes (see Section 4.5.1), theoretical descriptions based on the beyond mean field approaches (see, e.g., [431]) or symmetry-guided models (see, e.g., [432]) reproduce the general trends of the experimental findings, although fine nuclear structure details are often difficult to be reproduced, as for example the relative position of the prolate and oblate minima (see Ref. [108] ad references therein).

4.5.3. The Pt isotopes

In neutron-deficient Pt isotopes (Z = 78), potential energy surface calculations in (β, γ) coordinates, from mean field approaches, show a complex scenario of shape coexistence, with oblate and prolate minima less distinct than in Hg isotopes, and with significant softness to γ deformation (see Fig. 76). Only in systems around A = 190, at rather large deformation ($\beta_2 \sim 0.5$), mean-field approaches predict deep secondary PES minima located at 4–5 MeV above the ground state, rather stiff in the direction of triaxiality – they are candidates for shape-isomer states (see also Figs. 68 and 69). Finally, in systems heavier than ^{192}Pt, the potential becomes very soft in the γ direction and then spherical around A = 198.

Experimentally, extended yrast rotational bands have been observed in Pt nuclei around mid-shell (N = 104), i.e., at A = 178–186. All bands are characterized by rather similar and regular behavior, consistent with well deformed configurations. Lifetime measurements of 2_1^+ to 8_1^+ states yield B(E2) values of the order of 100 W.u., corresponding to quadrupole moments $Q_t \sim 5$–8 eb, thus confirming a significant collectivity (see Fig. 77 and relative inset) [67,446–451]. In the same nuclei, low-lying 0^+ states have also been identified as bandheads of weakly deformed structures extending up to several units of spin. In heavier Pt isotopes, with A > 190, multiple 0^+ excitations are reported, with very limited information on electromagnetic B(E/Mλ) transition probabilities, including E0 strength, what prevents a detailed interpretation of the structure of such supposedly triaxial/spherical systems.

Traditionally, the structure of mid-shell (N = 104) Pt nuclei has been interpreted by extending the picture which describes well the Pb and Hg neutron-deficient isotopes. According to this picture, a strongly deformed state is an intruder configuration formed by two-proton excitations into the $h_{9/2}$ orbital which is energetically favorable due to particularly strong attractive interaction between valence protons and neutrons in such arrangement [452–455]. In Pt isotopes, this mechanism could result in a highly deformed (proton 2p-6h) intruder configuration crossing the "normal" (proton 4h) less deformed configuration and becoming the ground state around mid-shell. At each end of the shell, the highly-deformed intruder should rise again in energy, above the "normal" structure. Within this picture, the anomalies observed in the low-spin behavior in ^{176,178}Pt and in ^{188}Pt can be ascribed to the interactions between two bands based on different configurations. By applying a schematic two-band mixing model, the amplitudes of the two configurations in each state can be calculated, resulting in admixture of 15% up to more than 50% intruder state into the ground state, going from ^{176}Pt to ^{184}Pt [452].

The Pt energy systematics was also shown to be well reproduced by configuration mixing calculations performed using the Interacting Boson Model [456], which describes separately the different configurations (i.e., a regular configuration composed of pure valence excitations (N_B bosons), and a deformed 2p-2h excitation involving $N_B + 2$ bosons) [457,458].

It is important to note that the two-configuration mixing interpretation of neutron-deficient Pt isotopes is not unique. In Ref. [459], an alternative, simpler description of the low-spin structure of neutron-deficient Pt was proposed by McCutchan et al. based on the interacting boson model (IBA) using a simple, single configuration, two-parameter Hamiltonian. In this case, the energies of the excited states of Pt isotopes are considered without assumptions on the structure of the different bands, only taking their ordered appearance in energy (as shown in Fig. 70). It was found that energies and electromagnetic transition strengths could be well reproduced over the entire Pt isotopic chain in terms of a transition from spherical nuclei (with soft energy surfaces) to deformed nuclei (with increasingly γ-soft surfaces), as the neutron number increases. Within this single configuration approach, light Pb and Hg isotopes (their low-lying 0_2^+ energies, in particular) are however not reproduced, what underlines the marked difference between Hg/Pb and Pt isotopes.

The ambiguity in the interpretation of the structure of Pt isotopes, discussed above, clearly points to the importance of extended, high-precision measurements, especially of lifetimes of non-yrast states, in order to distinguish between competing theoretical approaches in this complex region of the nuclear chart. As an example, a precise estimate of the B(E2; $0_3^+ \rightarrow 2_{1,2}^+$) value in ^{196}Pt (for which an upper limit exists only, see Table 25), could allow to distinguish between a spherical and γ-soft vibration (i.e., the so-called U(5) and O(6) symmetries in the IBM approach) [460].

4.5.4. The Po isotopes

In even–even polonium isotopes, above Z = 82, the level systematics reveals low-lying intruding structure for A = 190–210, similarly to what observed in neutron-deficient Pb and Hg nuclei. Indeed, a shape coexistence scenario was predicted in light Po isotopes already in the 90's by Oros et al. [462], which concluded that the ground state of the heavier $^{194-210}$Po isotopes is spherical, while the first (oblate-like) deformed ground state should appear in ^{192}Po. Only in the lightest masses, with A $\leq$ 190, the ground state was expected to be prolate.

The early predictions for Po isotopes, mentioned above, are supported by a series of experimental studies of polonium isotopes employing different techniques, including α-, β- and in-beam γ-decay studies, performed, in particular, at Jyväskylä (JYFL) and ISOLDE [422,423,463–465]. The data are consistent with the picture of a deformed intruder structure becoming the ground state in light isotopes, at variance from Hg isotopes (which "mirror" the Polonium ones with respect to Z = 82), where the intruder structure never becomes the ground state. Laser spectroscopy studies of radii in a wide range of Polonium isotopes also point to the deviation from sphericity around ^{198}Po [466], namely earlier than predicted by theory [462] and to what observed in Pb and Hg isotones.

Table 24
Experimental information available on 0^+ excitations in Pt isotopes (A = 176–192). See also Fig. 34, 35 and caption of Table 8 for detailed explanations.

Nucleus	E_i [MeV]	I_i^π	$T_{1/2}$ [ps]	E_f [MeV]	I_f^π	E_γ or E_{e^-} [MeV]	BR [%]	E/Mλ	B(E/Mλ)/ρ^2(E0) [W.u.]/[m.u.]	HF	Refs.
^{176}Pt	0.443	0_2^+	<0.7 10^3	0.0	0_1^+	0.443		E0	>4		[33,67]
				0.264	2_1^+	0.179		[E2]	>75.4	<0.066	
^{178}Pt	0.421	0_2^+	<0.7 10^3	0.0	0_1^+	0.421		E0	>2		[33,67]
				0.170	2_1^+	0.251		[E2]	>13.7	<0.36	
^{180}Pt	0.478	0_2^+		0.0	0_1^+	0.478		E0			[67]
				0.153	2_1^+	0.325		[E2]			
	1.178	0_3^+		0.677	2_2^+	0.500	11.5	[E2]			
				0.153	2_1^+	1.024	88.5	(E2)			
^{182}Pt	0.500	0_2^+		0.155	2_1^+	0.345	76.3	E2			[67]
				0.0	0_1^+	499.3	23.7	E0			
	1.152	(0_3^+)		0.155	2_2^+	0.997	100.0	(E2)			
^{184}Pt	0.492	0_2^+		0.0	0_1^+	0.492	54.5	E0			[67]
				0.163	2_1^+	0.329	45.5	E2			
^{186}Pt	0.472	0_2^+		0.0	0_1^+	0.472		E0			[67]
				0.192	2_1^+	0.280	100.0	E2			
^{188}Pt	0.799	0_2^+		0.0	0_1^+	0.799		E0			[67]
				0.266	2_1^+	0.533	97.2	E2			
				0.606	2_2^+	0.193	2.8	[E2]			
^{190}Pt	0.921	0_2^+		0.0	0_1^+	0.921	1.5	E0			[67]
				0.296	2_1^+	0.625	73.2	E2			
				0.598	2_2^+	0.323	25.3	E2			
^{192}Pt	1.195	0_2^+		0.0	0_1^+	1.195		E0			[67]
				0.317	2_1^+	0.879	76.3	E2			
				0.612	2_2^+	0.583	23.3	E2			
	1.547	0_3^+		0.0	0_1^+	1.547	0.9	(E0)			
				0.317	2_1^+	1.230	7.6	[E2]			
				0.612	2_2^+	0.934	91.5	[E2]			
	1.629	0_4^+		0.317	2_1^+	1.313	91.8	E2			
				0.612	2_2^+	1.017	8.2	[E2]			

Additional 0^+ states from (p,t) reaction studies (no γ-decay reported) [67,220]:
^{190}Pt: 0_3^+: 1.670(5) MeV;
^{192}Pt: $0^+_{5,6,7,8,9}$, (0^+_{10}): 1.882, 2.111, 2.386, 2.491, 2.500, 2.743 MeV.

Being mid-shell nuclei with Z > 82 closer to the proton dripline, spectroscopic studies of Po isotopes via fusion-evaporation reactions become increasingly difficult, not least due to the larger significance of the fission reaction channel. In the case of ^{190}Po, the yrast band structure has been investigated up to spin (14^+) confirming its prolate nature [467], while collective oblate rotational bands, extending to spin 10^+ and 16^+, have been reported in ^{192}Po and ^{194,196}Po, respectively [464], and interpreted as built on two-proton excitations across the Z = 82 gap (4p-2h states) (see also the kinematic moment of inertia reported in Fig. 75). The collectivity of such bands has been verified by lifetime measurements in ^{194,196}Po [468,469]. As shown in Fig. 70, in A = 192–202 Po isotopes excited 0^+ states also appear – they follow the typical parabolic behavior expected for shape coexisting structures, therefore they are candidates for being the band heads of the collective bands.

In heavy Po isotopes (A > 198), according to beyond-mean-field (BMF) studies, the potential-energy surfaces are soft, pointing toward the possibility of triaxial structures [431]. Finally, around the N = 126 shell closure, excited 0^+ states are reported in ^{208,212,214}Po which show significantly retarded E2 decay (HF $\gg$ 10) toward the first excited 2_1^+ state [439,470,471](see Fig. 35 and Table 26). For these states, similar and small (∼1) E0 strengths are also found, what suggests that the corresponding wave functions might not differ much from each other. Such 0_2^+ excitations in ^{208,212,214}Po isotopes are expected to be of similar type of the two-neutron-hole 0_2^+ excitation in ^{206}Pb [444], namely fairly pure few particle excitations rather well described within a shell model approach, with hindrances in the $0_2^+ \rightarrow 2_1^+$ E2 strength arising from cancellation of terms. We note that the 0_2^+ states in ^{212,214}Po are α-emitting states.

5. Shape coexistence and triaxiality in mid-shell nuclei

In this section, a selection of recent results in heavy regions of the nuclear chart away from shell closures is discussed, focusing on phenomena such as shape coexistence, triaxiality and highly deformed shapes and their interpretation based on the best available models.

Table 25
Experimental information available on 0^+ excitations in Pt isotopes (A = 194–200). See also Fig. 34, 35 and caption of Table 8 for detailed explanations.

Nucleus	E_i [MeV]	I_i^π	$T_{1/2}$ [ps]	E_f [MeV]	I_f^π	E_γ or E_{e^-} [MeV]	BR [%]	$E/M\lambda$	$B(E/M\lambda)/\rho^2(E0)$ [W.u.]/[m.u.]	HF	Refs.
^{194}Pt	1.267	0_2^+	6.1(14)	0.0	0_1^+	1.267	0.1	E0	0.16(4)		[33,67]
				0.328	2_1^+	0.939	33.3	E2	$0.63(^{+20}_{-13})$	7.94	
				0.622	2_2^+	0.645	66.7	E2	$8.2(^{+15}_{-16})$	0.61	
	1.479	0_3^+		0.0	0_1^+	1.479	5.2	E0			
				0.328	2_1^+	1.151	93.9	E2			
				0.622	2_2^+	0.857	0.9	[E2]			
	1.547	0_4^+	$0.175(^{+14}_{-11})$	0.0	0_1^+	1.548	0.2	E0	9.8(12)		[33,67]
				0.328	2_1^+	1.219	79.2	E2	$14.3(^{+10}_{-11})$	0.35	
				0.622	2_2^+	0.925	20.6	E2	$14.4(^{+10}_{-12})$	0.35	
	1.894	0_5^+		0.0	0_1^+	1.893	1.2	(E0)			
				0.328	2_1^+	1.565	98.8	[E2]			
	2.085	0_6^+		0.0	0_1^+	2.086	0.5	E0			
				0.328	2_1^+	1.757	7.8	(E2)			
				0.622	2_2^+	1.463	89.6	(E2)			
				1.797	1_1^-	0.288	2.1	[E1]			
	2.164	0_7^+		0.0	0_1^+	2.164	2.3	E0			
				0.328	2_1^+	1.835	73.9	E2			
				0.622	2_2^+	1.542	4.5	[E2]			
				1.797	1_1^-	0.366	5.5	[E1]			
				1.924	1_1^+	0.239	9.2	M1			
				2.114	1_3^+	0.050	4.6	M1			
	2.356	0_8^+		0.0	0_1^+	2.357	0.2	E0			
				0.328	2_1^+	2.028	7.5	[E2]			
				1.512	2_3^+	0.844	<1.9	[E2]			
				1.924	1_1^+	0.432	3.9	[M1]			
				2.216	1_4^+	0.141	82.9	M1			
				2.287	$(1^+,2^+)$	0.070	3.7	[M1]			
^{196}Pt	1.135	(0_2^+)	$4.2(^{+17}_{-6})$	0.0	0_1^+	1.135	<0.024	E0	<0.05		[33,67]
				0.356	2_1^+	0.780	71.9	E2	2.8(15)	1.8	
				0.689	2_2^+	0.447	28.1	E2	18(10)	0.28	
	1.403	(0_3^+)	1.6(3)	0.689	2_2^+	0.714	<2.3	[E2]	<0.41	>12	[33,67]
				0.356	2_1^+	1.047	96.4	(E2)	<5	>1	
				1.135	0_2^+	0.267		E0	210(50)		
				0.0	0_1^+	1.403	1.3	E0	10.3(22)		
	1.823	0_4^+		0.689	2_2^+	1.135	<0.8	[E2]			
				0.356	2_1^+	1.468	100.0	[E2]			
				0.0	0_1^+	1.823	<0.11	E0			
	1.919	0_5^+		0.689	2_2^+	1.230	15.2	[E2]			
				0.356	2_1^+	1.563	84.6	[E2]			
				0.0	0_1^+	1.919	0.1	E0			
	2.199	0_6^+		0.689	2_2^+	1.511	100.0	[E2]			
				0.0	0_1^+	2.199	0.1	E0			
^{198}Pt	0.915	0_2^+		0.407	2_1^+	0.507	100.0	[E2]	26(7)	0.19	[67]
	1.481	0_3^+		0.407	2_1^+	1.074	100.0	[E2]			
^{200}Pt	1.118[a]	(0_2^+)		0.0	0_1^+	1.118		(E0)			[67]
	1.583[a]	0_3^+		0.0	0_1^+	1.583		(E0)			
				0.470	2_1^+	1.113	100	[E2]			

[a] γ-ray not observed, but (E0) multipolarity suggested from e^- measurements in ^{198}Pt(t,pγ) [461].
Additional 0^+ states from (p,t) and (t,p) reaction studies (no γ-decay reported) [67]:
^{194}Pt: 0_9^+, (0_{10}^+): 2.511, 2.769 MeV;
^{198}Pt: $0_{4,5}^+$: 1.869(5), 2.802(7) MeV;
^{200}Pt: $0_{4,5}^+$: 2.014(6), 2.253(7) MeV.

5.1. Oblate–prolate shape coexistence in A = 120–130 nuclei

Nuclei with oblate shapes in their ground states are much more rare than those with prolate shapes, and only in limited regions of the nuclear chart a competition between oblate and prolate shapes can be found, e.g., in A ∼ 70 nuclei of Se and Kr [231,348] (see also Section 4.3.2), and around proton-rich Pb and Hg isotopes (see Section 4.5).

At high spin, only few oblate bands were observed in different mass regions [15], characterized by normal and super deformation, often evolving from prolate shapes, as for example in nuclei with A ≈ 130 [472] and in neutron-rich Hf isotopes [473].

In recent years, experimental effort has been made to search for oblate bands in strongly-deformed proton-rich A ∼ 120 nuclei, and in Ba isotopes around A ∼ 130, for which predictions exist since long time, based on different theory approaches [474–476]. Standard tools in these searches are fusion-evaporation reactions which allow to reach very high spins.

Table 26
Experimental information available on 0^+ excitations in Po isotopes (A = 196–210). In the cases of ^{204,206}Po, no 0^+ excited states are reported in literature [67]. See also Fig. 34, 35 and caption of Table 8 for detailed explanations.

Nucleus	E_i [MeV]	I_i^π	$T_{1/2}$ [ps]	E_f [MeV]	I_f^π	E_γ or E_{e^-} [MeV]	BR [%]	E/Mλ	B(E/Mλ)/ρ^2(E0) [W.u.]/[m.u.]	HF	Refs.
^{196}Po	0.558	0_2^+		0.0	0_1^+	0.558		[E0]			[67,465]
				0.463	2_1^+	0.095[a]					
^{198}Po	0.816	0_2^+	<0.4 10^3	0.0	0_1^+	0.816	69.0	E0	$3.2(^{+21}_{-18})$		[33,67,465]
				0.605	2_1^+	0.211	31.0	[E2]	≥15.3	≤0.33	
^{200}Po	1.137	0_2^+		0.0	0_1^+	1.137		E0			[67]
^{202}Po	1.758	0_2^+		0.0	0_1^+	1.758		E0			[67]
^{208}Po	1.272	0_2^+	465(20)	0.0	0_1^+	1.272	77.0	E0	1.05(12)		[33,67,439]
				0.687	2_1^+	0.585[a]	<23	[E2]	≤0.06	≥83	
^{210}Po	2.609	0_2^+		0.0	0_1^+	2.609		E0			[67]
				1.181	2_1^+	1.427	100(49)	E2			
				2.394	1_1^+	0.215	≤42				
^{212}Po	1.801[b]	0_2^+	34(4)	0.0	0_1^+	1.800	13.0	E0	1.67(31)		[33,67,471]
				0.727	2_1^+	1.074	50.0	[E2]	0.078(9)	64	
				1.621	1_1^+	0.180	26.0	[M1]	0.011(1)		
				^{208}Pb(g.s.)	0_1^+	10.549(E_α)	27.0	α decay			
^{214}Po	1.415[b]	0_2^+	99(3)	0.0	0_1^+	1.415	25.8	E0	1.40(10)		[33,67,470]
				0.609	2_1^+	0.806	74.1	[E2]	0.164(5)	31	
				^{210}Pb(g.s.)	0_1^+	9.080(E_α)	0.1	α decay			
	1.743	$0_3^{(+)}$		0.609	2_1^+	1.134	100.0	(E2)			
	2.017	0_4^+		1.765	1_1^+	0.253	0.5	[M1]			
				1.661	2_3^+	0.356	0.3	[E2]			
				1.378	2_2^+	0.640	1.3	[E2]			
				0.609	2_1^+	1.408	100.0	(E2)			
				0.0	0_1^+	2.017[b]	0.0023	E0			
				^{210}Pb(g.s.)	0_1^+	9.670(E_α)	0.0016	α decay			

[a] γ ray not seen, E_γ from level energies difference.
[b] α emitting state [471].

Rich information on high spin states in ^{119}Cs, including spin and parity as deduced from measured angular correlation (anisotropy) ratios, have been obtained in an experimented performed at the Jyväskylä Laboratory with the JUROGAM 3+MARA setup, employing the ^{58}Ni(^{64}Zn,3p) fusion-evaporation reaction with a beam energy of 255 MeV [477]. The experiment was devoted to the search for oblate bands, with enhanced sensitivity provided by tagging on long-lived isomers and daughter nuclei of the β decay of the implanted recoils, detected with five clover germanium detectors surrounding the MARA focal-plane detection system. A partial level scheme of ^{119}Cs is shown in Fig. 78(a), showing the bands assigned to prolate shapes, with labels 1, 4 and 5, and the oblate band, labeled as 3, with cartoons showing the orbits and angular momenta of the odd proton, with respect to the prolate and oblate ^{118}Xe core, respectively. It is found that both Band 1, prolate, and Band 3, oblate, have a $11/2^-$ bandhead, and that the oblate band (which is negative-parity) does not decay to the other negative-parity bands, all interpreted as based on a prolate shape. This can be explained by the existence of a barrier between the oblate and prolate minima which, according to theory predictions, can be as high as 5 MeV [475,476]. In addition, a very different orientation of the spin of the odd proton relative to the core may result in a K forbidden decay between the different structures. Calculations of the potential energy surface in the (β, γ) plane for the $\pi h_{11/2}$ configuration, performed with the tilted axis cranking covariant density functional theory (TAC-CDFT) [478–480], were found to exhibit a minimum around $\beta \approx 0.3$, but very soft in the γ direction, as shown in Fig. 78(c). The energy minimum pathway indicates that the oblate shape is favored for β smaller than 0.2 (which should correspond to the deformation of Band 3), while the prolate shape becomes favored for larger β values, which correspond to the deformation of the other measured bands (Band 1, in particular). Such calculations support the co-existence of prolate and oblate minima, however no significant barrier separating the minima is expected within this framework.

As one can see in Fig. 78(b), the experimental values for the moments of inertia and the projection of the total spin on the cranking axis for both the prolate (Band 1) and oblate (Band 3) band are well reproduced by the TAC-CDFT calculations, assuming deformation parameters $\epsilon_2 = 0.32$ and -0.17, respectively. A similar good agreement was achieved for all other measured bands, thus supporting the oblate–prolate shape coexistence predicted by theory, close to the ground state, in the strongly-deformed ^{119}Cs nucleus. A similar scenario is also expected in other nuclei close to the proton drip line, for which ground-state oblate shapes are predicted.

Moving now to the opposite side of the valley of stability, nuclei with mass A = 130, and around N = 76, have often been reported, at low spin, as characterized by a triaxial shape rather soft in the γ deformation, while at high spins a shape change is observed toward nearly axial symmetry, both for high-K isomers, as well as for several bands with very sizeable deformation [135,481,482]. This situation occurs in ^{130}Ba, for example, which is characterized by a band with marked staggering between odd and even spins,

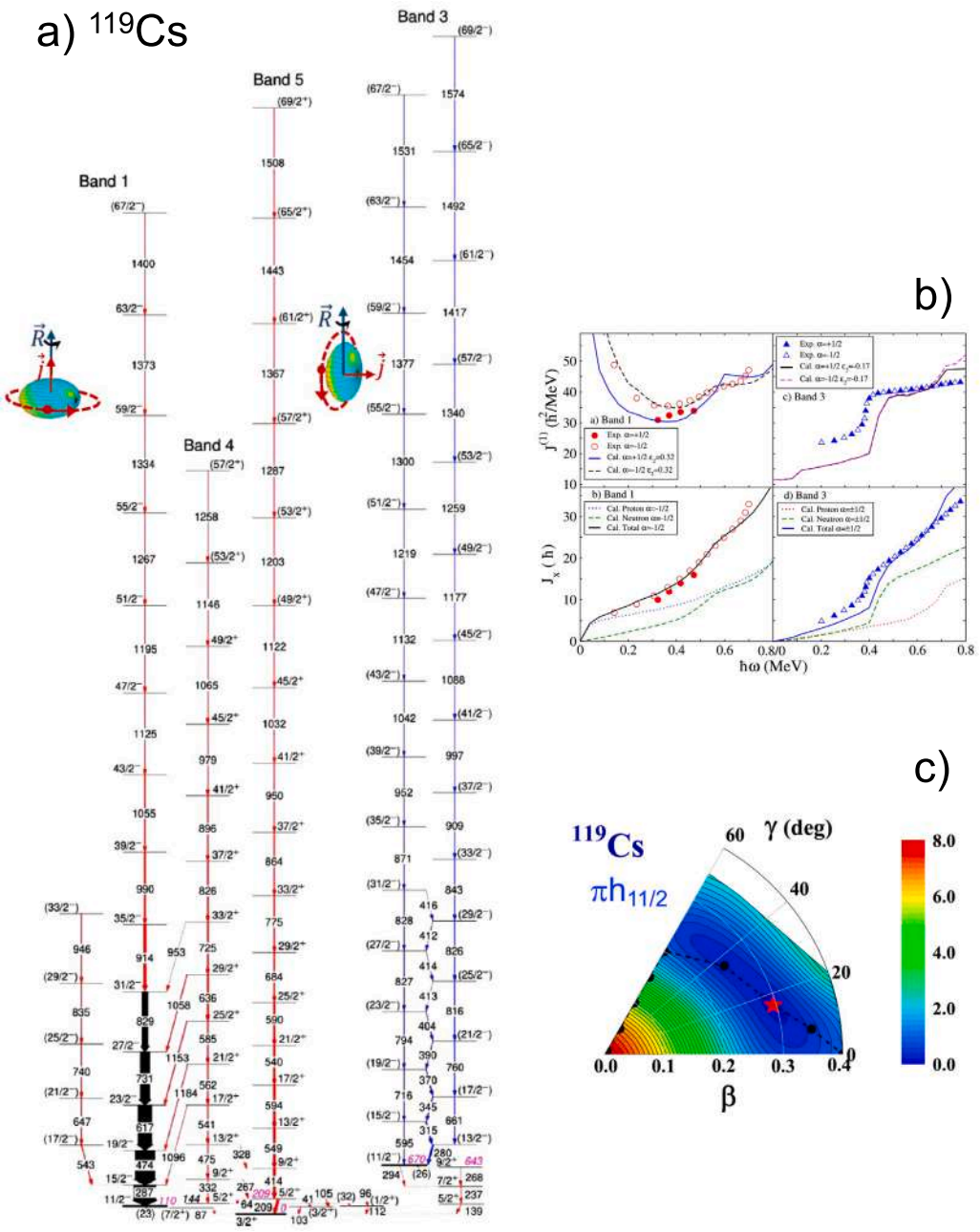

Fig. 78. Panel (a): Partial level scheme of ^{119}Cs. Bands 1, 4, 5 are assigned as prolate, Band 3 as oblate shape. Orbits and angular momenta of the odd proton are also schematically drawn. Panel (b): moments of inertia $J^{(1)}$, and projections of the angular momentum on the cranking axis J_x, for Bands 1 and 3, for experimental states with signature $\alpha = +1/2$ and $\alpha = -1/2$ (filled and open symbols) in comparison with PNC-CSM model calculations, assuming axially symmetric shapes. Panel (c): potential energy surface of in the $\beta-\gamma$ deformation plane for the configuration $\pi h_{11/2}$, calculated by the TAC-CDFT model. Contour lines are in step of 0.2 MeV, the energy minimum pathway and absolute energy minimum are denoted by black dots and red star, respectively.
Source: Adapted from [477].

what is generally considered as a fingerprint of γ softness. In addition, a nearly axially symmetric prolate shape, long-lived, high-K isomer ($K^{\pi} = 8^{-}$) has been recently discovered [482].

In general, the γ-softness of the nuclear shape facilitates the coexistence of different shapes, from prolate to oblate, depending on the specific configuration. In the case of ^{130}Ba, extensive high-spin spectroscopy was recently performed at the Legnaro National Laboratory of INFN (Italy), employing a fusion evaporation reaction induced by a 65-MeV ^{13}C beam impinging on a ^{122}Sn

target [483]. By using a complex setup made of the GALILEO HPGe spectrometer [301] coupled to the charged-particle and neutron-detector arrays EUCLIDES and NWall, the reaction channel of interest could be selected up to high spins, revealing the existence of five new positive parity bands. Detailed theoretical investigation, employing several theoretical models (i.e., total Routhians surfaces (TRS) [135], tilted axis cranking (TAC) [484], particle rotor model (PRM) [485], and projected shell model (PSM) [486]), were performed in order to establish the nature of the newly observed bands. The rotational structures turned out to be built on different shapes, including oblate and prolate shapes polarized by rotation aligned two-proton and two-neutron configurations. Prolate collective rotations around axes with different orientations were also identified. It is concluded that the nucleus ^{130}Ba represents one of the best examples of shape coexistence in which exotic rotations appear, at medium and high spins, in a γ-soft nucleus.

5.2. Multiple excitations in $N = 88$, 90, and 92 isotones

A recent comprehensive systematic study of the many bands measured in even–even isotopes, with neutron numbers $N = 88$ to 92 and proton numbers Z = 62 (Sm) to 70 (Yb), was made by Majola et al. [487]. The main aim was to shed light on the nature of low-lying rotational bands based on the excited $K^\pi = 0^+_2$, 0^+_3 and $K^\pi = 2^+_\gamma$ states. Traditionally, within the Bohr and Mottelson picture [3], β and γ vibrations are the quadrupole vibrations of the nuclear shape, and the band built on the 0^+_2 state is considered to be the β-vibrational band, the 0^+_3 state is considered to be the second β band, while the bandhead of the γ-vibrational band is taken to be the second excited 2^+_γ state. These states have been extensively studied over the years, and recent works indicate that other modes of excitations may contribute to their formation, including shape coexistence and triaxiality [367,419,488].

In the work of Majola et al. the experimental determination of a large set of level energies and branching ratios between bands represented a major step forward to deduce their electromagnetic properties to be compared to nuclear models. Several data sets were collected with the JUROGAM II array at the JYFL laboratory and with the AFRODITE array at iThemba laboratory. In order to determine the magnetic or electric nature of the transitions, linear polarization measurements were also performed by using HPGe detectors of clover type positioned close to 90^0, which were treated as Compton polarimeters (the polarization anisotropy is positive for pure stretched electric transitions such as E1's and E2's which preferably scatter in the perpendicular direction with respect to the beam axis, while it is negative for a stretched pure magnetic dipole transitions).

For such extensive data sets, predictions were made using a five-dimensional collective Hamiltonian (5DCH) based on the covariant density functional theory (CDFT) of Zhao et al. [489]. Potential energy surfaces (PES) were computed using the CDFT, as a function of the quadrupole shape parameters (β, γ). Examples of calculated PES are shown in Fig. 79 for isotopes of Sm, Gd, Dy, Er, and Yb.It can be seen that all the nuclei exhibit prolate-like shape in their ground states but also show more or less different softness/rigidness in the β and γ directions. One can notice that for each isotopic chain, from N = 88 to 92, the quadrupole deformation β of the global minimum increases and the PES around it becomes a little bit more rigid in the γ direction. For each isotonic chain, from Sm to Yb, the PES around the global minimum becomes softer in the γ direction, while in the β direction it is largely influenced by the development of a secondary local minimum. In the case of the Er and Yb isotopes, the secondary local minimum develops at $\beta \approx 0.45$ and $\gamma \approx 10°$. These minima correspond to a nuclear shape similar to that of the well-known triaxial superdeformed bands observed in nearby Lu isotopes, such as $^{163-165}$Lu [490–492]. It is clear from these calculation that the effect of shape coexistence could be very important in ^{162}Yb, because the triaxial superdeformed minimum becomes very close in energy to the global minimum. The counterpart of the Yb minimum is present in the PES of the Er isotopes, although it is less well developed.

A detailed comparison, is reported in Ref. [487], between the experimental data and the associated predictions of the various quantities, i.e., energy spectra, moment of inertia of the various bands as deduced from the energy levels, transition ratios and probabilities (the in-band B(E2) and the B(E2) branching ratios). Guided by the adopted covariant density functional theory approach, a complex scenario of different types of excitations emerges in these nuclei. While the reader is recommended a careful reading of the extensive material in Ref. [487], here we draw attention only on the bandhead energies of the 0^+_2 and 2^+_γ bands, shown in Fig. 80, as a function of Z. It is observed that the 2^+_γ bandhead shifts toward lower energy as Z increases, in agreement with the observation that the PES around the global minimum becomes softer in the γ direction from Sm to Yb for each isotonic chain. Instead, for the 0^+_2 band, a minimum in the experimental bandhead energy is found between Z = 64 and Z = 68 for each isotope. The calculated minima agree for $N = 88$ and $N = 90$, but for $N = 92$, the minimum is too soft, leading to the energy of the band head to be underestimated by over 400 keV in ^{162}Yb. Nevertheless, the calculated bandhead energies and moments of inertia, found for Er and Yb to be higher than those of the ground state band, are accurate enough to reproduce most of the band crossings observed in the data.

From the comparison between data and theory, Majola et al. suggest that, among the investigated nuclei,namely ^{150,152,154}Sm, ^{152,154,156}Gd, ^{154,156,158}Dy, ^{156,158,160}Er, and ^{158,160,162}Yb, only ^{160}Er and ^{162}Yb have a band, the one built on 0^+_2, that can be understood as having large components in a triaxial superdeformed minimum, and thus as being formed by shape-coexisting states. In contrast, in all other cases, the 0^+_2 bands are interpreted as vibrational excitation. Moreover, experimentally, the ground-state band shows, in both N and Z, a trend for the moments of inertia which is consistent with a variation of the quadrupole deformation, in agreement with theory. Only the E0 rates are generally overestimated by the CDFT theory Zhao et al. [489].

In spite of the general agreement between theory and experiment, it is important to underline that a significant point of discrepancy also emerges from the work of Majola et al. [487]. It concerns the 0^+_3 excitations in Sm, Gd and Yb isotopes, which are predicted at nearly twice the energy of the 0^+_2 bandhead. This would be expected for a two-phonon β-vibration, while, experimentally, the 0^+_3 states are located very low in energy, especially in ^{154}Sm and ^{156}Gd isotopes., thus pointing to a different excitation mode. As discussed in Section 5.3, an alternative interpretation for the structure of these mid-shell nuclei has been recently proposed by Otsuka et al. which predicts a prevailing triaxiality driven by the monopole tensor interaction [419,493].

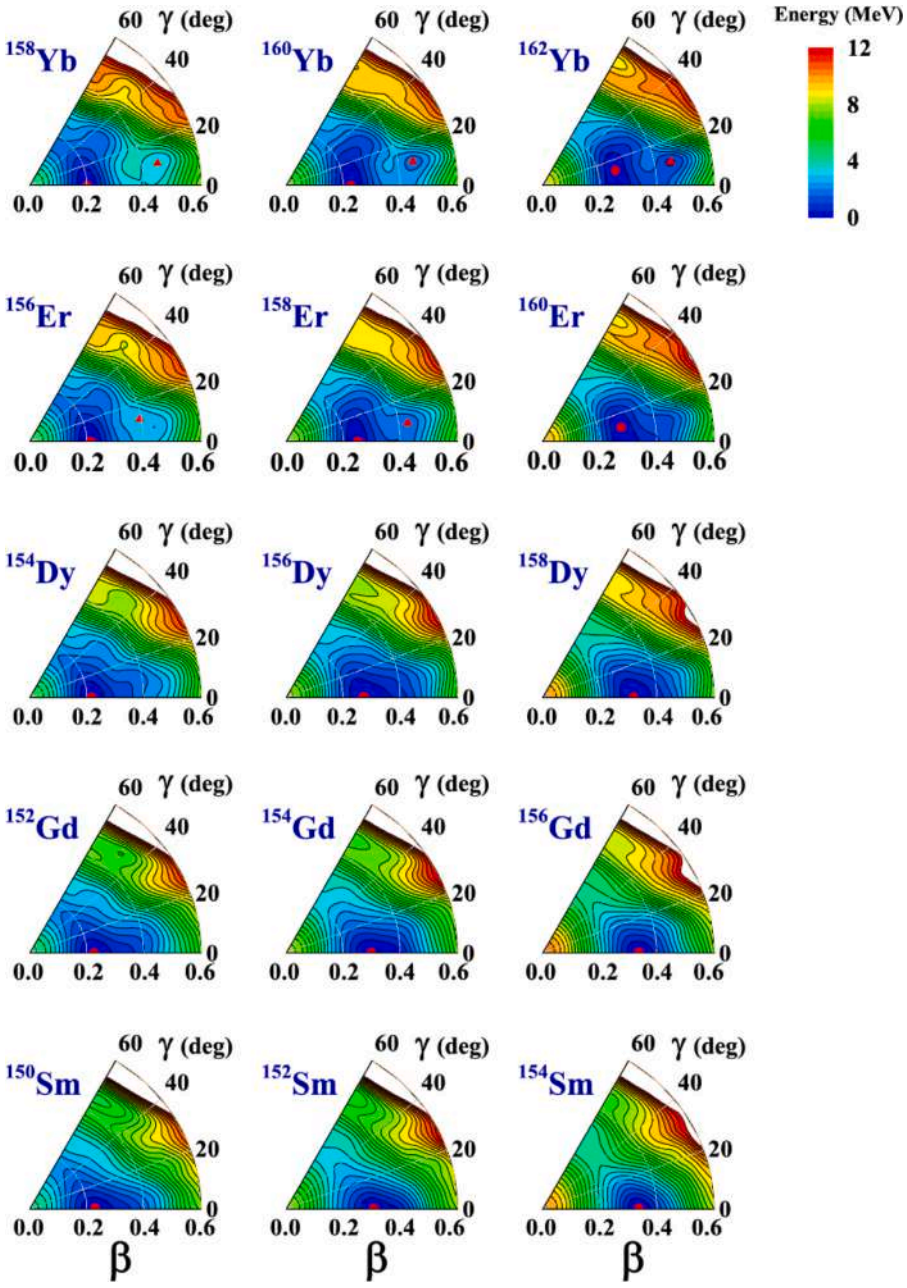

Fig. 79. Potential energy surfaces of $N = 88$, $N = 90$, and $N = 92$ isotones in the β-γ plane, calculated by the covariant density functional of Zhao et al. [489]. Minima are marked with red symbols; circles and triangles represent the global and secondary minima, respectively. The energy spacing in the contour lines is 0.25 MeV.
Source: Taken from [487].

5.3. Prevailing triaxiality in heavy nuclei

The deformed shapes of heavy nuclei have long been supposed to be axially-symmetric prolate [494–496]. This view has been shared by many nuclear structure models and theories, for instance, the microscopic–macroscopic model [227]. It has recently become possible to assess this view theoretically with quantum many-body calculations including various correlations due to nucleon–nucleon interactions in nuclei, without having assumptions on shapes [419]. One of the features relevant to the shape

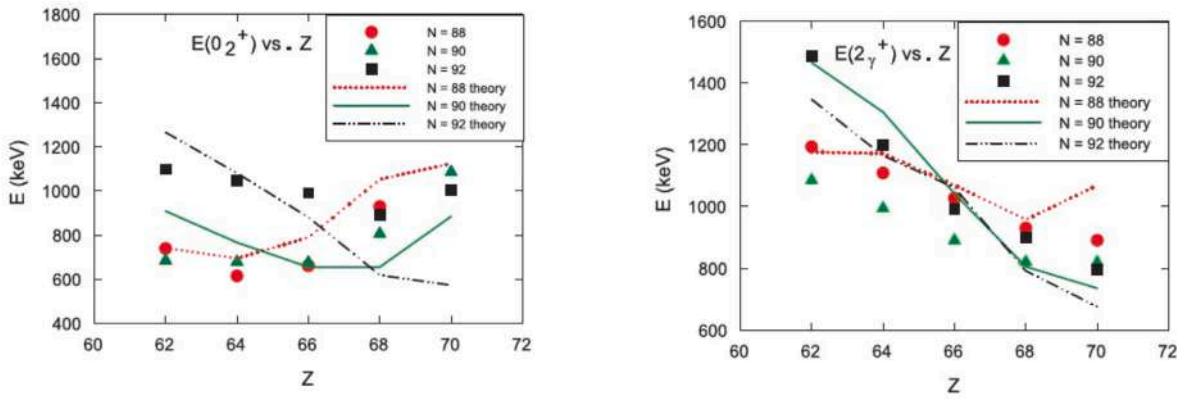

Fig. 80. Experimental bandhead energies (symbols) of the 2^+_γ (left) and 0^+_2 (right) bands as a function of Z, in Sm to Yb nuclei. Lines correspond to predictions from covariant density functional theory (CDFT).
Source: Taken from [487].

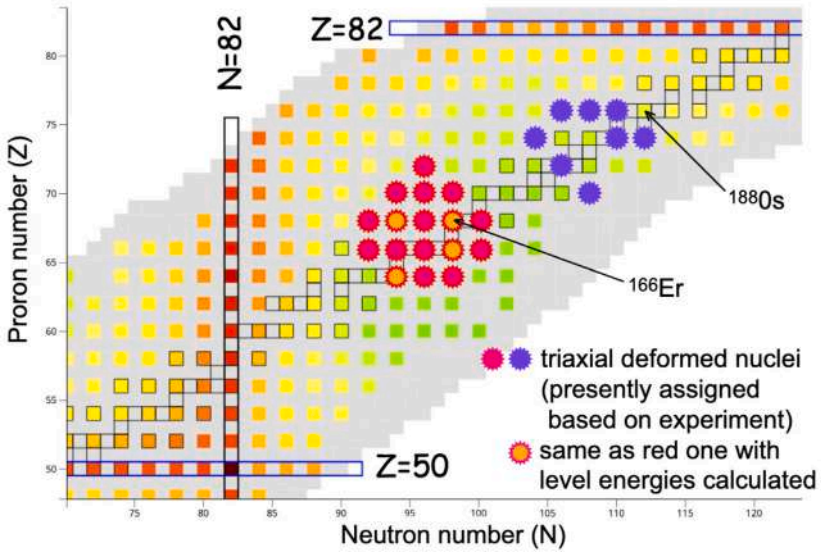

Fig. 81. Portion of the nuclear chart focusing on triaxially deformed heavy nuclei, indicated by red and purple star symbols. These nuclei experimentally show the second 2^+ level below the second 0^+ level. The background color patterns of the squares are from the NUDAT3 diagram by the National Nuclear Data Center [67], with green squares implying the first 2^+ levels below 0.1 MeV, while red squares (e.g., N = 82 isotones) those above 1 MeV.
Source: Figure taken from Ref. [493] with a modified caption.

coexistence is the prevailing triaxiality, as exemplified for ^{154}Sm, where prolate-like ground band and triaxial side bands are shown to co-exist, in good agreement with experiments [419]. The E2 transitions between different shapes are not enhanced, but are not strongly forbidden either. They belong to the category of mixed-shapes. As this trend seems to be general and some nuclei are shown to be triaxially deformed in their ground and low-lying states (see the case of ^{166}Er in Refs. [419,497], as well as Fig. 81), it is of great interest whether there are some cases with different triaxialities, separated by barriers high enough to produce sizeable HF values.

6. Shape ensemble in nuclei at finite temperature

Gamma spectroscopy has been a very powerful tool also to study nuclear shape in nuclei at finite temperature, in particular when the excitation energy of the nucleus is much higher that the nucleon binding energy.

The sampling of nuclear shapes via the dipole vibration corresponding to the Giant Dipole Resonance (GDR) has been the subject of many experimental and theoretical investigations in particular up to approximately 15 years ago [498]. A central issue in this

connection is the Brink-Axel hypothesis, stating that a dipole nuclear oscillation can occur also in excited nuclear states. Indeed, a series of experiments using reactions induced by light and heavy ions and measuring spectra of gamma-rays in the 2–20 MeV interval show the presence of the decay from the Giant Dipole Resonance with main features of its strength function, of Lorentzian shape, that are deduced via analyses based on the statistical model, changing with the value of the temperature and angular momentum of the nucleus on which the GDR is built [46].

A wealth of experimental data was obtained during the years mainly using fusion-evaporation reactions with different target and projectile types and different excitation energy (see, e.g., [498–500]). These data were shown to provide an important testing ground for theoretical models that reproduced rather well the experimentally observed changes of the GDR width, as a function of angular momentum and temperature. This behavior reflects the role played by quantal and thermal fluctuations in the damping mechanism of giant vibrations. Indeed, the study of the giant dipole resonance properties at high temperature and increasing angular momentum resulted as one of the most important tools to investigate the nuclear structure under extreme conditions. In particular, the evolution of the width of the GDR line shape with angular momentum and temperature reflects the role played by quantal and thermal fluctuations in the mechanism of damping of the dipole vibration [46].

Macroscopically, the large width of the GDR built on ground state is mainly induced by two processes, the collisional damping and in-homogeneous damping. Collisional damping occurs due to the binary collisions between nucleons and collisions between a nucleon and the nuclear surface. In the binary collision between two nucleons, a nucleon can change its state of motion by promoting a particle in the Fermi sea into a state above the Fermi surface. Since the particle–particle correlations are considerable larger than the particle–hole correlations and Pauli blocking is more effective in the bulk than in the nuclear surface, the probability of nucleon–nucleon collision (2-body collision) is negligible compared to the nucleons colliding with the nuclear surface. Thus, the nuclear surface plays a central role in the collisional damping process. On the other hand, inhomogeneous damping occurs due to the deformation of the nucleus. If the ground state of the nucleus is deformed, there is a possibility of nucleons vibrating along the different principle axes, producing different centroid energy components. Thus, the GDR line shape splits according to the dimension of the different principle axes producing a large width [46].

To discuss the effects of the nuclear shape deformation and the sensitivity of the GDR on ensembles of shapes characterizing nuclei at high excitation energy, we focus here on two cases. One concerns the ^{88}Mo compound nucleus at high temperature and very high rotational frequency, and the other is the interesting open problem of the GDR built on superdeformed states. The latter is particularly relevant in the search for *extreme shape coexistence*, since in highly deformed systems the GDR strength function is expected to show a large splitting of its Lorentzian shape, with a low energy component having centroid energy close or below the particle threshold, as observed in few light systems around A = 45 [501–503]. Furthermore, the low energy component was found to be correlated with the cold structures of high deformations [504,505], therefore a possibility exists that extreme deformations of hot compound nuclei might be preserved during the evaporation process, leading to a preferential feeding of super- or hyper-deformed structure [506]. This is a challenging topic for future investigation with powerful instrumentation based on efficient detection systems for both discrete, low-energy γ-rays (e.g., tracking arrays [507]) and high-energy γ transitions (e.g., large scintillators arrays, such as PARIS [508,509]).

6.1. Giant dipole resonance built on a hot rotating ^{88}Mo compound nucleus

While most of the existing information on the GDR in hot nuclei concerns the temperature interval 1.2–2.0 MeV, the work on the ^{88}Mo nucleus addresses the region 2–3.5 MeV for which only few studies exist. This nucleus has a distribution of shapes changing considerably as a function of temperature, as it can be seen in Fig. 82 (from [510]).

The main difficulty to address this excitation energy region, 120–260 MeV, is to pin down in the best possible way the excitation of the compound nucleus as the fusion-evaporation is not the only possible reaction and, in addition, pre-equilibrium effects reduce the temperature on the nucleus on which the GDR is built.

The decay of compound ^{88}Mo nuclei was investigated in an experiment performed at the TANDEM+ALPI accelerator of Legnaro National Laboratories(Italy) using ^{48}Ti beams at 300 and 600 MeV that impinged on a ^{40}Ca target [510]. With the detection system GARFIELD and HECTOR it was possible to measure the heavy reaction residues, charged particles and γ-rays produced in these collisions. The maximum values of the transferred angular momentum reached, respectively 78$\hbar$ and 84 $\hbar$, both values exceeding 64$\hbar$, which corresponding to the spin value at which the fission barrier of ^{88}Mo vanishes.

In order to interpret the experimental information on the GDR strength functions and on the effective GDR widths, theoretical approaches using two distinct techniques of modeling the giant resonance were employed. The first one is based on the version of the liquid drop model, LSD, reported in [511], supplemented with the thermal shape fluctuation method (TFM) (see Ref. [512]) and the other is based on the phonon damping model (PDM) [513].

The left part of Fig. 83 (panels (a), (b) and (c), (d)) shows that the predictions reproduce very well the experimental data. In addition, the data at high temperature are compared with the data in the mass region at lower temperature. This is displayed in the right part of Fig. 83 together with the phenomenological expression derived from the many data in the region of temperature up to 2 MeV [514]. The comparison evidences that the phenomenological expression does not account for the ^{88}Mo data at 3 MeV. Consequently more data are needed to determine a general phenomenological expression which could be valid also in the T = 3–4 MeV region.

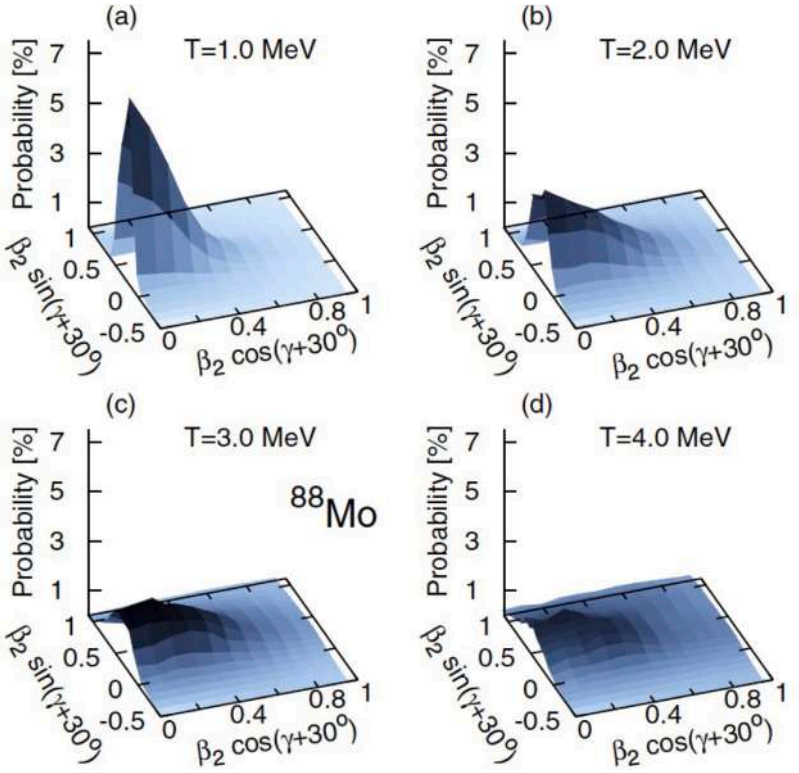

Fig. 82. The nuclear-shape probability distributions for ^{88}Mo at temperatures T = 1, 2, 3, and 4 MeV and spin 40$\hbar$ in panels (a), (b), (c), and (d), respectively. The energy minimization is performed over the (β, γ) plane.
Source: Adapted from [510].

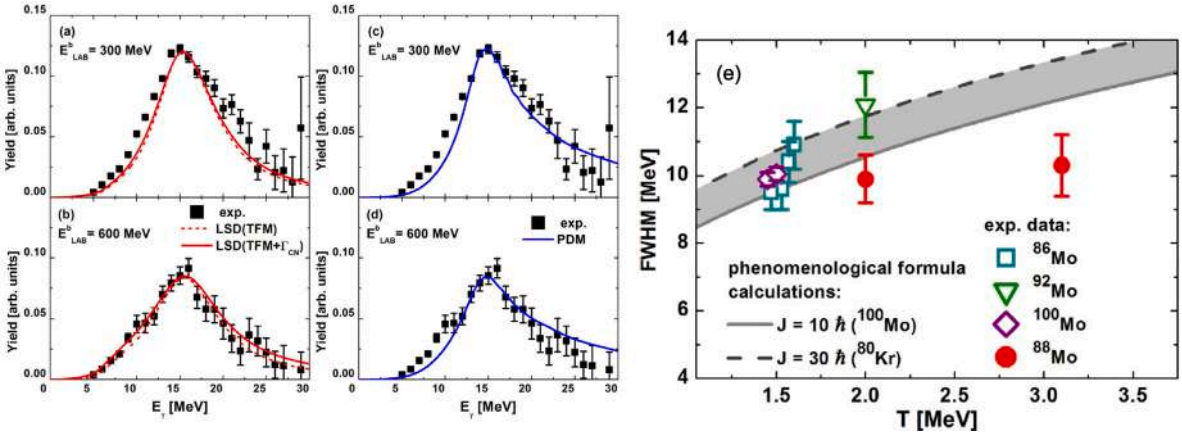

Fig. 83. Panels (a) and (b): Comparison of the GDR strength functions extracted from the experimental data and the effective model values based on the macroscopic Liquid Drop Model with thermal fluctuation, for the beam energies of (a) 300 MeV and (b) 600 MeV. The theoretical GDR strength functions are estimated with a constant (dashed line) and a temperature-dependent (solid line) intrinsic GDR width. Panels (c) and (d): Analogous to panels (a) and (b), with model predictions based on the PDM phonon model, for beam energies of (c) 300 MeV and (d) 600 MeV. Panel (e): Measured GDR widths as a function of temperature for nuclei in the mass region of ^{88}Mo (full circles) compared with predictions obtained using the expression proposed in [514] based on the experimental systematics at lower excitation energies (open symbols).
Source: Adapted from [510].

6.2. Search for the giant dipole resonance built on superdeformed states

One of the intriguing questions not yet answered concerns the population mechanism of superdeformed states, found to exist in many nuclei. In the '90s, it has been suggested [515] that the rather intense population of superdeformed bands (of the order of 1%) is connected to the E1 cooling of the nucleus that is expected to be enhanced due to the large splitting of the GDR strength function, when it is built on these states, and to the level density of the superdeformed states.

To find evidence of the GDR built on excited states is very challenging because of the very low statistics that one can obtain in the high energy spectra when gating on the transitions of the superdeformed bands with the typical intensities of only 1%–2%. Attempts have been made to prove the proposed E1 cooling mechanism, the first one made in the late '80s, by P. Taras et al., [516] in the case of ^{149}Gd, by employing the 8π spectrometer.

Other attempts, made almost two decades ago, exploited more efficient setups and specific features of superdeformed structures of some nuclei that allowed a more efficient gating. This was the case of the ^{143}Eu nucleus which is characterized by the presence of a very intense continuum of E2 type that was found to originate from superdeformed configurations and to have a decay path feeding only particular low-spin states [517]. At low spins, due to the coexistence of both normally deformed, almost spherical, (ND) and triaxially deformed (TD) shapes, this nucleus has a very complex and irregular level scheme and it becomes superdeformed (SD) at high spins. It is therefore expected that one should see the γ decay of the GDR built on superdeformed states by comparing the high-energy γ-spectrum gated by low spin ND transitions (populated partly by the SD decay) with that gated by low spin TD transitions (not populated by the SD decay).

The two top and bottom-left panels of Fig. 84 show the results of an experiment made with the array EUROBALL coupled to the 8 large volume BaF_2 detectors of the HECTOR array (for the measurement of high-energy γ rays) [504,518]. The left top panel is the plot of the ratio of the intensity population of the SD yrast, of the superdeformed bands, and of the superdeformed continuum with the population intensity of states corresponding to triaxial shapes with small deformation. One sees that this is well described by the low energy tail of GDR line shape built on a nucleus with a superdeformed quadrupole deformation. In the right panel the high energy γ-ray spectrum double gated by the lines of the SD yrast band (filled circles) gives only some indication of an excess yield in the region around 10 MeV (in spite of the low statistics), compared to the spectrum gated by low spin transitions of the triaxial shape, which is not populated by SD states. Because of the large error bars it is was not possible to find a clear signal.

Although the direct gating is a way to find a compelling evidence on the role of the GDR in feeding superdeformed states, it is interesting to obtain also a somewhat more inclusive information by comparing the ratio of high energy spectra which were obtained gating on the transitions of the ND (Normal deformed) and TD (triaxial deformed) states of ^{143}Eu (see bottom left panel of Fig. 84). Since the selected transitions of the ND stated are known to be populated by transitions of SD configurations in the regions of discrete and continuum states, this gating selects the gamma cascades leading to superdeformed configurations. The measured ratio is shown in the bottom left part of Fig. 84. The measured ratio deviates from one (by approximately 15%–30%) between 7 to 10 MeV region, where one expects to find the low energy component of the GDR built on a superdeformed nucleus. Effects related to the population of different spin regions are not very likely because the two type of transitions have very similar fold distributions. The corresponding statistical model calculations were made for two values of the level density parameter. The value corresponding to lower density of states, as expected for superdeformed states, gives a better account of the data.

Another interesting attempt to obtain information on the E1 response of the GDR built on extreme deformations was made for the nucleus ^{46}Ti also using the EUROBALL array coupled to the 8 large volume BaF BaF_2 detectors and the EUCLIDES array for charged particles, and using the reaction ^{18}O + ^{28}Si reaction at 105 MeV bombarding energy [502,505]. These data seem to suggest that the low-energy component of the GDR feeds preferentially the highly-deformed band of the residual nucleus ^{42}Ca, as shown on the right bottom part of Fig. 84, similarly to what observed in the case of ^{143}Eu. It is interesting to note that indications of large deformations of the compound nucleus ^{46}Ti were also obtained by an independent measurement of charged particle emission.

One can then conclude that the experimental results on both ^{143}Eu and ^{46}Ti give tentative support to the hypothesis of Herskind et al. [515] of a special role played by the low energy component of the GDR in feeding the SD structures, although new measurements allowing direct gating with discrete transitions of superdeformed bands are needed for an unambiguous conclusion. In addition, other mass regions and the competition with particle feeding should be investigated.

7. Conclusions and perspectives

In this review, we have examined in detail, from the point of view of shape coexistence, the decay properties of the 0^+ excitations in even–even nuclei around Z = 20 (Ca), 28 (Ni), 50 (Sn), 82 (Pb) proton shell closures and along Z = 36 (Kr), Z = 38 (Sr) and Z = 40 (Zr) isotopic chains. The decay properties of the 0^+ fission shape isomers in the actinides region, and superdeformed (SD) states at the decay-out spin in medium/heavy mass systems have also been discussed, being among the primary examples of shape coexistence. Comparisons with theory predictions based on various models are presented – they are instrumental in shedding light on the microscopic structure of the considered states and the properties of their decays.

The survey shows a multifaceted scenario of shape coexistence phenomena which are categorized using, as a primary quantity, the hindrance of the E2 transitions de-exciting 0^+ states and SD decay-out states. Only a small number of 0^+ cases (26 out of a total of 207 examined excitations, i.e., ~13%) turns out to exhibit a significantly hindered decay (HF > 10). No other examples of hindered 0^+ decays, between Z = 18 (Ar) and Z = 92 (U) isotopes, are reported in the literature, except for 0^+_3 in ^{50}Cr, 0^+_3 in ^{172}Yb, 0^+_2 in ^{186}Os and 0^+_3 in ^{192}Os, which were not examined here. In selected cases, the significant hindrance was interpreted as a consequence of a localization of the excited 0^+ state wave function in a specific region of the (β, γ) deformation plane, in

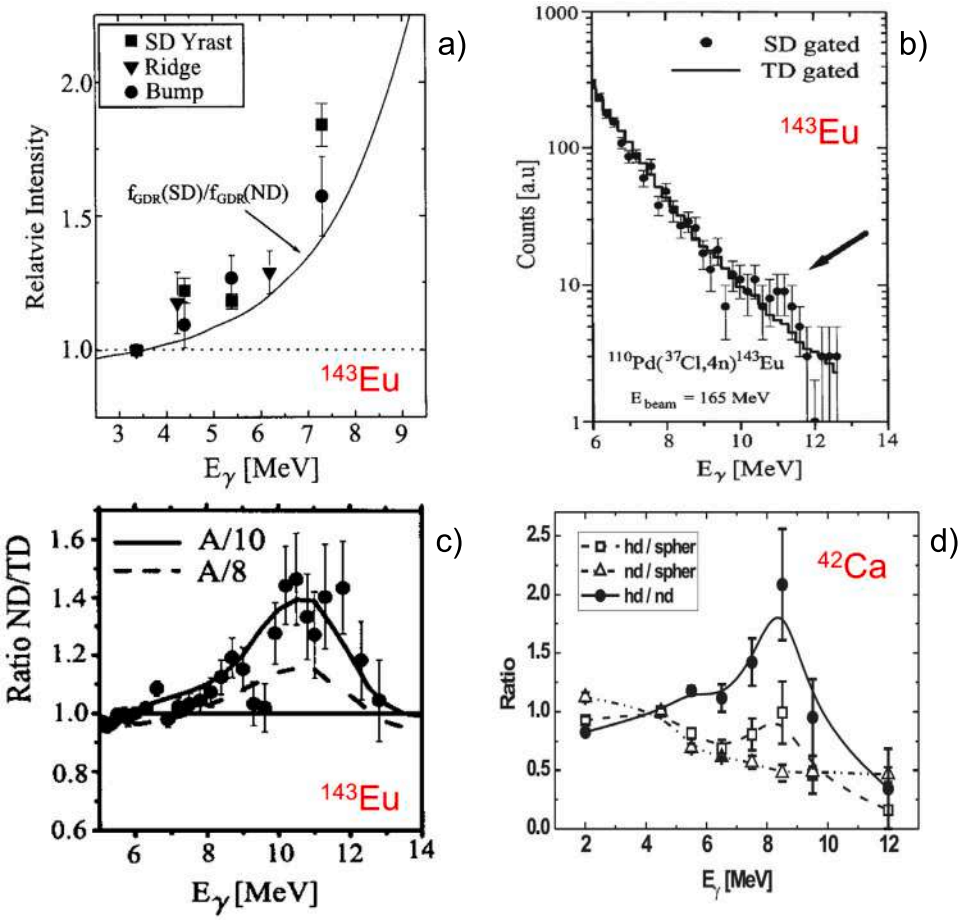

Fig. 84. Panel (a): Intensity of the SD yrast band (squares), ridges (triangles) and E2 quasi-continuum distribution (circles, called 'bump'), of ^{143}Eu, as a function of the high-energy gating transition (normalized at 3 MeV). The full curve gives the ratio between the SD and the spherical GDR strength functions. It represents a lower limit for the feeding of the SD nucleus by E1-decay from the GDR. Panel (b): Comparison of the high-energy γ-ray spectrum double gated by the lines of the SD yrast band (circles) with the spectrum gated by the triaxial configuration (line) of ^{143}Eu. The region of the low energy component of the GDR built on a superdeformed configuration is indicated by the arrow. Panel (c): The ratio of two spectra gated by transitions in ^{143}Eu corresponding to the ND configuration fed by SD transition and by transitions from the triaxial deformed configuration. The statistical model prediction of the compound nucleus decay is also shown. The calculations assume different values for the level density parameter in the SD well (i.e., A/8 and A/10) and the presence of a low energy component due to a superdeformed nucleus in the GDR line shape. Panel (d): The intensity ratios between γ transitions proceeding within spherical ("spher"), normal deformed ("nd") and highly-deformed ("hd") bands in ^{42}Ca as a function of the γ-ray energy from the GDR decay. The lines are statistical model calculations.
Source: Adapted from [504,505,518].

correspondence with a secondary minimum in the Potential Energy Surface. We refer here to the fission shape isomers in ^{236,238}U (with exceptional hindrances HF $\sim 10^8$) and to the shape-isomer-like 0^+_4 excitation in ^{66}Ni, which displays a modest hindrance, of the order of 25. Potential other candidates for this scenario, although not fully established, are 0^+_3 in ^{96}Sr, 0^+_4 in ^{96,98}Zr, and 0^+_3 in ^{112,114}Cd. In creating secondary deep minima, the role of the tensor force was shown to be decisive, leading to a complex scenario of multiple coexisting shapes, including shape-isomer-like structures, in better agreement with experimental results, as compared with mean-field based approaches. In all other cases of 0^+ states exhibiting hindered decays between states localized in different, but not so deep minima of the PES (e.g., the 0^+_4 state in ^{64}Ni), or between states with similar deformation (e.g., the spherical excitations 0^+_2 in ^{58}Ni and 0^+_3 in ^{66}Ni), microscopic quantum mechanical effects (e.g., correlation/cancellation between matrix elements connecting initial and final states) are considered to be responsible for generating a hindrance. The vast majority of the examined 0^+ states demonstrates instead a not hindered decay (i.e., HF < 10), although the half lives vary over a very wide range, from sub ps to hundreds ns, depending on the transition energy. Here, the absence of a retardation in the decay is interpreted as a consequence of mixing of initial and final state wavefunctions.

In the case of SD states at the decay-out spins, only very few B(E/Mλ) reduced transition probabilities are experimentally available for the transitions linking the SD states to lower-lying normal deformed states (i.e., for ~20 SD bands out of more than 350 known in literature, corresponding to $\lesssim$10%), from which HF values can be extracted. Large hindrances, of the order of 10^2–10^4 are deduced for medium/heavy mass systems, from Zr (A ~ 100), to Dy (A ~ 150) and Hg/Pb (A ~ 190), which are well explained in terms of

a sizeable barrier in the potential energy surface, still present at the decay-out spin (of the order of 10–30 $\hbar$) and separating the SD configuration (located in a secondary minimum) from the states in the main minimum. For lower masses, the decay-out occurs at much lower spins, often close to 0. Here, the barrier picture is not directly applicable and the wave functions mix significantly, resulting in the absence of hindrance for the SD decay-out.

From the survey presented in this review, it clearly emerges the importance of understanding the nature of 0^+ states, among which band heads of well-deformed rotational bands, well developed at higher spins, can be found. Future experimental work is needed to fully characterize the structure of 0^+ states in different mass regions, including measurements of quadrupole moments, E0 monopole strength, single- and multi-nucleon transfer reaction cross sections, in addition to detailed information on their γ-decay properties, including state lifetimes which are most often missing or only limits exist. This appears now to be possible, with a high degree of precision, by employing state-of-the-art detection systems based, for example, on tracking arrays like AGATA [140,144] and GRETA [145], coupled to high-granularity detection systems for light-charged particles and conversion electrons (e.g., GRIT [519], ORRUBA [520], SLICES [521] and SPEDE [522]), and to magnetic spectrometers (e.g., PRISMA [523,524] and VAMOS [525,526]).

The systematics of hindrance factors for the decay of low-lying 0^+ excitations and the analyses of the origin of these hindrances show that shape isomerism is a quite rare phenomenon outside of the actinide region. Even if it exists, the magnitude of hindrance is several orders lower. It still can be that 0^+ states with well isolated wave functions in secondary PES minima exist, in particular in heavy nuclei in the Pt-Ra region, where pronounced barriers (governing the decay-out of SD bands at higher spins) may survive down to spin 0, as predicted by macroscopic–microscopic model based on the Lublin-Strasbourg-Drop approach [417]. However, such states would lie in an excitation-energy region between 4 and 8 MeV, characterized by very high density of states, therefore, their population with significant cross section would be extremely difficult (also exploiting direct population mechanisms based on multi-nucleon transfer reactions with heavy ions [527]), and the study of their decay properties will be a challenge even for the most powerful detection setups.

Another area of exploration for shape isomerism can be very exotic nuclei, not currently accessible, where deep secondary minima can be created, for instance, by the action of the tensor force, similarly to what has been observed in few examined cases close to the stability line [21,68]. In this context, the guidance from theory is crucial. Predictions from mean-field based approaches already point to very-neutron rich regions of the nuclear chart, for example around Cd, Sn, Ba, Xe and Yb [528–530], where extremely elongated shapes (superdeformed or even hyperdeformed, i.e., with axes ratios significantly exceeding 2:1) are expected to well develop at high spins. Following these structure down to low spins, or populating directly 0^+ states in these systems, may give access to remarkable examples of shape isomerism. The topic has been only preliminarily explored by Herskind and collaborators [506,531] with large arrays based of Anti-Compton Shields (i.e., EUROBALL and GAMMASPHERE [36,39]), exploiting complex analysis of quasi-continuum distributions in multi-dimensional spectra of correlated γ transitions. Such studies will become central in future investigation with powerful detection systems offering improved sensitivity (like γ-ray tracking arrays [532,533]), and employing reactions with intense radioactive ion beams from upcoming facilities.

In our review, we have also shown that fully quantum-mechanical approaches have reached a significant predictive power to model the structure of 0^+ states, as well as low-lying members of structures built on these 0^+ excitations. Such theoretical approaches, however, are still restricted, by computing capabilities, to light- and medium-mass nuclei, since they are not as straightforward as earlier approaches involving numerical computations of smaller scales. Nevertheless, it seems that they will become more accessible in near future due to various developments inside and outside nuclear physics. As a consequence, a significant step is expected toward a unified description of shape coexistence phenomena, from 0^+ excitations to SD rotational bands at higher spins, including also triaxiality, which starts to appear as a quite common feature of nuclei, at variance from past interpretations often based on phonon excitations.

The impact of shape ensembles at finite temperature on the decay properties of highly-excited states (Giant Dipole Resonances) has also been discussed in the review, as a tool for probing the robustness of shape-coexistence phenomena with angular momentum and temperature. It was also speculated that extreme deformations of hot compound nuclei, formed in fusion reactions, might be preserved during the evaporation process, leading to a preferential feeding of super- and hyper-deformed shapes at high angular momenta [506]. This also represents an important topic for future investigations with powerful setups based on high-efficiency detection systems for high-energy γ-rays (e.g., the PARIS array [508,509]), in particular in exotic regions of the nuclear chart.

CRediT authorship contribution statement

S. Leoni: Writing – original draft, Conceptualization. **B. Fornal:** Writing – original draft, Conceptualization. **A. Bracco:** Writing – original draft, Conceptualization. **Y. Tsunoda:** Writing – original draft, Conceptualization. **T. Otsuka:** Writing – original draft, Conceptualization.

Declaration of competing interest

The authors declare the following financial interests/personal relationships which may be considered as potential competing interests: Silvia Leoni reports financial support was provided by University of Milan and INFN. Silvia Leoni reports a relationship with University of Milan and INFN that includes: employment, funding grants, and travel reimbursement. If there are other authors, they declare that they have no known competing financial interests or personal relationships that could have appeared to influence the work reported in this paper.

Acknowledgments

The authors are grateful to Dr. Nicolae Marginean and Dr. Enrico Vigezzi for extensive and inspiring discussions on achievements and perspectives in this fascinating nuclear structure field. The support by the POLITA (INFN (Italy)–COPIN (Poland)) Collaboration Agreement is acknowledged. T.O. acknowledges KAKENHI grants (JP19H05145, JP21H00117). Y. T. and T. O. also acknowledge valuable support by MEXT as 'Priority Issue on Post-K computer' (Elucidation of the Fundamental Laws and Evolution of the Universe, hp190160), 'Program for Promoting Researches on the Supercomputer Fugaku' (Simulation for basic science: from fundamental laws of particles to creation of nuclei, JPMXP1020200105, hp200130, hp210165, hp220174), and 'Program for Promoting Researches on the Supercomputer Fugaku' (Simulation for basic science: approaching the new quantum era, JPMXP1020230411, hp230207), and JICFuS.

References

[1] G.P. Moss, Pure Appl. Chem. 68 (1996) 2193, http://dx.doi.org/10.1351/pac199668122193.
[2] Conformational Isomerism; https://www.wikiwand.com/en/Conformational_isomerism#/overview.
[3] A. Bohr, B.R. Mottelson, Nuclear Structure 1 and 2, World Scientific Publishing, Singapore, 1999.
[4] H. Jahn, E. Teller, Proc. R. Soc. Lond. Ser. A Math. Phys. Eng. Sci. 161 (1937) 220, http://dx.doi.org/10.1098/rspa.1937.0142.
[5] P.G. Reinhard, E. Otten, Nuclear Phys. A 420 (1984) 173, http://dx.doi.org/10.1016/0375-9474(84)90437-8.
[6] W. Nazarewicz, Int. J. Mod. Phys. E 02 (supp01) (1993) 51, http://dx.doi.org/10.1142/S0218301393000479.
[7] W. Nazarewicz, Nuclear Phys. A 574 (1994) 27, http://dx.doi.org/10.1016/0375-9474(94)90037-X.
[8] P. Ring, P. Schuck, The Nuclear Many-Body Problem, Springer, Berlin, 1980.
[9] N. Schunck, L.M. Robledo, Rep. Progr. Phys. 79 (11) (2016) 116301, http://dx.doi.org/10.1088/0034-4885/79/11/116301.
[10] D.L. Hill, J.A. Wheeler, Phys. Rev. 89 (1953) 1102, http://dx.doi.org/10.1103/PhysRev.89.1102.
[11] S. Polikanov, et al., Sov. Phys.—JETP 15 (1962) 1016.
[12] S. Bjørnholm, J.E. Lynn, Rev. Mod. Phys. 52 (1980) 725, http://dx.doi.org/10.1103/RevModPhys.52.725.
[13] P. Thirolf, D. Habs, Prog. Part. Nucl. Phys. 49 (2) (2002) 325, http://dx.doi.org/10.1016/S0146-6410(02)00158-8.
[14] J. Bonn, G. Huber, H.J. Kluge, L. Kugler, E. Otten, Phys. Lett. B 38 (1972) 308, http://dx.doi.org/10.1016/0370-2693(72)90253-5.
[15] K. Heyde, J.L. Wood, Rev. Mod. Phys. 83 (2011) 1467, http://dx.doi.org/10.1103/RevModPhys.83.1467.
[16] J. Bron, et al., Nuclear Phys. A 318 (1979) 335, http://dx.doi.org/10.1016/0375-9474(79)90653-5.
[17] M. Hotchkis, et al., Nuclear Phys. A 530 (1991) 111, http://dx.doi.org/10.1016/0375-9474(91)90758-X.
[18] J. Skalski, S. Mizutori, W. Nazarewicz, Nuclear Phys. A 617 (1997) 282, http://dx.doi.org/10.1016/S0375-9474(97)00125-5.
[19] C. Chandler, et al., Phys. Rev. C 56 (1997) R2924, http://dx.doi.org/10.1103/PhysRevC.56.R2924.
[20] F. Becker, et al., Eur. Phys. J. A 4 (2) (1999) 103, http://dx.doi.org/10.1007/s100500050209.
[21] N. Marginean, et al., Phys. Rev. Lett. 125 (2020) 102502, http://dx.doi.org/10.1103/PhysRevLett.125.102502.
[22] K. Heyde, J.L. Wood, J. Phys. G: Nucl. Part. Phys. 17 (1991) 135, http://dx.doi.org/10.1088/0954-3899/17/2/007.
[23] K. Wimmer, et al., Phys. Rev. Lett. 105 (2010) 252501, http://dx.doi.org/10.1103/PhysRevLett.105.252501.
[24] P.E. Garrett, M. Zielińska, E. Clément, Prog. Part. Nucl. Phys. 124 (2022) 103931, http://dx.doi.org/10.1016/j.ppnp.2021.103931.
[25] E. Caurier, F. Nowacki, A. Poves, J. Retamosa, Phys. Rev. C 58 (1998) 2033, http://dx.doi.org/10.1103/PhysRevC.58.2033.
[26] J. Dowie, et al., Phys. Lett. B 811 (2020) 135855, http://dx.doi.org/10.1016/j.physletb.2020.135855.
[27] L. Morris, et al., Phys. Rev. C 104 (2021) 054323, http://dx.doi.org/10.1103/PhysRevC.104.054323.
[28] N. Tsunoda, T. Otsuka, K. Takayanagi, N. Shimizu, T. Suzuki, Y. Utsuno, S. Yoshida, H. Ueno, Nature 587 (7832) (2020) 66, http://dx.doi.org/10.1038/s41586-020-2848-x.
[29] K. Heyde, P. Van Isacker, M. Waroquier, J. Wood, R. Meyer, Phys. Rep. 102 (1983) 291, http://dx.doi.org/10.1016/0370-1573(83)90085-6.
[30] J. Wood, K. Heyde, W. Nazarewicz, M. Huyse, P. van Duppen, Phys. Rep. 215 (1992) 101, http://dx.doi.org/10.1016/0370-1573(92)90095-H.
[31] J. Wood, E. Zganjar, C. De Coster, K. Heyde, Nuclear Phys. A 651 (1999) 323, http://dx.doi.org/10.1016/S0375-9474(99)00143-8.
[32] J.L. Wood, K. Heyde, J. Phys. G: Nucl. Part. Phys. 43 (2) (2016) 020402, http://dx.doi.org/10.1088/0954-3899/43/2/020402.
[33] T. Kibédi, A. Garnsworthy, J. Wood, Prog. Part. Nucl. Phys. 123 (2022) 103930, http://dx.doi.org/10.1016/j.ppnp.2021.103930.
[34] P. Nolan, F. Beck, D.B. Fossan, Annu. Rev. Nucl. Part. Sci. 45 (1) (1994) 561, http://dx.doi.org/10.1146/annurev.ns.44.120194.003021.
[35] J. Simpson, Z. Phys. A 358 (1997) 139, https://link.springer.com/article/10.1007/s002180050290.
[36] G. de Angelis, A. Bracco, D. Curien, Europhys. News 34 (2003) 181, http://dx.doi.org/10.1051/epn:2003503.
[37] W. Korten, S. Lunardi, Scientific and technical activity report 1997–2003, 2003, Available at http://euroball.lnl.infn.it/EBmore/EB_Final_Report.pdf.
[38] M.A. Delaplanque, R.M. D (Eds.), Gammasphere Proposal, 1997, Preprint LBNL-5202.
[39] I.Y. Lee, M.A. Deleplanque, K. Vetter, Rep. Progr. Phys. 66 (2003) 1095, http://dx.doi.org/10.1088/0034-4885/66/7/201.
[40] R.V.F. Janssens, T.L. Khoo, Anna. Rev. Nucl. Part. Sci. 41 (1991) 321, http://dx.doi.org/10.1146/annurev.ns.41.120191.001541.
[41] D. Ward, P. Fallon, Adv. Nucl. Phys., Springer, 2001, p. 167, http://dx.doi.org/10.1007/0-306-47915-X_3.
[42] S. Aberg, H. Flocard, W. Nazarewicz, Ann. Rev. Nucl. Part. Sci. 40 (1) (1990) 439, http://dx.doi.org/10.1146/annurev.ns.40.120190.002255.
[43] S.G. Nilsson, I. Ragnarsson, Shapes and Shells in Nuclear Structure, Cambridge University Press, Cambridge, 1995.
[44] A. Afanasjev, D. Fossan, G. Lane, I. Ragnarsson, Phys. Rep. 322 (1999) 1, http://dx.doi.org/10.1016/S0370-1573(99)00035-6.
[45] S. Frauendorf, Rev. Mod. Phys. 73 (2001) 463, http://dx.doi.org/10.1103/RevModPhys.73.463.
[46] P.F. Bortignon, A. Bracco, R.A. Broglia, Giant Resonances: Nuclear Structure at Finite Temperature, Harwood Academic, Amsterdam, 1998.
[47] N. Bohr, J.A. Wheeler, Phys. Rev. 56 (1939) 426, http://dx.doi.org/10.1103/PhysRev.56.426.
[48] K.L.G. Heyde, The Nuclear Shell Model, Springer Berlin Heidelberg, Berlin, Heidelberg, 1990, pp. 54–135, http://dx.doi.org/10.1007/978-3-642-97203-4_4.
[49] E. Caurier, G. Martínez-Pinedo, F. Nowacki, A. Poves, A.P. Zuker, Rev. Mod. Phys. 77 (2005) 427, http://dx.doi.org/10.1103/RevModPhys.77.427.
[50] Y. Tsunoda, T. Otsuka, Configuration interaction approach to atomic nuclei: The shell model, 2022, pp. 1–49, http://dx.doi.org/10.1007/978-981-15-8818-1_17-1.
[51] T. Otsuka, M. Honma, T. Mizusaki, N. Shimizu, Y. Utsuno, Prog. Part. Nucl. Phys. 47 (2001) 319, http://dx.doi.org/10.1016/S0146-6410(01)00157-0.
[52] N. Shimizu, T. Abe, Y. Tsunoda, Y. Utsuno, T. Yoshida, T. Mizusaki, M. Honma, T. Otsuka, Prog. Theor. Exp. Phys. 2012 (2012) http://dx.doi.org/10.1093/ptep/pts012.01A205.
[53] N. Shimizu, T. Abe, M. Honma, T. Otsuka, T. Togashi, Y. Tsunoda, Y. Utsuno, T. Yoshida, Phys. Scr. 92 (6) (2017) 063001, http://dx.doi.org/10.1088/1402-4896/aa65e4.
[54] N. Shimizu, Physics 4 (3) (2022) 1081, http://dx.doi.org/10.3390/physics4030071.

[55] Y. Tsunoda, T. Otsuka, N. Shimizu, M. Honma, Y. Utsuno, Phys. Rev. C 89 (2014) 031301, http://dx.doi.org/10.1103/PhysRevC.89.031301.
[56] M. Girod, J.P. Delaroche, D. Gogny, J.F. Berger, Phys. Rev. Lett. 62 (1989) 2452, http://dx.doi.org/10.1103/PhysRevLett.62.2452.
[57] P. Van Duppen, E. Coenen, K. Deneffe, M. Huyse, K. Heyde, P. Van Isacker, Phys. Rev. Lett. 52 (1984) 1974, http://dx.doi.org/10.1103/PhysRevLett.52.1974.
[58] A.N. Andreyev, et al., Nature 405 (2000) 430, http://dx.doi.org/10.1038/35013012.
[59] P. Möller, A. Sierk, R. Bengtsson, H. Sagawa, T. Ichikawa, At. Data Nucl. Data Tables 98 (2012) 149, http://dx.doi.org/10.1016/j.adt.2010.09.002.
[60] T. Otsuka, et al., Rev. Mod. Phys. 92 (2020) 015002, http://dx.doi.org/10.1103/RevModPhys.92.015002.
[61] T. Otsuka, Physics 4 (1) (2022) 258, http://dx.doi.org/10.3390/physics4010018.
[62] T. Otsuka, T. Suzuki, R. Fujimoto, H. Grawe, Y. Akaishi, Phys. Rev. Lett. 95 (2005) 232502, http://dx.doi.org/10.1103/PhysRevLett.95.232502.
[63] J.P. Schiffer, et al., Phys. Rev. Lett. 92 (2004) 162501, http://dx.doi.org/10.1103/PhysRevLett.92.162501.
[64] T. Otsuka, Y. Tsunoda, J. Phys. G: Nucl. Part. Phys. 43 (2016) 024009, http://dx.doi.org/10.1088/0954-3899/43/2/024009.
[65] M. Sanchez-Vega, et al., Phys. Rev. C 60 (1999) 024303, http://dx.doi.org/10.1103/PhysRevC.60.024303.
[66] J. Ojala, et al., Commun. Phys. 5 (2022) 213, http://dx.doi.org/10.1038/s42005-022-00990-4.
[67] National Nuclear Data Center, Brookhaven; https://www.nndc.bnl.gov.
[68] S. Leoni, et al., Phys. Rev. Lett. 118 (2017) 162502, http://dx.doi.org/10.1103/PhysRevLett.118.162502.
[69] K. Löbner, Phys. Lett. B 26 (1968) 369, http://dx.doi.org/10.1016/0370-2693(68)90614-X.
[70] H. Morinaga, T. Yamasaki, In-Beam Gamma-Ray Spectroscopy, Elsevier Science, Nort-Holland, Netherlands, 1976.
[71] K. Alder, A. Bohr, T. Huus, B. Mottelson, A. Winther, Mod. Phys. 28, 432, http://dx.doi.org/10.1103/RevModPhys.28.432.
[72] A. Görgen, W. Korten, J. Phys. G: Nucl. Part. Phys. 43 (2) (2016) 024002, http://dx.doi.org/10.1088/0954-3899/43/2/024002.
[73] M. Zielińska, et al., Eur. Phys. J. A 52 (2016) 99, http://dx.doi.org/10.1140/epja/i2016-16099-8.
[74] M. Rocchini, M. Zielińska, Physics 3 (2021) 1237, http://dx.doi.org/10.3390/physics3040078.
[75] K. Kumar, Phys. Rev. Lett. 28 (1972) 249, http://dx.doi.org/10.1103/PhysRevLett.28.249.
[76] D. Cline, Ann. Rev. Nucl. Part. Sci. 36 (1986) 683, http://dx.doi.org/10.1146/annurev.ns.36.120186.003343.
[77] M. Zielińska, Low-Energy Coulomb Excitation and Nuclear Deformation, Springer International Publishing, Cham, 2022, p. 43, http://dx.doi.org/10.1007/978-3-031-10751-1_2.
[78] E.L. Church, J. Weneser, Phys. Rev. 103 (1956) 1035, http://dx.doi.org/10.1103/PhysRev.103.1035.
[79] J. Dowie, T. Kibédi, T. Eriksen, A. Stuchbery, At. Data Nucl. Data Tables 131 (2020) 101283, http://dx.doi.org/10.1016/j.adt.2019.06.002.
[80] T. Kibédi, R. Spear, At. Data Nucl. Data Tables 89 (1) (2005) 77, http://dx.doi.org/10.1016/j.adt.2004.11.002.
[81] B.A. Brown, A.B. Garnsworthy, T. Kibédi, A.E. Stuchbery, Phys. Rev. C 95 (2017) 011301, http://dx.doi.org/10.1103/PhysRevC.95.011301.
[82] E. Ideguchi, et al., Phys. Rev. Lett. 128 (2022) 252501, http://dx.doi.org/10.1103/PhysRevLett.128.252501.
[83] P. Duval, D. Goutte, M. Vergnes, Phys. Lett. B 124 (1983) 297, http://dx.doi.org/10.1016/0370-2693(83)91457-0.
[84] J.E. García-Ramos, K. Heyde, Phys. Rev. C 92 (2015) 034309, http://dx.doi.org/10.1103/PhysRevC.92.034309.
[85] J. Lay, A. Vitturi, L. Fortunato, Y. Tsunoda, T. Togashi, T. Otsuka, Phys. Lett. B 838 (2023) 137719, http://dx.doi.org/10.1016/j.physletb.2023.137719.
[86] E. Flynn, O. Hansen, J. Sherman, N. Stein, J. Sunier, Nuclear Phys. A 264 (1976) 253, http://dx.doi.org/10.1016/0375-9474(76)90431-0.
[87] D. Evers, W. Assmann, K. Rudolph, S. Skorka, P. Sperr, Nuclear Phys. A 198 (1972) 268, http://dx.doi.org/10.1016/0375-9474(72)90784-1.
[88] D. Evers, W. Assmann, K. Rudolph, S. Skorka, P. Sperr, Nuclear Phys. A 230 (1974) 109, http://dx.doi.org/10.1016/0375-9474(74)90533-8.
[89] W. Alford, R. Lindgren, D. Elmore, R. Boyd, Nuclear Phys. A 243 (2) (1975) 269, http://dx.doi.org/10.1016/0375-9474(75)90248-1.
[90] H. Fielding, R. Anderson, C. Zafiratos, D. Lind, F. Cecil, H. Wieman, W. Alford, Nuclear Phys. A 281 (1977) 389, http://dx.doi.org/10.1016/0375-9474(77)90504-8.
[91] P. Guazzoni, et al., Phys. Rev. C 74 (2006) 054605, http://dx.doi.org/10.1103/PhysRevC.74.054605.
[92] P. Guazzoni, et al., Phys. Rev. C 85 (2012) 054609, http://dx.doi.org/10.1103/PhysRevC.85.054609.
[93] P. Guazzoni, et al., Phys. Rev. C 69 (2004) 024619, http://dx.doi.org/10.1103/PhysRevC.69.024619.
[94] P. Guazzoni, et al., Phys. Rev. C 83 (2011) 044614, http://dx.doi.org/10.1103/PhysRevC.83.044614.
[95] P. Guazzoni, et al., Phys. Rev. C 60 (1999) 054603, http://dx.doi.org/10.1103/PhysRevC.60.054603.
[96] J. Bjerregaard, O. Hansen, O. Nathan, R. Chapman, S. Hinds, Nuclear Phys. A 131 (3) (1969) 481, http://dx.doi.org/10.1016/0375-9474(69)90589-2.
[97] J.H. Bjerregaard, O. Hansen, O. Nathan, L. Vistisen, R. Chapman, S. Hinds, Nuclear Phys. A 110 (1968) 1–10, URL https://www.osti.gov/biblio/4547370.
[98] F. Flavigny, et al., Phys. Rev. C 99 (2019) 054332, http://dx.doi.org/10.1103/PhysRevC.99.054332.
[99] D. Pauwels, et al., Phys. Rev. C 86 (2012) 064318, http://dx.doi.org/10.1103/PhysRevC.86.064318.
[100] M. Stryjczyk, et al., Phys. Rev. C 98 (2018) 064326, http://dx.doi.org/10.1103/PhysRevC.98.064326.
[101] J. Wauters, et al., Phys. Rev. Lett. 72 (1994) 1329, http://dx.doi.org/10.1103/PhysRevLett.72.1329.
[102] D.S. Delion, A. Florescu, M. Huyse, J. Wauters, P. Van Duppen, A. Insolia, R.J. Liotta, Phys. Rev. Lett. 74 (1995) 3939, http://dx.doi.org/10.1103/PhysRevLett.74.3939.
[103] D.S. Delion, A. Florescu, M. Huyse, J. Wauters, P. Van Duppen, A. Insolia, R.J. Liotta, Phys. Rev. C 54 (1996) 1169, http://dx.doi.org/10.1103/PhysRevC.54.1169.
[104] T. Nikšić, P. Marević, D. Vretenar, Phys. Rev. C 89 (2014) 044325, http://dx.doi.org/10.1103/PhysRevC.89.044325.
[105] J.L. Egido, Phys. Scr. 91 (2016) 073003, http://dx.doi.org/10.1088/0031-8949/91/7/073003.
[106] S. Quan, Q. Chen, Z.P. Li, T. Nikšić, D. Vretenar, Phys. Rev. C 95 (2017) 054321, http://dx.doi.org/10.1103/PhysRevC.95.054321.
[107] T. Togashi, Y. Tsunoda, T. Otsuka, N. Shimizu, Phys. Rev. Lett. 117 (2016) 172502, http://dx.doi.org/10.1103/PhysRevLett.117.172502.
[108] B.A. Marsh, et al., Nat. Phys. 14 (12) (2018) 1163, http://dx.doi.org/10.1038/s41567-018-0292-8.
[109] S. Polikanov, et al., Sov. Phys.—JETP 17 (1963) 544, http://www.jetp.ras.ru/cgi-bin/dn/e_017_03_0544.pdf.
[110] G.N. Flevor, et al., Sov. Phys.—JETP 18 (1964) 964, http://www.jetp.ras.ru/cgi-bin/dn/e_018_04_0964.pdf.
[111] J. Randrup, C. Tsang, P. Möller, S. Nilsson, S. Larsson, Nuclear Phys. A 217 (1973) 221, http://dx.doi.org/10.1016/0375-9474(73)90192-9.
[112] S. Bjørnholm, J. Borggreen, L. Westgaard, V. Karnaukhov, Nuclear Phys. A 95 (3) (1967) 513, http://dx.doi.org/10.1016/0375-9474(67)90846-9.
[113] G.N. Flerov, V.A. Druin, Radioactive Properties of Nuclei of Heaviest Elements (Review); RADIOAKTIVNYE SVOISTVAYADER NAIBOLEE TYAZHELYKH ELEMENTOV, USSR, 1966.
[114] V. Strutinsky, Nuclear Phys. A 95 (2) (1967) 420, http://dx.doi.org/10.1016/0375-9474(67)90510-6.
[115] I. Ragnarsson, S.G. Nilsson, R.K. Sheline, Phys. Rep. 45 (1978) 1, http://dx.doi.org/10.1016/0370-1573(78)90004-2.
[116] N. Lark, G. Sletten, J. Pedersen, S. Bjørnholm, Nuclear Phys. A 139 (3) (1969) 481, http://dx.doi.org/10.1016/0375-9474(69)90273-5.
[117] P. Reiter, PhD. Thesis University of Heidelberg (1988).
[118] P. Russo, J. Pedersen, R. Vandenbosch, Nuclear Phys. A 240 (1) (1975) 13, http://dx.doi.org/10.1016/0375-9474(75)90434-0.
[119] E. Migneco, G. Russo, R. De Leo, A. Pantaleo, Phys. Rev. C 16 (1977) 1919, http://dx.doi.org/10.1103/PhysRevC.16.1919.
[120] S. Oberstedt, J. Theobald, H. Weigmann, J. Wartena, C. Børkholz, Nuclear Phys. A 573 (1994) 467, http://dx.doi.org/10.1016/0375-9474(94)90353-0.
[121] S. Leoni, B. Fornal, N. Mărginean, J.N. Wilson, Eur. Phys. J. Spec. Top. 233 (2024) 1061, http://dx.doi.org/10.1140/epjs/s11734-024-01175-6.
[122] V. Metag, D. Habs, H. Specht, Phys. Rep. 65 (1) (1980) 1, http://dx.doi.org/10.1016/0370-1573(80)90006-X.
[123] V. Pashkevich, Nuclear Phys. A 133 (2) (1969) 400, http://dx.doi.org/10.1016/0375-9474(69)90641-1.

[124] Chin Fu Tsang, S.G. Nilsson, Nuclear Phys. A 140 (2) (1970) 275, http://dx.doi.org/10.1016/0375-9474(70)90326-X.
[125] I. Ragnarsson, T. Bengtsson, G. Leander, S. AAberg, Nuclear Phys. A 347 (1) (1980) 287, http://dx.doi.org/10.1016/0375-9474(80)90530-8.
[126] M.J.A. de Voigt, J. Dudek, Z. Szymański, Rev. Mod. Phys. 55 (1983) 949, http://dx.doi.org/10.1103/RevModPhys.55.949.
[127] B. Singh, R. Zywina, R.B. Firestone, Nucl. Data Sheets 97 (2) (2002) 241, http://dx.doi.org/10.1006/ndsh.2002.0018.
[128] Z. Szymanski, Fast Nuclear Rotation, Cambridge (United Kingdom), 1983.
[129] S. Frauendorf, Phys. Scr. 93 (2018) 043003, http://dx.doi.org/10.1088/1402-4896/aaa2e9.
[130] R. Bengtsson, S. Larsson, G. Leander, P. Möller, S. Nilsson, S. AAberg, Z. Szymański, Phys. Lett. B 57 (1975) 301, http://dx.doi.org/10.1016/0370-2693(75)90455-4.
[131] K. Neergård, V. Pashkevich, S. Frauendorf, Nuclear Phys. A 262 (1) (1976) 61, http://dx.doi.org/10.1016/0375-9474(76)90440-1.
[132] G. Andersson, et al., Nuclear Phys. A 268 (1976) 205, http://dx.doi.org/10.1016/0375-9474(76)90461-9.
[133] R. Wyss, J. Nyberg, A. Johnson, R. Bengtsson, W. Nazarewicz, Phys. Lett. B 215 (1988) 211, http://dx.doi.org/10.1016/0370-2693(88)91422-0.
[134] R.F. Casten, A. Frank, M. Moshinsky, S. Pittel (Eds.), Contemporary Topics in Nuclear Structure Physics. Proceedings, International Conference, Cocoyoc, Mexico, June 9-14, 1988, 1988.
[135] R. Wyss, J. Nyberg, A. Johnson, R. Bengtsson, W. Nazarewicz, Phys. Lett. B 215 (1988) 211, http://dx.doi.org/10.1016/0370-2693(88)91422-0.
[136] W. Nazarewicz, R. Wyss, A. Johnson, Nuclear Phys. A 503 (1989) 285, http://dx.doi.org/10.1016/0375-9474(89)90238-8.
[137] Y. Shimizu, E. Vigezzi, R. Broglia, Nuclear Phys. A 509 (1990) 80, http://dx.doi.org/10.1016/0375-9474(90)90376-W.
[138] P.J. Twin, et al., Phys. Rev. Lett. 57 (1986) 811, http://dx.doi.org/10.1103/PhysRevLett.57.811.
[139] M.A. Riley, J. Simpson, E.S. Paul, Phys. Scr. 91 (12) (2016) 123002, http://dx.doi.org/10.1088/0031-8949/91/12/123002.
[140] S. Akkoyun, et al., Nucl. Instrum. Methods A 668 (2012) 26, http://dx.doi.org/10.1016/j.nima.2011.11.081.
[141] A. Gadea, et al., Nucl. Instrum. Methods A 654 (1) (2011) 88, http://dx.doi.org/10.1016/j.nima.2011.06.004.
[142] E. Clement, et al., Nucl. Instrum. Methods Phys. Res. A 855 (2017) 1, http://dx.doi.org/10.1016/j.nima.2017.02.063.
[143] A. Bracco, G. Duchêne, Z. Podolyák, P. Reiter, Prog. Part. Nucl. Phys. 121 (2021) 103887, http://dx.doi.org/10.1016/j.ppnp.2021.103887.
[144] A. Bracco, E. Clément, A. Gadea, W. Korten, S. Leoni, J. Simpson, Eur. Phys. J. A 59 (2023) 243, http://dx.doi.org/10.1140/epja/s10050-023-01140-2.
[145] S. Paschalis, et al., Nucl. Instrum. Methods Phys. Res. A 709 (2013) 44, http://dx.doi.org/10.1016/j.nima.2013.01.009.
[146] P. Fallon, A. Gade, I.Y. Lee, 66 (1) (2016) 321. http://dx.doi.org/10.1146/annurev-nucl-102115-044834.
[147] D. Kleppner, Phys. Today 44 (12) (1991) 9, http://dx.doi.org/10.1063/1.2810343.
[148] A. Lopez-Martens, T. Lauritsen, S. Leoni, T. Døssing, T. Khoo, S. Siem, Prog. Part. Nucl. Phys. 89 (2016) 137, http://dx.doi.org/10.1016/j.ppnp.2016.02.003.
[149] M. Deleplanque, Nuclear Phys. A 421 (1984) 339, http://dx.doi.org/10.1016/0375-9474(84)90352-X.
[150] E.F. Moore, et al., Phys. Rev. Lett. 63 (1989) 360, http://dx.doi.org/10.1103/PhysRevLett.63.360.
[151] T. Lauritsen, et al., Phys. Rev. Lett. 88 (2002) 042501, http://dx.doi.org/10.1103/PhysRevLett.88.042501.
[152] S. Siem, et al., Phys. Rev. C 70 (2004) 014303, http://dx.doi.org/10.1103/PhysRevC.70.014303.
[153] E. Vigezzi, R. Broglia, T. Døssing, Phys. Lett. B 249 (1990) 163, http://dx.doi.org/10.1016/0370-2693(90)91236-5.
[154] K. Yoshida, M. Matsuo, Y. Shimizu, Nuclear Phys. A 696 (1) (2001) 85, http://dx.doi.org/10.1016/S0375-9474(01)01123-X.
[155] E. Vigezzi, R. Broglia, T. Døssing, Nuclear Phys. A 520 (1990) c179, http://dx.doi.org/10.1016/0375-9474(90)91145-H.
[156] R.U. Haq, A. Pandey, O. Bohigas, Phys. Rev. Lett. 48 (1982) 1086, http://dx.doi.org/10.1103/PhysRevLett.48.1086.
[157] O. Bohigas, M. Giannoni, C. Schmit, Phys. Rev. Lett. 52 (1984) 1, http://dx.doi.org/10.1103/PhysRevLett.52.1.
[158] C. Petrache, et al., Phys. Lett. B 415 (1997) 223, http://dx.doi.org/10.1016/S0370-2693(97)01245-8.
[159] D. Bazzacco, et al., Phys. Rev. C 49 (1994) R2281, http://dx.doi.org/10.1103/PhysRevC.49.R2281.
[160] C.M. Petrache, et al., Phys. Rev. Lett. 77 (1996) 239, http://dx.doi.org/10.1103/PhysRevLett.77.239.
[161] M.A. Deleplanque, et al., Phys. Rev. C 52 (1995) R2302, http://dx.doi.org/10.1103/PhysRevC.52.R2302.
[162] S. Perriès, et al., Phys. Rev. C 60 (1999) 064313, http://dx.doi.org/10.1103/PhysRevC.60.064313.
[163] S. Lunardi, et al., Phys. Rev. C 52 (1995) R6, http://dx.doi.org/10.1103/PhysRevC.52.R6.
[164] J. Domscheit, et al., Nuclear Phys. A 660 (1999) 381, http://dx.doi.org/10.1016/S0375-9474(99)00392-9.
[165] S. Törmänen, et al., Phys. Lett. B 454 (1999) 8, http://dx.doi.org/10.1016/S0370-2693(99)00346-9.
[166] D.P. McNabb, et al., Phys. Rev. C 61 (2000) 031304, http://dx.doi.org/10.1103/PhysRevC.61.031304.
[167] R.G. Henry, et al., Phys. Rev. Lett. 73 (1994) 777, http://dx.doi.org/10.1103/PhysRevLett.73.777.
[168] T. Lauritsen, et al., Phys. Rev. C 62 (2000) 044316, http://dx.doi.org/10.1103/PhysRevC.62.044316.
[169] B. Herskind, A. Bracco, R.A. Broglia, T. Døssing, A. Ikeda, S. Leoni, J. Lisle, M. Matsuo, E. Vigezzi, Phys. Rev. Lett. 68 (1992) 3008, http://dx.doi.org/10.1103/PhysRevLett.68.3008.
[170] T. Døssing, B. Herskind, S. Leoni, A. Bracco, R. Broglia, M. Matsuo, E. Vigezzi, Phys. Rep. 268 (1) (1996) 1, http://dx.doi.org/10.1016/0370-1573(95)00060-7.
[171] A. Lopez-Martens, et al., Phys. Rev. Lett. 77 (1996) 1707, http://dx.doi.org/10.1103/PhysRevLett.77.1707.
[172] S. Leoni, A. Lopez-Martens, Phys. Scr. 91 (6) (2016) 063009, http://dx.doi.org/10.1088/0031-8949/91/6/063009.
[173] A. Bracco, S. Leoni, Rep. Progr. Phys. 65 (2002) 299, http://dx.doi.org/10.1088/0034-4885/65/2/204.
[174] S. Leoni, et al., Phys. Rev. C 79 (2009) 064306, http://dx.doi.org/10.1103/PhysRevC.79.064306.
[175] S. Leoni, et al., Phys. Rev. C 79 (2009) 064307, http://dx.doi.org/10.1103/PhysRevC.79.064307.
[176] D. Rudolph, et al., Phys. Rev. Lett. 80 (1998) 3018, http://dx.doi.org/10.1103/PhysRevLett.80.3018.
[177] D. Rudolph, et al., Phys. Rev. Lett. 82 (1999) 3763, http://dx.doi.org/10.1103/PhysRevLett.82.3763.
[178] D. Rudolph, et al., Phys. Rev. Lett. 86 (2001) 1450, http://dx.doi.org/10.1103/PhysRevLett.86.1450.
[179] D. Rudolph, et al., Phys. Rev. C 63 (2000) 021301, http://dx.doi.org/10.1103/PhysRevC.63.021301.
[180] D. Rudolph, et al., Phys. Rev. Lett. 89 (2002) 022501, http://dx.doi.org/10.1103/PhysRevLett.89.022501.
[181] E. Ideguchi, et al., Phys. Rev. Lett. 87 (2001) 222501, http://dx.doi.org/10.1103/PhysRevLett.87.222501.
[182] K. Hadyńska-Klęk, et al., Phys. Rev. Lett. 117 (2016) 062501, http://dx.doi.org/10.1103/PhysRevLett.117.062501.
[183] M. Lach, et al., Eur. Phys. J. A 16 (2003) 309, http://dx.doi.org/10.1140/epja/i2002-10125-6.
[184] C.E. Svensson, et al., Phys. Rev. Lett. 85 (2000) 2693, http://dx.doi.org/10.1103/PhysRevLett.85.2693.
[185] E. Ideguchi, et al., Phys. Lett. B 686 (1) (2010) 18, http://dx.doi.org/10.1016/j.physletb.2010.02.031.
[186] D. Rudolph, et al., Phys. Rev. C 65 (2002) 034305, http://dx.doi.org/10.1103/PhysRevC.65.034305.
[187] J. Retamosa, E. Caurier, F. Nowacki, A. Poves, Phys. Rev. C 55 (1997) 1266, http://dx.doi.org/10.1103/PhysRevC.55.1266.
[188] E. Caurier, F. Nowacki, A. Poves, Phys. Rev. Lett. 95 (2005) 042502, http://dx.doi.org/10.1103/PhysRevLett.95.042502.
[189] E. Caurier, J. Menéndez, F. Nowacki, A. Poves, Phys. Rev. C 75 (2007) 054317, http://dx.doi.org/10.1103/PhysRevC.75.054317.
[190] T. Inakura, S. Mizutori, M. Yamagami, K. Matsuyanagi, Nuclear Phys. A 710 (2002) 261, http://dx.doi.org/10.1016/S0375-9474(02)01164-8.
[191] R.R. Rodríguez-guzmán, J.L. Egido, L.M. Robledo, Int. J. Mod. Phys. E 13 (2004) 139, http://dx.doi.org/10.1142/S0218301304001862.
[192] Y. Taniguchi, M. Kimura, Y. Kanada-En'yo, H. Horiuchi, Phys. Rev. C 76 (2007) 044317, http://dx.doi.org/10.1103/PhysRevC.76.044317.
[193] Y. Kanada-En'yo, M. Kimura, Phys. Rev. C 72 (2005) 064322, http://dx.doi.org/10.1103/PhysRevC.72.064322.

[194] Y. Taniguchi, Y. Kanada-En'yo, M. Kimura, Progr. Theoret. Phys. 121 (2009) 533, http://dx.doi.org/10.1143/PTP.121.533.
[195] E.K. Warburton, J.A. Becker, B.A. Brown, Phys. Rev. C 41 (1990) 1147, http://dx.doi.org/10.1103/PhysRevC.41.1147.
[196] K. Hadyńska-Klęk, et al., Phys. Rev. C 97 (2018) 024326, http://dx.doi.org/10.1103/PhysRevC.97.024326.
[197] Y. Shimizu, E. Vigezzi, T. Døssing, R. Broglia, Nuclear Phys. A 557 (1993) 99, http://dx.doi.org/10.1016/0375-9474(93)90534-5.
[198] S. Hilaire, M. Girod, Eur. Phy. J. A 33 (2) (2007) 237, http://dx.doi.org/10.1140/epja/i2007-10450-2.
[199] R. Krücken, A. Dewald, P. von Brentano, D. Bazzacco, C. Rossi-Alvarez, Phys. Rev. C 54 (1996) 1182, http://dx.doi.org/10.1103/PhysRevC.54.1182.
[200] C. Andreoiu, et al., Phys. Rev. Lett. 91 (2003) 232502, http://dx.doi.org/10.1103/PhysRevLett.91.232502.
[201] R. Broda, J. Phys. G: Nucl. Part. Phys. 32 (2006) R151, http://dx.doi.org/10.1088/0954-3899/32/6/R01.
[202] R.M. Pérez-Vidal, et al., Eur. Phys. J. A 59 (2023) 114, http://dx.doi.org/10.1140/epja/s10050-023-01027-2.
[203] I. Stefan, et al., Phys. Lett. B 779 (2018) 456, http://dx.doi.org/10.1016/j.physletb.2018.02.037.
[204] C.E. Svensson, et al., Phys. Rev. Lett. 82 (1999) 3400, http://dx.doi.org/10.1103/PhysRevLett.82.3400.
[205] A.N. Wilson, et al., Phys. Rev. Lett. 104 (2010) 162501, http://dx.doi.org/10.1103/PhysRevLett.104.162501.
[206] T.L. Khoo, et al., Phys. Rev. Lett. 76 (1996) 1583, http://dx.doi.org/10.1103/PhysRevLett.76.1583.
[207] A.N. Wilson, et al., Phys. Rev. Lett. 90 (2003) 142501, http://dx.doi.org/10.1103/PhysRevLett.90.142501.
[208] A.N. Wilson, et al., Phys. Rev. Lett. 95 (2005) 182501, http://dx.doi.org/10.1103/PhysRevLett.95.182501.
[209] K. Hauschild, et al., Phys. Rev. C 55 (1997) 2819, http://dx.doi.org/10.1103/PhysRevC.55.2819.
[210] A. Lopez-Martens, et al., Phys. Lett. B 380 (1) (1996) 18, http://dx.doi.org/10.1016/0370-2693(96)00367-X.
[211] R. Krücken, et al., Phys. Rev. C 55 (1997) R1625, http://dx.doi.org/10.1103/PhysRevC.55.R1625.
[212] G. Hackman, et al., Phys. Rev. Lett. 79 (1997) 4100, http://dx.doi.org/10.1103/PhysRevLett.79.4100.
[213] J. Robin, et al., Phys. Rev. C 78 (2008) 034319, http://dx.doi.org/10.1103/PhysRevC.78.034319.
[214] C.J. Chiara, et al., Phys. Rev. C 73 (2006) 021301, http://dx.doi.org/10.1103/PhysRevC.73.021301.
[215] C. Finck, et al., Phys. Lett. B 467 (1999) 15, http://dx.doi.org/10.1016/S0370-2693(99)01139-9.
[216] C. Andreoiu, et al., Eur. Phys. J. A 14 (2002) 317, http://dx.doi.org/10.1140/epja/i2002-10011-3.
[217] E.K. Johansson, et al., Phys. Rev. C 80 (2009) 014321, http://dx.doi.org/10.1103/PhysRevC.80.014321.
[218] C.E. Svensson, et al., Phys. Rev. C 63 (2001) 061301, http://dx.doi.org/10.1103/PhysRevC.63.061301.
[219] C.J. Chiara, et al., Phys. Rev. C 67 (2003) 041303, http://dx.doi.org/10.1103/PhysRevC.67.041303.
[220] Experimental Unevaluated Nuclear Data List (XUNDL); https://www.nndc.bnl.gov/ensdf/xundl/.
[221] A. Faessler, U. Götz, B. Slavov, T. Ledergerber, Phys. Lett. B 39 (1972) 579, http://dx.doi.org/10.1016/0370-2693(72)90001-9.
[222] M. Cailliau, J. Leterssier, H. Flocard, P. Quentin, Phys. Lett. B 46 (1973) 11, http://dx.doi.org/10.1016/0370-2693(73)90461-9.
[223] S. Frauendorf, V. Pashkevich, Phys. Lett. B 55 (1975) 365, http://dx.doi.org/10.1016/0370-2693(75)90360-3.
[224] F. May, V. Pashkevich, S. Frauendorf, Phys. Lett. B 68 (1977) 113, http://dx.doi.org/10.1016/0370-2693(77)90179-4.
[225] P. Bonche, S. Krieger, P. Quentin, M. Weiss, J. Meyer, M. Meyer, N. Redon, H. Flocard, P.H. Heenen, Nuclear Phys. A 500 (2) (1989) 308, http://dx.doi.org/10.1016/0375-9474(89)90426-0.
[226] M. Girod, J.P. Delaroche, J.F. Berger, Phys. Rev. C 38 (1988) 1519, http://dx.doi.org/10.1103/PhysRevC.38.1519.
[227] P. Möller, A.J. Sierk, R. Bengtsson, H. Sagawa, T. Ichikawa, Phys. Rev. Lett. 103 (2009) 212501, http://dx.doi.org/10.1103/PhysRevLett.103.212501.
[228] P. Möller, A.J. Sierk, A. Iwamoto, Phys. Rev. Lett. 92 (2004) 072501, http://dx.doi.org/10.1103/PhysRevLett.92.072501.
[229] J. Ljungvall, et al., Phys. Rev. Lett. 100 (2008) 102502, http://dx.doi.org/10.1103/PhysRevLett.100.102502.
[230] J. Henderson, et al., Phys. Rev. Lett. 121 (2018) 082502, http://dx.doi.org/10.1103/PhysRevLett.121.082502.
[231] S.M. Fischer, D.P. Balamuth, P.A. Hausladen, C.J. Lister, M.P. Carpenter, D. Seweryniak, J. Schwartz, Phys. Rev. Lett. 84 (2000) 4064, http://dx.doi.org/10.1103/PhysRevLett.84.4064.
[232] J. Smallcombe, et al., Phys. Rev. C 106 (2022) 014312, http://dx.doi.org/10.1103/PhysRevC.106.014312.
[233] Z. Elekes, et al., Phys. Lett. B 844 (2023) 138072, http://dx.doi.org/10.1016/j.physletb.2023.138072.
[234] N. Marchini, et al., Phys. Lett. B 844 (2023) 138067, http://dx.doi.org/10.1016/j.physletb.2023.138067.
[235] A.D. Ayangeakaa, et al., Phys. Rev. Lett. 123 (2019) 102501, http://dx.doi.org/10.1103/PhysRevLett.123.102501.
[236] A.M. Forney, et al., Phys. Rev. Lett. 120 (2018) 212501, http://dx.doi.org/10.1103/PhysRevLett.120.212501.
[237] Y. Toh, et al., Phys. Rev. C 87 (2013) 041304, http://dx.doi.org/10.1103/PhysRevC.87.041304.
[238] J. Sun, et al., Phys. Lett. B 734 (2014) 308, http://dx.doi.org/10.1016/j.physletb.2014.05.069.
[239] A. Gottardo, et al., Phys. Rev. Lett. 116 (2016) 182501, http://dx.doi.org/10.1103/PhysRevLett.116.182501.
[240] F.H. Garcia, et al., Phys. Rev. Lett. 125 (2020) 172501, http://dx.doi.org/10.1103/PhysRevLett.125.172501.
[241] S. Leoni, C. Michelagnoli, J.N. Wilson, Riv. Nuovo Cimento 45 (2022) 461, http://dx.doi.org/10.1007/s40766-022-00033-2.
[242] A. Dewald, et al., Phys. Rev. C 78 (2008) 051302, http://dx.doi.org/10.1103/PhysRevC.78.051302.
[243] E.R. Gamba, et al., Phys. Rev. C 100 (2019) 044309, http://dx.doi.org/10.1103/PhysRevC.100.044309.
[244] P. Garrett, et al., Phys. Lett. B 809 (2020) 135762, http://dx.doi.org/10.1016/j.physletb.2020.135762.
[245] P.E. Garrett, et al., Phys. Rev. C 106 (2022) 064307, http://dx.doi.org/10.1103/PhysRevC.106.064307.
[246] K. Wrzosek-Lipska, et al., Phys. Rev. C 86 (2012) 064305, http://dx.doi.org/10.1103/PhysRevC.86.064305.
[247] K. Nomura, R. Rodríguez-Guzmán, L.M. Robledo, Phys. Rev. C 95 (2017) 064310, http://dx.doi.org/10.1103/PhysRevC.95.064310.
[248] M. Bender, H. Flocard, P.H. Heenen, Phys. Rev. C 68 (2003) 044321, http://dx.doi.org/10.1103/PhysRevC.68.044321.
[249] J. Berger, M. Girod, D. Gogny, Comput. Phys. Comm. 63 (1991) 365, http://dx.doi.org/10.1016/0010-4655(91)90263-K.
[250] AMEDEE database, Hartree-Fock-Bogoliubov calculations based on the D1S; https://www-phynu.cea.fr/science_en_ligne/carte_potentiels_microscopiques/carte_potentiel_nucleaire_eng.htm.
[251] C.D. O'Leary, et al., Phys. Rev. C 61 (2000) 064314, http://dx.doi.org/10.1103/PhysRevC.61.064314.
[252] W.J. Kossler, J. Winkler, C.D. Kavaloski, Phys. Rev. 177 (1969) 1725, http://dx.doi.org/10.1103/PhysRev.177.1725.
[253] A.R.L. Kennington, et al., Phys. Rev. Lett. 124 (2020) 252702, http://dx.doi.org/10.1103/PhysRevLett.124.252702.
[254] J. Bjerregaard, O. Hansen, O. Nathan, R. Chapman, S. Hinds, R. Middleton, Nuclear Phys. A 103 (1967) 33, http://dx.doi.org/10.1016/0375-9474(67)90789-0.
[255] W. Dixon, R. Storey, J. Simpson, Nuclear Phys. A 202 (3) (1973) 579, http://dx.doi.org/10.1016/0375-9474(73)90644-1.
[256] W.P. Alford, R.A. Lindgren, D. Elmore, R.N. Boyd, Phys. Rev. C 10 (1974) 1013, http://dx.doi.org/10.1103/PhysRevC.10.1013.
[257] W. Bohne, et al., Nuclear Phys. A 284 (1977) 14, http://dx.doi.org/10.1016/0375-9474(77)90682-0.
[258] S.M. Lenzi, F. Nowacki, A. Poves, K. Sieja, Phys. Rev. C 82 (2010) 054301, http://dx.doi.org/10.1103/PhysRevC.82.054301.
[259] F. Nowacki, A. Poves, E. Caurier, B. Bounthong, Phys. Rev. Lett. 117 (2016) 272501, http://dx.doi.org/10.1103/PhysRevLett.117.272501.
[260] A. Illana, et al., Phys. Rev. C 108 (2023) 044305, http://dx.doi.org/10.1103/PhysRevC.108.044305.
[261] M. Anguiano, J. Egido, L. Robledo, Nuclear Phys. A 696 (2001) 467, http://dx.doi.org/10.1016/S0375-9474(01)01219-2.
[262] S. Hellgartner, et al., Phys. Lett. B 841 (2023) 137933, http://dx.doi.org/10.1016/j.physletb.2023.137933.
[263] M. Rocchini, et al., Phys. Rev. C 103 (2021) 014311, http://dx.doi.org/10.1103/PhysRevC.103.014311.
[264] S. Péru, M. Martini, Eur. Phys. J. A 50 (2014) http://dx.doi.org/10.1140/epja/i2014-14088-7.

[265] D. Rudolph, et al., Phys. Rev. Lett. 96 (2006) 092501, http://dx.doi.org/10.1103/PhysRevLett.96.092501.
[266] M. Albers, et al., Phys. Rev. C 94 (2016) 034301, http://dx.doi.org/10.1103/PhysRevC.94.034301.
[267] M. Albers, et al., Phys. Rev. C 88 (2013) 054314, http://dx.doi.org/10.1103/PhysRevC.88.054314.
[268] D. Little, et al., Phys. Rev. C 106 (2022) 044313, http://dx.doi.org/10.1103/PhysRevC.106.044313.
[269] M.A.P. Brown, et al., Phys. Rev. C 97 (2018) 035505, http://dx.doi.org/10.1103/PhysRevC.97.035505.
[270] G. Martínez-Pinedo, A. Poves, E. Caurier, A.P. Zuker, Phys. Rev. C 53 (1996) R2602, http://dx.doi.org/10.1103/PhysRevC.53.R2602.
[271] C. Kremer, et al., Phys. Rev. Lett. 117 (2016) 172503, http://dx.doi.org/10.1103/PhysRevLett.117.172503.
[272] N. Shimizu, Y. Utsuno, T. Mizusaki, T. Otsuka, T. Abe, M. Honma, Phys. Rev. C 82 (2010) 061305, http://dx.doi.org/10.1103/PhysRevC.82.061305.
[273] N. Shimizu, Y. Utsuno, T. Mizusaki, M. Honma, Y. Tsunoda, T. Otsuka, Phys. Rev. C 85 (2012) 054301, http://dx.doi.org/10.1103/PhysRevC.85.054301.
[274] B. Crider, et al., Phys. Lett. B 763 (2016) 108, http://dx.doi.org/10.1016/j.physletb.2016.10.020.
[275] B. Olaizola, et al., Phys. Rev. C 95 (2017) 061303, http://dx.doi.org/10.1103/PhysRevC.95.061303.
[276] L.J. Evitts, et al., Phys. Rev. C 99 (2019) 024306, http://dx.doi.org/10.1103/PhysRevC.99.024306.
[277] L. Evitts, et al., Phys. Lett. B 779 (2018) 396, http://dx.doi.org/10.1016/j.physletb.2018.01.076.
[278] M. Honma, T. Otsuka, B.A. Brown, T. Mizusaki, Phys. Rev. C 69 (2004) 034335, http://dx.doi.org/10.1103/PhysRevC.69.034335.
[279] T. Mizusaki, T. Otsuka, M. Honma, B. Brown, Nuclear Phys. A 704 (2002) 190c, http://dx.doi.org/10.1016/S0375-9474(02)00779-0.
[280] S. Suchyta, et al., Phys. Rev. C 89 (2014) 021301, http://dx.doi.org/10.1103/PhysRevC.89.021301.
[281] F. Recchia, et al., Phys. Rev. C 88 (2013) 041302, http://dx.doi.org/10.1103/PhysRevC.88.041302.
[282] F. Flavigny, et al., Phys. Rev. C 91 (2015) 034310, http://dx.doi.org/10.1103/PhysRevC.91.034310.
[283] W.F. Mueller, et al., Phys. Rev. C 61 (2000) 054308, http://dx.doi.org/10.1103/PhysRevC.61.054308.
[284] A. and Poves, J. Phys. G: Nucl. Part. Phys. 43 (2016) 024010, http://dx.doi.org/10.1088/0954-3899/43/2/024010.
[285] A. Morales, et al., Phys. Lett. B 765 (2017) 328, http://dx.doi.org/10.1016/j.physletb.2016.12.025.
[286] R. Taniuchi, et al., Nature 569 (7754) (2019) 53, http://dx.doi.org/10.1038/s41586-019-1155-x.
[287] S.N. Liddick, et al., Phys. Rev. C 73 (2006) 044322, http://dx.doi.org/10.1103/PhysRevC.73.044322.
[288] N. Hoteling, et al., Phys. Rev. C 82 (2010) 044305, http://dx.doi.org/10.1103/PhysRevC.82.044305.
[289] S.N. Liddick, et al., Phys. Rev. C 87 (2013) 014325, http://dx.doi.org/10.1103/PhysRevC.87.014325.
[290] B. Olaizola, et al., J. Phys. G: Nucl. Part. Phys. 44 (2017) 125103, http://dx.doi.org/10.1088/1361-6471/aa915e.
[291] J. Ljungvall, et al., Phys. Rev. C 81 (2010) 061301, http://dx.doi.org/10.1103/PhysRevC.81.061301.
[292] W. Rother, et al., Phys. Rev. Lett. 106 (2011) 022502, http://dx.doi.org/10.1103/PhysRevLett.106.022502.
[293] M.P. Carpenter, R.V.F. Janssens, S. Zhu, Phys. Rev. C 87 (2013) 041305, http://dx.doi.org/10.1103/PhysRevC.87.041305.
[294] N.J.A. Awwad, H. Abusara, S. Ahmad, Phys. Rev. C 101 (2020) 064322, http://dx.doi.org/10.1103/PhysRevC.101.064322.
[295] C. Song, Z. Li, D. Vretenar, J. Meng, Sci. China Phys. Mech. Astron. 54 (2011) 222, http://dx.doi.org/10.1007/s11433-010-4219-3.
[296] T.R. Rodríguez, J.L. Egido, Phys. Rev. C 81 (2010) 064323, http://dx.doi.org/10.1103/PhysRevC.81.064323.
[297] J. Berger, M. Girod, D. Gogny, Nuclear Phys. A 428 (1984) 23, http://dx.doi.org/10.1016/0375-9474(84)90240-9.
[298] A. Passoja, R. Julin, J. Kantele, J. Kumpulainen, M. Luontama, W. Trzaska, Nuclear Phys. A 438 (1985) 413, http://dx.doi.org/10.1016/0375-9474(85)90383-5.
[299] C. Mihai, et al., Phys. Rev. C 75 (2007) 044302, http://dx.doi.org/10.1103/PhysRevC.75.044302.
[300] D. Ahalpara, K. Bhatt, S. Pandya, C. Praharaj, Nuclear Phys. A 371 (2) (1981) 210, http://dx.doi.org/10.1016/0375-9474(81)90064-6.
[301] A. Goasduff, et al., Nucl. Instrum. Methods Phys. Res. A 1015 (2021) 165753, http://dx.doi.org/10.1016/j.nima.2021.165753.
[302] M. Koizumi, et al., Nuclear Phys. A 730 (2004) 46, http://dx.doi.org/10.1016/j.nuclphysa.2003.10.010.
[303] S. Calinescu, et al., Phys. Rev. C 104 (2021) 034318, http://dx.doi.org/10.1103/PhysRevC.104.034318.
[304] M. Rocchini, et al., Phys. Rev. Lett. 130 (2023) 122502, http://dx.doi.org/10.1103/PhysRevLett.130.122502.
[305] C. Shand, et al., Phys. Lett. B 773 (2017) 492, http://dx.doi.org/10.1016/j.physletb.2017.09.001.
[306] R. Kamermans, H.W. Jongsma, J. van der Spek, H. Verheul, Phys. Rev. C 10 (1974) 620, http://dx.doi.org/10.1103/PhysRevC.10.620.
[307] K.G. Leach, et al., Phys. Rev. C 88 (2013) 031306, http://dx.doi.org/10.1103/PhysRevC.88.031306.
[308] J.L. Tracy, et al., Phys. Rev. C 98 (2018) 034309, http://dx.doi.org/10.1103/PhysRevC.98.034309.
[309] P. Singh, et al., Phys. Rev. Lett. 121 (2018) 192501, http://dx.doi.org/10.1103/PhysRevLett.121.192501.
[310] E. Clément, et al., Phys. Rev. Lett. 116 (2016) 022701, http://dx.doi.org/10.1103/PhysRevLett.116.022701.
[311] E. Clément, et al., Phys. Rev. C 94 (2016) 054326, http://dx.doi.org/10.1103/PhysRevC.94.054326.
[312] A. Chakraborty, et al., Phys. Rev. Lett. 110 (2013) 022504, http://dx.doi.org/10.1103/PhysRevLett.110.022504.
[313] J. Skalski, P.H. Heenen, P. Bonche, Nuclear Phys. A 559 (1993) 221, http://dx.doi.org/10.1016/0375-9474(93)90188-4.
[314] P. Moller, J. Nix, W. Myers, W. Swiatecki, At. Data Nucl. Data Tables 59 (1995) 185, http://dx.doi.org/10.1006/adnd.1995.1002.
[315] A. Holt, T. Engeland, M. Hjorth-Jensen, E. Osnes, Phys. Rev. C 61 (2000) 064318, http://dx.doi.org/10.1103/PhysRevC.61.064318.
[316] J.E. Garcıa-Ramos, K. Heyde, R. Fossion, V. Hellemans, S. De Baerdemacker, Eur. Phys. J. A 26 (2005) 221, http://dx.doi.org/10.1140/epja/i2005-10176-1.
[317] C. Özen, D.J. Dean, Phys. Rev. C 73 (2006) 014302, http://dx.doi.org/10.1103/PhysRevC.73.014302.
[318] K. Sieja, F. Nowacki, K. Langanke, G. Martínez-Pinedo, Phys. Rev. C 79 (2009) 064310, http://dx.doi.org/10.1103/PhysRevC.79.064310.
[319] M. Böyükata, P.V. Isacker, Ä. Uluer, J. Phys. G: Nucl. Part. Phys. 37 (2010) 105102, http://dx.doi.org/10.1088/0954-3899/37/10/105102.
[320] R. Rodríguez-Guzmán, P. Sarriguren, L. Robledo, S. Perez-Martin, Phys. Lett. B 691 (2010) 202, http://dx.doi.org/10.1016/j.physletb.2010.06.035.
[321] A. Petrovici, K.W. Schmid, A. Faessler, J. Phys.: Conf. Ser. 312 (2011) 092051, http://dx.doi.org/10.1088/1742-6596/312/9/092051.
[322] A. Petrovici, Phys. Rev. C 85 (2012) 034337, http://dx.doi.org/10.1103/PhysRevC.85.034337.
[323] J. Xiang, Z. Li, Z. Li, J. Yao, J. Meng, Nuclear Phys. A 873 (2012) 1, http://dx.doi.org/10.1016/j.nuclphysa.2011.10.002.
[324] H. Mei, J. Xiang, J.M. Yao, Z.P. Li, J. Meng, Phys. Rev. C 85 (2012) 034321, http://dx.doi.org/10.1103/PhysRevC.85.034321.
[325] S. Raman, C. Nestor, P. Tikkanen, At. Data Nucl. Data Tables 78 (2001) 1, http://dx.doi.org/10.1006/adnd.2001.0858.
[326] G. Kumbartzki, et al., Phys. Lett. B 562 (2003) 193, http://dx.doi.org/10.1016/S0370-2693(03)00608-7.
[327] J.K. Hwang, A.V. Ramayya, J.H. Hamilton, Y.X. Luo, A.V. Daniel, G.M. Ter-Akopian, J.D. Cole, S.J. Zhu, Phys. Rev. C 73 (2006) 044316, http://dx.doi.org/10.1103/PhysRevC.73.044316.
[328] V. Karayonchev, et al., Phys. Rev. C 102 (2020) 064314, http://dx.doi.org/10.1103/PhysRevC.102.064314.
[329] N. Gavrielov, A. Leviatan, F. Iachello, Phys. Rev. C 99 (2019) 064324, http://dx.doi.org/10.1103/PhysRevC.99.064324.
[330] N. Gavrielov, A. Leviatan, F. Iachello, Phys. Scr. 95 (2020) 024001, http://dx.doi.org/10.1088/1402-4896/ab456b.
[331] J.E. García-Ramos, K. Heyde, Phys. Rev. C 100 (2019) 044315, http://dx.doi.org/10.1103/PhysRevC.100.044315.
[332] L. Bettermann, et al., Phys. Rev. C 82 (2010) 044310, http://dx.doi.org/10.1103/PhysRevC.82.044310.
[333] J.M. Régis, et al., Phys. Rev. C 95 (2017) 054319, http://dx.doi.org/10.1103/PhysRevC.95.054319.
[334] G. Jung, B. Pfeiffer, L.J. Alquist, H. Wollnik, P. Hungerford, S.M. Scott, W.D. Hamilton, Phys. Rev. C 22 (1980) 252, http://dx.doi.org/10.1103/PhysRevC.22.252.
[335] W. Urban, T. Rząca-Urban, J. Wiśniewski, I. Ahmad, A.G. Smith, G.S. Simpson, Phys. Rev. C 99 (2019) 064325, http://dx.doi.org/10.1103/PhysRevC.99.064325.

[336] S. Cruz, et al., Phys. Lett. B 786 (2018) 94, http://dx.doi.org/10.1016/j.physletb.2018.09.031.
[337] F. Buchinger, et al., Phys. Rev. C 41 (1990) 2883, http://dx.doi.org/10.1103/PhysRevC.41.2883.
[338] W. Urban, et al., Phys. Rev. C 104 (2021) 064309, http://dx.doi.org/10.1103/PhysRevC.104.064309.
[339] F. Schussler, et al., Nuclear Phys. A 339 (1980) 415, http://dx.doi.org/10.1016/0375-9474(80)90024-X.
[340] J. Park, et al., Phys. Rev. C 93 (2016) 014315, http://dx.doi.org/10.1103/PhysRevC.93.014315.
[341] J. Dechargé, D. Gogny, Phys. Rev. C 21 (1980) 1568, http://dx.doi.org/10.1103/PhysRevC.21.1568.
[342] J.P. Delaroche, M. Girod, J. Libert, H. Goutte, S. Hilaire, S. Péru, N. Pillet, G.F. Bertsch, Phys. Rev. C 81 (2010) 014303, http://dx.doi.org/10.1103/PhysRevC.81.014303.
[343] J. Libert, M. Girod, J.P. Delaroche, Phys. Rev. C 60 (1999) 054301, http://dx.doi.org/10.1103/PhysRevC.60.054301.
[344] H. Duckwitz, et al., Nuclear Phys. A 965 (2017) 13, http://dx.doi.org/10.1016/j.nuclphysa.2017.05.077.
[345] S. Cruz, et al., Phys. Rev. C 102 (2020) 024335, http://dx.doi.org/10.1103/PhysRevC.102.024335.
[346] E. Bouchez, et al., Phys. Rev. Lett. 90 (2003) 082502, http://dx.doi.org/10.1103/PhysRevLett.90.082502.
[347] A. Gade, et al., Phys. Rev. Lett. 95 (2005) 022502, http://dx.doi.org/10.1103/PhysRevLett.95.022502.
[348] E. Clément, et al., Phys. Rev. C 75 (2007) 054313, http://dx.doi.org/10.1103/PhysRevC.75.054313.
[349] K. Langanke, D. Dean, W. Nazarewicz, Nuclear Phys. A 728 (2003) 109, http://dx.doi.org/10.1016/j.nuclphysa.2003.08.024.
[350] A. Petrovici, K. Schmid, A. Faessler, Nuclear Phys. A 665 (2000) 333, http://dx.doi.org/10.1016/S0375-9474(99)00811-8.
[351] P. Bonche, H. Flocard, P. Heenen, S. Krieger, M. Weiss, Nuclear Phys. A 443 (1985) 39, http://dx.doi.org/10.1016/0375-9474(85)90320-3.
[352] M. Yamagami, K. Matsuyanagi, M. Matsuo, Nuclear Phys. A 693 (2001) 579, http://dx.doi.org/10.1016/S0375-9474(01)00918-6.
[353] M. Bender, P. Bonche, P.H. Heenen, Phys. Rev. C 74 (2006) 024312, http://dx.doi.org/10.1103/PhysRevC.74.024312.
[354] M. Girod, J.P. Delaroche, A. Görgen, A. Obertelli, Phys. Lett. B 676 (2009) 39, http://dx.doi.org/10.1016/j.physletb.2009.04.077.
[355] T.R. Rodríguez, Phys. Rev. C 90 (2014) 034306, http://dx.doi.org/10.1103/PhysRevC.90.034306.
[356] P. Möller, A. Sierk, R. Bengtsson, H. Sagawa, T. Ichikawa, At. Data Nucl. Data Tables 98 (2) (2012) 149, http://dx.doi.org/10.1016/j.adt.2010.09.002.
[357] R. Dunlop, et al., Phys. Rev. C 88 (2013) 045501, http://dx.doi.org/10.1103/PhysRevC.88.045501.
[358] A. Giannatiempo, et al., Phys. Rev. C 72 (2005) 044308, http://dx.doi.org/10.1103/PhysRevC.72.044308.
[359] A. Giannatiempo, A. Nannini, A. Perego, P. Sona, M.J.G. Borge, O. Tengblad, Phys. Rev. C 52 (1995) 2444, http://dx.doi.org/10.1103/PhysRevC.52.2444.
[360] A. Giannatiempo, A. Nannini, A. Perego, P. Sona, M.J.G. Borge, K. Riisager, O. Tengblad, Phys. Rev. C 47 (1993) 521, http://dx.doi.org/10.1103/PhysRevC.47.521.
[361] S.A. Gillespie, et al., Phys. Rev. C 104 (2021) 044313, http://dx.doi.org/10.1103/PhysRevC.104.044313.
[362] K. Krane, Appl. Radiat. Isot. 69 (1) (2011) 201, http://dx.doi.org/10.1016/j.apradiso.2010.07.024.
[363] M.N. Nino, et al., Phys. Rev. C 93 (2016) 024301, http://dx.doi.org/10.1103/PhysRevC.93.024301.
[364] S. Rajbanshi, et al., Phys. Rev. C 104 (2021) L031302, http://dx.doi.org/10.1103/PhysRevC.104.L031302.
[365] T. Togashi, Y. Tsunoda, T. Otsuka, N. Shimizu, M. Honma, Phys. Rev. Lett. 121 (2018) 062501, http://dx.doi.org/10.1103/PhysRevLett.121.062501.
[366] L.M. Robledo, T.R. Rodríguez, R.R. Rodríguez-Guzmín, J. Phys. G: Nucl. Part. Phys. 46 (2018) 013001, http://dx.doi.org/10.1088/1361-6471/aadebd.
[367] P.E. Garrett, J.L. Wood, S.W. Yates, Phys. Scr. 93 (2018) 063001, http://dx.doi.org/10.1088/1402-4896/aaba1c.
[368] J.C. Batchelder, et al., Phys. Rev. C 86 (2012) 064311, http://dx.doi.org/10.1103/PhysRevC.86.064311.
[369] M. Löffler, H. Scheerer, H. Vonach, Nucl. Instrum. Methods 111 (1973) 1, http://dx.doi.org/10.1016/0029-554X(73)90090-6.
[370] P. Guazzoni, et al., Phys. Rev. C 72 (2005) 044604, http://dx.doi.org/10.1103/PhysRevC.72.044604.
[371] P. Guazzoni, et al., Phys. Rev. C 78 (2008) 064608, http://dx.doi.org/10.1103/PhysRevC.78.064608.
[372] S. Ganguly, et al., Nuclear Phys. A 789 (2007) 1, http://dx.doi.org/10.1016/j.nuclphysa.2007.01.092.
[373] J. Gableske, et al., Nuclear Phys. A 691 (2001) 551, http://dx.doi.org/10.1016/S0375-9474(01)00564-4.
[374] M. Wolińska-Cichocka, et al., Eur. Phys. J. A 24 (2005) 259, http://dx.doi.org/10.1140/epja/i2004-10144-3.
[375] C.M. Petrache, et al., Phys. Rev. C 99 (2019) 024303, http://dx.doi.org/10.1103/PhysRevC.99.024303.
[376] J.L. Pore, et al., Eur. Phys. J. A 53 (2017) 27, http://dx.doi.org/10.1140/epja/i2017-12213-x.
[377] A. Bäcklin, N. Jonsson, R. Julin, J. Kantele, M. Luontama, A. Passoja, T. Poikolainen, Nuclear Phys. A 351 (3) (1981) 490, http://dx.doi.org/10.1016/0375-9474(81)90184-6.
[378] M. Spieker, et al., Phys. Rev. C 97 (2018) 054319, http://dx.doi.org/10.1103/PhysRevC.97.054319.
[379] D. Bandyopadhyay, N. Warr, C. Fransen, N. Boukharouba, V. Werner, S. Yates, J. Weil, M. McEllistrem, Nuclear Phys. A 747 (2005) 206, http://dx.doi.org/10.1016/j.nuclphysa.2004.10.003.
[380] R.A. Meyer, L. Peker, Z. Phys. A 283 (4) (1977) 379, http://dx.doi.org/10.1007/BF01409518.
[381] J.R. Comfort, W.J. Braithwaite, J.R. Duray, S. Yoshida, Phys. Rev. Lett. 29 (1972) 442, http://dx.doi.org/10.1103/PhysRevLett.29.442.
[382] J. Kern, P. Garrett, J. Jolie, H. Lehmann, Nuclear Phys. A 593 (1995) 21, http://dx.doi.org/10.1016/0375-9474(95)00314-Q.
[383] C. Fahlander, et al., Nuclear Phys. A 485 (1988) 327, http://dx.doi.org/10.1016/0375-9474(88)90106-6.
[384] P.E. Garrett, et al., Phys. Rev. C 101 (2020) 044302, http://dx.doi.org/10.1103/PhysRevC.101.044302.
[385] P.E. Garrett, et al., Phys. Rev. Lett. 123 (2019) 142502, http://dx.doi.org/10.1103/PhysRevLett.123.142502.
[386] D. Jerrestam, et al., Nuclear Phys. A 571 (1994) 393, http://dx.doi.org/10.1016/0375-9474(94)90067-1.
[387] R.M. Clark, et al., Phys. Rev. Lett. 87 (2001) 202502, http://dx.doi.org/10.1103/PhysRevLett.87.202502.
[388] A. Görgen, et al., Phys. Rev. C 65 (2002) 027302, http://dx.doi.org/10.1103/PhysRevC.65.027302.
[389] T. Gray, et al., Phys. Lett. B 834 (2022) 137446, http://dx.doi.org/10.1016/j.physletb.2022.137446.
[390] A. Gade, J. Jolie, P. von Brentano, Phys. Rev. C 65 (2002) 041305, http://dx.doi.org/10.1103/PhysRevC.65.041305.
[391] M. Siciliano, et al., Phys. Rev. C 104 (2021) 034320, http://dx.doi.org/10.1103/PhysRevC.104.034320.
[392] P.E. Garrett, et al., Phys. Rev. C 86 (2012) 044304, http://dx.doi.org/10.1103/PhysRevC.86.044304.
[393] M. Luontama, J. Kantele, R. Julin, A. Passoja, T. Poikolainen, M. Pylvänäinen, Nucl. Instrum. Methods Phys. Res. A 159 (1979) 339, http://dx.doi.org/10.1016/0029-554X(79)90659-1.
[394] P.E. Garrett, H. Lehmann, J. Jolie, C.A. McGrath, M. Yeh, W. Younes, S.W. Yates, Phys. Rev. C 64 (2001) 024316, http://dx.doi.org/10.1103/PhysRevC.64.024316.
[395] P.E. Garrett, K.L. Green, H. Lehmann, J. Jolie, C.A. McGrath, M. Yeh, S.W. Yates, Phys. Rev. C 75 (2007) 054310, http://dx.doi.org/10.1103/PhysRevC.75.054310.
[396] R. Julin, J. Kantele, M. Luontama, A. Passoja, T. Poikolainen, A. Bäcklin, N.G. Jonsson, Z. Phys. A 296 (4) (1980) 315, http://dx.doi.org/10.1007/BF01438525.
[397] D. Bandyopadhyay, et al., Phys. Rev. C 76 (2007) 054308, http://dx.doi.org/10.1103/PhysRevC.76.054308.
[398] D.K. Sharp, et al., Phys. Rev. C 100 (2019) 024329, http://dx.doi.org/10.1103/PhysRevC.100.024329.
[399] J. Kumpulainen, R. Julin, J. Kantele, A. Passoja, E. Verho, JYFL Annu. Rep. (1986) 52.
[400] J.R. Vanhoy, et al., Phys. Rev. C 68 (2003) 034315, http://dx.doi.org/10.1103/PhysRevC.68.034315.
[401] J.R. Vanhoy, et al., Phys. Rev. C 69 (2004) 064323, http://dx.doi.org/10.1103/PhysRevC.69.064323.
[402] S.F. Hicks, et al., Phys. Rev. C 86 (2012) 054308, http://dx.doi.org/10.1103/PhysRevC.86.054308.

[403] A. Barabash, P. Hubert, A. Nachab, S. Konovalov, I. Vanyushin, V. Umatov, Nuclear Phys. A 807 (2008) 269, http://dx.doi.org/10.1016/j.nuclphysa.2008.04.009.
[404] J. Dawson, D. Degering, M. Köhler, R. Ramaswamy, C. Reeve, J.R. Wilson, K. Zuber, Phys. Rev. C 78 (2008) 035503, http://dx.doi.org/10.1103/PhysRevC.78.035503.
[405] T. Bloxham, et al., Phys. Rev. C 82 (2010) 027308, http://dx.doi.org/10.1103/PhysRevC.82.027308.
[406] T. Bloxham, et al., Submission to xundl: data from the ^{128,130}te(p, t)^{126,128}te reaction, 2010, Preprint.
[407] B. Hadinia, et al., Phys. Rev. C 72 (2005) 041303, http://dx.doi.org/10.1103/PhysRevC.72.041303.
[408] J. Rikovska, N. Stone, P. Walker, W. Walters, Nuclear Phys. A 505 (1989) 145, http://dx.doi.org/10.1016/0375-9474(89)90368-0.
[409] C. Mihai, et al., Phys. Rev. C 83 (2011) 054310, http://dx.doi.org/10.1103/PhysRevC.83.054310.
[410] S.F. Hicks, et al., Phys. Rev. C 71 (2005) 034307, http://dx.doi.org/10.1103/PhysRevC.71.034307.
[411] S.F. Hicks, et al., Phys. Rev. C 95 (2017) 034322, http://dx.doi.org/10.1103/PhysRevC.95.034322.
[412] H. Fielding, R. Anderson, P. Kunz, D. Lind, C. Zafiratos, W. Alford, Nuclear Phys. A 304 (2) (1978) 520, http://dx.doi.org/10.1016/0375-9474(78)90248-8.
[413] W. Alford, R. Anderson, P. Batay-Csorba, R. Emigh, D. Lind, P. Smith, C. Zafiratos, Nuclear Phys. A 323 (1979) 339, http://dx.doi.org/10.1016/0375-9474(79)90114-3.
[414] S. Krieger, P. Bonche, M. Weiss, J. Meyer, H. Flocard, P.H. Heenen, Nuclear Phys. A 542 (1) (1992) 43, http://dx.doi.org/10.1016/0375-9474(92)90395-Z.
[415] K. Pomorski, B. Nerlo-Pomorska, A. Dobrowolski, J. Bartel, C.M. Petrache, Eur. Phys. J. A 56 (2020) 107, http://dx.doi.org/10.1140/epja/s10050-020-00115-x.
[416] T. Nikšić, D. Vretenar, P. Ring, G.A. Lalazissis, Phys. Rev. C 65 (2002) 054320, http://dx.doi.org/10.1103/PhysRevC.65.054320.
[417] B. Nerlo-Pomorska, K. Pomorski, J. Bartel, C. Schmitt, Eur. Phys. J. A 53 (2017) 67, http://dx.doi.org/10.1140/epja/i2017-12259-8.
[418] D.A. Meyer, et al., Phys. Rev. C 74 (2006) 044309, http://dx.doi.org/10.1103/PhysRevC.74.044309.
[419] T. Otsuka, Y. Tsunoda, T. Abe, N. Shimizu, P. Van Duppen, Phys. Rev. Lett. 123 (2019) 222502, http://dx.doi.org/10.1103/PhysRevLett.123.222502.
[420] T. Kühl, P. Dabkiewicz, C. Duke, H. Fischer, H.J. Kluge, H. Kremmling, E.W. Otten, Phys. Rev. Lett. 39 (1977) 180, http://dx.doi.org/10.1103/PhysRevLett.39.180.
[421] S. Sels, et al., Phys. Rev. C 99 (2019) 044306, http://dx.doi.org/10.1103/PhysRevC.99.044306.
[422] R. Julin, T. Grahn, J. Pakarinen, P. Rahkila, J. Phys. G: Nucl. Part. Phys. 43 (2016) 024004, http://dx.doi.org/10.1088/0954-3899/43/2/024004.
[423] K. Wrzosek-Lipska, L.P. Gaffney, J. Phys. G: Nucl. Part. Phys. 43 (2016) 024012, http://dx.doi.org/10.1088/0954-3899/43/2/024012.
[424] N. Bree, et al., Phys. Rev. Lett. 112 (2014) 162701, http://dx.doi.org/10.1103/PhysRevLett.112.162701.
[425] K. Wrzosek-Lipska, et al., Eur. Phys. J. A 55 (8) (2019) 130, http://dx.doi.org/10.1140/epja/i2019-12815-2.
[426] B. Olaizola, et al., Phys. Rev. C 100 (2019) 024301, http://dx.doi.org/10.1103/PhysRevC.100.024301.
[427] R. Kern, et al., Phys. Rev. C 99 (2019) 011303, http://dx.doi.org/10.1103/PhysRevC.99.011303.
[428] L.P. Gaffney, et al., Phys. Rev. C 89 (2014) 024307, http://dx.doi.org/10.1103/PhysRevC.89.024307.
[429] M. Siciliano, et al., Phys. Rev. C 102 (2020) 014318, http://dx.doi.org/10.1103/PhysRevC.102.014318.
[430] C. Müller-Gatermann, et al., Phys. Rev. C 99 (2019) 054325, http://dx.doi.org/10.1103/PhysRevC.99.054325.
[431] J.M. Yao, M. Bender, P.H. Heenen, Phys. Rev. C 87 (2013) 034322, http://dx.doi.org/10.1103/PhysRevC.87.034322.
[432] J.E. García-Ramos, K. Heyde, Phys. Rev. C 89 (2014) 014306, http://dx.doi.org/10.1103/PhysRevC.89.014306.
[433] L. Próchniak, S.G. Rohoziński, J. Phys. G: Nucl. Part. Phys. 36 (12) (2009) 123101, http://dx.doi.org/10.1088/0954-3899/36/12/123101.
[434] W. Nazarewicz, Phys. Lett. B 305 (1993) 195, http://dx.doi.org/10.1016/0370-2693(93)90107-S.
[435] G.D. Dracoulis, et al., Phys. Rev. C 67 (2003) 051301, http://dx.doi.org/10.1103/PhysRevC.67.051301.
[436] M. Bender, P. Bonche, T. Duguet, P.H. Heenen, Phys. Rev. C 69 (2004) 064303, http://dx.doi.org/10.1103/PhysRevC.69.064303.
[437] R.R. Rodríguez-Guzmán, J.L. Egido, L.M. Robledo, Phys. Rev. C 69 (2004) 054319, http://dx.doi.org/10.1103/PhysRevC.69.054319.
[438] J. Pakarinen, et al., Phys. Rev. C 75 (2007) 014302, http://dx.doi.org/10.1103/PhysRevC.75.014302.
[439] R. Julin, J. Kantele, M. Luontama, T. Poikolainen, V. Rahkonen, Phys. Lett. 65 (1976) 337, http://dx.doi.org/10.1016/0370-2693(76)90236-7.
[440] J.N. Orce, T. Kibédi, G.D. Dracoulis, R. Julin, S.W. Yates, J. Phys. G: Nucl. Part. Phys. 31 (2005) S1705, http://dx.doi.org/10.1088/0954-3899/31/10/058.
[441] P. Van Duppen, E. Coenen, K. Deneffe, M. Huyse, J.L. Wood, Phys. Rev. C 35 (1987) 1861, http://dx.doi.org/10.1103/PhysRevC.35.1861.
[442] J. Penninga, W. Hesselink, A. Balanda, A. Stolk, H. Verheul, J. van Klinken, H. Riezebos, M. de Voigt, Nuclear Phys. A 471 (1987) 535, http://dx.doi.org/10.1016/0375-9474(87)90098-4.
[443] J. Heese, et al., Phys. Lett. B 302 (4) (1993) 390, http://dx.doi.org/10.1016/0370-2693(93)90415-E.
[444] J.W. Tape, E.G. Adelberger, D. Burch, L. Zamick, Phys. Rev. Lett. 29 (1972) 878, http://dx.doi.org/10.1103/PhysRevLett.29.878.
[445] C.W. Ma, W.W. True, Phys. Rev. C 8 (1973) 2313, http://dx.doi.org/10.1103/PhysRevC.8.2313.
[446] C. Müller-Gatermann, et al., Phys. Rev. C 97 (2018) 024336, http://dx.doi.org/10.1103/PhysRevC.97.024336.
[447] Fransen, Christoph, et al., EPJ Web Conf. 223 (2019) 01016, http://dx.doi.org/10.1051/epjconf/201922301016.
[448] C.B. Li, et al., Phys. Rev. C 90 (2014) 047302, http://dx.doi.org/10.1103/PhysRevC.90.047302.
[449] K. Gladnishki, et al., Nuclear Phys. A 877 (2012) 19, http://dx.doi.org/10.1016/j.nuclphysa.2012.01.001.
[450] J.C. Walpe, U. Garg, S. Naguleswaran, J. Wei, W. Reviol, I. Ahmad, M.P. Carpenter, T.L. Khoo, Phys. Rev. C 85 (2012) 057302, http://dx.doi.org/10.1103/PhysRevC.85.057302.
[451] A. Rohilla, et al., Eur. Phys. J. A 53 (4) (2017) 64, http://dx.doi.org/10.1140/epja/i2017-12256-y.
[452] G.D. Dracoulis, A.E. Stuchbery, A.P. Byrne, A.R. Poletti, S.J. Poletti, J. Gerl, R.A. Bark, J. Phys. G: Nucl. Phys. 12 (1986) L97, http://dx.doi.org/10.1088/0305-4616/12/3/005.
[453] G.D. Dracoulis, Phys. Rev. C 49 (1994) 3324, http://dx.doi.org/10.1103/PhysRevC.49.3324.
[454] D. Seweryniak, et al., Phys. Rev. C 58 (1998) 2710, http://dx.doi.org/10.1103/PhysRevC.58.2710.
[455] P. Davidson, et al., Nuclear Phys. A 657 (1999) 219, http://dx.doi.org/10.1016/S0375-9474(99)00340-1.
[456] P.D. Duval, B.R. Barrett, Phys. Lett. B 100 (1981) 223, http://dx.doi.org/10.1016/0370-2693(81)90321-X.
[457] S. King, et al., Phys. Lett. B 443 (1998) 82, http://dx.doi.org/10.1016/S0370-2693(98)01333-1.
[458] M. Harder, K. Tang, P. Van Isacker, Phys. Lett. B 405 (1997) 25, http://dx.doi.org/10.1016/S0370-2693(97)00612-6.
[459] E.A. McCutchan, R.F. Casten, N.V. Zamfir, Phys. Rev. C 71 (2005) 061301, http://dx.doi.org/10.1103/PhysRevC.71.061301.
[460] R. Casten, J. Cizewski, Phys. Lett. B 185 (1987) 293, http://dx.doi.org/10.1016/0370-2693(87)91002-1.
[461] S.W. Yates, E.M. Baum, E.A. Henry, L.G. Mann, N. Roy, A. Aprahamian, R.A. Meyer, R. Estep, Phys. Rev. C 37 (1988) 1889, http://dx.doi.org/10.1103/PhysRevC.37.1889.
[462] A. Oros, K. Heyde, C. De Coster, B. Decroix, R. Wyss, B. Barrett, P. Navratil, Nuclear Phys. A 645 (1999) 107, http://dx.doi.org/10.1016/S0375-9474(98)00602-2.
[463] N. Bijnens, et al., Phys. Rev. Lett. 75 (1995) 4571, http://dx.doi.org/10.1103/PhysRevLett.75.4571.
[464] R. Julin, K. Helariutta, M. Muikku, J. Phys. G: Nucl. Part. Phys. 27 (2001) R109, http://dx.doi.org/10.1088/0954-3899/27/7/201.
[465] N. Kesteloot, et al., Phys. Rev. C 92 (2015) 054301, http://dx.doi.org/10.1103/PhysRevC.92.054301.
[466] M. Seliverstov, et al., Phys. Lett. B 719 (2013) 362, http://dx.doi.org/10.1016/j.physletb.2013.01.043.
[467] D.R. Wiseman, et al., Eur. Phys. J. A 34 (2007) 275, http://dx.doi.org/10.1140/epja/i2007-10507-2.

[468] T. Grahn, et al., Phys. Rev. C 80 (2009) 014323, http://dx.doi.org/10.1103/PhysRevC.80.014323.
[469] T. Grahn, et al., Phys. Rev. Lett. 97 (2006) 062501, http://dx.doi.org/10.1103/PhysRevLett.97.062501.
[470] B. Bengtson, H. Nielsen, N. Rud, Nuclear Phys. A 319 (1979) 21, http://dx.doi.org/10.1016/0375-9474(79)90168-4.
[471] B. Bengtson, H. Nielsen, N. Rud, K. Wilsky, Nuclear Phys. A 378 (1982) 1, http://dx.doi.org/10.1016/0375-9474(82)90379-7.
[472] E.S. Paul, C.W. Beausang, D.B. Fossan, R. Ma, W.F. Piel, N. Xu, L. Hildingsson, G.A. Leander, Phys. Rev. Lett. 58 (1987) 984, http://dx.doi.org/10.1103/PhysRevLett.58.984.
[473] U.S. Tandel, et al., Phys. Rev. Lett. 101 (2008) 182503, http://dx.doi.org/10.1103/PhysRevLett.101.182503.
[474] P. Möller, et al., At. Data Nucl. Data Tables 94 (5) (2008) 758, http://dx.doi.org/10.1016/j.adt.2008.05.002.
[475] L.M. Robledo, R.R. Rodríguez-Guzmán, P. Sarriguren, Phys. Rev. C 78 (2008) 034314, http://dx.doi.org/10.1103/PhysRevC.78.034314.
[476] H.L. Wang, J. Yang, M.L. Liu, F.R. Xu, Phys. Rev. C 92 (2015) 024303, http://dx.doi.org/10.1103/PhysRevC.92.024303.
[477] K. Zheng, et al., Phys. Lett. B 822 (2021) 136645, http://dx.doi.org/10.1016/j.physletb.2021.136645.
[478] P. Zhao, S. Zhang, J. Peng, H. Liang, P. Ring, J. Meng, Phys. Lett. B 699 (2011) 181, http://dx.doi.org/10.1016/j.physletb.2011.03.068.
[479] J. Meng, J. Peng, S.Q. Zhang, P.W. Zhao, Front. Phys. 8 (1) (2013) 55, http://dx.doi.org/10.1007/s11467-013-0287-y.
[480] Y.K. Wang, Phys. Rev. C 96 (2017) 054324, http://dx.doi.org/10.1103/PhysRevC.96.054324.
[481] Y.H. Qiang, et al., Phys. Rev. C 99 (2019) 014307, http://dx.doi.org/10.1103/PhysRevC.99.014307.
[482] C.M. Petrache, et al., Phys. Rev. C 86 (2012) 044321, http://dx.doi.org/10.1103/PhysRevC.86.044321.
[483] C. Petrache, et al., Phys. Lett. B 795 (2019) 241, http://dx.doi.org/10.1016/j.physletb.2019.06.040.
[484] S. Frauendorf, Nuclear Phys. A 677 (2000) 115, http://dx.doi.org/10.1016/S0375-9474(00)00308-0.
[485] B. Qi, S. Zhang, J. Meng, S. Wang, S. Frauendorf, Phys. Lett. B 675 (2009) 175, http://dx.doi.org/10.1016/j.physletb.2009.02.061.
[486] Y. Sun, Phys. Scr. 91 (4) (2016) 043005, http://dx.doi.org/10.1088/0031-8949/91/4/043005.
[487] S.N.T. Majola, et al., Phys. Rev. C 100 (2019) 044324, http://dx.doi.org/10.1103/PhysRevC.100.044324.
[488] J.F. Sharpey-Schafer, et al., Eur. Phys. J. A 55 (2) (2019) 15, http://dx.doi.org/10.1140/epja/i2019-12665-x.
[489] P.W. Zhao, Z.P. Li, J.M. Yao, J. Meng, Phys. Rev. C 82 (2010) 054319, http://dx.doi.org/10.1103/PhysRevC.82.054319.
[490] S.W. Ødegård, et al., Phys. Rev. Lett. 86 (2001) 5866, http://dx.doi.org/10.1103/PhysRevLett.86.5866.
[491] D.R. Jensen, et al., Phys. Rev. Lett. 89 (2002) 142503, http://dx.doi.org/10.1103/PhysRevLett.89.142503.
[492] G. Schönwasser, et al., Phys. Lett. B 552 (2003) 9, http://dx.doi.org/10.1016/S0370-2693(02)03095-2.
[493] T. Otsuka, Y. Tsunoda, Y. Utsuno, N. Shimizu, T. Abe, H. Ueno, Prevailing triaxial shapes in heavy nuclei driven by nuclear tensor force, 2023, http://dx.doi.org/10.48550/arXiv.2303.11299.
[494] A. Bohr, Mat. Fys. Medd. Dan. Vid. Selsk. 26 (1952) 14, https://gymarkiv.sdu.dk/MFM/kdvs/mfm%2020-29/mfm-26-14.pdf.
[495] A. Bohr, in: S. Lundqvist (Ed.), Nobel Lectures, Physics 1971-1980, World Scientific Publishing, Singapore, 1992, https://www.nobelprize.org/uploads/2018/06/bohr-lecture-1.pdf.
[496] A. Bohr, B.R. Mottelson, Nuclear Structure Vol. 2, World Scientific Publishing, Singapore, 1999, http://refhub.elsevier.com/S0146-6410(24)00023-1/sb3.
[497] Y. Tsunoda, T. Otsuka, Phys. Rev. C 103 (2021) L021303, http://dx.doi.org/10.1103/PhysRevC.103.L021303.
[498] A. Bracco, F. Camera, Phys. Scr. 91 (8) (2016) 083002, http://dx.doi.org/10.1088/0031-8949/91/8/083002.
[499] D. Pandit, S. Mukhopadhyay, S. Pal, A. De, S. Banerjee, Phys. Lett. B 713 (2012) 434, http://dx.doi.org/10.1016/j.physletb.2012.06.033.
[500] D. Santonocito, et al., Phys. Rev. C 90 (2014) 054603, http://dx.doi.org/10.1103/PhysRevC.90.054603.
[501] M. Kicińska-Habior, K. Snover, J. Behr, C. Gossett, Y. Alhassid, N. Whelan, Phys. Lett. B 308 (1993) 225, http://dx.doi.org/10.1016/0370-2693(93)91276-S.
[502] A. Maj, et al., Nuclear Phys. A 731 (2004) 319, http://dx.doi.org/10.1016/j.nuclphysa.2003.11.043.
[503] B. Dey, et al., Phys. Rev. C 97 (2018) 014317, http://dx.doi.org/10.1103/PhysRevC.97.014317.
[504] G. Benzoni, et al., Phys. Lett. B 540 (2002) 199, http://dx.doi.org/10.1016/S0370-2693(02)02175-5.
[505] M. Kmiecik, et al., Acta Phys. Pol. B 36 (2005) 1169, URL https://www.actaphys.uj.edu.pl/fulltext?series=Reg&vol=36&page=1169.
[506] R.G. Henry, et al., Acta Phys. Pol. B 38 (2007) 1421, URL http://www.actaphys.uj.edu.pl/fulltext?series=Reg&vol=38&page=1421.
[507] F. Camera, J. Isaak, A. Maj, S. Siem, Eur. Phys. J. A 59 (2023) 168, http://dx.doi.org/10.1140/epja/s10050-023-01076-7.
[508] A. Maj, et al., Acta Phys. Pol. B 40 (2009) 565, URL https://api.semanticscholar.org/CorpusID:118296111.
[509] F. Camera, A. Maj, PARIS white book, 2021, URL http://slcj.uw.edu.pl/en/the-paris-white-book/.
[510] M. Ciemał a, et al., Phys. Rev. C 91 (2015) 054313, http://dx.doi.org/10.1103/PhysRevC.91.054313.
[511] K. Pomorski, J. Dudek, Phys. Rev. C 67 (2003) 044316, http://dx.doi.org/10.1103/PhysRevC.67.044316.
[512] M. Kmiecik, et al., Phys. Rev. C 70 (2004) 064317, http://dx.doi.org/10.1103/PhysRevC.70.064317.
[513] N. Dinh Dang, M. Ciemala, M. Kmiecik, A. Maj, Phys. Rev. C 87 (2013) 054313, http://dx.doi.org/10.1103/PhysRevC.87.054313.
[514] D. Kusnezov, W.E. Ormand, Phys. Rev. Lett. 90 (2003) 042501, http://dx.doi.org/10.1103/PhysRevLett.90.042501.
[515] B. Herskind, B. Lauritzen, K. Schiffer, R.A. Broglia, F. Barranco, M. Gallardo, J. Dudek, E. Vigezzi, Phys. Rev. Lett. 59 (1987) 2416, http://dx.doi.org/10.1103/PhysRevLett.59.2416.
[516] P. Taras, et al., Phys. Rev. Lett. 61 (1988) 1348, http://dx.doi.org/10.1103/PhysRevLett.61.1348.
[517] S. Leoni, B. Herskind, T. Døssing, A. Ataç, M. Piiparinen, Phys. Rev. Lett. 76 (1996) 3281, http://dx.doi.org/10.1103/PhysRevLett.76.3281.
[518] A. Bracco, F. Camera, S. Leoni, Nuclear Phys. A 682 (2001) 449c, http://dx.doi.org/10.1016/S0375-9474(00)00672-2.
[519] GRIT website. URL http://grit.in2p3.fr/.
[520] ORRUBA website. URL https://orruba.org/orruba/.
[521] N. Marchini, et al., Nucl. Instrum. Methods Phys. Res. A 1020 (2021) 165860, http://dx.doi.org/10.1016/j.nima.2021.165860.
[522] P. Papadakis, et al., Eur. Phys. J. A 54 (3) (2018) 42, http://dx.doi.org/10.1140/epja/i2018-12474-9.
[523] A. Stefanini, et al., Nuclear Phys. A 701 (1) (2002) 217, http://dx.doi.org/10.1016/S0375-9474(01)01578-0.
[524] D. Montanari, et al., Eur. Phys. J. A 47 (1) (2011) 4, http://dx.doi.org/10.1140/epja/i2011-11004-9.
[525] M. Rejmund, et al., Nucl. Instrum. Methods Phys. Res. A 646 (2011) 184, http://dx.doi.org/10.1016/j.nima.2011.05.007.
[526] Y.H. Kim, et al., Eur. Phys. J. A 53 (8) (2017) 162, http://dx.doi.org/10.1140/epja/i2017-12353-y.
[527] R.M. Pérez-Vidal, et al., Eur. Phys. J. A 59 (2023) 114, http://dx.doi.org/10.1140/epja/s10050-023-01027-2.
[528] H. Abusara, A.V. Afanasjev, Phys. Rev. C 79 (2009) 024317, http://dx.doi.org/10.1103/PhysRevC.79.024317.
[529] N. Schunck, J. Dudek, B. Herskind, Phys. Rev. C 75 (2007) 054304, http://dx.doi.org/10.1103/PhysRevC.75.054304.
[530] J. Dudek, T. Werner, L. Riedinger, Phys. Lett. B 211 (1988) 252, http://dx.doi.org/10.1016/0370-2693(88)90898-2, URL https://www.sciencedirect.com/science/article/pii/0370269388908982.
[531] P. Fallon, Acta Phys. Pol. B 36 (2005) 1003, URL https://www.actaphys.uj.edu.pl/fulltext?series=Reg&vol=36&page=1003.
[532] W. Korten, et al., Eur. Phys. J. A 56 (2020) 137, http://dx.doi.org/10.1140/epja/s10050-020-00132-w.
[533] G. de Angelis, et al., Eur. Phys. J. A 59 (7) (2023) 144, http://dx.doi.org/10.1140/epja/s10050-023-01032-5.